HAL open science

Long-range electrodynamic interactions among biomolecules

Mathias Lechelon

▶ To cite this version:

Mathias Lechelon. Long-range electrodynamic interactions among biomolecules. Biological Physics [physics.bio-ph]. Aix-Marseille Université, 2017. English. NNT : . tel-03598314

HAL Id: tel-03598314
https://hal.science/tel-03598314v1

Submitted on 4 Mar 2022

HAL is a multi-disciplinary open access archive for the deposit and dissemination of scientific research documents, whether they are published or not. The documents may come from teaching and research institutions in France or abroad, or from public or private research centers.

L'archive ouverte pluridisciplinaire **HAL**, est destinée au dépôt et à la diffusion de documents scientifiques de niveau recherche, publiés ou non, émanant des établissements d'enseignement et de recherche français ou étrangers, des laboratoires publics ou privés.

Université d'Aix-Marseille
Faculté des Sciences de Luminy
Ecole doctorale de Physique et Sciences de la Matière
Centre de Physique Théorique - UMR 7332

Thèse de Doctorat
Mention Biophysique

Defended by

Mathias LECHELON

Long-range electrodynamic interactions among biomolecules

Defended on December 11th, 2017, before a jury composed of:

Prof. Marco PETTINI, Centre de Physique Théorique, Aix-Marseille Université, France. **Thesis Supervisor**
Dr. Pierre FERRIER, Centre d'Immunologie Marseille Luminy, Marseille, France. **Thesis Co-supervisor**
Prof. Stefano RUFFO, International School for Advanced Studies, Trieste, Italy. **Referee**
Prof. Jack TUSZYNSKI, Department of Oncology and Department of Physics, University of Alberta , Edmonton, Canada. **Referee**
Dr. Didier MARGUET, Centre d'Immunologie Marseille Luminy, Marseille, France.**Examiner**
Prof. Luca VARANI, Institut d'Electronique des Systèmes, Marseille, France.**Examiner**
Dr. Jérémie TORRES, Institut d'Electronique des Systèmes, Marseille, France.**Examiner**
Prof. James STURGIS, Laboratoire d'Ingénierie des Systèmes Macromoléculaires, Aix Marseille Université, France.**Invited**
Prof. Marius REGLIER, Institut des Sciences Moléculaires de Marseille/BiosCiences, Aix Marseille Université , France. **Invited**

TABLE OF CONTENTS

Acknowledgments 5

Résumé long 7

PART I General framework **1**

CHAPTER 1 Theoretical framework 3

1.1 Motivation 3

1.2 Molecular interactions 5

1.2.1 Repulsion due to excluded volume 5

1.2.2 Van der Waals forces 6

1.2.3 Hamaker theory 8

1.2.4 Electrostatic interactions and Coulomb law 8

1.2.5 Screening of electrostatic interactions 9

1.2.6 From a biologic point of view 10

1.3 Brownian motion 11

1.4 Electrodynamic interactions in biology 13

1.4.1 From Jordan to Fröhlich 13

1.4.2 Fröhlich theory 14

1.4.3 Fröhlich rate equations 16

1.4.4 Need for out-of-equilibrium excitation 19

1.4.5 Experimental investigations 19

1.4.6 Behavior of electromagnetic fields in intracellular medium 21

CHAPTER 2 Technical background 23

2.1 Energy transfer 23

2.1.1 Energy level 23

2.1.2 To provide energy to the biological systems 24

2.2 Spectroscopic techniques 25

2.2.1 Raman spectroscopy 26

2.2.2 Terahertz spectroscopy devices 27

2.3 Optical techniques to study dynamics 29

2.3.1 Finding the suitable technique 30

2.3.2 Fluorescence Fluctuation Spectroscopy 31

2.4 Previous work 36

2.4.1 Experimental assessment of the contribution of electrodynamic interactions to long-distance recruitment of biomolecular partners: Theoretical basis . . . 36
2.4.2 Experimental detection of long-distance interactions between biomolecules through their diffusion behavior: Numerical study . . . 40

PART II Original contributions **43**

CHAPTER 3 Signature of collective oscillations of biomolecules . . . 45
3.1 Introduction . . . 45
3.1.1 Context . . . 45
3.1.2 Classical out-of-equilibrium phonon condensation . . . 46
3.2 Experimental work . . . 48
3.2.1 Devices . . . 48
3.2.2 Experimental detection of collective vibrations . . . 49
3.2.3 Experimental activation time scale of the collective mode . . . 52
3.2.4 Spectroscopic detection details . . . 56
3.3 Discussion . . . 57

CHAPTER 4 Experimental detectability of long range interactions . . . 62
4.1 Materials and Methods . . . 63
4.1.1 Materials . . . 63
4.1.2 FCS measurements . . . 64
4.1.3 FCCS measurements . . . 65
4.2 Experimental results . . . 66
4.2.1 Autocorrelation and data treatment . . . 67
4.3 Numerical simulations . . . 74
4.3.1 Model potential . . . 75
4.3.2 Numerical algorithm . . . 76
4.3.3 Long-time diffusion coefficient . . . 79
4.3.4 Simulation Parameters . . . 80
4.4 Additional information . . . 82
4.4.1 Quenching of the dye . . . 82
4.4.2 Checking possible crowding effects . . . 82
4.4.3 Comparison between FCS and FCCS outcomes . . . 82
4.5 Concluding remarks . . . 86

CHAPTER 5 FCS at high concentrations . . . 88
5.1 BSA with subpopulation labeled . . . 88
5.1.1 Pilot experiments previously performed . . . 88
5.1.2 Experiments involving wells coating . . . 89

5.2 Preliminary results with Optic Density filters 89
5.2.1 FCS with density filters 90
5.2.2 Improvement of SNR through statistics 90
5.2.3 FCS measurements at high concentration 91
5.3 Understanding the phenomenon at short lag times 92
5.3.1 Methods 92
5.3.2 Results 94
5.4 Discussion 99
CHAPTER 6 Experimental evidence of activation of long-range electrodynamic interactions 101
6.1 All BSA molecules labeled 102
6.2 RPE 107
6.2.1 Light intensity peaks as clusters evidences 108
6.2.2 Information out of correlated data 114
6.2.3 Input energy and threshold 116
6.3 Toward biologically relevant excitation sources 121
6.4 Discussion 123
CHAPTER 7 Conclusion 127
Appendix 130
Résumé 150
Abstract 151

Acknowledgments

I would like to express my sincere gratitude to my supervisor Prof. Marco Pettini, for his guidance and his support through these three years of PhD. I would like also to thank my co-supervisor Pierre Ferrier for his advices. I thank Ilaria Nardecchia for her precious help during my first year of thesis, and also Matteo Gori through these three years.

I would like to thank the following persons for their help and advices concerning the experiments: Jérémie Torres for the experiments concerning the terahertz spectroscopy; Sophie Brustlein, Sébastien Mailfert, Ruixing Wang and Dr. Didier Marguet for the FCS and FCCS techniques.

I am grateful to Dr. Pierre Ferrier, Dr. Didier Marguet, Prof. Marco Pettini, Prof. Marius Reglier, Prof. James Sturgis, Dr. Jérémie Torres, Prof. Jack Tuszynski, Prof. Stefano Ruffo and Prof. Luca Varani for accepting to be part of my jury.

I would like to thank my family and my friends.

Finally I also thank the ones I have forgotten in these acknowledgments.

Résumé long

Les progrès réalisés en biologie moléculaire et cellulaire sont systématiquement liés à une meilleure connaissance de la structure et des interactions fonctionnelles des biomolécules telles que l'ADN, l'ARN et les protéines. Même si ces éléments constitutifs de la matière vivante ne montrent pas d'ordre systématique apparent, il a été démontré que les processus biologiques ont une organisation temporelle bien précise, présentant un ordre dynamique. Les cellules vivantes accueillent ainsi des réactions chimiques qui sont catalysées par des enzymes et dont l'action critique peut accélérer de plusieurs ordres de grandeur le taux de réaction des biomolécules, en abaissant leur énergie d'activation. De même, les protéines qui interagissent avec les acides nucléiques comme l'ADN ou ARN (par exemple les hélicases, les polymérases, les nucléases, les recombinases) modulent certains processus essentiels impliquant ces acides nucléiques comme la duplication et la réparation de l'ADN, ou encore l'expression de gènes et leur recombinaison, et ceci avec une efficacité étonnante. Une telle efficacité soulève une question fondamentale d'un point de vue physique. Les réactions biochimiques étant pour la plupart stéréospécifiques, deux partenaires (ou plus) doivent être en contact étroit et présenter une orientation spatiale bien définie pour initier des réactions particulières. Mais comment les différents acteurs d'un processus biologique donné peuvent-ils se trouver de manière efficace? Ou plus précisément, comment une protéine peut-elle recruter efficacement le co-facteur approprié, ou se lier de manière sélective à la bonne cible d'ADN/ARN dans un environnement encombré de biomolécules? En d'autres termes, quelles forces physiques amènent tous ces acteurs au bon endroit, dans le bon ordre et dans un délai raisonnablement court pour permettre aux cellules un fonctionnement adapté, et développer ainsi la vie cellulaire? La façon la plus classique pour aborder ces questions évoque généralement le mouvement brownien. A la température physiologique, les molécules d'eau distribuées de façon omniprésente subissent un mouvement chaotique et entrent en collision avec des composants plus volumineux ou plus lourds. Le résultat de ces collisions simultanées est une force d'intensité et de direction aléatoires. Par conséquent, les grandes molécules se déplacent de façon diffuse dans les espaces cellulaires et tôt ou tard rencontreront leurs partenaires moléculaires. Cependant, ce phénomène permet-il de répondre de manière pertinente à notre problématique? De nombreux doutes émergent lorsque l'on essaie d'estimer l'activation de certains processus biochimiques, comme mentionnés ci-dessus, via la diffusion Brownienne. En effet, il s'avère que les protéines sont capables de trouver leurs partenaires entre 10 et 100 fois plus vite qu'elles ne le feraient grâce au mouvement

Brownien [157]. Sur la base de ces résultats, de nombreux auteurs ont supposé que les effets électrostatiques pourraient avoir une incidence critique sur le temps nécessaire à deux partenaires biomoléculaires pour se réunir. Cependant, les effets électrostatiques ne sont dominants que sur de très courtes distances, ce qui n'est pas le cas des champs électrodynamiques qui peuvent avoir une influence sur de très longues distances à l'échelle cellulaire.

Les biomolécules typiques (comme par exemple les protéines ou les acides nucléiques) sont chargées électriquement et ont de ce fait des moments dipolaires permanents. Il est donc naturel d'envisager le rôle que pourraient jouer les interactions intermoléculaires électrostatiques dans l'organisation dynamique mentionnée précédemment. Sur ce point, il convient de souligner que des progrès significatifs ont été réalisés dans la compréhension des interactions qui agissent à courte distance, c'est-à-dire comparables à la taille typique des biomacromolécules (environ 50Å pour les protéines) ou plus courte [31]. Mais les interactions électrostatiques peuvent aussi agir à longue distance comme dans les interactions dipôle-dipôle ou interactions Coulombiennes et, par conséquent, pourraient jouer un rôle dans l'organisation dynamique des réactions biomoléculaires dans la matière vivante. Cependant, la présence importante des ions dans le milieu intracellulaire abaisse la longueur de Debye à des valeurs inférieures à 10Å, ce qui raccourcit également la plage d'action des interactions Coulombiennes et dipolaires. De plus, la constante diélectrique de l'eau, omniprésente dans la matière vivante, est très élevée à température ambiante ($\epsilon = 80$), ce qui implique une réduction supplémentaire de la force des interactions électrostatiques. C'est peut-être pour ces raisons que les interactions intermoléculaires à longue distance ont été jusqu'ici peu étudiées en biologie. Néanmoins, bien que les interactions électrostatiques entre charges/dipôles dans l'électrolyte du cytoplasme cellulaire soient exponentiellement atténuées en fonction de la distance, l'écrantage de Debye s'avère généralement inefficace pour les interactions impliquant des champs électriques oscillants. Il a en effet été démontré expérimentalement qu'un électrolyte en conditions physiologiques soumis à un champs électrique oscillant à une fréquence supérieure à 250MHz se comporte comme un diélectrique pure (c'est-à-dire sans propriétés conductrices, de telle sorte que l'écrantage de Debye n'est plus efficace) [122, 36]. En d'autres termes, les charges/dipôles oscillant plus vite qu'une certaine fréquence ne sont pas écrantés par les charges electrostatiques et sont donc capables d'exercer des forces longue distance. Dans ce contexte, il convient également de noter que les champs électriques à haute fréquence ne sont pas écrantés par les ions libres ni affaiblis par la constante diélectrique de l'eau, qui, au-delà de quelques centaines de GHz, tombe de 80 à environ 4 [46]. Dans l'ensemble, on peut légitimement s'interroger sur le rôle de ces interactions électrodynamiques dans l'organisation des réactions biomoléculaires, par exemple en ce qui concerne les interactions attractives (potentiel négatif), qui facilitent la ren-

contre de partenaires biomoléculaires sur de longues distances. Dans ce cas, cela impliquerait que les forces électrodynamiques puissent avoir des propriétés résonantes de sorte qu'une biomolécule particulière ne serait attirée que par sa cible spécifique, et non par d'autres biomolécules voisines. A ce stade, il convient de noter que les interactions électrodynamiques sont particulièrement bien connues en électrodynamique quantique (QED) lorsqu'elles se produisent entre deux atomes neutres ou de petites molécules. Dans ce cas, il a été démontré que les interactions à longue distance sont présentes lorsqu'un des atomes est à l'état excité et que les énergies de transition des deux atomes sont à peu près similaires, c'est-à-dire à la résonance [156, 109] (les conditions hors résonance conduiraient à des interactions à courte portée). C'est la condition de dégénérescence de l'échange qui implique que les atomes sont dans un état d'enchevêtrement quantique. Cependant, comme les états intriqués sont fragiles, leur persistance sur de longues distances (plus de 50Å) dans l'environnement bruyant de la matière vivante pourrait être remise en question. Par conséquent, les interactions quantiques à longue distance entre les biomolécules sont peu probables. D'autre part, les interactions électrodynamiques peuvent également être dérivées de façon classique [140, 141]. Dans ce cas, il est possible de démontrer, comme en QED, que les interactions électrodynamiques ne sont efficaces à longue distance que dans des conditions de résonance. Ici, la résonance signifie que les moments dipolaires des deux molécules sont dues à des vibrations conformationnelles plutôt qu'à des mouvements électroniques oscillant à une fréquence commune.
Des preuves expérimentales de l'existence d'excitations collectives au sein de macromolécules ayant une pertinence biologique ont été décrites pour les protéines [125, 32, 2] et pour les polynucléotides (ADN et ARN) [124, 126, 33, 139, 49] via l'observation de modes d'oscillation basse fréquence en spectroscopie Raman et infrarouge. Ces caractéristiques spectrales sont généralement attribuées à des modes cohérents d'oscillations collectives de la molécule entière (protéine ou ADN) ou d'une fraction de ses atomes, qui pourraient être assez fortes pour être ressenties par d'autres macromolécules lointaines malgré le bruit thermique. Appliquées à la dynamique biomoléculaire, ces excitations cohérentes pourraient donner lieu à de fortes interactions dipolaires entre les biomolécules qui seraient encore actives bien au-delà de la longueur de Debye, à condition que les moments dipolaires des molécules oscillent avec la même fréquence, comme mentionné ci-dessus. Par ailleurs, Fröhlich estimait sur la base d'arguments théoriques [52, 56, 57] que les vibrations collectives des systèmes biologiques métaboliquement actifs se situeraient dans une gamme de fréquence entre 0,1 et 10 THz. Ceci est conforme aux caractéristiques spectrales des biomolécules standards [106]. On constate en particulier que la gamme des fréquences pertinentes est supérieure à 100 GHz, de sorte que les champs électromagnétiques correspondants ne sont pratiquement pas affectés par le milieu environnant (longueur de Debye et dispersion diélectrique, voir ci-dessus). Pour en revenir à la théorie des interactions électrodynamiques, Fröhlich a souligné, entre autre, que des interactions longue

distance peuvent se produire à la résonance, même si le système est proche de l'équilibre thermique. Pourtant, après des études théoriques et des estimations numériques, nous avons constaté que l'énoncé ci-dessus est erroné: outre la résonance, les dipôles oscillants doivent être hors de l'équilibre thermique pour interagir efficacement sur de longues distances [140, 141]. Plus explicitement, il s'est avéré qu'un système de dipôles interagissant à équilibre thermique donne lieu à une situation où les modes normaux du système, caractérisés respectivement par des oscillations en phase et hors phase, contribuent de la même manière à la dynamique globale, annulant ainsi tout effet à longue distance, de nature dipolaire. Ainsi, une condition hors équilibre thermique, caractérisée par la forte excitation d'un mode normal particulier du système en interaction, est requise pour que l'attraction ou la répulsion nette à longue distance puisse émerger entre les dipôles. D'un point de vue biologique, le résultat mentionné ci-dessus soulève une nouvelle question: les biomolécules des cellules vivantes peuvent-elles faire l'objet d'une telle redistribution énergétique dans l'espace des modes? Une réponse possible est encore une fois fournie par la théorie de Fröhlich [52]. Le phénomène de condensation détaillé ci-dessus, qui se caractérise par l'émergence du mode de fréquence le plus bas contenant presque toute l'énergie fournie par l'environnement, peut également être considéré comme une distribution d'énergie hors équilibre entre les modes normaux de deux molécules en interaction. Dans les systèmes biologiques, l'approvisionnement énergétique de l'environnement pourrait provenir de l'énergie métabolique issue, par exemple, de l'hydrolyse de l'adénosine triphosphate (ATP) ou de la guanosine triphosphate (GTP), ainsi que des collisions ioniques. Des travaux récents montrent que la présence de certains ions peut augmenter le taux de certaines réactions biomoléculaires, suggérant ainsi que ces ions, par leurs collisions sur des sites spécifiques des biomolécules concernées, transfèrent de l'énergie externe [136]. D'autre part, le mode de fréquence le plus bas correspond toujours à une configuration de moindre énergie qui, dans le cas de deux molécules polaires en interaction, est le mode caractérisé par une forte attraction (oscillations en phase). Ainsi, si un mécanisme tel que la condensation de Fröhlich (ou plus généralement les synchronisations dynamiques) entre molécules s'avère effectivement actif dans les systèmes biologiques, cela pourrait impliquer des interactions attractives à longue distance entre biomolécules, à condition que ces dernières partagent des fréquences communes dans leur spectre vibratoire. On suppose qu'une variété de biomolécules partage des fréquences similaires avec leurs partenaires spécifiques (en raison d'analogies ou de complémentarités conformationnelles spécifiques qui sont cruciales pour que la réaction chimique ait réellement lieu), ce qui réduirait le temps de rencontre entre ces molécules et augmenterait ainsi l'efficacité de réactions biochimiques particulières. Des éléments caractéristiques sont également présents dans les cellules: certaines études de spectroscopie Raman de cellules bactériennes et mammaliennes ont révélé que les systèmes métaboliquement actifs présentent de nombreuses raies Raman dans la gamme de 0,1 à 10 THz, alors que ces

résonances n'ont pas été observées dans les cellules au repos [172]. Etant donné qu'il faut s'attendre à un large éventail de réactions chimiques importantes sur le plan biologique pour les cellules métaboliquement actives comparativement aux cellules au repos, un tel résultat pourrait être compatible avec la présence d'effets de résonance qui influent sur la dynamique de la rencontre de partenaires biologiques apparentés. Rowlands a ainsi observé des effets pouvant provenir d'interactions longue distance du même type que celles décrites par Fröhlich. Il a notamment observé que les érythrocytes [148, 149] ont tendance à s'accumuler les uns sur les autres et à former des *rouleaux*. Rowlands [147] a également découvert que ces forces attractives se manifestent lorsque les globules rouges se trouvent à une distance mutuelle d'environ 4 μm ou moins. Les interactions entre ces cellules sont affaiblies ou disparaissent soit lorsque celles-ci sont privées de réserve d'énergie métabolique, lorsque leur membrane est désorganisée, ou même lorsque le potentiel membranaire quasi-statique est considérablement réduit. Une autre conséquence pertinente de la théorie de la cohérence de Fröhlich concerne les effets des champs électromagnétiques faibles dans les systèmes biologiques. Les travaux de Fröhlich ont ainsi inspiré quelques expériences sur l'influence des ondes millimétriques EMF (10-100 GHz) sur les systèmes biologiques. Notamment les travaux de Grundler et Keilmann [69, 68] sur la croissance des cellules de levure irradiées par un champ électromagnétique de 42 GHz avec des effets sur les taux de division cellulaire et par rapport au contrôle non irradié, ainsi que les travaux de Belyaev et al. [166] concernant l'apparente dépendance aux résonances de la conformation de la chromatine d'E.coli irradiée avec de faibles EMF, à une fréquence proche de 52 GHz. Les explications possibles de ces effets de résonance en réponse aux EMF externes impliqueraient des changements conformationnels des biomolécules qui, à leur tour, modifieraient les champs endogènes générés par leurs vibrations à basse fréquence dans l'environnement cellulaire.

Le premier chapitre de cette thèse s'intéresse aux différents phénomènes impliqués dans les interactions entre les biomolécules. La définition des interactions courte et longue distance est alors importante: dans le premier cas quand la distance entre les molécules r augmente, la limite du potentiel converge; dans le second cas, la limite du potentiel diverge quand r augmente.
Les différentes intéractions moléculaires sont ensuite brièvement rappellées: le volume d'exclusion dû à l'impossibilité des nuages d'électrons moléculaires de se chevaucher à très courte portée; les forces de Van der Waals à une échelle légèrement supérieure, qui induisent des interactions entre molécules et atomes, chargés ou neutres, avec une longueur d'action de quelques Å; enfin les interactions électrostatiques qui sont considérées comme longues distances mais dont l'action dans les milieux biologiques est réduite à quelques Ångströms à cause de la valeur élevée de la constante diélectrique de l'eau et de la forte concentration en ions des milieux. Le mouvement Brownien est abordé dans la suite de

ce chapitre. Il est décrit dans un premier temps pour comprendre son caractère aléatoire et son incomptabilité pour décrire la réalisation de phénomènes dynamiques guidés et précis des interactions biomoléculaires, puis dans un second temps via l'observation de molécules par une méthode de Spectroscopie à Correlation de Fluorescence (FCS) qui a été un outil important lors de cette étude. Ce chapitre se termine enfin sur la théorie des interactions électrodynamiques longue distance entre biomolécules, développée par Fröhlich dans un premier temps, nécessitant un apport d'énergie dans un second temps, et enfin les premières observations réalisées sur ces bases.

Le second chapitre est axé sur la partie technique de notre étude. Le transfert d'énergie a été abordé dans un premier temps, puis l'excitation des protéines via l'utilisation d'un laser et de fluorochromes fixés de manière covalente sur les protéines d'intérêt. Les méthodes pour détecter les interactions longues distances ont ensuite été décrites: nous avons utilisé tout d'abord des appareils de spectroscopie THz basé sur deux types de sondes, l'une fabriquée à partir d'un guide d'onde et d'un microfil pour la détection de champs proche, et la seconde à partir d'un transistor couplé à une antenne plasmonique. Ces techniques de spectroscopie permettent ainsi de déterminer labsorption de faisceaux THz de la solution de protéines étudiée. La seconde méthode utilisée pour étudier ces interactions est basée sur la détection de changement du comportement de la diffusion des protéines en solution. Pour cela nous avons utilisé des techniques de Spectroscopie de Corrélation ou Cross-Corrélation de Fluorescence (FCS et FCCS respectivement) avec des protéines et des marqueurs fluorescents. La fin de ce chapitre se concentre sur une étude théorique et des simulations numériques concernant ce type de technique pour la détection d'interactions longue distance, et dont les résultats confirment la possibilité et la pertinence de ce genre de mesure dans notre étude.

La partie II de cette thèse concerne ma contribution originale à cette étude et débute avec le chapitre 3 détaillant les mesures réalisées par spectroscopie THz. Nous avons donc dans un premier temps utilisé une protéine globulaire connue (l'Albumine de Serum Bovin ou BSA) marquée de manière covalente avec un fluorochrome (Alexa Fluor 488) pour permettre un transfert d'énergie à partir de la lumière absorbée. L'utilisation de dispositifs de spectroscopie terahertz basée sur des détecteurs à champs proche a permis de confirmer l'apparition de pics d'absorption vers des fréquences proches de 314 GHz, une fois les protéines de l'échantillon mises hors équilibre thermique. Les résultats obtenus suite aux expérimentations montrent la présence d'un seuil d'intensité (lorsque l'apport d'énergie du laser optique dépasse 10μW) qui laisse apparaître une raie spectrale autour de 0,314THz quand ce seuil est dépassé. En utilisant un formalisme classique pour l'analyse de condensation de phonon hors équilibre, nous avons calculé l'intensité du mode normal de vibration de la protéine BSA en fonction de la puissance de la source injectée

à la protéine. Les résultats mettent aussi en évidence un comportement semblable à celui d'un seuil d'intensité du mode fondamental qui accumule l'énergie aux dépens des modes excités, en accord avec les résultats expérimentaux. Ce seuil est également mieux mis en évidence en augmentant le nombre de modes dans les calculs numériques. Les résultats expérimentaux et théoriques présentés dans ce chapitre concordent également pour ce qui est de l'apparition d'un effet de saturation se produisant pour des valeurs élevées du taux d'apport d'énergie.
Ces premiers résultats sont en accord avec la théorie et semblent donc confirmer la possibilité d'activer des vibrations collectives de protéines hors équilibre.

Dans le chapitre 4, des expérimentations ont été réalisées pour étudier la dynamique des protéines dans des conditions similaires à celles utilisées dans le chapitre précédent. Cette étude expérimentale a été réalisée dans le but de déterminer si l'utilisation d'un appareil de Spectroscopie à Corrélation de Fluorescence serait adaptée pour étudier la diffusion de particules soumises à des forces longue distance, ici électrostatiques. Les travaux présentés dans ce chapitre concluent une étude de faisabilité visant à évaluer l'adéquation des études de diffusion pour détecter les forces intermoléculaires à longue distance, et notamment les interactions intermoléculaires électrodynamiques dans le cadre d'une future expérimentation dans des conditions adéquates. Les deux articles cités en fin du chapitre 2 de cette thèse [140, 117] ont ainsi traité ce problème d'un point de vue théorique et numérique respectivement. Les résultats des expérimentations présentés dans cette partie ont permis une vraie avancée en confirmant la possibilité d'utiliser ce type d'appareil FCS pour détecter des interactions intermoléculaires longue distance. Bien que notre but ultime soit de détecter les interactions intermoléculaires électrodynamiques à longue distance, nous avons pour l'instant testé cette technique sur un système avec interactions à longue distance intégrées, c'est-à-dire une solution de molécules de charges opposées qui interagissent par des interactions électrostatiques non écrantées. Nous avons constaté que le FCS est approprié pour détecter les interactions intermoléculaires dans les systèmes dilués, c'est-à-dire lorsque les molécules solvatées interagissent à de grandes distances, dans les expérimentations reportées dans cette thèse jusqu' à 2500Å environ. En outre, l'excellente concordance quantitative entre les résultats expérimentaux et les simulations numériques correspondantes est pertinente. D'une part, cela confirme que les phénomènes observés, à savoir le changement soudain de la valeur du coefficient de diffusion lorsque la distance intermoléculaire moyenne est abaissée au-dessous d'une valeur critique, ainsi que sa valeur en fonction de la distance intermoléculaire, sont en fait dus à l'interaction électrostatique entre les molécules solvatées. D'autre part, ceci valide l'algorithme numérique et les approximations adoptées, suggérant que ce schéma numérique peut être appliqué pour interpréter les résultats expérimentaux obtenus sur des systèmes avec des supposées interactions électrodynamiques excitées.

Après validation de la technique, et compte tenu des concentrations trop importantes de protéines fluorescentes dans les échantillons, nous avons testé et rapporté dans le chapitre 5 de cette thèse, l'utilisation de filtres de densité optique (filtres OD) pour des appareils de FCS et FCCS (Spectroscopie à Cross-Corrélation de Fluorescence). Les mesures ont pu être réalisées avec succès en FCCS, mais des problèmes techniques mettant en cause l'adsorption des protéines aux puits, et la présence de fluorochromes libres en solution ne nous ont pas permis de conclure de manière satisfaisante quant à la diffusion de la BSA. Comme l'affirment Gregor et al. [67], la précision statistique d'une mesure de FCS s'échelonne approximativement avec le carré du taux de fluorescence. Selon cette hypothèse et en considérant une mesure d'une minute avec une solution contenant un marqueur fluorescent à concentration fixe, le temps nécessaire pour effectuer des mesures similaires avec les filtres OD1, OD1.3 et OD2 serait d'environ 100 minutes, 2000 minutes et 10000 minutes respectivement. En se basant sur les résultats de nos simulations FCS et des expériences FCCS, nous pouvons conclure que l'utilisation de filtres OD ne modifie pas la forme des Fonctions de Cross-Correlation (CCF), mais augmente leur bruit. La comparaison des mesures réalisées avec le fluorophore AT488 à différentes concentrations de 1nM, 1μM et 50μM indique des temps de diffusion avec une erreur inférieure à 10%. Cette différence pourrait être diminuée et probablement permettre des mesures de temps de diffusion égaux, en augmentant le nombre d'acquisitions réalisées avec l'augmentation des valeurs de filtre OD, mais aussi en considérant différents paramètres pour le calcul de la fonction de corrélation, afin de diminuer le bruit.

Dans le chapitre 6, pour pallier aux problèmes rencontrés avec l'adsorption de la BSA aux cuvettes et le détachement des fluorophores, nous avons utilisé pour ces mêmes expérimentations en FCCS avec filtres OD, une protéine ayant un rôle important dans la photosynthèse en tant que pigment assimilateur absorbant la lumière verte et bleue, la R-phycoerythrine (RPE). Les résultats obtenus montrent que lorsque la puissance du laser utilisée avec le dispositif FCCS est suffisamment faible (expériences réalisées à 33μW), la diffusion est brownienne à partir de la concentration la plus faible (26nM correspondant à une distance intermoléculaire moyenne de 4000Å) jusqu'aux concentrations les plus élevées testées (6,05μM correspondant à une distance moyenne entre les protéines de 650Å). Cependant, lorsque la puissance du laser est augmentée (76μW et 320μW), des pics d'intensité sont visibles sur les traces enregistrées pour les concentrations les plus élevées (à partir de 800Å et 1050Å respectivement). Ce phénomène s'accompagne également de taches lumineuses observées sur les vidéos. L'analyse de corrélation des traces montre des temps de diffusion beaucoup plus longs que ceux attendus pour le mouvement brownien. Ces résultats sont conformes à la théorie précédemment développée, ce qui laisse penser que ces pics d'intensité et les taches visibles sur la vidéo sont des agrégats

formés grâce aux interactions électrodynamiques à longue portée. Enfin, le temps de relaxation des pics d'intensité est une autre preuve de la présence des agrégats dans les solutions. L'hypothèse de formation d'agrégats est également étayée par l'observation de pics d'intensité similaires dans des expériences impliquant la liaison de marqueurs fluorescents à des nanoparticules, où des pics de fluorescence sont visibles lorsque plusieurs marqueurs se lient à de grosses particules [130]. L'Analyse de l'Intensité des Pics (PIA) a également été utilisée pour mesurer la liaison des protéines aux vésicules lipidiques et aux érythrocytes [7]. Une critique constructive concernant la formation de ces agrégats et contre l'hypothèse des interactions électrodynamiques à longue portée serait de considérer que le phénomène est dû à la dénaturation des protéines. Cependant, l'état d'oligomérisation de la RPE rend sa stabilité structurelle extrêmement élevée [108]. Les changements d'absorption et d'émission de la RPE donnent également des informations ses modifications conformationnelles, induites par la chaleur ou la dénaturation chimique [167]. Le pH est un facteur important qui peut mener à la dénaturation des protéines, et Ogawa et al. [121] ont rapporté que la RPE est dénaturée à faible pH (pH=3) et crée des agrégats irréversibles. Dans cet article, ils comparent également la sédimentation de la RPE en fonction du pH de la solution. Liu et al. [98] affirment dans un autre article que la RPE présente une plus grande stabilité fonctionnelle dans la plage de pH de 3,5 à 10 par rapport à la stabilité structurelle. Dans nos expériences avec la RPE, les mesures ont été réalisées à pH=5 (pour une solution à distance intermoléculaire entre les protéines de RPE de 2000Å environ), et l'agrégation observée est réversible, reproductible et a un temps de relaxation inférieur à 7 secondes. La température est un autre paramètre qui peut conduire à la dénaturation des protéines. Dans leur article, Vaidya et al.[167] ont montré que la fluorescence de la RPE chute pour des températures supérieures à 62,8°C. De nombreux articles dans la littérature traitent également de certaines propriétés des protéines du phycobilisome (PBS) qui pourraient être étroitement liées au comportement observé précédemment. C'est le cas par exemple de la protéine caroténoïde orange (OCP) qui absorbe la fluorescence du PBS pour réduire l'excès d'énergie absorbée [155]. La superradiance d'excitons dans des cristaux de RPE a également été décrite [170]. Définie comme un phénomène d'émission spontanée de lumière provenant d'un ensemble de systèmes optiquement excités, elle a été observée à environ 600 nm avec une largeur de bande de 19,6 nm et est supposément utilisée pour le transfert d'énergie entre les protéines du PBS telles que la RPE et la phycocyanine (PC). Ce phénomène est étroitement lié à la théorie que nous avons développée, et il est possible qu'un autre exciton soit excité à des longueurs d'onde plus longues, et utilisé pour interagir à longues distances.

En conclusion de ce résumé, nous présentons dans cette thèse les premières preuves expérimentales concernant la possibilité d'activer des interactions intermoléculaires électrodynamiques à longue portée entre biomolécules. Cela pourrait ouvrir de nouvelles voies de recherche et

étendre des recherches similaires à celles rapportées ici à d'autres molécules identiques, à des molécules avec des interactions provenant de partenaires différents (ligand-récepteur, ADN-protéine) et à différents mécanismes d'excitation (par exemple l'hydrolyse ATP), à la fois in vitro et in vivo.

PART I

General framework

CHAPTER 1 Theoretical framework

This first chapter introduces the theoretical framework of our study on long range electrodynamic interactions. Starting with the description of the pathways-complexity at the molecular level, this chapter will then go through the main inter-molecular interactions encountered between biomolecules. In addition to electrostatic, chemical, dispersive forces and so on, we add the possibility of long-distance electrodynamic interactions (EDIs). Most of the concepts to which we refer concerning EDIs, have been pioneered by Herbert Fröhlich since the end of the 60's. In particular, the activation of long range electrodynamic forces acting between biomolecules were since then invoked as a possible explanation of the experimentally observed huge speed of enzymatic reactions, and more generally of the fast and precise functioning of the molecular machinery at work in living matter.

1.1 Motivation

Living beings are able to interact with or react to their environment and regulate the processes occurring at many levels down to the molecular one in remarkable ways. This property is called homeostasis and is driven by many complex interactions in cells through biomolecules mainly proteins and nucleic acids. One can understand how complex such processes are when looking at cell signaling pathways as shown, as an example by figure 1.1.

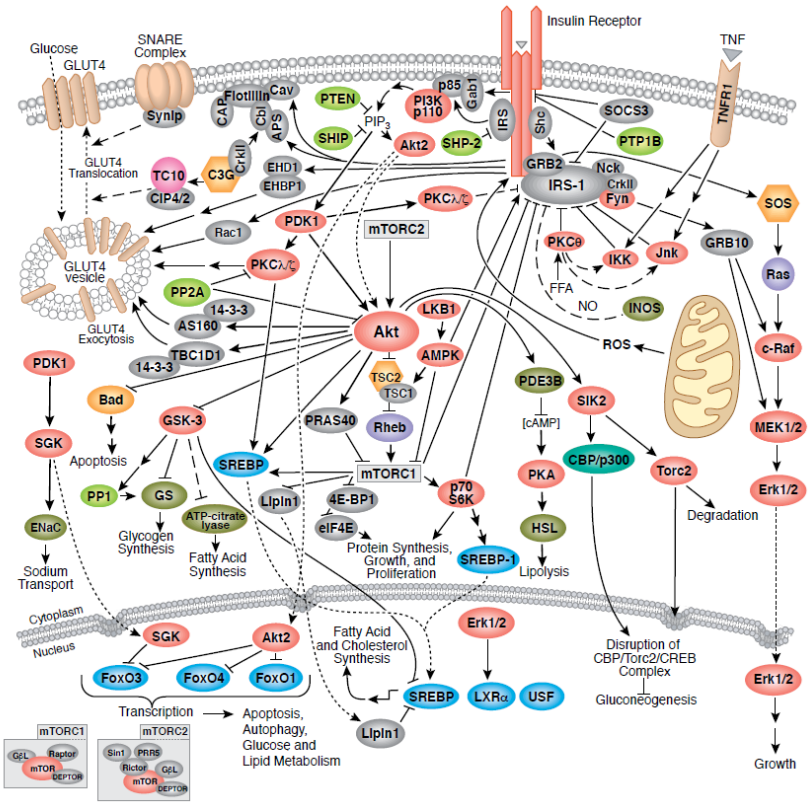

Figure 1.1: Insulin and Glucose signaling from https://www.cellsignal.com/

Two major questions arise when taking a look at these pathways:

- What makes the biomolecules to interact and stick together at short distances?
- How can these biomolecules find each others in cells at a large distance, that is, up to several hundreds of nanometers?

While interactions among biomolecules such as DNA, RNA or proteins do not exhibit strict spatial organization, the maintenance of the homeostasis and of the cell functions are based on a precise timing, with temporally, or dynamically, driven patterns. It implies that the right biomolecules have to be at the right place, at the right time and following the right sequence/organization. Biomolecules are generically experiencing Brownian diffusion, due to random collisions with water molecules, however such efficient encounters between cognate partners of biochemical reactions can hardly be explained only by such random forces, especially when the concentration of one interactor is low, because random encounters alone would lead to average meeting times much larger than the observed ones.

During the last decades, an attempt to account for accelerating mechanisms resorted to the idea of facilitated diffusion, that has been proposed by Richter and Eigen [15] to describe the *unspecifically binding of the repressor to the DNA and its diffusion along the*

chain to the operator region that serves as a target for this process. But while this model explains how molecules can quickly find their targets by sliding on the DNA strands, it fails to explain how free simple components in bulk cytoplasm can be recruited with such a precision.
Consequently, the present understanding and description of the biomolecular dynamics can be considered incomplete, and, in fact, a progress was sought by putting forward the hypothesis of the existence of mutual interactions between the biomolecular components within the cellular length scale (distances between 0.1 and 1μm), making the cognate partners able to interact dynamically and with precision. The selectivity of the interactions is another major characteristic to establish the encounter between the right molecules, and an activation mechanism is required in order to make these interactions act only at the right moment.
The following sections first describe time with short range interactions that are important for many reactions between biomolecules but are not effective at long ranges. Then electrostatic long range interactions are described, taking places in presence of charges, thought these are screened in biological media due to the high ions concentration. Finally, the Fröhlich theory is explored, revealing that electrodynamic long range interactions are possible.

1.2 Molecular interactions

Before to start, the long range and short range interaction potentials $V(\boldsymbol{r})$ are defined below. Considering r the distance between the interacting particles in a d-dimensional space, we have the following two possibilities:

$$\lim_{|\boldsymbol{r}|\to+\infty} V(\boldsymbol{r})r^d < +\infty \tag{1.1}$$

$$\lim_{|\boldsymbol{r}|\to+\infty} V(\boldsymbol{r})r^d > +\infty \tag{1.2}$$

When r increases, if the limit in equation 1.1 converges, then the potential is said to be a short range one. On the other hand, if the limit in equation 1.2, then the potential is said to be a long range one.

1.2.1 Repulsion due to excluded volume

The shortest range interactions that occur between molecules are excluded volumes forces, also known as steric repulsion. They are electromagnetic interactions due to the inhability of the molecular electron clouds to overlap, leading to repulsive forces. The excluded volume can basically be described as the volume that is inaccessible to the other

molecules in the system and is typically extended up to ten times the Bohr radius.

Their physical origin is in the Pauli's exclusion principle. These repulsions are characterized by a very short range and an intensity which steeply increases when two molecules approach each other and are described by empirical potentials. For globular macromolecules, the ideal hard sphere potential is given by:

$$U(\vec{r}) = \begin{cases} \infty & \text{if } r \leq R \\ 0 & \text{if } r > R \end{cases} \tag{1.3}$$

where R is the radius of the hard sphere.
Two other more realistic repulsive potentials are usually represented by a power law potential

$$U(\vec{r}) = \left(\frac{R}{r}\right)^n \tag{1.4}$$

where n is an integer taken between 9 and 16, and by an exponential potential

$$U(\vec{r}) = c\ e^{-r/R_0} \tag{1.5}$$

where c and R_0 are adjustable constant, with R_0 about 0.02 nm.

1.2.2 Van der Waals forces

On a slightly larger scale, Van der Waals forces are present. These forces induce interactions between all atoms and molecules, charged or neutral, with an action range in the order of the Ångström. These forces belong to quantum mechanics and quantum electrodynamics, and can be described as follow: the electrons motion of two atoms (non polar, considered in their ground state with no net charge excess and with a vanishing average dipole moment), creates at any time finite electric dipole moments leading the atoms to interact through a dispersion force. These forces result in the creation of an instantaneous dipole which generates an electric field polarizing the neutral atoms situated nearby, leading to an instantaneous, non vanishing induced dipolar moment. The energy of two isolated neutral atoms is corrected by a dipole-dipole interaction potential at the first-order perturbation expansion which is proportional to the product of the averages of the two dipole moments. This contribution vanishes when the two atoms are both in the fundamental state. Due to the coupling between instantaneous dipole fluctuations, the second-order perturbative correction is found to be proportional to $1/r^6$.

The Van der Waals forces have three origins leading to three different types of interactions as described below:

- *Keesom's interactions* or *orientation effects*, are established among two permanent dipoles whose orientation fluctuate due to thermal noise; electrostatic interactions tend to correlate the orientation of the molecules giving rise to the *Keesom potential*:

$$U(\vec{r})_{orient} = -\frac{\mu_1^2\mu_2^2}{3k_BT\left(4\pi\varepsilon_0\varepsilon_r\right)^2}\frac{1}{r^6} \tag{1.6}$$

- *Debye's interactions*, or *inductive effects*, among permanent dipoles and the dipolar moment induced by them in a non polar molecule. The Debye potential is given by [38]:

$$U(\vec{r})_{ind} = -\frac{\mu_1^2\alpha_2 + \mu_2^2\alpha_1}{\left(4\pi\varepsilon_0\varepsilon_r\right)^2}\frac{1}{r^6} \tag{1.7}$$

  where $\alpha_{1,2}$ are the polarizabilities of the molecules;

- *London's interactions*, or *dispersive interactions*, among two non polar molecules with polarizabilities α_i and first ionization energies corresponding to $h\nu_i$, whose expression is given by [44, 99]:

$$U(\vec{r})_{disp} = -\frac{1}{\left(4\pi\varepsilon_0\right)^2}\frac{3h\nu_1\nu_2\alpha_1\alpha_2}{2\left(\nu_1+\nu_2\right)r^6} \tag{1.8}$$

  where h is the Planck constant.

Keesom's and Debye's interactions are described in terms of classical electrodynamics, as they involve polar molecules. On the other hand, London's interactions between non polar molecules (although polarizable) can only be described by quantum mechanics. In the general case, two polar or polarizable molecules interact through the superposition of the previously mentioned interactions, decreasing with a power law r^{-6}, where r is the intermolecular distance:

$$\begin{aligned} U(\boldsymbol{r})_\nu &= U(\boldsymbol{r})_{orient} + U(\boldsymbol{r})_{ind} + U(\boldsymbol{r})_{disp} = \\ &= -\frac{1}{r^6}\left[\underbrace{\frac{\mu_1^2\mu_2^2}{3\left(4\pi\varepsilon_0\varepsilon_r\right)^2\kappa_BT}}_{\text{Keesom}} + \underbrace{\frac{\mu_1^2\alpha_2+\mu_2^2\alpha_1}{\left(4\pi\varepsilon_0\varepsilon_r\right)^2}}_{\text{Debye}} + \underbrace{\frac{3}{4}\frac{h\nu\alpha_1\alpha_2}{\left(4\pi\varepsilon_0\right)^2}}_{\text{London}}\right] \end{aligned} \tag{1.9}$$

which is known as Van der Waals potential. As $U(\boldsymbol{r}) \propto 1/r^6$, the corresponding force decays as $1/r^7$. Below are the main characteristics of these forces:

- anisotropy of the interaction, due to the dependence of the polarizability on the relative orientation of the molecules;

- non additivity, because of many body effects of reflection for the fields generated by molecules;

- retardation effects, only affecting the dispersive component, as it is an electrodynamic potential. These forces can then behave differently when the intermolecular distances are increased by a few nanometers, and Casimir and Polder have shown how these effects are appreciable on a length scale around $30nm$ and that for distances greater then $100nm$ London potential decreases as r^{-7} [25].

1.2.3 Hamaker theory

Hamaker derived in 1937 the Van der Waals interaction potential for two extended spheres of radii R_1 and R_2 in the vacuum [70], with two approximations: he neglected the retardation effects for all distance, and considered that the potential between two extended molecules is not affected by many body effects (neglecting the contribution of the other surrounding molecules) yielding then

$$\begin{aligned} U(z; R_1, R_2) = &- \frac{A}{6}\left[\frac{2R_1R_2}{z^2-(R_1+R_2)^2}+\right. \\ &\left.+\frac{2R_1R_2}{z^2-(R_1-R_2)^2}+\ln\left(\frac{z^2-(R_1+R_2)^2}{z^2-(R_1-R_2)^2}\right)\right]. \end{aligned} \tag{1.10}$$

where A is the so called *Hamacker coefficient*, whose value strongly depends on the properties of the medium surrounding the spheres (which can even change the sign of A), $z = R_1 + R_2 + r$ is the distance between the centres, i.e. the sum of the radii R_1,R_2 and r is the distance between the spheres surfaces.
Recent studies have pointed out that Van der Waals interactions among proteins have a range of the order $\sim 3-5AA$ and can be considered as contact interactions, therefore inadequate to drive the dynamical organization in cells if this requires to go beyond random encounters between reaction partners.

1.2.4 Electrostatic interactions and Coulomb law

Electrostatics basically describe forces exerted by electric charges between them, this is known as Coulomb law. Protons and electrons hold these charges, positive and negative respectively, indivisibles and called in this case elementary charges e, with $e = 1.602176628 \times 10^{-19}$ coulombs. If the electrons are free to move in a material this is considered a conductor, while if all the charges are fixed it is considered an insulator.
Electrostatic interactions are mainly found in three different forms: between charge/charge, charge/dipole, dipole/dipole and multipolar interactions.

- Charge/charge
  The basic expression for the pure Coulombic force between two charges Q_1 and Q_2

in a dielectric medium is:

$$\vec{F}(\vec{r}) = \frac{Q_1 Q_2}{4\pi\varepsilon_0\varepsilon_r}\frac{1}{r^2}\hat{r} \tag{1.11}$$

and the corresponding pair potential is given by:

$$U(\vec{r}) = -\frac{Q_1 Q_2}{4\pi\varepsilon_0\varepsilon_r}\frac{1}{r} \tag{1.12}$$

where r is the inter-charge distance, ε_0 is the vacuum permittivity and ε_r is the relative permittivity of the medium [1].

- Charge/dipole
  For the charge-dipole interactions the angle-averaged free energy is given by:

$$U(\vec{r}) = \frac{-Q^2\mu^2}{6\left(4\pi\varepsilon_0\varepsilon_r\right)^2 k_B T}\frac{1}{r^4} \tag{1.13}$$

  where k_B is the Boltzmann constant, T is the temperature and μ is the dipole moment.

- Dipole/dipole
  For the interaction between two permanent dipoles μ_1 and μ_2, usually referred to as the Keesom or orientation interaction, the angle-averaged free energy is:

$$U(\vec{r}) = \frac{-\mu_1^2\mu_2^2}{3\left(4\pi\varepsilon_0\varepsilon_r\right)^2 k_B T}\frac{1}{r^6} \tag{1.14}$$

  Hydrogen bonds are a specific case of dipole/dipole interactions. They occur when an hydrogen atom is covalently bound to an atom with a high electronegativity (usually oxygen, nitrogen or fluorine) creating a dipole by decentralizing the electron cloud around the electronegative atom. These interactions make water boiling point high compared to other liquids.

1.2.5 Screening of electrostatic interactions

As seen before, the electrostatic interactions are then considered as long range interaction as they satisfy the equation 1.2. In Coulomb's law (equation 1.12), the potential depends on the permittivity of the medium $\varepsilon(\omega) = \varepsilon_0\varepsilon_r(\omega)$. While the vacuum permittivity ε_0 is constant, the relative permittivity varies according to the medium. Water is the *universal solvent* in living systems, and one has thus to consider its rather high static dielectric value of ε=80 (at 20°C), when using Coulomb's law. The strength of Coulomb

[1] The permittivity, $\varepsilon(\omega) = \varepsilon_0\varepsilon_r(\omega)$, is a property of the medium as defined by means of Coulombs law Equation 1.12. The relative permittivity of a material for a frequency of zero ($\nu = 0$) is known as its static relative permittivity or as its dielectric constant.

interactions is therefore weakened by a factor of about 80 with respect to the vacuum. Beside water, ions are also necessary for vital cellular activity, participating for example to the resting membrane potential, the neuron activation or the muscle contractions. Thus they are involved in the strength reduction of the Coulomb interactions, and they change the behavior of the potential energy function, which decreases exponentially with the distance, quickly decaying to zero beyond a characteristic distance κ^{-1} called Debye screening length. The screened Coulomb interactions are then described according to the Deby-Hückel theory by the following equation:

$$U(\vec{r}) = -\frac{Q_1 Q_2}{4\pi\varepsilon_0\varepsilon_r}\frac{e^{-\kappa(r-2R)}}{(1+\kappa R)^2}\frac{1}{r} \tag{1.15}$$

κ is the inverse Debye-Hückel length, and is defined as follows:

$$\kappa = \left(\frac{e^2 N_A}{\varepsilon_0\varepsilon_r k_B T}\sum_j Z_j^2 n_j\right)^{1/2} \tag{1.16}$$

where e is the electronic charge, N_A is the Avogadro's number, Z_j is the ionic valence and n_j is the number concentration of the jth ion. In aqueous electrolyte solutions, typical values for κ^{-1} are about 10nm and 1nm for solutions of 10^{-3}M and 0.1M respectively.

1.2.6 From a biologic point of view

Analyzing the biomolecular interactions in cells has lead to the description of networks connecting many of the cell molecules, called the interactome. The interactomics being a science comparing these interactomes. They are mostly used to describe protein-protein interactions (PPIs) as proteins are the main agents of biological functions, but also enter genetic interactions.

PPIs thus concerns us directly as we are interested in proteins interactions. However, nowadays they are mainly described as physical contacts considering hydrophobic or electrostatic interactions, protrusion, planarity, accessible surface area and many other parameters, some being obligatory, some permanent and some others transient [82]. Most of these PPIs are due to hydrophobic effects, though hydrogen bonds, electrostatic interactions, and covalent bonds are also found. But could long range elctrodynamic interactions enter the PPIs schemes? These electrodynamic interactions could bring new information about protein association prediction and the way they interact.

1.3 Brownian motion

Brownian motion is a natural phenomenon describing the random motion of particles immersed in a fluid, subject to shocks with the molecules of the surrounding fluid.

Historically, Brownian motion is explicitly referring to Robert Brown, a naturalist who observed in 1828 the chaotic motion of very small particles of pollen grains in water. Similar observations have also been made during the 18th and 19th centuries by Jan Ingenhousz and John Tuberville Needham for example. While these motions were soon attributed to collisions with the microscopic constituents of matter, their origins has been debated until the beginning of the 20th century.
The difficulty in modeling the Brownian motion comes from its stochastic properties leading to a statistically null displacement. More specifically the sum of the particles velocities cancels out at a time t, and the barycenter of a particle trajectory overlaps its starting point. Louis Bachelier showed in 1900 that Brownian motion is characterized by the root mean square and not the arithmetic mean, which has lead to the mean squared displacement (MSD):

$$MSD = \langle |\vec{r}(t) - \vec{r}(0)|^2 \rangle \tag{1.17}$$

where $\vec{r}(t)$ denotes the observed position of the Brownian particle at time t. The MSD is then increasing linearly with time. Few years later, the theory of Brownian motion was developed by Einstein[43] and, independently at the same time, by Smoluchowki [168], soon followed by experimental confirmation by J. Perrin in 1908 [131, 132]. In 1905, Einstein proposed a statistical mechanical approach to study the behavior of these macroscopic particles in suspension, which was revolutionary. By attributing the origin of the observed motion of suspended particles to random collisions with environmental molecules, he looked for macroscopic observable and he realized that the quantity involving Brownian motion which can be best observed is the diffusivity:

$$D = \lim_{t \to \infty} \frac{1}{6t} \langle |\vec{r}(t) - \vec{r}(0)|^2 \rangle \tag{1.18}$$

where t is simply taken as some satisfactorily long time of observation, and there is no need for fine temporal resolution as there would be if the velocity was to be measured. If the diffusion is considered in a two-dimensional system, then the factor 6 in equation 1.18 becomes 4, and similarly, in one-dimensional systems it becomes 2. The particle motion is therefore attributed to random collisions with solvent molecules, and it is a random motion at least when viewed on a time scale τ larger than the time required to dissipate the velocity acquired in a single collision. Between two collisions with molecules, the velocity $\vec{v}$ of a particle is dissipated by friction with the environment, exerting a force F

which is described by Stokes's law as follow:

$$m\frac{\partial \vec{v}}{\partial t} = \vec{F} = -6\pi\eta R\vec{v} \tag{1.19}$$

where η is the viscosity of the fluid, R is the particle radius and v is the velocity. The characteristic time scale for the speed dissipation after a collision is:

$$t_0 = \frac{m}{6\pi\eta R}. \tag{1.20}$$

This time is usually very short. As an example, if $R = 1\mu m$ and m is calculated assuming the same density of the solvent (water), the time scale is $t_0 \simeq 10^{-7}s$. But considering long time scales such as $\tau \gg t_0$, the motion then has a diffusive character.
Einstein related the diffusivity D of a Brownian particle to its hydrodynamic friction coefficient f_0 with an argument based on equilibrium statistical mechanics, and found the following equation known as Stokes-Einstein equation:

$$D_0 = \frac{k_B T}{f_0} \tag{1.21}$$

When considering spherical particles of radius r, Stokes' law gives:

$$f_0 = 6\pi\eta r \tag{1.22}$$

with η the viscosity of the medium, and Stokes-Einstein equation for macroscopic spheres in this medium becomes:

$$D_0 = \frac{k_B T}{6\pi\eta a}. \tag{1.23}$$

To this point we have focused on Brownian motion in simple model solutions, but what is happening in cells of living systems? We have first to consider the diffusion of the biomolecules as a whole, being a function of their concentration, charge, ionic strength of the medium, modulating the interactions both electrostatically and electrodynamically, the interacting particles affecting both the individual and the suspensions behavior on microscopic and macroscopic scales respectively.
The number of proteins in the cellular environment and their concentration are therefore important information when referring to protein diffusion in cells. Half of the total dry mass is made of proteins, and Ron Milo has estimated in his article [111] that there are about 2 to 4.10^6 proteins/μm^3 in bacteria, yeast and mammalian cells. With such high concentrations of proteins, a phenomenon called molecular crowding appears, involving the reduction of the available volume for the solvent. In their article, Banks et al. [12] have imitated the crowded conditions of cellular environment by studying the diffusion of tracer proteins in highly concentrated random-coil polymer and globular protein solutions,

and they observed an anomalous diffusion indicating the behavior of the proteins in the cytoplasm and nucleus.
As seen earlier in equation 1.17, the MSD has been presented in case of normal diffusion or Brownian diffusion, and increases linearly with time. The solution of the diffusion equation thus yields:

$$MSD = 6Dt. \tag{1.24}$$

But in complex media, one might expect the MSD to obey a power law:

$$MSD = 6\Gamma t^{\alpha}, \tag{1.25}$$

where Γ is a constant which does not depend on time. The MSD is then describing 3 different behaviors according to α:

- If $\alpha = 1$, the diffusion is normal
- If $\alpha < 1$, the diffusion is anomalous and is called subdiffusion
- If $\alpha > 1$, the diffusion is anomalous and is called superdiffusion

1.4 Electrodynamic interactions in biology

Could there be additional phenomena beside Brownian motion that could make biomolecules to interact one with the other even if separated by long distances? Could there be long range interactions between biomolecules?

1.4.1 From Jordan to Fröhlich

We have previously seen that many short range interactions are already described in biology. Electrostatic forces, which are long range interactions in vacuum, are also present but are screened and therefore become short range, due to the high dielectric constant of water and the concentration of ions in cells. Then we have described the Brownian motion as a possible mechanism driving proteins encounters, but since it is a random motion, time and place of the interactions are not precisely controlled and random forces are neither efficient nor selective. As a consequence, electrodynamic interactions can be seen as possible forces to overcome these limitations.
Two oscillating dipoles can indeed electrodynamically interact, and the long range nature of the interaction potential can be selected according to the proximity of the dipoles frequencies that is when the dipoles are at resonance. Two molecules with dipole moments oscillating at the same frequency can therefore undergo a resonant interaction described

by:

$$U(r) \propto -1/r^3 \tag{1.26}$$

with r the intermolecular distance.
If the molecules are oscillating dipoles off-resonance then the interaction potential consequently generated created is similar to a Van der Waals potential i.e.:

$$U(r) \propto -1/r^6, \tag{1.27}$$

which is a short range potential as seen in equation 1.1. Thinking of biomolecules as dipoles being able to interact with electrodynamic forces is a relevant approach because the interactions can be switched on when the dipoles are oscillating at resonance, and switched off when the dipoles oscillate off resonance or at rest. This type of interaction being frequency-selective could be very helpful during the approach of a molecule toward its specific cognate partner. Pascual Jordan was one of the first to describe a similar model, proposing that resonant interactions within a quantum framework could play a significant role in autocatalytic reactions or influence the process of biological synthesis in such a way that replicas of molecules present in the cell could be formed [83, 84]. He proposed first that the attraction of identical molecules (or of molecules containing identical groups of atoms), could be caused by quantum mechanical resonance phenomena. He wrote that these interactions could influence the reproduction of biologically specific molecules, for example antibodies or enzymes. However some other scientists such as Pauling and Delbrück have questioned his theory [129], estimating that such forces occurring between two molecules, could not be strong enough to create a specific attraction between proteins under the thermal conditions of excitation and perturbation prevailing in living organisms. The selectivity described between biomolecules have also been proposed to come from the basis of usual Van der Waals forces [128, 79].
In parallel in 1968, a dynamical model has been proposed by Herbert Fröhlich [52], to account for the capacity of biological systems to self-regulate, emphasizing that under specific conditions of energy supply to the systems, part of this supply would not be completely thermalized but would be used to create order in response to environmental perturbation.

1.4.2 Fröhlich theory

Herbert Fröhlich was a British physicist elected a Fellow of the Royal Society in 1951, born in Germany in 1905 and died in 1991 in England. As stated by his wife Franchon Fröhlich in G. J. Hyland's book [77], *"... he frequently left the jigsaw unfinished, but in a form that allowed others to come along and complete it at a later date"*. In this same book, G. J. Hyland resume the work of Fröhlich saying *his most influential work has been*

his introduction of the methods of quantum field theory into solid-state physics and he has been a pioneer in many topics and predicted *(i) a neutral meson and a quartet of vector mesons, (ii) a partial anticipation of the Lyddane-Sachs-Teller relation, (iii) an interaction between the nuclear spins in a metal mediated by conduction electrons, (iv) hot electron physics, (v) ferroelectric soft modes, (vi) polaritons, (vii) a phonon-mediated electron-electron attraction as the basis of superconductivity, (viii) sliding modes in low-dimensional conducting systems, (ix) the importance of size effects in finite samples, both in solid-state physics and biology.*

Fröhlich first introduction to biology, as reported in [77], was around 1938 in Bristol, thanks to his endocrinologist friend Max Reiss. The latter told him that the membrane potential in living cells is about 100mV, and Frölich estimated the membrane vibration around 50GHz considering an elastic constant corresponding to a sound speed of 10^5 cm/s. But the first scientific contribution of Fröhlich in biology began around 1965. He met Maurice Marois, a professor of Medicine at the Sorbonne who invited him to help organizing the first international conference entitled *Theoretical Physics and Biology*, conferences that continued until 1988. Soon after, in 1968 he then published his first article related to biology, named *Long-Range Coherence and Energy Storage in Biological Systems* [52] which is one of his most influential works. In this article he states that biological systems are expected to have a branch of longitudinal electric modes in a frequency region between 10^{11} and 10^{12} $\sec^{-1}$ thanks to electric dipole components such as:

- The cell membrane.
- Certain chemical bonds and particularly hydrogen bonds.
- Regions containing non-localized electrons.

According to Fröhlich, the systems would thus behave like Bose Einstein condensates: *if the rate of energy supply is sufficiently large then the energy gets channeled into a single mode which then presents a strongly excited coherent longitudinal electric vibration.*

In the end of the article few techniques are proposed to detect these long range interactions:

- Raman-like scattering
- Investigation of infrared properties
- And indirect methods considering screening of these interactions between cells.

But at that time the technology was not enough powerful to make such measurements, and the radiation generating and detecting techniques exhibited the famous terahertz gap. About this Fröhlich exclaimed *"How typical for Nature to take advantages of our experimental incapabilities!"* .

1.4.3 Fröhlich rate equations

If we consider non homogeneous systems with charged particles, long waves electric vibrations are expected, with the lowest frequency, say $\nu_1 = \omega_1/2\pi$, different from zero. The system of interest is considered to have ω_z independant vibrating modes $(\omega_1, \omega_2 \ldots \omega_z)$ that are just interacting with the environment. When excited by an energy supply from a source, the total contribution of the set of normal modes is given by:

$$W_s = \sum_{k=i}^{z} \langle s_i \rangle h\nu_i \tag{1.28}$$

with $\langle s_i \rangle$ the average number of energy quanta supplied to the $i-th$ mode, with frequency ν_i.
The Fröhlich model is based on three main ingredients:

- A system of Z independent quantum oscillators (bosons) coupled to a pump and a thermal bath.
- A linear coupling to the energy source.
- A non linear coupling term so that a quantum of energy is destroyed and one or more quanta are created, the thermal bath compensating the energy difference.

Thus the system of interest is an open system with oscillators subjected to collective motions (or normal modes) at frequencies ω_i where $\omega_1 < \omega_2 < \ldots < \omega_Z$ $(1 \leq i \leq Z)$. Considering $\langle n_i \rangle$ as the average number of quanta (or phonons) in the mode with frequency ω_i, and $\langle s_i \rangle$ the rate of the energy supply to this mode, the rate equation of phonons transfer in the ith normal mode postulated by Fröhlich is [52, 56]:

$$\begin{aligned} \frac{d\langle n_i \rangle}{dt} &= \langle s_i \rangle - \varphi_i \left[\langle n_i \rangle e^{\beta\hbar\omega_i} - (\langle n_i \rangle + 1) \right] \\ &\quad - \sum_{j=1}^{Z} \Lambda_{ij} \left[\langle n_i \rangle (\langle n_j \rangle + 1) - \langle n_j \rangle (\langle n_i \rangle + 1) e^{\beta\hbar(\omega_j - \omega_i)} \right] \end{aligned} \tag{1.29}$$

where $\varphi_i \equiv \varphi(\beta, \omega_i)$ is the coefficient associated to the loss of energy to the bath related with the linear excitation or de-excitation of the mode i, and $\Lambda_{ij} \equiv \Lambda(\beta, \omega_i, \omega_j)$ is the coefficient associated to the redistribution of energy within the system connected with the quadratic excitation of the mode i with the de-excitation of the mode j, or the quadratic excitation of the mode j with the de-excitation of the mode i [144]. The coefficients φ_i and Λ_{ij} both generally depend on the temperature. This equation 1.29 describes the change in time of the average occupation number n_i of the ith normal mode.
The oscillators are independent and at thermal equilibrium, when the pumping rate is zero $S = \sum_i \langle s_i \rangle = 0$, the average number of quanta in each mode is given by the Planck

distribution function:

$$\langle n_i \rangle = \frac{1}{e^{\beta\hbar\omega_i} - 1}. \tag{1.30}$$

However, when there is an energy supply, the steady state solution of the Fröhlich's rate equation shows that under some conditions the energy fed into the system is condensed in the lowest vibrational mode instead of being thermalized, due to the non-linear couplings. When the stationary state is achieved, $\langle \dot{n}_i \rangle = 0$, Fröhlich showed that if the total rate of external energy supply to the system S exceeds a certain threshold, the average number of phonons present in the set of oscillators increases linearly, $\langle N \rangle = \sum_i \langle n_i \rangle$. This is similar to the Einstein condensation of a Bose gas, with the condensation into the lowest mode ω_1. Thus while the secondary modes of the system are quickly saturated, the system has an infinite capacity for energy storage at increasing N. And for high enough values of S, $\langle n_1 \rangle \sim \langle N \rangle$. This thus means that each oscillator tends to vibrate around the frequency of the lowest vibrational mode, ω_1.

Considering the macromolecules as giant oscillating dipoles, let us see when selective long range electrodynamic interactions may be activated between them. If two dipolar molecules A and B vibrate at ω_A and ω_B respectively, the potential behave differently according to the frequency values:

- When $\omega_A \simeq \omega_B$, the creation of a giant dipole activates a long range interaction, with $U(\vec{r}) \sim r^{-3}$.
- When $\omega_A \gg \omega_B$, the intermolecular interaction is a short range one, with $U(\vec{r}) \sim r^{-6}$.

The overall interaction potential is therefore described as follow [54]:

$$U(\vec{r}) = -\frac{\alpha}{r^3} - \frac{\beta}{r^6} \tag{1.31}$$

with α and β the interaction coefficients. New frequencies ω_+ and ω_- are given by:

$$\omega_\pm^2 = \frac{1}{2}\left(\omega_A^{\,2} + \omega_B^{\,2}\right)\left[1 \pm (q^2 + Q^2)^{1/2}\right] \tag{1.32}$$

where

$$q = \frac{\omega_A^{\,2} - \omega_B^{\,2}}{\omega_A^{\,2} + \omega_B^{\,2}} \tag{1.33}$$

and

$$Q = \frac{\gamma e^2 (z_a z_b^{1/2})}{M R^3 (\omega_A^{\,2} + \omega_B^{\,2})} \tag{1.34}$$

γ is a size/shape dependent coupling parameter, $z_{a,b}$ are the numbers of elementary charges e of the molecular dipoles of equal mass M, and R is the distance between the macromolecules. Q is essentially the ratio of the interaction energy between the two giant dipoles (at some given excitation level) to their internal potential energies [52, 57, 56]. The collective vibrations are expected in a frequency range of $10^9 - 10^{12}$Hz, and more precisely $10^{10} - 10^{11}$Hz for the membranes, 10^9Hz for the DNA and RNA, and $10^{12} - 10^{14}$Hz for proteins [57].

Fröhlich's model can also be described in a classical way with real oscillators instead of quantum fluctuations. With a one dimensional model for simplification, and two oscillating dipoles vibrating at frequencies ω_A and ω_B respectively to model the persistent elastic vibrations of the two molecules, the interaction energy between A and B has been computed for two different cases.
Firstly, if we consider the dipoles as oscillating at different frequencies such as $\omega_A \gg \omega_B$, or $\omega_A \ll \omega_B$, then the energy values of the system are given by:

$$\begin{aligned} E =& \hbar\omega_A \left(n_+ + \frac{1}{2}\right) + \hbar\omega_B \left(n_- + \frac{1}{2}\right) + \\ & \frac{\hbar\beta^{\ 2}}{2\left(\omega_A^{\ 2} - \omega_B^{\ 2}\right) M^2 R^6} \left\{ \frac{1}{\omega_A}\left(n_+ + \frac{1}{2}\right) - \frac{1}{\omega_B}\left(n_- + \frac{1}{2}\right) \right\} + ... \end{aligned} \tag{1.35}$$

with M being the mean mass, R is the mutual separation between A an B, n_+, n_- are integers, and $\beta = \zeta q^2 (Z_A Z_B)^{1/2}/4\pi\varepsilon_0$ (with Z_A and Z_B the effective number of charges of A and B respectively). The first two terms of equation 1.35 correspond to the unperturbed energies of the molecules A and B considered as isolated ($R \to \infty$). The last term provides the lowest order correction to the unperturbed energy of the system and due to the interaction, this interaction potential energy is proportional to R^{-6}. This interaction is functionally the same as the London interaction, but with a different physical origin.
Secondly, at resonance, when $\omega_A \simeq \omega_B = \omega$, the energy is defined by:

$$\begin{aligned} E =& \hbar\omega \left(n_+ + n_- + 1\right) + \\ & \frac{\hbar\beta}{2M\omega R^3}\left(n_+ - n_-\right) - \frac{\hbar\beta^2}{8M^2\omega^3 R^6}\left(n_+ - n_- + 1\right) + ... \end{aligned} \tag{1.36}$$

The first order correction to the energy of the system corresponds to the interaction energy between the two molecules at resonance and is proportional to R^{-3}. The corresponding force is then

$$f(R) = -\frac{3\hbar\beta}{2M\omega R^4}\left(n_+ - n_-\right). \tag{1.37}$$

1.4.4 Need for out-of-equilibrium excitation

At variance with a long-standing belief, it is shown that sizable resonant long-range interactions may exist only if the interacting system is out of thermal equilibrium. Long-range electrodynamic interactions in biological systems are to be considered as occurring between molecules whose dipole moments are due to conformational vibrations rather than electronic transitions. According to Fröhlich, the possibility of long-range interactions between two biological "real dipoles" may occur at resonance even if the system of dipoles is close to thermal equilibrium. Among others, an intriguing results of Fröhlich computations is the possibility of observing resonant long-range interactions even if the system of oscillating dipoles is at thermal equilibrium. In the dipole approximation, the thermal average potential was given by [54, 57]

$$U(r) \propto \frac{1}{r^3}\left(\frac{1}{\epsilon(\omega_+)} - \frac{1}{\epsilon(\omega_-)}\right) + O\left(\frac{1}{r^6}\right) \tag{1.38}$$

where $\epsilon(\omega_\pm)$ stands for the permittivity of the medium at the normal frequencies $\omega_\pm$ of the interacting system. In refs [141, 143], it has been proved that the form of the potential (1.38) is incorrect, suggesting that long-range interactions exist only if the system is out of equilibrium. This circumstance might perhaps explain why these EDIs have hitherto eluded experimental detection if all the attempts have been performed in systems at thermal equilibrium.

1.4.5 Experimental investigations

Following the first hypothesis of collective vibrations, some scientific teams have performed experiments to explore the field. Some of them have first experimented with cells, and twenty years later after the proposal of the theory, Fröhlich wrote a paper about some of these experiments [58]. First, he described the influence of energy flux as required by the theory, through sharp temperature changes yielding to drastic changes in cress roots and luminescent bacteria, supporting the existence of phase transition. However it does note prove the existence of characteristic vibrations, and some observations made by Rowlands have helped to investigate this way [147]. The erythrocytes that he observed used to array themselves in stacks called *rouleaux*. He also found that when the cells were at a distance of 4μm, attractive forces were present. And these interactions could disappear or at least weakened when the red cells are deprived of metabolic energy stores, or when the membranes are disorganized. Moreover, Fröhlich reported that the membrane vibrations have been estimated in the range 10^{10} - 10^{11} Hz, and that membrane vibrations for erythrocytes have been measured at 36.7 GHz [18], in agreement with the theory. Finally, metabolically active systems of bacterial and mammalian cells have shown many Raman lines in the range of 10^{10} - 10^{13} Hz, when no resonance were observed in resting cells [172].

Collective excitations have been observed for biomolecules essentially through Raman spectroscopy (see chapter 2.2.1 for more details about the technique). In a first place, Raman lines observed on DNA have been attributed to inter-helical vibrations [164, 165]. Both A-form and B-form of the DNA have been shown to have bands at 85 cm^{-1}. The A-form also have a band at 22 cm^{-1} which tends to soften and disappear according to the A-B conformational changes.
For proteins, studies on collective vibrations started in 1972, with the observations of Brown et al. [21] who found that the α-chemotrypsin protein had a Raman band near 29 cm^{-1}, and Genzel et al. [62] later found a similar vibration for the lysozyme near 25 cm^{-1} on the Raman spectrum. Painter et al. have also reported, in an article [125] in 1982, a list of low-frequency modes in Raman spectra observed for different proteins and visible on figure 1.2. According to the size and the shape, low frequency modes are detected around 15 - 35 cm^{-1} for globular proteins.

Protein	Molecular Weight		Observed Raman Line (cm^{-1})
Insulin	Monomer	5800	22
	Dimer	11,600	
Ribonuclease A		13,700	Not observed
Lysozyme[a]		14,000	25
β-Lactoglobulin	Monomer	18,000	25
	Dimer	36,000	
α-Chymotrypsin[b]		22,600	29
Pepsin[b]		35,000	20
Ovalbumin		44,000	22
Concanavalin A		55,000	20
Bovine serum albumin		67,000	14
Bovine immunoglobulin G		150,000	28
			36 sh.
Adolase		158,000	32
Thyroglobulin		669,000	17
Silk		Unknown	Not observed

[a] Data from W. Varnell and M. Karplus (personal communication).
[b] Data from G. Zerbi (personal communication).

Figure 1.2: Table from [125], with low-frequency Raman bands observed for some biomolecules.

Finally, the idea of electrodynamic interactions among biomolecules also leads to the question of the impact of external electromagnetic fields (EMF) on biological systems. Fröhlich work has thus inspired some researches involving millimetric EMF (in the range 10 - 100 GHz), such as Grundler and Keilmann who made yeast cells grow in EMF of 42 GHz and confirmed a non-thermal resonant microwave sensitivity by comparing with non irradiated cells [69, 68]. Belyaev et al. [166] also studied millimeter waves effects on chromatin conformation in Escherichia coli (E. coli) cells and rat thymocytes, and they found a strong dependence of millimeter waves effects on frequency and polarization at non-thermal power densities. One of the possible explanation for the EMF effects on biological systems is the conformational change of the biomolecules (such as proteins), which would lead to a modification of the endogenous fields generated by their low-frequency vibrations.

1.4.6 Behavior of electromagnetic fields in intracellular medium

With this new hypothesis of electrodynamic interactions among biomolecules in vivo, there is a remaining question: *Is the cellular environment suitable in propagating such electrodynamic field?* The question is worth asking because electrostatic field is indeed screened, as described before, making the Debye length less than 10 Å with the high ionic strength of the intracellular medium and the high dielectric constant of water. However when dealing with electrodynamic fields, the Debye screening is generally inefficient. Xammar Oro et al. [123, 36] have experimentally shown that an electrolyte solution with physiological-like conditions is expected to behave like a pure dielectric when it is submitted to an electric field oscillating with a frequency higher than 250 MHz. This basically means that if the molecular dipoles oscillate with an higher frequency than this threshold, the electrolyte in the surrounding is not going to screen this electrodynamic field, leading to possible long range interactions.

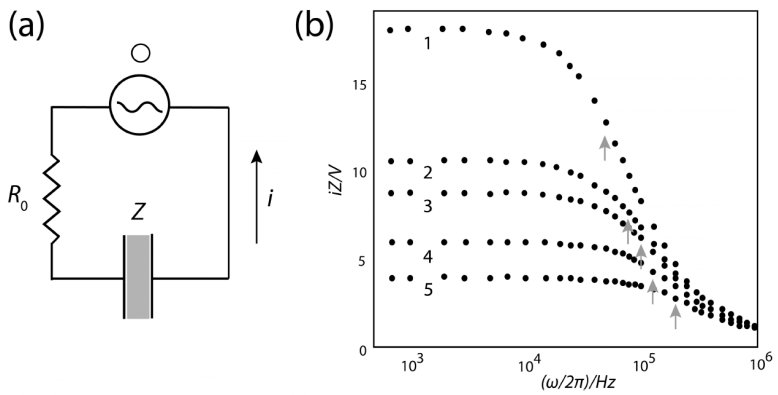

Figure 1.3

In addition, the dieletric properties of water are different when subject to high-frequency electric field. As reported by Ellison et al. [46], ε_r is about 4 when the electrodynamic field is beyond a few hundred of GHz. The relative permittivity, which corresponds to the ratio of the absolute permittivity of the medium of interest to the vacuum permittivity with $\epsilon_r(\omega) = \epsilon(\omega)/\epsilon_0$, can also be treated as a complex function of the frequency ϵ of the applied field because it depends on its frequency, and it is then described as

$$\epsilon_r(\omega) = \epsilon_r'(\omega) - i\epsilon_r''(\omega) \tag{1.39}$$

with i the imaginary unit. Figure 1.4 shows the behavior of the real and imaginary components of the relative permittivity according to the frequency of the applied field.

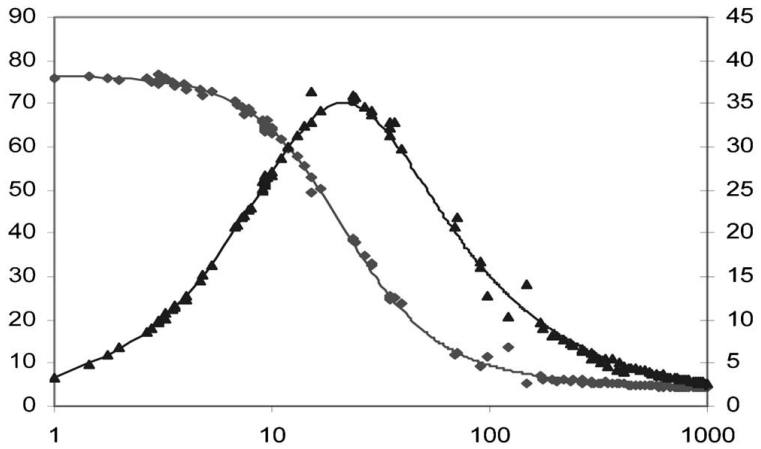

Figure 1.4: Adapted from [46]. Water permittivity at 300 Kelvin as a function of frequency (in GHz), for theoretical (lines) and experimental measurements (dots). The real part of permittivity ϵ' is reported with diamonds (referred to the left axis), and the imaginary part ϵ" with triangles (referred to the right axis).

CHAPTER 2 Technical background

2.1 Energy transfer

Understanding the energy transfer occurring in biomolecular systems of interest is an important milestone, and we have focused on photon absorption and emission. In a first time, we have used fluorochromes to supply energy to "switch on" collective vibrations of proteins. As seen previously, to study these collective vibrations, Raman spectroscopy has been one of the first techniques used to observe low frequency modes. Fourier Transform Infrared spectroscopy (FTIR) is also described as a complementary method to Raman spectroscopy for such studies. Moreover, we have used techniques involving fluorescent properties of some dyes or proteins as seen in part II, and fluorescence is a phenomenon that is described by electron rearrangement leading to similar vibrations or rotations of the molecules as seen in Raman and FTIR.

2.1.1 Energy level

Atoms, ions and molecules are described as quantum mechanical systems on atomic length scale or smaller. They have discrete values of energy and are therefore quantized. In accordance with our studies we are interested in molecules, and especially macro molecules such as proteins. In this case, the atomic orbitals of the atoms forming the molecule combine, leading to the formation of molecular orbitals. The atoms are thus chemically (or covalently) bond and three types of molecular orbitals are formed:

- Bonding orbitals with the lowest energy level.
- Anti-bonding orbitals with the highest energy levels.
- Non bonding orbitals with electron that do not participate to the bonding, and the energy level is the same as that of the constituent of the atom.

Energy transfers are done between molecules, and their environment, through photons, leading to change of electrons on energy levels (transitions). If the photon's energy $h\nu$ (with h the Planck's constant and ν the frequency) is exactly the same as between two energy levels, then it can be absorbed, or emitted according to the situation. In the case of absorption, a molecule goes from the ground state (lowest possible energy level) to the excited state (higher energy level) through the photon absorption. In the case of

emission, the molecule goes from the excited state to the ground state with the emission of a photon.

For a better visualization and understanding of the molecular energy level, they are often represented through molecular orbital diagram, Franck-Condon diagram and Jablonski diagram as seen on 2.1 from A to C respectively.

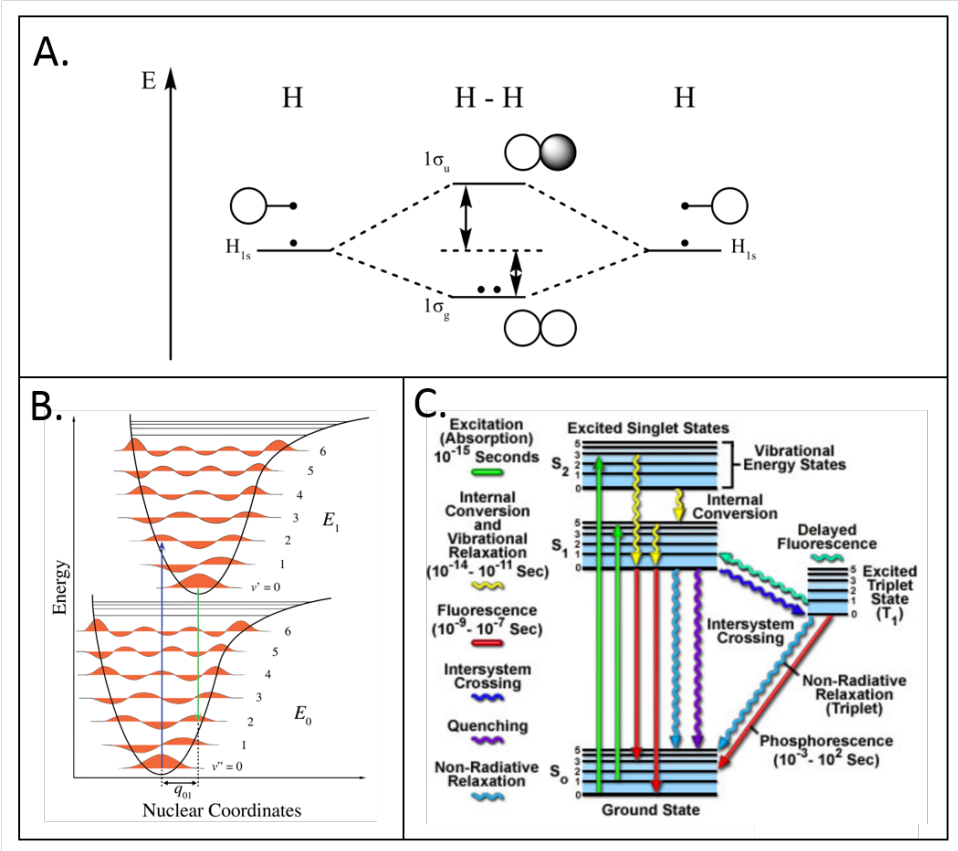

Figure 2.1: Examples of molecular orbital diagram in A, Franck-Condon diagram in B and Jablonski diagram in C.

2.1.2 To provide energy to the biological systems

As an energy input is required to excite the collective vibrations of proteins, we consider here the probable sources of energy available in the biological systems. In a first place, Adenosine Triphosphate (ATP) is often referred to the *molecular unit of currency of intracellular energy transfer.* It is used for transport work, mechanical work and chemical work in the cells. It is notably used as substrate for kinases to transfer phosphate groups onto proteins through a process called phosphorylation. When a phosphate group is removed from ATP, the reaction is exothermic and an important amount of energy is released (up to 30.5 kJ.mol^{-1} as seen later in chapter 6). This is of capital importance according to our research, and it has been envisaged as reported at the end of chapter 6. The transfer of energy through light is also considered. Indeed, some molecules in cells

are light-sensitive, and it is the case of the flavin cofactor which is known for its electron-transfer and redox catalysis. It is used in photoreceptor proteins such as cryptochromes, which are implicated as the active components controlling circadian rhytms [94]. Cryptochrome 2 is also used in optogenetic field as a tool for homo-oligomerization and hetero-oligomerization with its binding partner CIB1 [162]. The light source can be external to the biological system, such as the sun light which is used, for example, through photosynthesis in plants and bacteria. A protein present in a light-harvesting complex has been used in experiments performed in chapter 6. But internal light sources also exist. We can thus refer to biophotons which have been described as being emitted by biological tissues, ranging from 200 nm to 800 nm with a photon count from a few to a thousand photons per cm^2 [138]. They are produced through chemi-excitation via oxidative stress or enzyme catalysis [34].
Finally some studies also focused on the effect of sound vibrations to regulate gene transcription [63], facilitate enzymatic reactions [80] or more broadly to study transcriptomic, proteomic and hormonal changes [64]. Some plants have thus been reported to react at caterpillars chewing vibrations [8], or to locate water using sound [59]. Similar experiments have been quickly tested and reported in the appendix.
Among these possibilities to excite proteins, we have used light excitation. First, it is easy to switch on and off the energy input into the biological systems by controlling the laser power. Moreover, the light transduction into vibrational energy is facilitated with the use of fluorochromes. In comparison, ATP hydrolysis rate is harder to be controlled in vitro and the mechanism of sound transduction process is not known.

2.2 Spectroscopic techniques

Spectroscopy can be described as the study of the interaction between matter and electromagnetic radiation. It is therefore particularly adapted for our studies concerning the detection of long range electrodynamic interactions in biomolecules, and the first experimental part of the thesis as been based on a spectroscopic technique as seen in chapter 3.
There is a wide variety of spectroscopic techniques, each one suitable for a specific wavelength from a few picometers up to hundreds of micrometers and above. The suitable technique can be chosen according to the purpose of the study. For example, quantification of a compound can be estimated by resorting UV-visible spectroscopy with absorption or emission of the photons. When investigating the structure of some molecules, one can choose among many techniques, such as Nuclear Magnetic Resonance (NMR), or infrared spectroscopy for molecular vibrations. In our case, the collective vibrations have been estimated to appear in the THz range, corresponding to wavelengths from 0.01mm to 3 mm. It should be noted here that the terahertz region remained unexplored until

recently, and has been called the "terahertz gap", because of technological issues and impossibilities to detect or emit electromagnetic waves in this range. This explains why Raman spectroscopy researches were the first experiments performed to detect collective vibration of proteins.

In the following sections, we will thus explain how Raman spectroscopy works and the

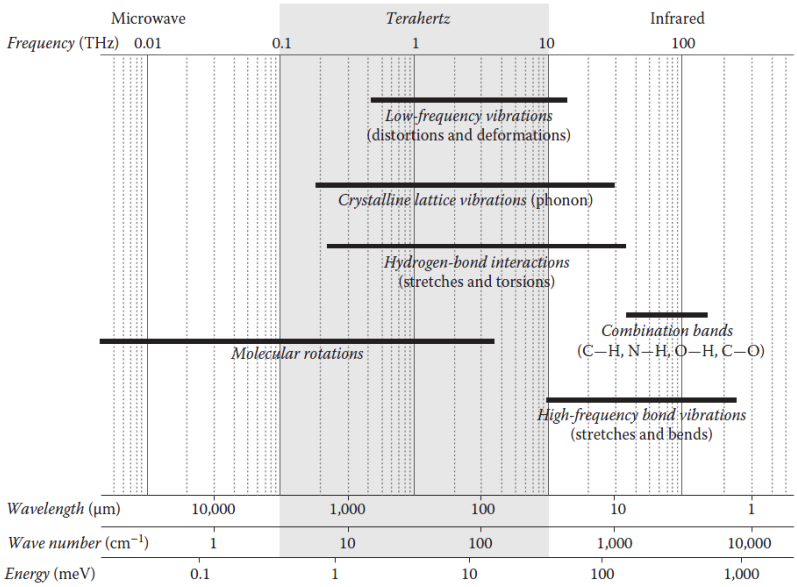

Figure 2.2: Characteristic energies in the electromagnetic spectrum around THz frequency region, from [154].

techniques we have used in the experiments seen in chapter 3 involving a near-field probe and a transistor.

2.2.1 Raman spectroscopy

Raman spectroscopy is a technique that uses Raman scattering to detect the vibrational characteristics of molecules. It has been theoretically predicted in 1923 by Smekal [153], and experimentally observed in 1928 by Raman and Krishnan. The technique of Raman spectroscopy was already developed in the 70' and it has been used in a first place to study Fröhlich condensation.

The Raman scattering is due to the inelastic scattering of light (compared to Rayleigh scattering which is an elastic scattering), leading to scattered photons with lower frequency than the incident photons (stokes Raman scattering), or with a higher frequency (anti-stokes Raman scattering). The difference of energy between the incident photons and scattered photons gives information about the vibrational characteristics of a compound, or its fingerprint. The photons emitted by the laser in such devices, create an oscillating polarization in the molecules, exiting them to a virtual energy state. The oscillating polarization of the molecule can thus couple with other polarizations of the

molecule such as vibrational and electronic excitations.

2.2.2 Terahertz spectroscopy devices

To investigate the THz characteristics of the proteins when brought out-of-equilibrium, we have used two different devices located at separated places.

2.2.2.1 Microwire-based THz spectroscopy

A constitutive element of the experimental setup is a tunable and continuous-wave primary source emitting in the 0.22-0.33 THz frequency range with an average power of 1 mW. The high spectral resolution (< 300 Hz) of the continuous-wave source allows an accurate detection of resonances. The emitted radiation beam is focused on the samples of protein solutions on which, at option, a 488 nm light beam – produced by an Argon laser – can also be focused. The blue light provides the proteins with the necessary energy to activate a collective vibrational state. The latter being an out-of-equilibrium state because it is kept by a non-thermal energy supply. The THz near-field scanning spectroscopy technique in aqueous medium is performed by resorting to a homemade micro-coaxial (i.e. subwavelength) near-field probe put inside a metallic rectangular waveguide connected to an heterodyne head and an electrical spectrum analyser. The subwavelength diameter of the wire allows an extremely focused enhancement of the longitudinal component of the electric field at its end over a volume of 4 pL. In 1995, F. Keilmann [85] highlighted the advantages of introducing a metal wire in a circular metal waveguide to produce probes for near-field microscopy in the far–infrared and microwaves frequency domains. The advantage of this method is to avoid the frequency cut–off when the diameter of the guide is a subwavelength one. The circular waveguide is transformed into a coaxial waveguide which does not have low frequency cut-off and which makes superfocalisation and high–resolution imaging possible. Howeverin the experiments reported in chapter 3, a rectangular waveguide was used, and this entails some different phenomena since the micro-wire is soldered along the long axis of the waveguide and bent to exit it. This has two main consequences: on the one hand, the micro-wire enables a modal transition and, on the other hand, it serves as a waveguide. The bent portion of the micro-wire allows the conversion of the fundamental mode TE_{01} inside the rectangular waveguide into a TM_{01} mode along the wire. To optimize the coupling efficiency between the near-field and the probe, a special care has been first paid to the positioning of the micro-wire inside the guide. More precisely, the maximum of the near field signal is theoretically attained for a wire positioned at $L_{inside} = p\frac{\lambda_{TE_{01}}}{4}$ from the open side of the waveguide, where $\lambda_{TE_{01}}$ is the wavelength of the TE_{01} mode at the considered frequency. At 0.3 THz, the micro-wire must be fixed at an entire multiple p of 250 μm. The best compromise between

efficiency and technical possibilities was found for $p = 4$ that gives $L_{inside} = 1$ mm. The second parameter to take into account is the angular positioning of the bent portion of the micro-wire inside the rectangular waveguide. The coupling is maximum when the wire is parallel to the orientation of the electric field in the guide, that is, along the long-axis of the rectangular waveguide. Finally we also paid attention to two relevant parameters that are the total length and the diameter of the wire. The intensity of the electric field is roughly sinusoidal and its maximum is attained when the total length L is a multiple of the half-wavelength. The best compromise between theory and technological possibilities has given a total length of $L = 2$ mm. Since the electric field intensity at the micro-wire extremity increases when the diameter decreases we used a wire of 12 μm diameter. All the measurements have been performed at room temperature. A drop of the protein solution sample is placed under the near-field probe which is directly immersed inside the solution. A typical experiment consists in measuring the near-field electric field intensity through a reference medium (water) and the protein solution sample. A sweep through the frequency domain accessible to the THz source is performed alternatively when the blue light is switched-on and off to yield a difference spectrum showing the absorption features that are attributed to collective vibrations of each protein molecule. The device used is visible on figure 2.3.

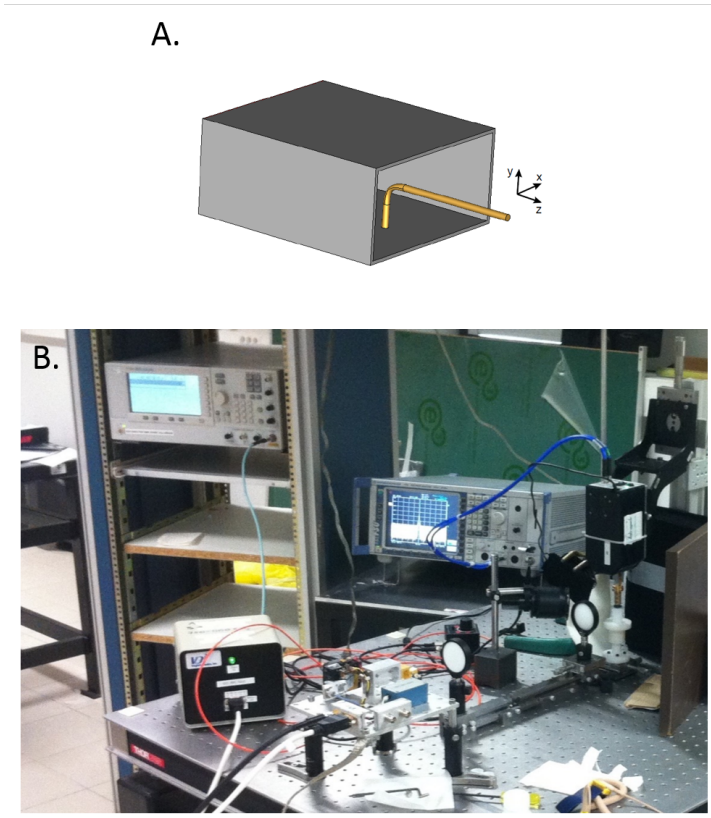

Figure 2.3: On panel A, a scheme of the antenna is visible. Panel B shows the device with the source and the probe.

2.2.2.2 Rectenna-based THz spectroscopy

In order to minimize the optical depth of water, in the second experiment (Rome) the probe domain was reduced to a volume of 10×10 microns in xy (horizontal plane), and to about 2 microns in z (vertical axis). To confine the THz radiation (wavelength λ around 1 mm) to such a deeply sub-wavelength region, a plasmonic antenna is used [65]. This device is based on two main components: a planar metal antenna with length close to $\lambda/2$ (bow-tie, broadband type) that produces a high THz field region with antenna feed gap of 10×10 microns; and a plasma wave FET transistor, which is a THz nonlinear electronic device integrated in the feed gap of the antenna, that provides an electric signal proportional to the THz field strength in the feed gap only. The plasma wave transistor was first introduced by Dyakonov and Shur in 1993 [40] and further developed by many authors [89], the main advantage being that standard microwave transistor technology can be employed for fabricating a device which is sensitive to THz radiation. The device is mounted in a package with a silicon lens pressed on the back of the semiconductor substrate and illuminated from below with a tunable THz oscillator (by Virginia Diodes Inc., 0.18 to 0.4 THz) through a set of off-axis parabolic mirrors. The resolution of the free-running oscillator is 2 GHz. After acquiring the empty-channel response spectrum of the device, a drop of protein solution was cast on the top (air) side of the device with a micropipette (a volume of 1 microliter was drop-casted). The drop extends over the entire antenna, but the radiation comes from below (i.e. from inside the substrate) and it is not attenuated by the whole drop. In this experiment absorption from molecules outside the antenna feedgap in the xy directions can be disregarded. Also, in the z direction the field extends for less than 2 microns due to the plasma wave properties (the extension of plasmonic field in the z direction is calculated by Finite Element Modeling simulations). Therefore, the number of molecules probed in this setup is that present in a $10 \times 10 \times 2$ micron volume, 10^{-6} times less than the number of molecules present in a 1 mm^3 diffraction limited focus. Some images of the rectenna and the full device are visible on figure 2.4.

2.3 Optical techniques to study dynamics

Beside the spectral signatures of the collective vibrations, we wanted to measure evidences of the change in the biomolecules dynamics when subject to the Fröhlich condensation. It brings complementary information as the spectrum does not provide the diffusion behavior.

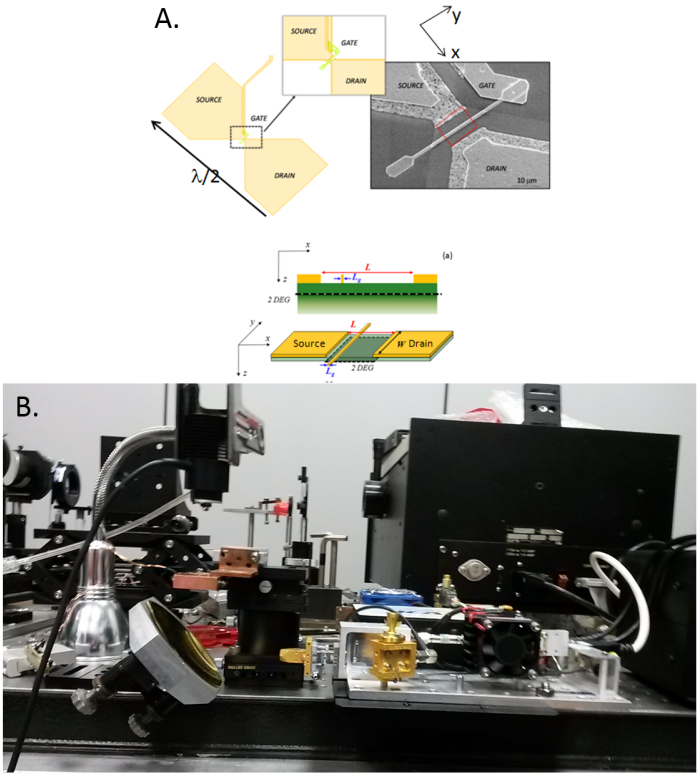

Figure 2.4: On panel A, schemes of the rectenna are visible. Panel B shows the device with the source and the probe.

2.3.1 Finding the suitable technique

We have envisaged to use AFM, FRAP, FRET, DLS and FCS techniques to this purpose. AFM, FRAP, FRET and DLS are going to be briefly described below, while FCS is more detailed because it is the technique we have chosen to study proteins dynamics.

- Atomic Force Microscopy (AFM) is an imaging tool, but it can also be used to measure inter and intramolecular interaction forces (Molecular Force Probe MFP). It works with a small spring-like cantilever with a tip that is "feeling" the surface of interest. For MFP, the cantilever only moves in the vertical direction, perpendicular to the specimen plane. Interestingly, membrane-mediated PPI has already been recorded with a similar device [26], and other experiments use proteins fixed on the cantilever to stretch proteins and polysaccharides [145, 107]. The idea was to use this AFM or MFP technique with a protein fixed on the cantilever, and reacting with other proteins in solution or on a substrate. However two major questions arise: *Can a protein still be subject to collective vibrations if it is fixed to an object such as the cantilever or the substrate? And would the device be sensitive and rapid enough to record forces acting between proteins in solution?*

- Fluorescence Recovery After Photobleaching (FRAP) is a technique that uses the photobleaching properties of the fluorophore to determine the kinetics of the dif-

fusion of the fluorophore. It works by photobleaching a spot on a sample, and studying how long it takes to the fluorescent particle to reorganize and reach a steady state. Unfortunately this technique is mainly used on membranes, and free proteins in solution would lead to issues regarding photobleaching and fluorescence recovering, due to the high diffusion coefficient of free moving proteins compared to diffusion in membranes.

- Fluorescence Resonance Energy Transfer or Förster Resonance Energy Transfer (FRET). This is a mechanism involving energy transfer between two chromophores, a donor and an acceptor. This phenomenon is a non-radiative dipole-dipole coupling, and it is therfore inversly proportional to r^6, with r the distance between the two chromophores. The fact that FRET helps measuring short range interaction (estimated up to 100Å), led us to consider this technique as non suitable for our purpose. The FRET efficiency can be measured with the variation of the acceptor emission intensity [35], the photobleaching of the solution [161], or measuring the fluorescence lifetime of the donor [35]. Though we have discarded the use of FRET to investigate collective vibrations and long range interactions, we are reconsidering using this method after the results shown in chapter 6 and the creation of clusters.

- Dynamic Light Scattering (DLS). This technique uses a monochromatique beam of light that is scattered in all directions when encountering the macromolecules in solutions. Because the scattering depends on the size and the shape of the particles, and because the solution is subject to intensity fluctuations due to Brownian motion, it is possible to obtain the diffusion coefficient D or its related hydrodynamic size. Larger particles diffuse slowly compared to smaller particles. The first digital autoccorrelator has been developed in 1969, and in 1970 the first experiments where realized to determine the diffusion coefficient of haemocyanin [51]. This technique has led to the development of Fluorescence Correlation Spectroscopy (FCS), and because analysis through correlation is similar in both techniques, it is explained in the next section related to FCS. Just like the previous techniques decribed, it has been envisaged, but did not fit to our expectation. The main issue with DLS is that it uses the scattering, while our experiments mainly involve light excitation of the dyes and the proteins. Most of the DLS setups are not suitable to be used with another excitation light source other than the monochromatic beam used for the scattering, and the fluorescence resulting from the dyes or proteins could complicate the results.

2.3.2 Fluorescence Fluctuation Spectroscopy

Most of our experiment have been based on FCS (Fluorescence Correlation Spectroscopy) and FCCS (Fluorescence Cross-Correlation Spectroscopy), as explained in the

following sections. The principle of the technique is to record the fluctuations of fluorescence (the technique is sometime also called Fluctuation Fluorescence Spectroscopy FFS) emitted in a confocal volume, then correlate the recorded trace which gives information about the diffusion time through the confocal volume. The technique has been developed starting from 1972 by Madge, Elson and Webb [135], and has been based on the DLS. It is frequently used to investigate translational and rotational diffusion, active transport and flow, photophysical and photochemical transformations, chemical reactions or molecular aggregation.

The signals of fluorescence recorded are analyzed after correlation, which is an efficient

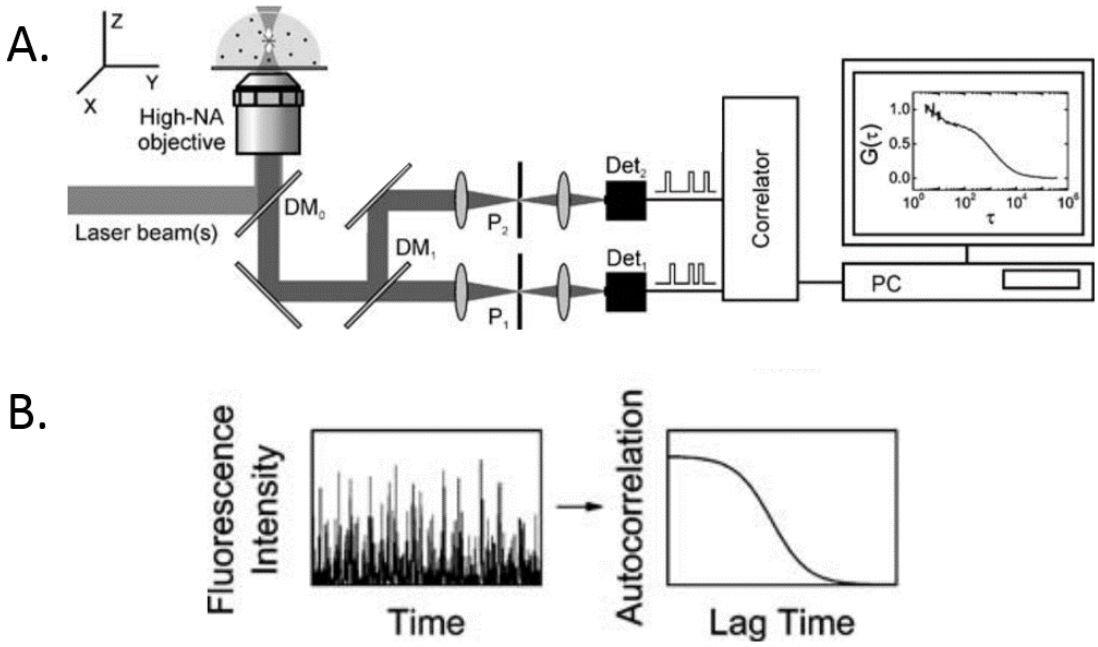

Figure 2.5: Adapated from [135]. Panel A shows a typical FCS setup. DM is used for dichroic mirror, P for pinhole and Det for detector. The excitation beam comes from the left of the figure, it is reflected by DM0, then is focused on the sample with the objective. The fluorescence light is emitted in response to the excitation beam, it passes through DM0, through the pinholes to improved the focus, and hits the detectors. The correlation is then performed. Panel B is a cartoon illustrating the concept of FCS.

method to study the fluctuations, as the following second-order intensity correlation function:

$$g_{ij}(\tau) = \frac{\langle F_i(t) F_j(t+\tau) \rangle}{\langle F_i \rangle \langle F_j \rangle} \tag{2.1}$$

with $F_{i,j}$ the fluorescence signals. If $F_i = F_j$ (signals recorded by the same detector) then equation 2.1 is referred to as auto-correlation function (ACF); If $F_i \neq F_j$ then it is a cross-correlation function (CCF).

The FCS techniques relies on the fluctuations of intensity, and as $F(t) = \langle F \rangle + \delta F(t)$ with $\langle F \rangle$ the average intensity and $\delta F(t)$ the fluctuations of the signal, one often reports

the related correlation function of fluorescence intensity fluctuations:

$$G_{ij}(\tau) = \frac{\langle \delta F_i(t) \delta F_j(t+\tau) \rangle}{\langle F_i \rangle \langle F_j \rangle}. \tag{2.2}$$

In most of the cases, one is only interested in translational/diffusive behavior of the fluorescent molecules, and the rotational diffusion can be neglected. Considering the detection volume defined as $W(r) = S(r)I(r)/I_0$ (with r the position of the volume element, I the excitation intensity, and $I_0 = max(I(r))$ describing the effective shape of the fluorescence detection volume), the detected fluorescence intensity is given by

$$F(t) = \int W(r) q c(r,t) dV, \tag{2.3}$$

with q is the molecular brightness of the fluorophore, with $q = I_0 \kappa \sigma_{\text{exc}} \phi$, where κ is the overall fluorescence detection efficiency for the fluorophore, σ_{exc} is its excitation cross-section and ϕ the fluorescence quantum yield.
One can show that the analytical model for ACF of FCS essentially depends on the diffusion time of the tracer through the confocal volume τ_D, the number of molecules in the confocal volume N, the shape of the confocal volume and particularly the structure parameter s describing the spatial properties of the detection volume $s = \omega_{xy}/\omega_z$ (where ω are $1/e^2$ radii of the sample volume directed perpendicularly to the optical axis and directed along the optical path), and for a one-component system in a 3D environment the ACF is defined as

$$G(\tau) = \frac{1}{N} \left(\frac{1}{(1+\tau/\tau_D)\sqrt{1+s^2\tau/\tau_D}} \right). \tag{2.4}$$

If we consider a 2D system, then equation 2.4 becomes:

$$G(\tau) = \frac{1}{N} \left(\frac{1}{(1+\tau/\tau_D)} \right). \tag{2.5}$$

There are also many other experimental parameters that can change the FCS analytical model. In a first place, some phenomenon can have a fast fluorescence dynamic, and affect the ACF at short lag time. This is the case for antibunching, due to the delay between each light quantum emission and the time spent by the fluorophores in the triplet state, which is a period where the fluorescence stops. While antibunching is most of time not recorded in FCS acquisitions due to higher time resolution acquisition, triplet blinking can be seen, and the analytical model yields the following ACF:

$$G(\tau) = \frac{1}{N} \left(1 + \frac{T}{1-T} exp\left(-\frac{\tau}{\tau_T} \right) \right) \left(\frac{1}{(1+\tau/\tau_D)\sqrt{1+s^2\tau/\tau_D}} \right), \tag{2.6}$$

with T the fractional population of the triplet state in the detection volume, and τ_T the triplet lifetime.
If there are M different species of non-interacting diffusing particles in a three-dimensional environment, the fluorescence correlation is given by:

$$G(\tau) = \frac{1}{N} \sum_{i=1}^{M} \frac{f_i}{(1 + \tau/\tau_{D,i})\sqrt{1 + s^2\tau/\tau_{D,i}}}, \tag{2.7}$$

where the M populations have diffusion times $\tau_{D,i}$, and must satisfy the condition: $\sum i = 1$ and $f_i = 1$.

Many important physically-relevant fitted parameters can be sort out of the experiments based on the previous ACFs.

- The correlation time, obtained with the following formula:

$$\tau_D = \frac{\omega_{xy}^2}{4D}, \tag{2.8}$$

  with D the diffusion coefficient of the observed dye.

- The average number of particles $\langle N \rangle$ in the detection volume, which can be used to calculate the particle concentration in the sample. It is given by

$$G(0) = \frac{1}{\langle N \rangle}. \tag{2.9}$$

  The fact that the estimated number of molecules in solution is inversely proportional to $G(0)$ leads to erroneously think that the ACF quality is decreased and cannot be exploited at high concentration. This has been investigated in chapter 5.

- The average sample intensity and the fluctuations behavior. This has been studied in chapter 6 and helped us identifying a phenomenon of interest.

Some other parameters can be found out based on the previous results, such as the concentration using N and the the confocal volume shape, or also the counts per particle based on the average intensity and the number of particles, which can help for example to determine the degree of labeling.

Many variations of the FCS exist. In the following experiments we have used both auto-correlation with one single fluorescent dye, and cross-correlation with one single fluorescent dye. For the auto-correlation analysis, only one detector is needed (for example DM1, P2 and Det2 are removed on figure 2.5) and the fluorescent signal is auto-correlated. The advantage of this technique is that the setup is much simpler because it only requires

one detector.

For the cross-correlation with one single color, the fluorescent beam is splitted (the dichroic mirror in figure 2.5 is replaced with a 50/50 beam splitter) and each of the two newly formed beams are recorded by separated detectors (Det1 and Det2 on figure 2.5). The cross-correlation of those two signals allows to remove the artifacts coming from the auto-correlation, such as the afterpulsing which is a response of the detector to a real signal pulse modifying the output correlation.

Finally, the calibration of the transversal waist size ω_{xy} helps to estimate the unknown diffusion coefficient of other particles using the equation 2.8. This is done by measuring the diffusion time of a dye with a known diffusion coefficient (we have used in the following experiment Rhodamine 6G or Alexa Fluor 488), using $\omega_{xy} = \sqrt{4D\tau_D}$.

The devices used in the experiments are visible on figure 2.6.

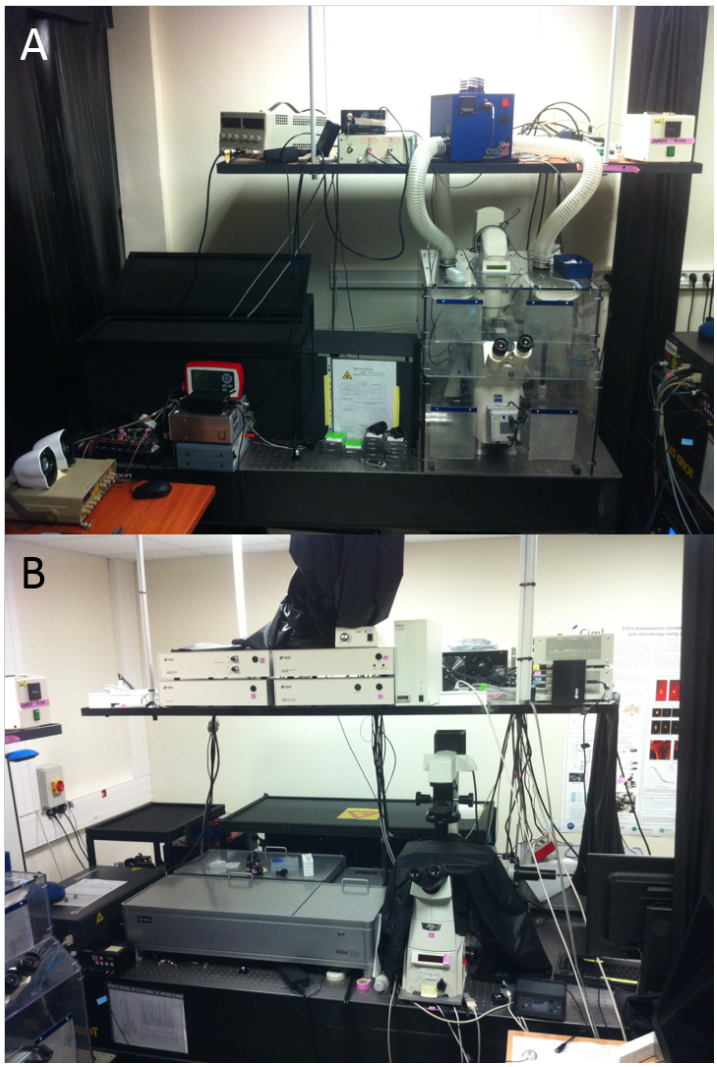

Figure 2.6: Panel A shows the FCS device. Panel B shows the FCCS device.

2.4 Previous work

The two following sections relate the work performed before this thesis. It has been of crucial help to build the experiments and to confirm the experimental results as seen in the chapter 6.

2.4.1 Experimental assessment of the contribution of electrodynamic interactions to long-distance recruitment of biomolecular partners: Theoretical basis

The numerical results reported in this article of our [140] are in favor of a positive answer to the main question addressed by the present work. Two one-dimensional models (visible on figure 2.7) have been designed to obtain the general form of the mean first-passage time $\tau(x)$ as a function of the initial intermolecular distance x and temperature T.

The numerical study of these models revealed qualitative differences in the mean first

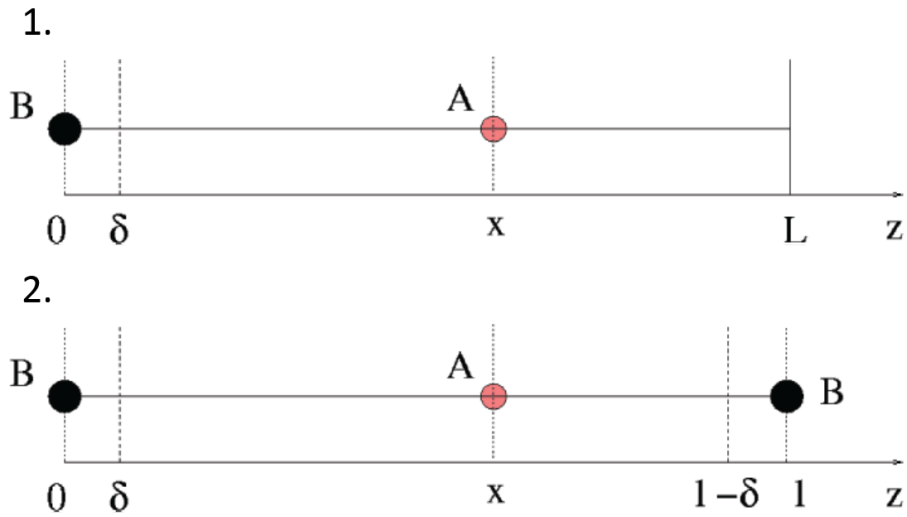

Figure 2.7: Panel 1: a generic initial condition of Model 1 ($t = 0$). Here x is the initial distance between A and B; δ is the distance at which A and B react, and L is the position of the reflecting barrier for A and the position of B is fixed. Panel 2: a generic initial condition of Model 2 ($t = 0$). Two molecules B are fixed at the boundaries $x = 0$ and $x = l$; x and $l - x$ are the initial distances between A and the Bs and δ is the distance at which A and B react.

passage time τ between the case of a pure Brownian diffusion of the molecule A and the case in which an attractive (resonant) potential U is added to a random force. In particular, in the latter case, the functional dependence of τ on the initial distance x between the molecule A and its target (molecule(s) B) demonstrates the existence of different patterns in the two models depending on the range of the x values considered :

- a deterministic pattern at small x values (small initial separations), characterized by a power law representative of the potential under consideration (x^5 for the resonant potential used, x^{p+2} for a general potential of the form $U(x) \propto x^{-p}$);
- a Brownian pattern at large initial separations, proportional to x or to x^2 depending upon the symmetry of the system (x for an asymmetric situation as described by Model 1, and x^2 for a symmetric one as described by Model 2);
- a steep transition pattern joining the two asymptotic ones in the case of Model 1, and a smooth crossover joining the two asymptotic ones in the case of Model 2.

Although complementary computations revealed some interesting features in the temperature dependence of τ, the corresponding degree of variation in a laboratory accessible interval of temperature is too weak to be experimentally detectable.

In any case, it is obvious that x must constitute an experimentally accessible control parameter so that the results mentioned in this article [140] may be used to predict the possible role of long-range intermolecular forces in biological processes. Notably, such an approach is not so usual. Indeed, most of the attempts made hitherto in this direction have resulted in experimental measurements of association constants k_a (characteristic of a reaction medium), which are predictable from the Smoluchowski theory also when intermolecular forces are considered [37, 120]. The focus of Smoluchovski theory is on the association constant k_a which represents the probability for two molecules to react per time unit, irrespective of their position. In the case of Brownian encounters, this is given by [16] $k_a^B = 4\pi RD \equiv 4\pi\delta kT/\gamma$ where R is the reaction radius that can be approximated to δ from the current study, and D is the sum of the diffusion coefficients of the two cognate partners. In the presence of some interaction potential U, one has $k_a^* = 4\pi R^* D$ where R has been replaced by [16, 37, 120] $R^* = R\left(\int_R^\infty r^{-2}e^{-U(r)/kT}dr\right)^{-1}$. Now, if k_a is experimentally measured for some reaction and it turns out that $k_a^B < k_a$, then this would indicate that some deterministic force is in action but one can hardly find out the law of the interaction potential because after integration over r there is no one-to-one correspondence between R^* (thus k_a^*) and the functional form of $U(r)$ [127]. On the other hand, in measuring $k_a < k_a^B$, we cannot be sure that the reaction is simply diffusion-driven because, in this case, chemical times could be long enough to make k_a smaller than the corresponding Brownian value. The advantage of our dynamical approach is that our models still apply by choosing δ as the distance at which A and B get in contact without reacting, and with the experimental technique discussed below (FCCS) we can make a distinction between the association time and the chemical times.

In the present situation x values might to some extent be considered in three dimension as the *average distance* between two molecular partners A and B, while this quantity can be easily controlled in laboratory experiments by varying the concentrations of the

reactants. Given the concentrations $C_A = N_A/V_A$ and $C_B = N_B/V_B$ (with $V_{A,B}$ = the initial volumes and $N_{A,B}$ = the number of molecules of the two species respectively; remark that these numbers are controlled through the molarity, i.e. a definite fraction of the Avogadro number), we get the estimate $x = C_{av}^{-1/3}$ for the average intermolecular distance from the average concentration $C_{av} = (N_A + N_B)/V$, where the reaction volume $V = V_A + V_B$. In practice, as an example, with $C_{av} = 1$nM we have $x \simeq 1\mu$m as the average distance between any two molecules, while with $C_{av} = 1\mu$M we have $x \simeq$ 1000Å. By working at equimolarity, that is $C_A = C_B$, then $C_{av}^{-1/3}$ is a good estimate of the average distance between one A and one B molecule. Working with nano-Moles of DNA and proteins (enzymes, transcription factors) is quite standard in molecular biology experiments. With such concentrations of reactants, both models (1 and 2) predict that the first passage time – that can be interpreted as the average encounter time between one A and one B molecule initially located at intermolecular distances of a few thousands of Angstroms – varies in the interval between a few tens of microseconds to about one millisecond in the presence of an attractive deterministic force that would sum up to the random force. On the contrary, in the very same conditions, random only driven encounters would exceed the above mentioned encounter times by one or two orders of magnitude. Again, the distance at which sizeable differences could be observed may vary significantly depending on the actual value of the resonant potential parameter $\mathcal{C}$, found in the formula of the long-range resonant potential $U(x) = -\mathcal{C}/x^3$. On the other hand, estimates in literature [148, 127, 137] suggest that these long-range resonance interactions could be effective up to distances in the order of 1μm (the action range is estimated by computing the distance at which the resonance interaction energy equals the level of thermal noise kT). In this respect, cautious estimates have been used for the parameter $\mathcal{C}$, focusing on conservative assumptions for average encounter time varying in the interval $10^{-5} - 10^{-3}$ seconds which can be readily detected with the aid of Fluorescence Cross-Correlation Spectroscopy (FCCS technology). This is a powerful technique which is being increasingly applied to the study of diffusion and chemical reaction rates in complex biological systems using fluorescently labeled macromolecules [103, 75, 10]. FCCS measures the spontaneous fluctuations of fluorescences $\delta F_1(t)$ and $\delta F_2(t)$ that arise from the diffusion of fluorescently labeled molecules of type 1 and 2, respectively - illuminated by two laser light beams of different colors - into or out of an open sampling volume. Even though the size of the detection volume is diffraction limited, the autocorrelation functions of $\delta F_{1,2}(t)$ and the cross-correlation function $\langle \delta F_1(t) \delta F_2(t) \rangle$ can be altered by processes occurring on smaller spatial scales. These correlation functions provide information on diffusion properties of fluorescent molecules.

Of course, we are well aware of the fact that the models studied in this article [140] are simplified descriptions of the reality. Indeed, protein-protein and protein-nucleic acid interactions in vivo generally take place within complex structural scaffolds such as the

membrane cytoskeleton or the chromatin envelope, which are themselves the subject of highly dynamical regulations (e.g., Refs. [112, 91]); and may also possibly interfere with the spatiotemporal control of the given reactions (e.g., Refs. [11, 28]). Should resonant electrodynamic interactions be involved within such an intricate context, it seems illusory at this stage to assess realistic $\mathcal{C}$ values simply based on the proposed experiments. In fact, regarding protein-DNA in vivo (physiological) interactions for instance, it may well be that the putative values fluctuate depending on a host of variables, possibly including - in a non-mutually exclusive way, charges on proteins and DNA, the effect of surrounding electrolytes, the nucleic-/amino-acid compositions, the length of accessible DNA, etc. However, we stress here that our initial goal, as described in this work, is to merely probe whether or not biological partners can take advantage, besides thermic diffusion, also of long-distance (0.1-1μm) forces of electrodynamic origin to eventually interact. If established, this novel concept would then in turn open new avenues of research to investigate long-standing biological issues, e.g., on the precise definition of which variables exactly pertain on protein-DNA interactions, and how a diffusing protein particle may actually recognize the particular cognate DNA site among many other locations also available. Since we do not expect dramatic qualitative changes out of the numerical simulations of equations describing the dynamics of the system in three dimensions[1], an experimental setup providing a practical realization of what has been investigated in the present work could be devised by resorting - as experimental probes - to three broad classes of interactions: protein-DNA, protein-RNA, and protein-protein (ligand-receptor). As DNA and RNA molecules have not a preassigned length, it is implicitly understood that only short fragments are to be considered (some tens or a few hundreds of base pairs, that is, oligonucleotides or plasmides respectively). The proteins interacting with DNA or RNA can be processing enzymes (helicases, polymerases, recombinases) or transcription factors normally bound at promoters, enhancers, insulators, or silencers. Thus, for example, one could choose two molecular species consisting, respectively, of a short double stranded DNA molecule (for example a synthetic oligonucteotide of ~ 100 base pairs or even less) and a protein with a site specific affinity for the chosen DNA molecule (i.e., a transcription factor). By labeling the DNA molecules and proteins with standard fluorophores their dynamical behavior can be followed by means of FCCS microscopy at different concentrations $C = C_A = C_B$ of the reactants to get a characteristic time scale as a function of $x = C^{-1/3}$. In this way such an experimental set up should provide - after data fitting - an estimate of the constant $\mathcal{C}$ for the resonant potential considered above. Thus, $\mathcal{C} = 0$ would mean that the reactants meet only under the action of Brownian diffusion, whereas $\mathcal{C} \neq 0$ would prove the existence at the same time of the long-range interactions evoked throughout this work and give quantitative information about them.

[1]The mean first passage time for Wiener-Einstein processes to attain a given absolute displacement is found to be independent of the dimensionality of the process in Ref [152]

2.4.2 Experimental detection of long-distance interactions between biomolecules through their diffusion behavior: Numerical study

At variance with the outcomes of the previous work, the substantial advance provided by this article [117] consists of a conceptual proof of feasibility of an experimental approach resorting to an actually measurable observable. In particular, this observable is the diffusion coefficient that can be measured by means of several available techniques like pulsed-field gradient nuclear magnetic resonance forced Rayleigh scattering (FRS), Fluorescence Recovery After Photobleaching (FRAP) and Fluorescence Correlation Spectroscopy (FCS) to mention some of them. The long-range electrodynamic forces we are after have been hitherto elusive to observation in spite of many studies on the diffusion behavior of biomolecules in solution. We surmise that no evidence has been until now reported about the presence of these interactions because they are not compatible with thermal equilibrium [141, 142] contrary to previous predictions [56]. The consequence being the need for an out-of-equilibrium driving of the biomolecules by means of a source of collective excitation. In order to achieve the above mentioned assessment about experimental detectability of electrodynamic intermolecular interactions, numerical simulations have been performed in [117], and the outcomes can be summarized as follows:
i) It has been found that, for dilute systems ($\langle d \rangle$ ranging from about 400Å up to 30000Å), the diffusion coefficient is sensitive to all the interactions considered. Starting with a uniform distribution of molecules in all the accessible volume, an interesting phenomenon is observed: the diffusion coefficient decreases independently of the repulsive or attractive nature of the molecular interactions (repulsive Coulomb with and without screening, attractive electrodynamic dipole-dipole).
ii) Moreover, in the gaseous-like phase, a decrease of the diffusion coefficient is always accompanied by an increase of chaos. On the contrary, when spatial order sets in, a decrease of the diffusion coefficient is always accompanied by a decrease of chaos. Even though it is well known that no simple relation exists between Lyapunov exponents and transport properties in dynamical systems, the qualitative correspondences observed are consistent with the intuitive idea that both phenomena are related to the intensity of intermolecular interactions.
iii) Nice transitional phenomena have been observed: for Coulomb interactions a first transition from purely stochastic diffusion to chaotic plus stochastic diffusion is found; then, at sufficiently high concentrations, a spatial ordering of the molecules is found resembling to a crystal-like structure. For dipole-dipole interactions an abrupt clustering transition is observed, which is strongly reminiscent of an equilibrium phase transition.
iv) The simple theoretical model proposed in [117] gives the good values of the diffusion coefficients computed along the dynamics in presence of intermolecular interactions within a few percent of error.

From the experimental point of view, it has been concluded that the variations of the diffusion coefficient D with respect to its Brownian value, as well as the patterns of D versus the average interparticle distance $\langle d \rangle$, are such that the practical possibility exists of experimentally tackling the problem of interest by means of, for example, one of the above mentioned techniques.

Finally it is considered that the results reported in [117] could be apply to two-dimensional systems like, for example, protein diffusion on lipid membranes. The same kind of computations reported can be performed also in two dimension. But a-priori we expect non-trivial differences between the two and three dimensional cases, for example, the potential $1/r^3$ is long-range in three dimension but short-range in two dimension because in the latter case the exponent 3 is larger than the spatial dimension. Another example of a difference is that in the absence of deterministic interactions a random "walker" in one and two dimension will always almost surely return to the starting point, whereas this is not the case in three dimension because after a theorem due to Polya the probability to return to the origin drops to about 0.34, and this of course affects also the encounter probability of two different objects.

PART II

Original contributions

CHAPTER 3 Signature of collective oscillations of biomolecules

3.1 Introduction

3.1.1 Context

Progress in terahertz technology has enabled to look at biological systems with terahertz radiation, that is, in an energy domain (a few meV) which is of the order of the activation energy of many biological processes. Among these, collective excitations driven by metabolic activity were hypothesized in the late '60s by H. Fröhlich to account for the huge speed of enzyme reactions and for the fast encounters of the cognate partners of biochemical reactions [53, 56]. In fact, collective oscillations of biomolecules, by bringing about giant oscillating dipole moments, would result in resonant (thus selective) electrodynamic forces acting at a long distance [53, 55, 52]. Fröhlich proposed a model where the activation mechanism of collective oscillations is a Bose-like condensation of the normal vibrational modes of a biomolecule. In this model a biomolecule is considered as an open system through which energy flows under the simultaneous action of an external supply and of dissipation due to radiative, dielectric, and viscous energy losses. The Bose-like condensation in the lowest vibrational mode is predicted to occur when the energy input rate exceeds some threshold value. However, the condensation phenomenon originally surmised by Fröhlich has been criticized and marginalized because its quantum formulation can be hardly maintained to be a realistic one for biomolecules. In fact, the frequency of collective oscillations is expected in the sub THz domain, around 10^{11} Hz, so that, at room temperature, $k_B T/\hbar\omega \gg 1$ which rules out a quantum description. Of course this does not apply to molecular orbitals and light induced electronic transitions which are always of quantum nature. Accordingly, we have worked out a classical version of the original Fröhlich model, finding that - remarkably - also in a classical context a Fröhlich-like phonon condensation phenomenon is possible (see bellow). This is illustrated in Figure 3.1 which, for an idealized macromolecule, displays the deviation from energy equipartition among the normal vibrational modes - computed by means of our classical version of the quantum Fröhlich model - as a function of the input energy amplitude a. When this parameter exceeds a threshold value, the lowest frequency mode deviates from equipartition by enhancing its strength at the expenses of the other normal modes. Though still representing a biomolecule in a very idealized way, this model predicts a classical condensation phenomenon worth an experimental effort to detect it.

Even though experimental evidence of the existence of collective modes of vibration of biomolecules has been provided *at thermal equilibrium* by means of Raman spectroscopy [126] already many years ago, and is still being the object of many investigations [1, 163, 48, 105], no experimental evidence was hitherto available of the possibility of exciting out-of-thermal-equilibrium collective oscillations of a biomolecule. Unveiling whether these can be activated amounts to understanding whether a necessary condition to activate long-range intermolecular electrodynamic forces [143] can be fulfilled. This is what motivated conceiving and performing the two biophysics experiments on which we report in the present work.

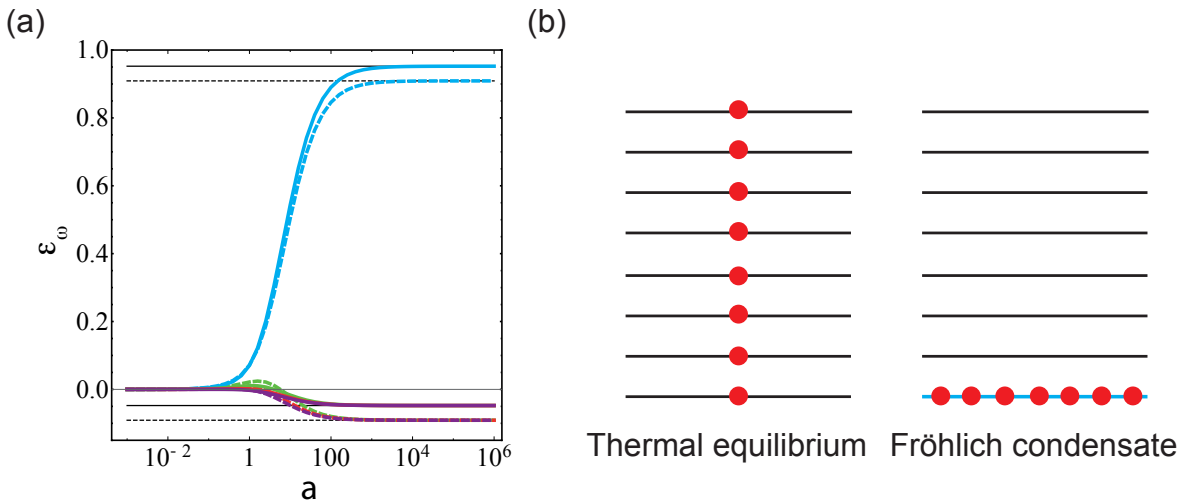

Figure 3.1: Classical Fröhlich-like condensation. At thermal equilibrium all the vibrational modes of a macromolecule fulfill energy equipartition. In the left panel this corresponds to $\epsilon_{\omega_i} = 0$. Non vanishing values of ϵ_{ω_i} (given in arbitrary units) refer to deviations from energy equipartition driven by increasing values of the injection energy rate denoted by the parameter a in abscissas (in arbitrary units). When the condensation sets in all the energy is concentrated in the lowest frequency vibrational mode. The right panel pictorially represents the two phases. The dotted and continuous lines refer to different spectral densities. The blue lines correspond to the lowest frequency mode $\omega = 1$. Only the a dependence of the five lowest modes is displayed.

3.1.2 Classical out-of-equilibrium phonon condensation

Some decades ago, the study of open systems far from thermodynamic equilibrium showed, under suitable conditions, the emergence of self-organization. Striking similarities were observed among very different physical systems having in common the fact of being composed of many non-linearly interacting subsystems. When a control parameter, typically the energy input rate, exceeds a critical value then the subsystems act cooperatively to self-organize in what is commonly referred to as a non-equilibrium phase transition. This fascinating topic was pioneered in the late '60s by H. Fröhlich with the model he proposed for the phonon condensation of a macromolecule[52, 56]. In his original papers Fröhlich did not provide the derivation of the rate equations for the time evolution

of the phonon occupation numbers. This was later explained by Wu and Austin [177] who provided a microscopic model from which the Fröhlich's rate equations can be derived. The Wu-Austin Hamiltonian, modeling the dynamics of the normal modes of a macromolecule, of the thermal bath surrounding it, and of the external energy pump, is written in second quantization formalism to yield Fröhlich's rate equations which were originally put forward in quantum version. Nevertheless, a quantum mechanical description of the dynamics of the internal vibrational modes of a protein to explain their condensation according to Fröhlich's mechanism seems rather questionable. In fact the thermal energy $k_B T$, at room temperature $T = 300\,\mathrm{K}$, is much larger than $\hbar\omega$ when $\omega \sim 10^{11}$ Hz, that is, in the frequency range of the observed collective vibrations of the BSA protein. Therefore, by proceeding to work out a classical analog of the original quantum model proposed by H. Fröhlich leading to the rate equations (1.29), lengthy computations [118] yield the rate equations for the average values of the mode amplitude $\langle J_i \rangle$ in the form

$$\begin{aligned}
\frac{d\langle J_i\rangle}{dt} =& s_{\omega_i} + \frac{\tilde{\eta}^2_{\omega_i}(\omega_i)\pi}{2}\left[\frac{k_B T_B}{\omega_i} - \langle J_{\omega_i}\rangle\right] + \sum_{\omega_j \in Z/\omega_i} \frac{k_B T_B \tilde{\chi}^2_{\omega_i\omega_j}\left(|\omega_i - \omega_j|\right)\pi}{2\,|\omega_i - \omega_j|}\Bigg[\left(\langle J_{\omega_j}\rangle - \langle J_{\omega_i}\rangle\right) + \\
&+ \frac{\omega_j - \omega_i}{k_B T_B}\langle J_{\omega_i}\rangle\langle J_{\omega_j}\rangle\Bigg] + \sum_{\substack{\omega_j,\omega_k,\omega_l \in Z \\ \omega_i+\omega_j-\omega_k-\omega_l=0}} \frac{16\pi\kappa^2_{(1)\omega_i\omega_j\omega_k\omega_l}}{\Delta\omega}\Big[\langle J_{\omega_j}\rangle\langle J_{\omega_k}\rangle\langle J_{\omega_l}\rangle + \\
&+ \langle J_{\omega_i}\rangle\langle J_{\omega_k}\rangle\langle J_{\omega_l}\rangle - 2\langle J_{\omega_i}\rangle\langle J_{\omega_j}\rangle\langle J_{\omega_l}\rangle\Big] + \\
&+ \frac{3\pi}{\Delta\omega}\Bigg[\sum_{\substack{\omega_j\omega_k\omega_l \in Z \\ \omega_i+\omega_j+\omega_k-\omega_l=0}} 3\kappa^2_{(2)\omega_i\omega_j\omega_k\omega_l}\langle J_{\omega_l}\rangle\big(\langle J_{\omega_j}\rangle\langle J_{\omega_k}\rangle + 2\langle J_{\omega_i}\rangle\langle J_{\omega_k}\rangle - \langle J_{\omega_i}\rangle\langle J_{\omega_j}\rangle\big) + \\
&+ \sum_{\substack{\omega_j\omega_k\omega_l \in Z \\ \omega_i-\omega_j-\omega_k-\omega_l=0}} \kappa^2_{(2)\omega_i\omega_j\omega_k\omega_l}\langle J_{\omega_l}\rangle\langle J_{\omega_k}\rangle\big(\langle J_{\omega_j}\rangle - \langle J_{\omega_i}\rangle\big)\Bigg]. \qquad i = 1,\ldots,N
\end{aligned} \tag{3.1}$$

where $s_{\omega_i} = \dfrac{k_B T_P \tilde{\xi}^2_{\omega_i}(\omega_i)\pi}{2\omega_i}$, and $\Delta\omega$ is the spectral resolution of the system representing the biomolecule. The rate equations have been derived in the limit of long time $t \gg \min_{\omega_i \in Z} \omega_i$; in this limit the contribution given by the term with coefficient $\kappa^2_{(3)\omega_i\omega_j\omega_k\omega_l}$ vanishes. In order to set the rate equations in nondimensional form one introduces the quantities

$$y_{\omega_i} = \frac{k_B T_B}{\omega_i}\langle J_{\omega_i}\rangle \tag{3.2}$$

$$\frac{\mathrm{d}y_{\omega_i}}{\mathrm{d}t} = a_{\omega_i} + b_{\omega_i}\left(1 - y_{\omega_i}\right) + \sum_{\substack{\omega_j \in Z \\ \omega_i \neq \omega_j}} c_{\omega_i\omega_j}(|\omega_j - \omega_i|)\left[\left(\frac{\omega_i}{\omega_j} y_{\omega_j} - y_{\omega_i}\right) + \frac{(\omega_j - \omega_i)}{\omega_j} y_{\omega_i} y_{\omega_j}\right] +$$
$$+ \sum_{\substack{\omega_j,\omega_k,\omega_l \in Z \\ \omega_i+\omega_j-\omega_k-\omega_l=0}} d^{(1)}_{\omega_i\omega_j\omega_k\omega_l} \frac{y_{\omega_l}}{\omega_l}\left[\frac{\omega_i}{\omega_j\omega_k} y_{\omega_i} y_{\omega_k} + \frac{1}{\omega_k\omega_l} y_{\omega_j} y_{\omega_k} - 2\frac{1}{\omega_j\omega_l} y_{\omega_j} y_{\omega_l}\right] +$$
$$+ \sum_{\substack{\omega_j\omega_k\omega_l \in Z \\ \omega_i+\omega_j+\omega_k-\omega_l=0}} 3d^{(2)}_{\omega_i\omega_j\omega_k\omega_l} \frac{y_{\omega_l}}{\omega_l}\left[\frac{\omega_i}{\omega_j\omega_k} y_{\omega_j} y_{\omega_k} + 2\frac{1}{\omega_k} y_{\omega_i} y_{\omega_k} - \frac{1}{\omega_j} y_{\omega_i} y_{\omega_j}\right] +$$
$$+ \sum_{\substack{\omega_j\omega_k\omega_l \in Z \\ \omega_i-\omega_j-\omega_k-\omega_l=0}} d^{(2)}_{\omega_i\omega_j\omega_k\omega_l} \frac{1}{\omega_k\omega_l} y_{\omega_k} y_{\omega_l}\left(\frac{\omega_i}{\omega_j} y_{\omega_j} - y_{\omega_i}\right) \tag{3.3}$$

where

$$a_{\omega_i} = \frac{\omega_i s_{\omega_i}}{k_B T_B} \qquad b_{\omega_i} = \frac{\tilde{\eta}^2_{\omega_i}(\omega_i)}{2} \qquad c_{\omega_i\omega_j}(|\omega_i - \omega_j|) = \frac{k_B T_B \chi^2_{\omega_i\omega_j}(|\omega_i - \omega_j|)}{2|\omega_i - \omega_j|}$$
$$d_{(1)\omega_i\omega_j\omega_k\omega_l} = \frac{16\pi\left(k_B T_B\right)\kappa^2_{(1)\omega_i\omega_j\omega_k\omega_l}}{\Delta\omega} \qquad d_{(2)\omega_i\omega_j\omega_k\omega_l} = \frac{3\pi\left(k_B T_B\right)^2\kappa^2_{(2)\omega_i\omega_j\omega_k\omega_l}}{\Delta\omega} \tag{3.4}$$

$$\epsilon_{\omega_i} = \frac{y_{\omega_i}}{\sum_{\omega_i \in Z} y_{\omega_i}} - \frac{1}{\sum_{\omega_i \in Z}} \tag{3.5}$$

according to the energy equipartition theorem, at thermal equilibrium it is $\epsilon_{(eq)\omega_i} = 0$ as follows from the energy equipartition principle; the range of values of this parameter is given by $\epsilon_{\omega_i} \in \left[-\frac{1}{\sum_{\omega_i \in Z}}, 1 - \frac{1}{\sum_{\omega_i \in Z}}\right]$.
The system of differential equations in (3.3) has been integrated for $y = y(t)$ and for two different sets Z_1 and Z_2 of equally spaced frequencies with $N_{Z_1} = 11$ and $N_{Z_2} = 21$. For these two sets the frequencies have been chosen such that $\omega_1 = \min_{\omega_i \in Z_1} \omega_i = \min_{\omega_i \in Z_2} \omega_i = 1$ and $\max_{\omega_i \in Z_1} \omega_i = \max_{\omega_i \in Z_2} \omega_i = 1$ in arbitrary units while the spacings among the frequencies have been set $(\Delta\omega)_{Z_1} = 1$ and $(\Delta\omega)_{Z_2} = 0.5$. The initial conditions have been chosen to correspond to thermodynamic equilibrium of the system, i.e. $y_{\omega_i}(0) = 1$. The integration time has been chosen sufficiently long to attain a stationary state.

3.2 Experimental work

3.2.1 Devices

Two separated and different experiments, performed in Montpellier (France) and in Rome (Italy), respectively, have been performed to get the terahertz non-equilibrium spectra of the model protein chosen. The former used a microwire as local probe whereas the latter used a nanorectenna. These setups have been previously described in chapter

2.

3.2.2 Experimental detection of collective vibrations

For both experiments a model protein has been chosen: the BSA (Bovine Serum Albumine) protein. This is mainly made out of α-helices, and is a "model" since it is largely studied in the biophysical chemistry literature. Our strategy to create a stationary out-of-thermal-equilibrium state of this molecule is to induce it by means of optical pumping, without involving any optical transition of the protein, through the excitation of some fluorochromes bound to each protein molecule. The optical excitation of these fluorochromes creates on each protein some "hot points" acting as the epicentres of a so-called "proteinquake" [6, 96] - better discussed in the following - and resulting in an energy transfer to the vibrational part of the protein. We used the Alexa488 fluorochrome which is covalently bonded at the lysine residues of the BSA and which is excited by means of an Argon laser (wavelength 488 nm). Some 0.19 eV per fluorochrome and per incident photon (the average energy difference between the absorbed and re-emitted photons) is thus available for an energy transfer to the protein and, partly, also to its environment. By attaching an average number of 5 fluorochromes per protein a considerable amount of energy ($\gg k_B T$) can be continuously pumped into each protein. Two THz-near-field absorption spectroscopy setups of watery solutions of the protein (at 1 mg/mL concentration) operating into two distinct laboratories, have been used at room temperature (Fig. 3.2 (a), (c)). In both experiments, THz radiation is produced by tunable, highly-spectrally-resolved ($<$ 300 Hz) and continuous-wave sources with an average power of 1 mW allowing an accurate detection of possible resonances. A typical experiment consists in three phases, during all of them the watery solution of proteins is illuminated with THz radiation performing a sweep in frequency, and thus allowing to measure the frequency dependence of the absorbed electromagnetic power (detected by the near-field probes) in the solution. During the first phase no extra illumination with the Argon laser is done; during the second phase the Argon laser is switched on to excite the fluorochromes bound to the proteins; finally, during the third phase the laser is switched off to check whether some memory and irreversible photochemistry effect (photobleaching) or sample heating are present. The use of near-field coupling of metal probes to the sample eliminates the Fabry-Perot interferences often seen in optical spectra taken in fluidic cells [66].

The first setup (Fig. 3.2 (a), (b)) used a micro-coaxial near-field probe put inside a metallic rectangular waveguide enabling a modal transition from TM_{01} Sommerfeld's to TE_{01} waveguide mode. The sub-wavelength diameter of the wire (12 μm) allows an extremely localized detection of the longitudinal component of the electric field at its end and on a volume of about 4 pL. The spectra were subtracted from the spectrum

of pure water in order to remove artifacts coming either from the water absorption or from the geometry of the experimental setup. The second setup [65] (Fig. 3.2 (c), (d)) used a near-field probe rectenna composed of a planar metal bow-tie antenna with dimensions close to half-a-wavelength (at 0.3 THz) that enhanced the THz field in the feed gap region (volume of about 0.2 pL) and a plasma-wave field-effect transistor (FET) integrated in the feed gap of the antenna. When illuminated by THz radiation, the antenna-coupled FET device provides a DC-voltage – between Source and Drain contacts – proportional to the THz-field intensity [40, 89, 119]. A hemispherical silicon lens pressed on the back of the semiconductor substrate focused the THz radiation on the antenna simultaneously eliminating Fabry-Perot interference in the substrate [39]. The spectrum of the protein solution obtained in the absence of blue light illumination was subtracted from the spectrum obtained with blue light illumination.

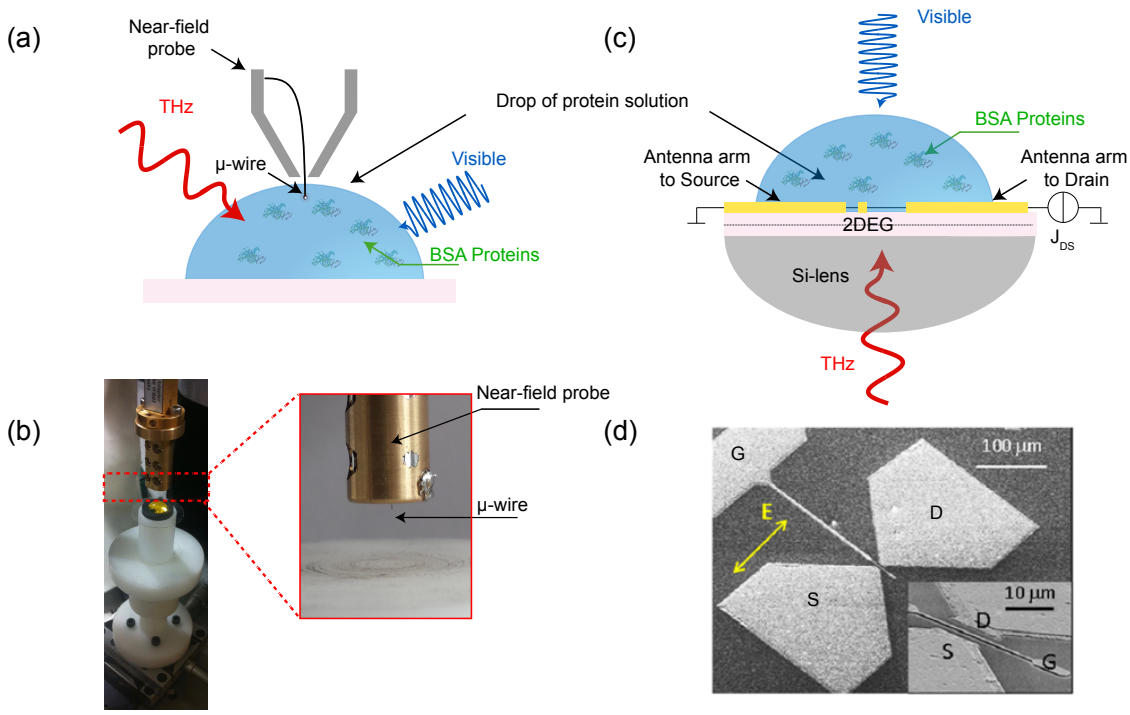

Figure 3.2: Experimental setups of THz absorption near-field spectroscopy. (a) A drop of the biological sample is placed under the near-field probe which is directly immersed inside the solution. (b) Picture of the near-field probe and its micro-wire. (c) A drop of the biological sample is placed above the near-field rectenna. (d) Electron-beam microscopy picture of the bow-tie antenna with its integrated FET.

Figure 3.3 (a) presents the spectra obtained using the micro-coaxial probe in the absence of blue light illumination (black circles) and in the presence of blue light illuminations of different durations (from 3 to 9 min). In the former case (no illumination), there was no specific spectral feature in the studied frequency range while in the latter case (with illumination) we observed spectral resonances which become more evident for increasing duration of illumination. In particular, the strongest resonance appeared at

0.314 THz accompanied by two other minor resonances situated at 0.278 and 0.285 THz; these values did not depend on the time of illumination and the strength of the resonances saturated after 9 min of illumination. These results have full reproducibility. Figure 3.3 (b) presents the spectra obtained using the rectenna probe for two durations of blue light illumination. The spectra with illumination-on versus illumination-off were taken several times (two of them reported to show reproducibility). Also in this case we observed the appearance of evident resonances whose strength saturated at increasing durations of illumination (10 and 15 minutes in the two experimental runs reported). Long excitation times are needed because, under our experimental conditions, the energy dissipation rate and the energy supply rate are almost equal, so that a long time is needed to accumulate enough energy into each protein in order to make intramolecular nonlinear interaction terms sufficiently strong to activate the condensation phenomenon.

The spectra obtained using the two previously described methods and for the longer durations of illumination are compared in Fig. 3.3 (c). The principal resonance at 0.314 THz is perfectly reproduced using two completely different and complementary setups. Since THz extinction in water is huge (2000 dB/cm), the emergence of this spectral feature of the protein out of the water absorption background must be associated with the activation of a giant dipole moment. And this can happen only as a consequence of the activation of a coherent oscillation of the whole molecule, possibly together with a dipole moment strengthening due to an electret-like structuring of water dipoles of the first hydration layers of the proteins as hydration shell might contribute to the magnitude of the protein dipole moment [160].

Since the BSA is a heart-shaped globular protein, a possible lowest frequency mode is of the hinge-bending kind, what suggests to get a first rough estimate of the frequency of a global oscillatory mode by schematizing the molecule as composed of two masses m, equal to half the total protein mass, joined by a spring of elastic constant k given by $k = EA_0/l_0$, where E is the Young modulus of the protein, A_0 and l_0 are its transverse section and length at rest, respectively. Using $m = 33$ kD, $A_0 \simeq 1.2 \times 10^{-13}$ cm^2, $l_0 \simeq 1.2 \times 10^{-7}$ cm, and $E = 6.75$ GPa, we find $\nu = (1/2\pi)\sqrt{k/m} \simeq 0.300$ THz which is close to the main resonance observed at 0.314 THz. Since the BSA molecule can be modeled to first order as a three-dimensional elastic nanoparticle [181], a more refined approximation is obtained by modeling the protein with an elastic sphere and then considering its vibrational frequencies.

The fundamental frequency of a spheroidal deformation mode of an elastic sphere is given by the formula [14]

$$\nu_0 = (1/2\pi)[2(2l+1)(l-1)]^{1/2} \left(\frac{E}{\rho R_H^2}\right)^{1/2} \tag{3.6}$$

which holds for $l \geq 2$. Using the following data for the BSA protein: Young modulus

$E = 6.75$ GPa obtained at room temperature using Brillouin light scattering of hydrated BSA proteins [133], hydrodynamic (Stokes) radius $R_H = 35$Å, and specific volume $1/\rho = 0.74$ derived from small-angle X-ray scattering (SAXS) experiments [114], we find for the lowest mode ($l = 2$) the frequency $\nu_0 = 0.308\ THz$ which agrees within an error of about 2% with the observed peak value at $\nu = 0.314\ THz$. Though such a modeling is unrealistic in what it does not take into account the details of the protein structure and the associated normal modes [158], it nonetheless catches a relevant aspect of the global deformation dynamics of the BSA molecule, namely the activation of a collective oscillation, also suggesting that the physical parameters adopted correspond quite well to the situation investigated. Secondary resonances are also present in both spectra. A possible explanation could be tentatively given considering torsional modes. These could be activated at the frequencies given by the relation [14]

$$\nu_t = \nu_0 \left(\frac{(2l+3)}{2(2l+1)} \right)^{1/2}, \qquad l \geq 2$$

where ν_0 is given by equation (3.6), whence, for $l = 2$ and $l = 3$, one finds $\nu = 0.257\ THz$ and $\nu = 0.246\ THz$ respectively. These could be associated with the two weaker absorption lines observed at $\nu = 0.278\ THz$ and $\nu = 0.285\ THz$. Here the larger discrepancy can be attributed to the non-spherical shape of the BSA, what entails the existence of different moments of inertia according to the rotation axis, whereas the breathing mode is insensitive to this fact. Minor peaks are observed at higher frequencies with the rectenna (falling outside the accessible frequency range of the near-field probe) when the protein solution is illuminated with blue laser light. However, the blue light illumination could produce spurious signals from the 2D electron gas of the FET junction as a consequence of electron-hole pairs excitation causing a change of the transistor channel conductivity. This effect is well known and studied in the literature [19] so that minor peaks could be instrumental artifacts due to this electron-hole pair creation effect.

3.2.3 Experimental activation time scale of the collective mode

In both cases of Montpellier and Rome experiments, the absorption feature, which is attributed to the activation of an out-of-equilibrium collective oscillation of the protein, appeared after several minutes of blue light irradiation: about 4 minutes in the Montpellier experiment, after 10 minutes in the Rome experiment (though in this latter case no measurement was performed before 10 minutes). In what follows we provide a consistency estimate of this long activation time with the physical conditions of the experiments. Going beyond a qualitative estimate is hardly feasible, and in any case would not affect the meaning of the experimental outcomes reported in the present work. Thus we proceed by estimating the balance between the energy input rate and the energy loss

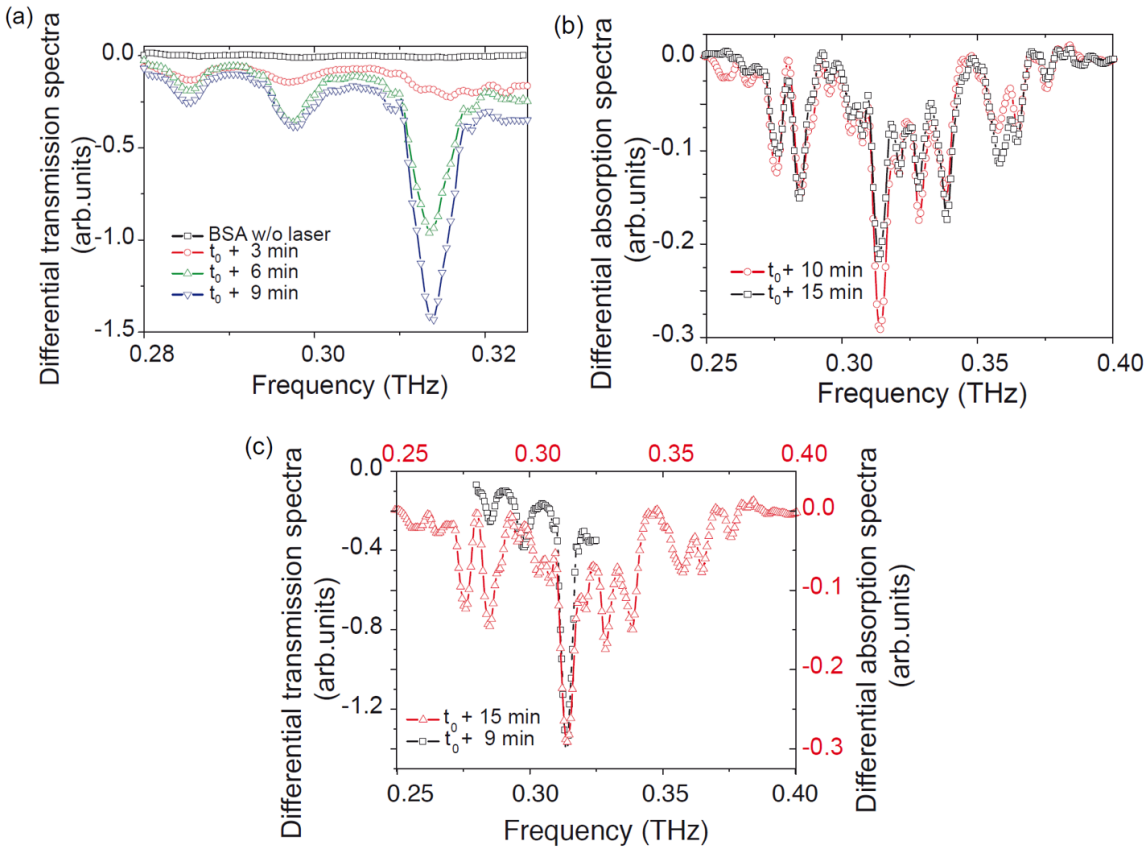

Figure 3.3: Differential transmission and absorption spectra as functions of the frequency. (a) Spectra obtained using the microwire probe after subtraction of the water spectrum in the absence of illumination and in the presence of illuminations for the reported durations. (b) Spectra obtained using the rectenna, after subtraction of the protein solution without illumination, for the reported durations. (c) Comparison of the two normalized spectra for the longest illumination durations.

rate of each molecule. As we shall discuss at the end of this Section, this long time is not an hindrance to the biological relevance of the phenomenon reported in the present work. An elementary account of the balance between energy gain and loss for each protein can be given by the equation

$$\frac{dE}{dt} = -\frac{2}{3}\frac{(Ze)^2|\ddot{\mathbf{x}}|^2}{c^3} - \Gamma + W \tag{3.7}$$

where E in the l.h.s is the numerical value of the energy of the system, the first term in the r.h.s. represents the radiative losses (bremsstrahlung) of the accelerated dipole of moment $Ze\mathbf{x}$, (where Z is the number of elementary charges e and $\mathbf{x}$ is the separation between the center of positive and negative charges) and W is the energy input rate due to the 488 nm light irradiation. Γ stands for other kind of energy losses leading to thermalization of the protein with its watery environment. For what concerns the energy input rate W, the energy difference between the entering photons, of wavelength 4.88×10^{-5} cm, and the fluorescently emitted photons, of wavelength 5.3×10^{-5} cm,

amounts to $3.18 \times 10^{-13} erg = 0.19$ eV. When the Argon laser operates at 500 μW the number of emitted photons per second is 1.2×10^{15}. The cross section of the fluorochrome Alexa488 is 3.2×10^{-16} cm^2 (free dye in water) [97], so that assuming a Gaussian beam section (at $1/e^2$) of 7.8×10^{-3} cm^2 (corresponding to a diameter of about 0.1 cm), we find that each Alexa488 molecule receives approximately 50 photons per second. Each protein molecule has an average number of $5 - 6$ fluorochromes attached to it so that, considering that part of them could be partly shadowed by the protein itself, we can assume that the average number of photons received by each protein per second belongs to the interval $120 \div 300$. Hence the upper bound for W is estimated between 3.8×10^{-11} erg s^{-1} and 9.5×10^{-11} erg s^{-1}. This estimate is obtained under the assumption that all the photons hitting the Alexa488 molecules are absorbed; the quantum yield of these dye molecules is high (92 %) so that practically all the harvested photons are converted into fluorescence thus providing an upper bound of the energy available for the protein excitation. Of course part of this energy can be dissipated in the surrounding environment in the form of heat. For what concerns the radiation losses, we proceed to estimate the time average value of $\overline{|\ddot{\mathbf{x}}|^2}$. Since the 63% of the N-isoform of the BSA protein consists of α-helices, we can assume that the so-called accordionlike vibrational modes of these helices provide the largest contribution to the protein extension and thus to the variation of the protein's dipole moment. At thermal equilibrium we can assume that the dipole elongation $\mathbf{x}(t)$ can be the result of an incoherent superposition like $\mathbf{x}(t) = \sum_{i=1}^{30} A_i \cos(\omega_i t + \xi_i)$, where the ξ_i are random phases, and the sum runs over the 30 α-helices of which the protein is composed. To compute the time average of $|\ddot{\mathbf{x}}|^2$ we have to estimate the quantity $\sum_{i=1}^{30} \frac{1}{2}\overline{A_i^2 \omega_i^4}$ (since the mixed terms average to zero). Using the formula $\omega_i = 2\pi(1/2L_i)(E/\rho)^{1/2}$ for the frequencies of the accordionlike modes of the α-helices [78], where $1/\rho = 0.74$, $E = 2.31 \times 10^{11}$ dyne cm^{-2} for α-helices, $L_i = 1.5N$ Å, where N is the number of amino acid residues, and assuming that A_i belongs to the interval $0.05L_i \div 0.1L_i$, and $Ze = -13 \times 4.803 \times 10^{-10} Fr$ for the BSA protein at neutral pH [13], we finally find:

$$\frac{2}{3}\frac{(Ze)^2}{c^3}\overline{|\ddot{x}|^2} \simeq 3.25 \times 10^{-12} \div 1.7 \times 10^{-11} erg\ s^{-1} \tag{3.8}$$

The range of values of the energy input rate and that of the radiative losses are thus almost overlapping. Making these estimates more precise is hardly feasible and is beyond the aims of the present work. What matters here is that since we experimentally observe the activation of the collective mode of the BSA molecules, the energy input rate W must exceed the rate of all the losses, radiative and non, and if this happens only by a small amount, then dE/dt can be so small as to require some minutes in order to

accumulate enough energy in each molecule. When the energy so accumulated exceeds a critical threshold value, the system undergoes a condensation transition channelling the largest fraction of the input energy into the lowest frequency mode(s). An elementary estimate of the rate of energy losses due to the bremsstrahlung in the condensed phase is obtained by entering into the Larmor formula (3.8) the dipole acceleration $|\ddot{\mathbf{x}}|$ computed from $\mathbf{x}(t) = A\cos(\omega_C t)$, putting $\omega_C = 0.314$ THz, which is the frequency of the collective mode, and assuming that the dipole elongation A is about 10 Å. The breakeven between the energy input and the radiative losses is then found for a dipole moment in the range $14500 \div 23000$ Debye, corresponding to an effective number of charges Z approximately in the range $290 \div 460$. In other words, in the condensed phase the total dipole of the protein oscillates at a low frequency (with respect to the accordion-like modes of the α-helices) so that the collective oscillation can be stable with respect to radiative losses up to the activation of large values of the protein dipole moment. We have neglected any estimate of the collisional losses - represented by Γ in equation (3.7) - because their estimate as viscous losses - on the basis of Stokes formula - gives an unreasonably high energy dissipation rate with respect to the energy input rate. If this were the case, no collective vibration would be observed at all. There is a vast literature about relaxation phenomena, thus thermalization, of proteins subject to different kinds of radiative excitations. The typical relaxation time scales are in the range of picoseconds to nanoseconds, with a remarkable exception - recently reported in [100] - where the thermalization of terahertz photons in a protein crystal happens on a micro- to milli-second time scale, which is interpreted as being due to Fröhlich condensation (no matter whether quantum or classical). To the contrary, typical picoseconds to nanoseconds relaxations usually pertain side chains relaxations or small groups of atoms. Also in the case of relaxations of collective modes detected with FIR spectroscopy or with THz Time Domain Spectroscopy [2, 90, 88] the physical conditions are very different with respect to our present experiments. In the mentioned literature the collective modes of proteins are probed at thermal equilibrium, thus in presence of all the other vibrational modes and under the action of weak exciting fields. In our experiments the protein molecules are out-of-thermal equilibrium and are strongly excited through an internal cascade of mode-mode couplings stemming from the fluorescence decay of the attached fluorochromes, and the THz radiation is only used to read the presence of the collective oscillation (see the preceding Subsection). On the other hand, it has been recently found that the hydration shell of the BSA protein is 25 Å thick [160], and this seem to be a generic property of solvated proteins [41]. The microrheology [169] of this kind of water-protein system, and in particular its high frequency viscoelasticity, is still an open research subject, making a quantitative estimate of the term Γ in equation (3.7) hardly feasible. A comment about the prospective biological relevance of the observed phenomenology is in order. The main energy source within living cells is provided by ATP hydrolysis. The typical intracellular concentration of ATP molecules

is given around 1 mM implying that a protein molecule in the cell undergoes around 10^6 collisions with ATP molecules per second [4]. Given the standard free-energy obtained from ATP hydrolysis estimated around 50 kJ.mol^{-1} = 8.306×10^{-13}erg, if we assume that only 1% or 2% of the collisions with ATP will provide energy, a power supply between 8.306×10^{-9}erg s^{-1} and 1.6×10^{-8}erg s^{-1} is potentially available. This could be at least two orders of magnitude larger than the power supplied to each protein in our experiments, but reasonably even much more than two orders of magnitude because we have assumed a hundred percent conversion efficiency of the energy supplied by the laser into internal vibrations of the protein. But this can be hardly the case, thus the condensation mechanism *in* vivo can be considerably faster.

3.2.4 Spectroscopic detection details

In both experiments, the collective oscillation of the BSA protein is seen as a spectroscopic absorption feature. At variance with standard absorption spectroscopy, where the radiation entering the absorbing medium is responsible for the creation of atomic or molecular excited states, in the experiments reported here the THz radiation is used to detect an already excited state of the molecules. Actually, the collective oscillation of the proteins makes them behave as very small antennas (Hertzian dipoles) with the characteristic property of antennas of simultaneously absorbing and emitting electromagnetic radiation. However, the absorption along the THz optical path cannot be compensated by the radiation emitted by the oscillating dipoles because it spreads over all the directions in space. The net result is an absorption feature. If we denote with $\vec{\mu}(t)$ the dipole moment of a protein and with $\vec{E}(t) = \vec{E}_0 \cos(\omega t)$ the electric field of the THz radiation, the attenuation of the electric energy density within the drop of protein solution is proportional to the work done by the electric field, that is, $L = -\vec{\mu}(t) \cdot \vec{E}(t)$. The oscillation of the dipole moment is necessarily damped, predominantly because of bremsstrahlung emission, so that, denoting by τ the lifetime of the activated collective oscillation and by ω_c its frequency, we can set $\vec{\mu}(t) = \vec{\mu}_0 e^{-t/\tau} \cos(\omega_c t)$. Thus, after averaging over all the relative orientations and all the phase differences ϕ between $\vec{\mu}(t)$ and $\vec{E}(t)$ such that the electric field does a positive work, we obtain

$$L(\omega) = 2 \int_0^{\pi} d\phi \int_0^{\infty} dt \mu_0 E_0 e^{-t/\tau} \omega_c \sin(\omega_c t) \cos(\omega t + \phi) \ . \tag{3.9}$$

This is the elementary attenuation process of the THz radiation. This process is repeated in time for each molecule at a rate proportional to the intensity of the drop illumination with the blue light. Moreover, the total attenuation is proportional to the concentration of absorbing molecules in the protein solution. Equation (3.9) gives for $L(\omega)$ a Lorentzian shape centered at ω_c, the resonance frequency of the collective oscillation of the BSA protein. Figure 3.4 shows three different shapes of the function $L(\omega)$ obtained for different

values of τ (in arbitrary units). These line shapes show that an already vibrating underdamped dipole absorbes the weak terahertz-radiation-probe with the same frequency pattern of the 0.314 THz absorption line reported in Figure 3 of the main text. The latter is well fitted by the $L(\omega)$ function by using a Q factor of 50 ($Q = \Delta\nu/\nu$, that is the ratio between the line width and the line frequency). In Figures 3.5a and 3.5b some control

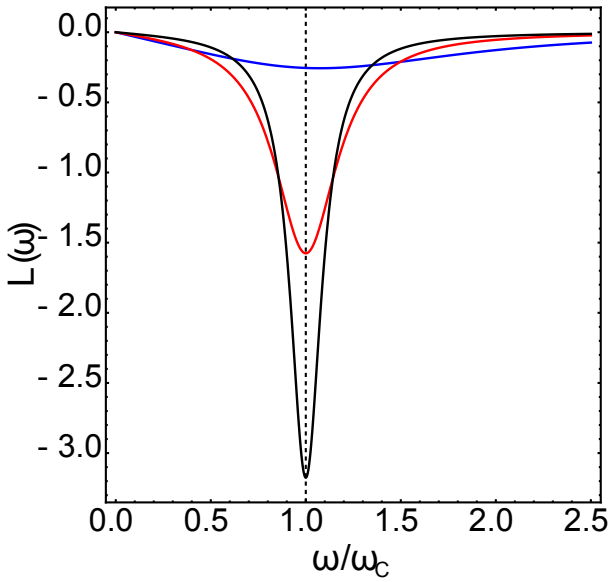

Figure 3.4: The function $L(\omega)$ of Eq.(3.9) is plotted in arbitrary units for three different values of τ. The blue line corresponds to $\tau = 1$, the red line to $\tau = 5$, the black line to $\tau = 10$, having set $\omega = 10$.

spectra are reported which have been obtained with the microwire antenna. The two groups of spectra refer to the blue light emitting laser switched off and on, respectively. The observed absorption line at 0.314 THz is clearly found only when the fluorochrome AF488 is bound to the BSA molecules and in presence of 488 nm laser light illumination of the protein solution. These spectra rule out any other origin of the observed absorption feature beside the proposed one in the main text of the present work. In Figure 3.6 the photoresponse spectra obtained with the rectenna probe highlight the same tendency. A clear difference is again observed between the spectra when the blue light illumination is switched off and on.

3.3 Discussion

Let us stress an important point: computational normal mode analysis for proteins has shown nearly continuous vibrational density of states [158] which have also been proved nearly uniformly optically active. Moreover, the coupling of these vibrational modes with water results in broad absorption features [73, 159]. But this is true at *thermal equilibrium*, whereas under out-of-equilibrium phonon condensation the energy content of all the normal modes is strongly depleted with the exception of the collective mode.

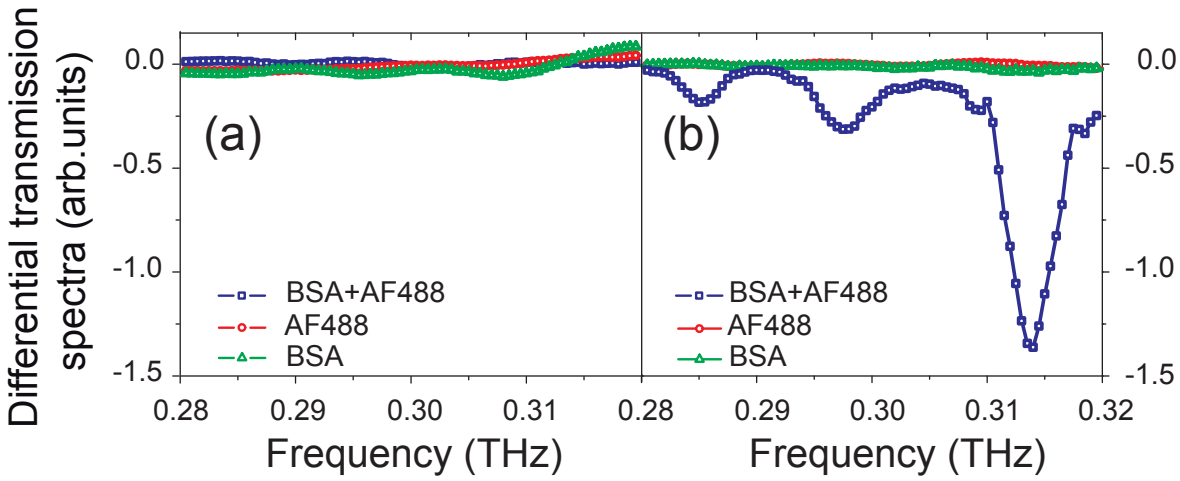

Figure 3.5: Differential transmission spectra of the microwire-based absorption spectra. (a) Without blue light illumination (laser OFF). Obtained with: solvated AF488 in water (red circles); solvated non-labelled BSA in water (green triangles); BSA labelled with AF488 solvated in water (blue squares). (b) With blue light illumination (laser ON). Obtained with: solvated AF488 in water (red circles); solvated non-labelled BSA in water (green triangles); BSA labelled with AF488 solvated in water (blue squares).

Whence a narrow absorption feature. And, in fact, the computation of the function $L(\omega)$ in 3.9 shows how a dipole actively oscillating at a given frequency entails an absorption feature of shape similar to the experimentally observed one.

According to our classical version of the Fröhlich model, it is also expected that the appearance of a collective oscillation should exhibit a threshold-like behaviour when increasing the energy flowing through the protein. Actually, Figure 3.7 (a) presents a clear threshold in the intensity of the resonance peak at 0.314 THz when the optical input power exceeds 10 μW. By using a classical formalism for the analysis of the out-of-equilibrium phonon condensation we have calculated the intensity of the normal vibrational modes of the BSA-protein as a function of the source power injected through the protein. Figure 3.7 (b) highlights a threshold-like behaviour of the intensity of the fundamental mode that accumulates the energy at the expenses of the excited modes, in *qualitative* agreement with the experimental outcome. By increasing the number of modes included in the calculation this threshold becomes more and more evident. The experimental and theoretical results reported in Figure 3.7 agree also in displaying a saturation effect occurring at large values of the energy input rate.

The observed spectra are certainly due to the light-excited protein because the spectral feature at 0.314 THz was not observed by illuminating: *i)* water alone; *ii)* a watery solution of the fluorochrome in the absence of the protein; *iii)* a watery solution of the BSA protein without the bound fluorochrome. On the other hand, the observed spectral line at 0.314 THz immediately disappears by switching off the laser. Remarkably, the spectra obtained with two independent and different experimental setups, based on two different methods of detection of the THz radiation, operated in two different labora-

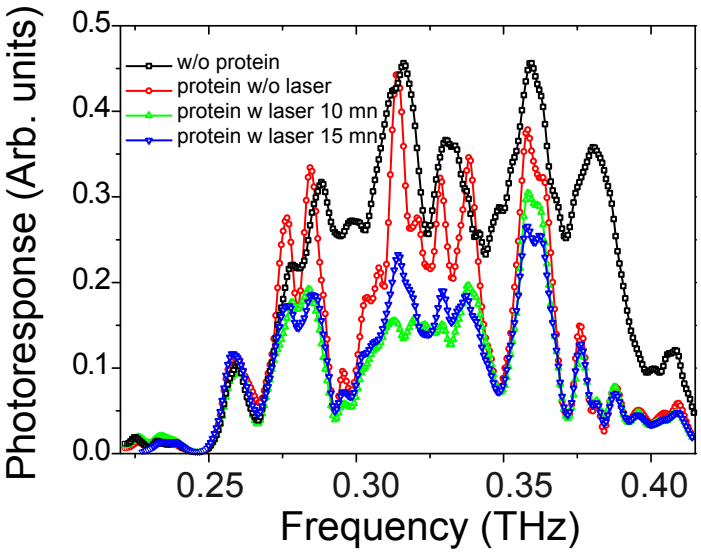

Figure 3.6: Raw data of the rectenna-based absorption spectra. Black squares correspond to the THz emitting source spectrum without the protein solution. Red circles correspond to the absorption spectrum of the BSA protein solution without blue light illumination. Green triangles correspond to the absorption spectrum of the BSA protein solution recorded after 10 minutes of blue light illumination. Blue triangles correspond to the absorption spectrum of the BSA protein solution recorded after 15 minutes of blue light illumination.

tories, show a strikingly good overlap of the respective absorption line profiles at 0.314 THz. A result in excellent agreement with the frequency of 0.308 THz predicted for the spheroidal (collective) vibrational mode computed on the basis of recent experimental measurements of the relevant parameters of the BSA protein. This triple concordance among the results so far obtained should be enough to exclude experimental artifacts. This notwithstanding various sources of artifact for the observed phenomenology were considered. A first objection suggests itself, namely that the observed phenomenology is just a trivial heating effect due to the laser light. This would be true in the absence of a frequency dependent response to the injection of energy into the proteins. Heating indeed means increasing of the kinetic energy of the atoms and group of atoms of the protein entailing energy equipartition among the vibrational modes of the protein. Hence neither a frequency dependent effect nor a threshold effect for the energy input rate would have been measured, but just a new thermal equilibrium state would have been achieved. To the contrary, each protein - submitted to continuous energy feeding and energy dissipation - behaves as an open system undergoing a non-equilibrium phase transition: when the ratio between energy gain and losses exceeds a critical value a collective behavior sets in producing the phonon condensation. Then another question arises about the conversion mechanism of the visible light energy absorbed by the electrons of the complex protein/dyes into the vibrational modes of the proteins. This mechanism of rapid intramolecular dissipation of energy through quake-like structural motions as a

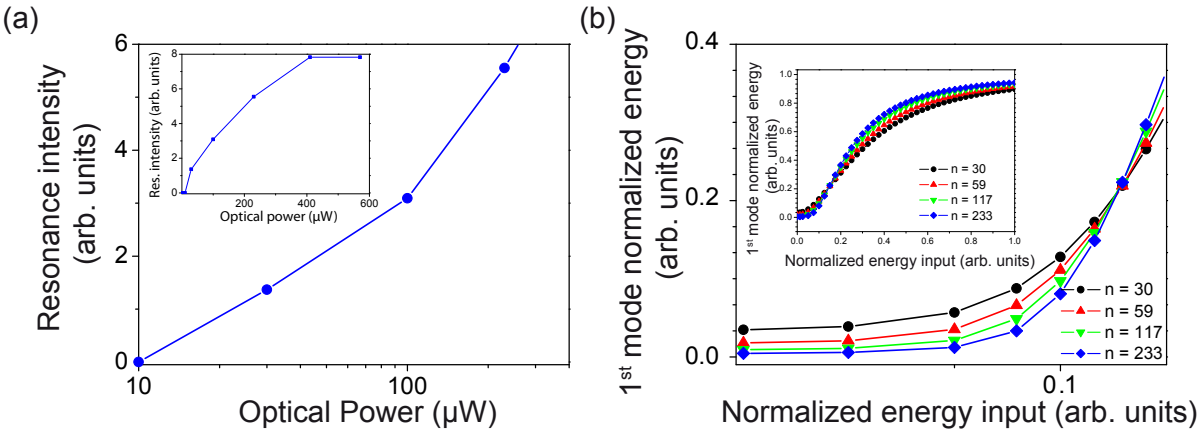

Figure 3.7: Threshold-like behaviour of giant dipolar oscillations. (a) Intensity of the resonant peak measured at 0.314 THz as a function of the optical laser power. (b) Normalized energy of the fundamental mode calculated as a function of the normalized source power. The different curves correspond to the reported numbers of normal modes of the BSA protein. Theory and experiment are in *qualitative* agreement.

consequence of a perturbation (such as the breaking of a chemical bond or the absorption of photons (through electronic transitions)) is being given increasing experimental attention [6, 96, 9, 20] and is referred to as "protein quake". Similarly to an earthquake, this effect describes how a protein strain is released at a focus or "hot-point" (in our case the fluorochromes) and then rapidly spreads as a structural deformation through waves, thus exciting protein vibrational modes. Another source of artifact could be the apparition of standing waves and related interferences, but these would have been easily identified. Furthermore, there would be no reason for such interferences - if any - to manifest themselves as a consequence of the excitation of fluorochromes through the blue light.

Several terahertz spectroscopic studies have reported about collective modes of proteins, still performed at thermal equilibrium and mainly carried on using dry or low-hydrated powders because of the very strong absorption of water [1, 163, 48, 105]. More recent studies also addressed solvated proteins [181, 42]. Other recent studies on solvated BSA in THz [23] and sub THz frequency range have shown [160] broad resonances due to an efficient coupling of low frequency modes of the protein with the surrounding water, but - again - all of these works are at *thermal equilibrium*. In common with these previous studies, our present work confirms the relevance of the coupling of the protein with the surrounding water molecules. In fact, the strong absorption feature that we observed in a watery solution of the BSA protein put *out of thermal equilibrium*, reveals that the protein vibrating in its collective mode has to be dressed by ordered layers of water molecules in order to attain an effective dipole moment sufficiently large to overcome the strong absorption of bulk water.

We anticipate that our result could open a broad domain of systematic investigations

about out-of-equilibrium activation mechanisms and properties of collective oscillations of different kinds of biomolecules. Furthermore, as our result explains why electrodynamic interactions between biomolecules have hitherto eluded detection, it motivates new efforts to detect them [117].

CHAPTER 4 Experimental detectability of long range interactions

While signatures of collective oscillations of biomolecules have been detected through THz spectroscopy and discussed in chapter 3, the experimental detectability of long-range interactions is still to be developed. As quoted before in the introduction and explained in [140] and [117], FCS has been envisaged as a relevant technique to such issue, thanks to its single molecule sensitivity and the information it provides like the diffusion time and the number of molecules in solutions.
Respectively, the first article [140] investigates why and how long-range intermolecular interactions of electrodynamic nature might influence the 3D encounter dynamics of biological partners. Based on a simple analytical study in one spatial dimension, it has been reported that quantitative and qualitative dynamical properties that will stand out in case such interactions play an active role at the biomolecular level. Moreover, non-negligible effects were reported in a parameter domain accessible to standard laboratory techniques suggesting that the contribution of long-range electrodynamic interactions in biological processes might be well estimated from experimental measurements. The physical observable chosen (the first encounter time between two interacting biomolecules) turns out hardly measurable in practice because it requires to follow the dynamics of single molecules.
Thus the second work [117] aims at filling this gap between theory and experimental feasibility, by investigating some transport properties of long range interactions acting among a set of particles freely moving in a fluid environment. With the one dimensional analytic results replaced by 3D numerical results in a more realistic context.
To finish, in this chapter, we report about the third and last step of a feasibility study concerning a possible strategy to detect long range electrodynamic forces acting among biomolecules. In living matter, resonant (thus selective) electrodynamic attractive interactions [143] could be a relevant mechanism of molecular recruitment at a distance, beyond all the well-known short-range forces (chemical, covalent bonding, H-bonding, Van der Waals). Unfortunately, because of technological limitations, an experimental proof or refutation of this possibility has been for a long time and is still sorely lacking. In our preliminary investigations in [140] and [117] we have put forward the idea that a possible experimental method to investigate whether these forces can be at work, when suitably activated, could come from the study of how the diffusion behavior of biomolecules in solution could change when their concentration is varied (that is, when

the average intermolecular distance is varied). The experimental technique envisaged in [117] was Fluorescence Correlation Spectroscopy (FCS), a well established experimental technique [101, 71, 47]. In order to check whether the study of molecular diffusion through the FCS technique can be actually effective to detect intermolecular long-range interactions, in this chapter we have chosen to tackle a system of molecules which interact through *b*uilt-in long range interactions, that is, through an electrostatic force field. Even if our ultimate goal is to detect electrodynamic intermolecular interactions, there are still several uncertainties concerning their activation and strength, therefore a preliminary assessment of the reliability of the experimental method - performed under perfectly controlled conditions - is timely. Thus we have now undertaken a successful experimental assessment of the method, a crucial step forward with respect to the two preceding works in Refs. [140] and [117]. We chose a system where the interacting molecules were a protein, white egg Lysozyme, and an oppositely charged dye, Alexa Fluor 488. These molecules were solvated in pure water, thus in the absence of Debye screening, and in salted water to confirm that the concentration dependent attenuation of the self diffusion coefficient is due to the electrostatic interparticle interactions. Molecular Dynamics simulations have been also performed, and their results are in excellent agreement with the experimentally observed phenomenology. We conclude that the FCS technique is actually a viable experimental procedure for an assessment of the strength of long-range intermolecular interactions and thus, sooner or later, also of electrodynamic intermolecular interactions.

4.1 Materials and Methods

4.1.1 Materials

Chicken egg white Lysozyme was purchased from Sigma (L6876) (St. Louis, MO); it was used without further purification and was either dissolved directly into bidistilled water or diluted in series. Even though dissolving a protein in pure water can strongly modify its 3D structure, in the present context this does not affect the phenomenon in which we are interested. AF488 5-TFP (Alexa Fluor 488 Carboxylic Acid, $2,3,5,6-$Tetrafluorophenyl Ester), 5-isomer (A30005) was purchased from Molecular Probes Invitrogen. The dye has excitation/emission of 495/515 nm and a molar extinction coefficient of $\varepsilon_{495} = 71,000$ M^{-1} cm^{-1}. Both the protein and dye concentrations have been determined measuring their absorbance with a Nanodrop 1000 Spectrophotometer (ThermoScientific), at 280 nm with a molar extinction coefficient of 36000 M^{-1} cm^{-1} and at 495 nm with a molar extinction coefficient of 71000 M^{-1} cm^{-1}, respectively. To change the ionic strength of the solution, sodium chloride (NaCl) has been diluted in bidistilled water getting molar concentrations of 20mM, 50mM, 100mM and 150mM.

Then these solutions are used to dilute the protein and the dye. The above mentioned chemically labelled Lysozyme molecules have been obtained by homemade labelling using 2 mg/mL of proteins with 0.7 times of A488 5-TFP in sodium bicarbonate at a pH $\approx$ 8.5, during one hour. This has been done in order to compare the results of AF488 diffusion time in our experiments with the Lysozyme diffusion time. Unconjugated dye was removed using a PD-mini-trap G25 (GE Health Care) according to the instructions of the manufacturer, using gravity protocol, and the degree of labelling was determined spectroscopically. As a container for the solutions, 8-wells Labtek chambered coverglass has been used.

4.1.2 FCS measurements

FCS measurements were performed on a custom-made apparatus based on an Axiovert 200 M microscope (Zeiss, Germany) with an excitation 488 nm Ar^+-ion laser beam focused through a Zeiss water immersion Apochromat 40X/1.2 numerical aperture objective. The fluorescence was collected by the same objective, separated from the excitation light using a dichroic mirror, and then delivered to an avalanche photodiode (SCPM AQR-13, Perkin Elmer) through 545/20 nm bandpass filter. A 50 μm diameter confocal pinhole reduced the out-of-focus fluorescence. The system has been switched on around 60 min prior to the measurements to allow for stabilization of all components. The laser waist $\omega_{x,y}$ was set by selecting with a diaphragm the lateral extension of the laser beam falling onto the back-aperture of the microscope objective [17] and was then estimated using the well known diffusion of Rhodamine 6G in water [134] $\omega_{x,y} = \sqrt{4D\tau_D}$. The literature diffusion coefficient for Rh6G [113] ($D_{Rh6G,22.5°C} = 426\mu\text{m}^2/\text{s}$) has been corrected to account for the experimental temperature (30°C) and the viscosity of water at the same temperature (Eqs.(4.8) and (4.9)), giving $D_{Rh6G,30°C} = 517\mu\text{m}^2/\text{s}$. For Rhodamine 6G sample we used a power of 300μW at the back-aperture objective, while for all the other samples, to avoid any saturation effect that would affect the shape of the excitation volume, we used a power of 100μW. The measurements have been performed in 8 well chamber slide using a volume of 400 μL. In order to check whether some artifacts could be caused by the sticking of either the dye or the protein molecules to the well walls, some tests have been performed with coated labteks. The coating was performed overnight, at room temperature, by putting 700μL of BSA in PBS at a concentration of 10 mg/ml in each well of the labtek. Then the labtek has been gently rinsed two times and dried. Tests performed with coated labtek have not shown differences (data not shown). The measurement time was of 200 s divided into 10 s runs. The experiments were performed at a temperature of 30°C and the samples were thermostated in the microscope system at least during two hours. Each measurement was repeated at least three times successively in different labtek wells. The AF488 concentration was fixed at 1 nM in all samples. The diffusion coefficients were

determined by measuring the apparent diffusion time of the fluorescent molecules through a confocal volume, always using the formula $D = \omega_{x,y}^2/4\tau_D$. The normalization of the diffusion coefficients was done by taking for D_0 the value of the diffusion coefficient of the AF488 obtained at 1 nM. Each reported value of D and its corresponding error bar are the outcomes of 20 measurements performed on four different samples and repeated for three independent experiments. Autocorrelation function calculations and fits were performed using the analytical expression given by Eq.(4.6). The ACF data were fitted to estimate the parameters N, τ_D, τ_T. Then, the resulting value of N and the corresponding count rate, were used to determine the brightness per molecule. The accuracy of the fit for each data set was assessed through the value of the χ^2 parameter and by inspection of the residuals, which were to be distributed uniformly around zero.

4.1.3 FCCS measurements

FCCS measurements were performed on a commercial FCS setup (ALBA FCSTM, from ISS Inc., Champaign, America) with two excitation picosecond/CW diode lasers operation at 488 and 640 nm (BDL-488-SMN, Becker and Hickl, Germany) with a repetition rate of 80 MHz, focused through a water immersion objective (CFI Apo Lambda S 40X/1.25 WI, Nikon). The fluorescence was collected by the same objective, splitted into two detection paths by a 50/50 beam splitter (Chroma 21000) and filtered by two Emission filters (525/40 nm band pass, Semrock FF02-525/40 and 675/67 nm band pass, Semrock FF02-675/67 for the green and red channels, respectively) and detected by two avalanche photodiodes (SPCM AQR-13 and SPCM ARQ-15, Perkin Elmer / Excelitas).

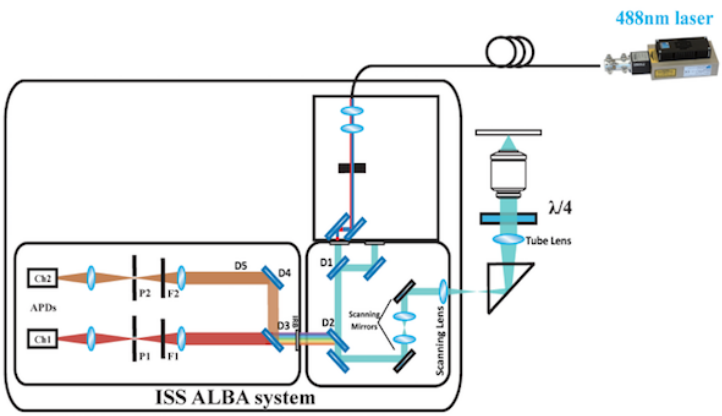

Figure 4.1: Schematic diagram of the FCCS apparatus. The excitation beam starts from the diode laser (on the top right of the image), goes through an optic fiber, through a set of lenses and a dichroic mirror (on the middle of the image), and reaches the sample placed in a confocal microscope through the objective (on the right). The emitted fluorescence beam goes back through the objective, is reflected on the dichroic mirror, then is splitted into two beams that are finally collected by two detectors (on the left). Other details in subsection 4.1.3.

4.2 Experimental results

In the present section we report about the effect of electrostatic long distance intermolecular interactions on the diffusion behavior of oppositely charged molecules. Molecular diffusion is detected using Fluorescence Correlation Spectroscopy (FCS). As mentioned in the Introduction, the interacting molecules considered in the present study are Lysozyme, a small globular protein of 14307 Da [24, 81] keeping a net positive charge for all pH values up to its isoelectric point, which is around pH = 11.35 [174], and Alexa Fluor 488 dye (hereinafter AF488) a very bright anionic fluorophore. FCS is a well established spectroscopic technique that enables a real time investigation of diffusion processes through a statistical analysis of the fluctuating fluorescence signal detected [101, 71, 47, 146, 72]. Self diffusion is affected by any interaction among the diffusing species, repulsive or attractive, that produce an attenuation depending on the interparticle interaction; the stronger the interaction the larger the deviation from Brownian diffusion [117]. The experimentally accessible parameters to implement this study are the average intermolecular distance $\langle d \rangle$ and the ionic strength of the electrolytic solution used, as already discussed in a preceding paper of ours [117]. The average intermolecular distance among molecules changes with their concentration as $\langle d \rangle = C^{-1/3}$, where C is the total number of molecules per reaction volume. The electrostatic interaction among the molecules in electrolytic solution is described by the Debye-Hückel potential [173]:

$$U_{\text{Debye}}(\mathbf{r}) = \frac{Z_1 Z_2 e^2}{\varepsilon_r |\mathbf{r}|} \cdot \frac{\exp\left[-\frac{2R}{\lambda_D}\left(\frac{|\boldsymbol{r}|}{2R} - 1\right)\right]}{(1 + R/\lambda_D)^2} \,, \tag{4.1}$$

where λ_D is the Debye screening length of the electrolytic solution, R is the molecular radius, e is the elementary charge and ε_r is the static dielectric constant of the medium. For a monovalent electrolyte, like NaCl which has been used throughout this study, the Debye length in Eq.(4.1) reduces to:

$$\lambda_D = \sqrt{\frac{\varepsilon_r \varepsilon_0 k_B T}{2 N_A e^2 I}} \,. \tag{4.2}$$

where ε_0 is the vacuum permittivity, k_B is the Boltzmann constant, N_A is the Avogadro constant and I is the ionic strength. Debye screening - due to small ions freely moving in the environment - is an essential feature of biological systems because it shortens the range of electrostatic interactions. In principle, counterions condensation effect can heavily affect the interaction among biomolecules so that "like likes like" effects can take place [104, 61]. Nevertheless for spherical macroions (as the proteins have been modeled in numerical simulations) the counterions condensation phenomenon does not take place, and the Debye potential properly accounts for the effect of counterions. In the limiting case of $\lambda_D \to +\infty$, charged particles in electrolytic solution are submitted to a pure

Coulomb potential given by:

$$U_{\text{Coul}}(\boldsymbol{r}) = \frac{Z_1 Z_2 (e)^2}{\varepsilon_r |\boldsymbol{r}|} \ , \tag{4.3}$$

that is, the Debye-Hückel short-range potential turns to a long-range one. By long-range interaction we mean an interaction potential falling off with the interparticle distance r as $1/r^\nu$ with $\nu \leq d$, d being the spatial dimension of the system. The main outcome of FCS measurements on a solution of oppositely charged molecules is the average time τ_D taken by a molecule of AF488 to cross the section of some observation volume in presence of different concentrations of Lysozyme. The measure of τ_D gives access to physical quantities as the diffusion coefficient D (Eq. (4.7)) and the hydrodynamic radius R_H (Eq.(4.8)). This study has been performed for different average values of the intermolecular interaction strength. The latter depends on the average intermolecular distance $\langle d \rangle$, and, possibly, on a variation of the Debye screening length. The average distance between any two interacting molecules is given by

$$\langle d \rangle = (C_{AF488} + C_{Lys})^{-1/3} \ , \tag{4.4}$$

where the concentration of the AF488 dye has been kept constant and equal to 1 nM, while the Lysozyme concentration covered a range between 0 and 0.69 mM (9.86 mg/ml). We proceeded by diluting a drop of a 100 nM watery solution of the AF488 dye into a larger quantity of Lysozyme solution so as to keep constant the dye concentration in the final mixture. If N_0/V_0 is the initial concentration of the dye, and if N_p/V_p is the initial concentration of the protein, then $C_{AF488} = N_0/(V_0 + V_p)$ and $C_{Lys} = N_p/(V_0 + V_p)$ so that Equation (4.4) trivially follows.

4.2.1 Autocorrelation and data treatment

The autocorrelation function $G(\tau)$, originated by molecules interacting and diffusing in and out of the observation volume, is defined by

$$G(\tau) = \frac{\langle \delta F(t) \delta F(t+\tau) \rangle}{\langle F(t) \rangle^2} \tag{4.5}$$

where $\langle F(t) \rangle$ is the average intensity, $\delta F(t)$ the intensity of fluctuations, and the brackets mean ensemble average. The general procedure consists in fitting $G(\tau)$ with the appropriate mathematical model describing the characteristics of the system under study. The analytical form of the autocorrelation function for a single molecular species, assuming a three-dimensional Gaussian profile of the excitation beam accounting for diffusion [101] and a triplet state of the dye [175], is obtained under the assumption that diffusion driven by random hits of water molecules and protein-dye dynamics driven by electrostatic forces

are independent processes:

$$G(\tau) = 1 + \frac{1}{N} \frac{1 + n_T \exp\left(-\frac{\tau}{\tau_T}\right)}{\left(1 + \frac{\tau}{\tau_D}\right)\sqrt{1 + s^2 \frac{\tau}{\tau_D}}} \ . \tag{4.6}$$

Here N stands for the number of molecules in the FCS observation volume, τ_D is the diffusion time through this volume, τ_T the triplet lifetime, $n_T = Tr/(1 - Tr)$, with Tr the fraction of molecules in the triplet state. The dimensionless parameter s, called structure parameter, describes the spatial properties of the detection volume. It is given by $s = \omega_{x,y}/\omega_z$, where the parameter ω_z is related to the length of the detection volume along the optical axis, and the radial waist $\omega_{x,y}$ is related to the radius of its orthogonal section. The diffusion coefficient D is expressed as a function of the radial waist $\omega_{x,y}$, and of the diffusion time τ_D by:

$$D = \omega_{x,y}^2 / 4\tau_D \ , \tag{4.7}$$

and for isolated molecules following a Brownian motion, the hydrodynamic radius R_H may be computed using the Stokes−Einstein equation:

$$R_H = \frac{k_B T}{6\pi\eta(T) D} \ , \tag{4.8}$$

where T is the absolute temperature, k_B the Boltzmann constant, and η the viscosity of the fluid. The viscosity of liquids is a decreasing function of temperature and is expressed empirically between 0°C and 370°C, with an error of 2.5 %, by the expression [3]

$$\eta(T) = A \times 10^{B/(T-C)} \ . \tag{4.9}$$

For water, the parameters A, B and C are equal to 2.414×10^{-5} Pa s, 247.8 K and 140 K, respectively. In Figure 4.2 some typical outcomes of the FCS measurements are displayed. These are the autocorrelation functions (ACFs) - defined in Eq.(4.5) - of fluorescence intensity fluctuations (for graphical reasons the normalized versions are displayed). To assess afterpulsing artefacts on the ACFs, Fluorescence Cross Correlation Spectroscopy (FCCS) measurements have been also performed, and the results so obtained are in perfect agreement with those found with FCS. Then the experimental ACFs are fitted by means of the analytic expression in Eq.(4.6) where we used $s = \omega_{x,y}/\omega_z = 0.2$ and τ_T was left free. Out of these measurements and fittings one obtains the diffusion times τ_D at different values of $\langle d \rangle$, and hence, according to Eq.(4.7), the values of the diffusion coefficient D of the AF488 molecules can be worked out after having performed an accurate measurement of the waist size $\omega_{x,y}$ by means of Rhodamine Rh6G used as a diffusion standard (details are given in Section 4.1). When the Lysozyme concentration is zero the

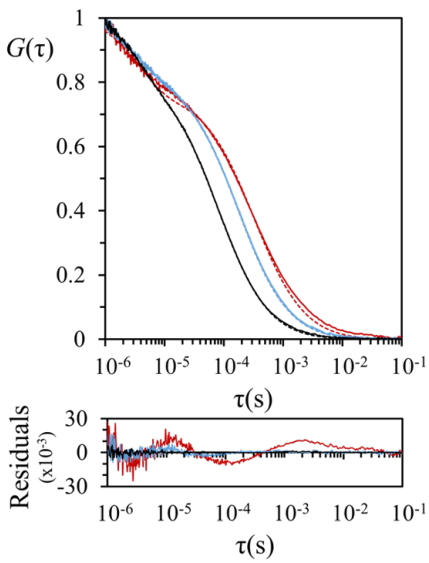

Figure 4.2: FCS measurements. Semilog plot of the normalized autocorrelation function of fluorescence fluctuations, defined in Eq.(4.6), obtained at $\langle d \rangle = 240$Å (red line), at $\langle d \rangle = 920$Å (blue line), and at $\langle d \rangle = 4200$Å (black line). Working temperature 30^oC.

solution contains only 1nM of AF488 corresponding to an average intermolecular distance of 11841.8Å. The diffusion coefficient of the dye in the absence of Lysozyme is used as the infinite dilution value D_0 of AF488. Then the average protein-dye distance is varied by varying the Lysozyme concentration. The fitted values of the parameters for solutions of variable concentrations of Lysozyme and 1nM of AF488 are reported in the Table shown in Figure 4.11. The number of fluorescent dye molecules N is observed to decrease at increasing Lysozyme concentration as a consequence of a quenching phenomenon already reported in the literature and briefly discussed in section 4.4.1. As several experiments have been performed on different days - so that the outcomes of the measures can be affected by even minor modifications of the FCS and FCCS setups - the values of the measured diffusion coefficient D are normalized to the infinite dilution value D_0, which is determined anew each time a new experiment is performed, and which corresponds to Brownian diffusion of the dye molecules. In Figure 4.3(a) we can observe that at low concentrations of Lysozyme, corresponding to an average interparticle distance larger than approximately 2500Å, the diffusion of the dye molecules is Brownian, that is, $D/D_0 \simeq 1$, where $D/D_0 = \tau_{D_0}/\tau_D$ (see Eq.(4.7)). By increasing the Lysozyme concentration the normalised diffusion coefficient is observed to markedly drop, and this is attributed to the attractive electrostatic interaction among the dye and protein molecules, as is qualitatively discussed below, and quantitatively discussed in Section 4.3. The larger the concentration of protein molecules the stronger the electrostatic attraction they exert upon the dye molecules. The dye diffusion can be slowed down - below the Brownian diffusion regime - through two mechanisms: on the one side, being attracted in every direction, the dye molecules undergo a sort of dynamical "frustration" [117]; on the other

side, the protein and the dye molecules can form temporary/"flickering" bound states. In Figure 4.3(b) the experimental outcomes obtained for the non-normalised D are plot-

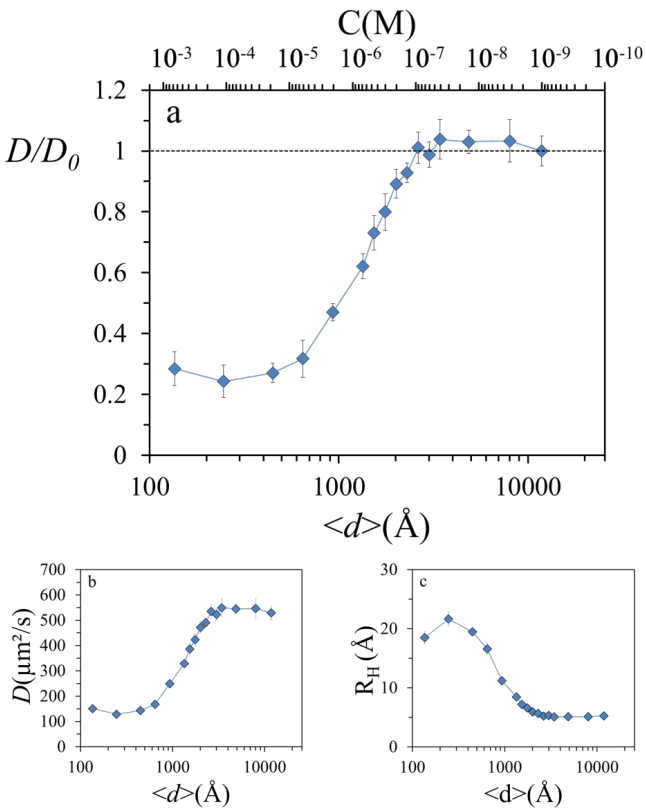

Figure 4.3: Semilog plot of the normalized diffusion coefficients D/D_0 of AF488 as a function of the distance in Å between proteins and dyes (a); semilog plot of the diffusion coefficient D for a single experiment with 0mM of NaCl in solution (b); semilog plot of hydrodynamic radius (c) of AF488 (1nM) versus the average distance between all the molecules in pure water.

ted as a function of the average intermolecular distance. The knowledge of the diffusion coefficient D allows to estimate the equivalent hydrodynamic radius R_H through the Stokes-Einstein equation (Eq.(4.8)); the variation of R_H as a function of $\langle d \rangle$ is reported in Figure 4.3(c). At infinite dilution, the diffusion coefficient D_0 of AF488 in water, and its corresponding hydrodynamic radius, are found to be equal to 532 ± 23.5 $\mu m^2/s$ and 5.2 ± 0.2 Å, respectively. Let us remark that the patterns of the ACFs reported in Figure 4.2 and Figure 4.9 are well fitted by the single species function in Eq.(4.6) even though a-priori a two-species ACF [1] could better take into account the possible presence of at least two subpopulations, one of dye molecules temporarily bounded to proteins, and the other of freely moving dye molecules. However, fitting the ACFs by taking as free pa-

[1] If there are M different species of non-interacting diffusing particles in the observation volume, the overall fluorescence autocorrelation is

$$G(\tau) = \frac{1}{N} \sum_{i=1}^{M} \frac{f_i[1 + \ n_T \exp(-\tau/\tau_T)]}{\left(1 + \frac{\tau}{\tau_{D,i}}\right) \sqrt{1 + s^2 \frac{\tau}{\tau_{D,i}}}}$$

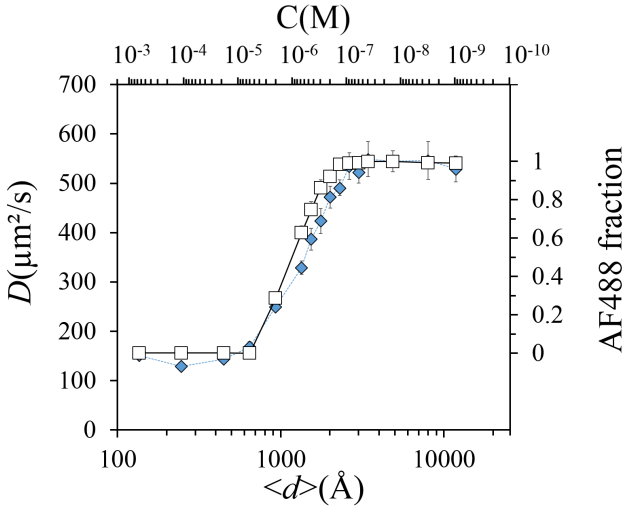

Figure 4.4: The diffusion coefficient (blue diamonds) and the fraction of free AF488 molecules (white squares) are compared. In the two-species fitting to compute the fraction of free dye molecules the following parameters have been kept fixed: τ_{AF488} =78.8μs, τ_{Lys} =210μs, triplet time of AF488 3.4μs, and triplet time of Lysozyme 3.34μs.

rameters both the diffusion time of the AF488 molecules and of the Lysozyme molecules leads to a poor quality results. To the contrary, an interesting result is found by performing a two-species fitting, where both the diffusion times of AF488 and of Lysozyme are kept fixed, to work out the relative population of free AF488 dye versus temporary bound AF488-Lysozyme states. The outcome is reported in Figure 4.4 in the form of the fraction of freely moving AF488 molecules with respect to the total population of AF488 molecules, and given as a function of both the average interparticle distance $\langle d \rangle$, given by Eq. (4.4), and particle concentration. It appears evident that when the diffusion of the AF488 molecules is Brownian the fraction of freely diffusing molecules is equal to 1, then this fraction drops parallely to the drop of the diffusion coefficient until almost all the AF488 molecules appear bounded to the Lysozyme molecules. This cross checks with the observation that the diffusion coefficient D measured at the lowest values of the intermolecular distances has to correspond to the condition where all the molecules of AF488 are bounded to the Lysozyme molecules for most of the time, thus in this case D must approximately equal the value of the Lysozyme diffusion coefficient (apart from a small difference due to a slightly modified Stokes radius). Therefore, the diffusion coefficient of Lysozyme molecules chemically labelled with AF488 has been measured. The value obtained is $D_{Lys} = 166.55 \pm 1 \mu\text{m}^2/\text{s}$ which is in fairly good agreement with that one corresponding to the lowest intermolecular distance in Figure 4.3(b). As a control, we use the white egg Lysozyme hydrodynamic radius $R_H = 20.5$Å reported in Ref.[176],

where N is the total number of molecules in the confocal volume. The M populations with diffusion times $\tau_{D,i}$ must satisfy the condition: $\sum_{i=1} f_i = 1$.

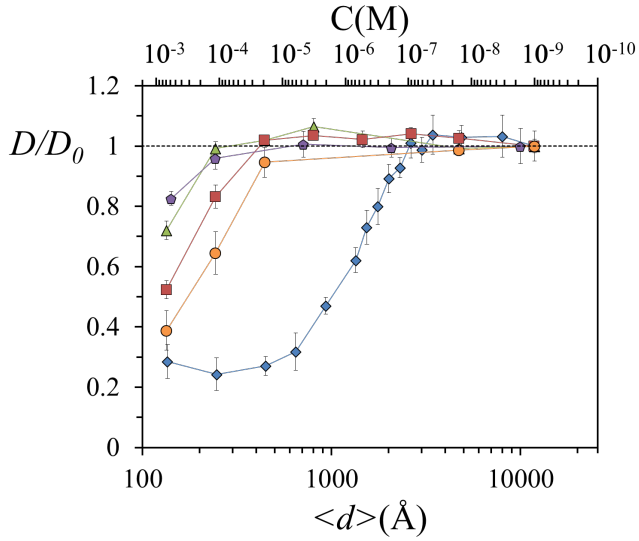

Figure 4.5: Semilog plot of the normalized diffusion coefficients D/D_0 at different concentrations of NaCl in solution: 0mM (blue diamonds), 20mM (orange circles), 50mM (red squares), 100mM (green triangles) and 150mM (purple rhombs).

and resorting to Eq.(4.8) relating R_H to the diffusion coefficient together with Eq. (4.9) for the water viscosity at our working temperature of 30°C, one finds $D_{Lys} = 138\mu\text{m}^2/\text{s}$ which is in fairly good agreement with our above reported value, considering that the calibration of our device is based on the outcomes of Ref. [134]. The temporary nature of these bound states is reasonably surmised because the random hits of water molecules, which drive molecular diffusion, are also continuously destroying the bound states. To support these qualitative arguments we can proceed by estimating and comparing some characteristic energy and time scales. A characteristic interaction length R_{el} is obtained by equating the electrostatic interaction energy with thermal energy giving

$$R_{el} = \frac{|Z_{Lys} Z_{dye}| e^2}{4\pi\varepsilon_r k_B T} \tag{4.10}$$

taking $Z_{Lys} = 10, Z_{dye} = -2$, e the electron charge, and the dielectric constant of water $\varepsilon_r \sim 76$ at $T = 303K$ $(30^\circ C)$, we have $R_{el} \sim 145\mathring{A}$ so that the mean time taken by a dye molecule to move on such a distance is

$$\tau_0 = \frac{R_{el}^2}{6D_0} \sim 66\ ns \tag{4.11}$$

having assumed $D_0 \simeq 532\mu\text{m}^2 s^{-1}$ (see below). The largest value of the electrostatic interaction energy between AF488 and Lysozyme is estimated as

$$E_{max} = \frac{Z_{Al} Z_{Lys} e^2}{4\pi\varepsilon_r R_{min}} \sim 150\ meV \tag{4.12}$$

where $R_{min} = R_{dye} + R_{Lys} = 25\mathring{A}$ is the minimum distance between AF488 and Lysozyme, and since at $30°C$ $k_BT \simeq 26$ meV, we compute the Kramers escape time from a bound state as the time for an AF488 molecule to reach a distance R_{el}, where the electrostatic interactions are equal to the thermal energy k_BT, that is

$$\tau_{Kr} = \tau_0 \exp\left[\frac{\Delta E}{k_BT}\right] \simeq 9\,\mu s \tag{4.13}$$

where $\Delta E = E_{max} - k_BT$; this gives an order of magnitude of the average trapping time of a molecule of AF488 by a Lysozyme molecule. For instance, at $\langle d \rangle = 1000\mathring{A}$ the free diffusion time of an AF488 molecule is

$$\tau_{free}(1000\mathring{A}) = \frac{(\langle d \rangle - 2R_{el})^2}{6D_0} \simeq 1.5\mu s \tag{4.14}$$

which is shorter than the average trapping time, as a consequence for this value of $\langle d \rangle$ the AF488 molecules are most of the time, but not permanently, trapped, and this is consistent with a small value of D/D_0. To the contrary, for $\langle d \rangle = 2500\mathring{A}$ the free diffusion time is approximately given by

$$\tau_{free}(2500\mathring{A}) \simeq 17\,\mu s \tag{4.15}$$

which is longer than the trapping time. Of course these are somewhat crude estimates but provide reasonable orders of magnitude and thus useful heuristic information. Finally, the existence also of temporary states of more than one dye molecule bounded to a single protein molecule is not excluded, but such a possibility is implicitly taken into account by the numerical simulations reported in Section 4.3. The above given natural explanation of the result displayed in Figure 4.3(a) can be further and nicely confirmed by acting on the effective range of the the intermolecular interaction potential according to Eq.(4.1). The range of the potential is controlled by the Debye screening length λ_D, which depends on the concentration of freely moving ions in the electrolytic solution. This is practically realized by adding to the watery solution of proteins and dyes different concentrations of sodium chloride. In order to change the action range of electrostatic interactions we chose five different NaCl concentrations: $0, 20, 50, 100, 150$ mM. The 0 mM concentration of NaCl implies that the molecules are solvated in pure water and submitted to a pure Coulombic potential (Eq.(4.3)), while the additions of salt in solution screens the electrostatic interaction between charged molecules (Eq.(4.1)). The Debye screening lengths for NaCl salt contents of $20, 50, 100$ and 150 mM, are equal to 21.4Å, 13.6Å, 9.6Å and 7.8Å (Eq.(5.1) for a temperature of 30°C), respectively. The effect of this action on λ_D is shown in Figure 4.5. The different patterns of $D(\langle d \rangle)$ are consistently showing that the higher the ionic strength (that is the shorter λ_D) the shorter the distance $\langle d \rangle$

at which D deviates from a Brownian value. In order to further cross check that

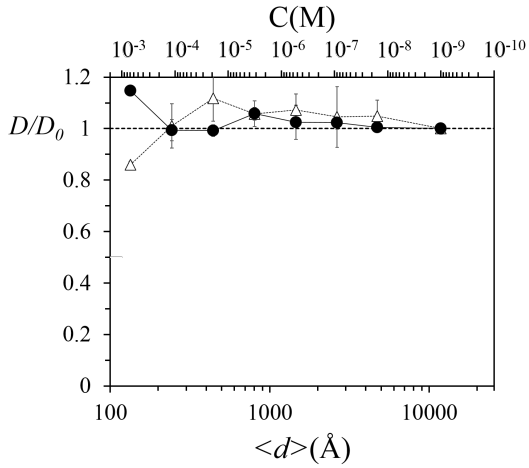

Figure 4.6: Normalised diffusion coefficients at isoelectric points of Myoglobin at pH=7 (full circles), and of Lysozyme at pH=11 (open triangles). Electrostatic interactions are switched off.

the observed lowering of the diffusion coefficient of the dye is due to its electrostatic interaction with the protein molecules, we have replaced Lysozyme (molecular weight = 14.3 kDa) with Myoglobin (molecular weight = 16.7 kDa). We chose Myoglobin because its isoelectric point happens to occur at pH=7, the pH value of our measurements, thus a mixture of AF488 and Myoglobin at pH=7 in pure water is expected to always give Brownian diffusion. And this is actually the case, as is shown by Figure 4.6. Then we also considered a solution of Lysozyme and AF488 at pH=11, the isoelectric point of Lysozyme. Also in this case no trace is left of the pattern of the diffusion coefficient reported when both the molecular species are charged (though in this case the buffer keeping at 11 the pH of the solution has a non-vanishing ionic strength). The fit of our ACFs using a $3D$ anomalous diffusion model has not highlight the existence of molecular crowding effects in our system. The last cross check has been the fit of our ACFs using a $3D$ anomalous diffusion model to study how molecular crowding effects were affecting our system. The results clearly show that crowding effects are negligible (see section 4.4.2).

4.3 Numerical simulations

We consider a system composed of two different molecular species A and B, modelled as spherical Brownian particles of radii R_A, R_B, and of net number of electric charges Z_A, Z_B, respectively. We refer to the number of each type of particle as N_A and N_B, respectively, and to $N = N_A + N_B$ as the total number of particles. Such molecules move in a fluid of viscosity η at a fixed temperature T. The friction exerted by the fluid environment on the particles is described by the Stokes' law $\gamma_i = 6\pi\eta R_i$. Particles interact through pairwise potentials $U(r)$ which depend on the distance r between their

centers. For the mutual distance between the i_k particle of type k and the j_l particle of type l we introduce the notation:

$$r_{i_k j_l} = |\mathbf{r}_{i_k} - \mathbf{r}_{j_l}| \ , \tag{4.16}$$

where $\boldsymbol{r}_i$ is the coordinate of the center of i-th particle so that $U_{kl}(r_{i_k j_l})$ represents the total interaction energy between these particles. We work under the assumption that the dynamics of the system is given by N coupled Langevin equations in the so called overdamped limit, where inertial effects are neglected [117, 60]:

$$\begin{aligned} \frac{d\boldsymbol{r}_{i_A}}{dt} = -\frac{1}{\gamma_A}\Bigg[\sum_{\substack{j_A=1 \\ j_A \neq i_A}}^{N_A} \boldsymbol{\nabla}_{\boldsymbol{r}_{i_A}} U_{AA}\left(r_{i_A j_A}\right) + \\ - \sum_{j_B=N_A+1}^{N_A+N_B} \boldsymbol{\nabla}_{\boldsymbol{r}_{i_A}} U_{AB}\left(r_{i_A j_B}\right)\Bigg] + \sqrt{\frac{2k_B T}{\gamma_A}}\boldsymbol{\xi}_{i_A}(t) \end{aligned} \tag{4.17}$$

$$\begin{aligned} \frac{d\boldsymbol{r}_{i_B}}{dt} = -\frac{1}{\gamma_B}\Bigg[\sum_{\substack{j_B=N_A+1 \\ j_B \neq i_B}}^{N_A+N_B} \boldsymbol{\nabla}_{\boldsymbol{r}_{i_B}} U_{BB}\left(r_{i_B j_B}\right) + \\ - \sum_{j_A=1}^{N_A} \boldsymbol{\nabla}_{\boldsymbol{r}_{i_B}} U_{AB}\left(r_{i_B j_A}\right)\Bigg] + \sqrt{\frac{2k_B T}{\gamma_B}}\boldsymbol{\xi}_{i_B}(t) \end{aligned} \tag{4.18}$$

$$i_A = 1, ..., N_A \qquad i_B = N_A + 1, ..., N_A + N_B$$

where k_B is the Boltzmann constant, and $\boldsymbol{\xi}(t) = (\boldsymbol{\xi}_1, ..., \boldsymbol{\xi}_N)$ stands for a $3N$-dimensional random process modelling the fluctuating force due to the collisions with water molecules, which is assumed to satisfy the following relations:

$$\begin{cases} \langle \xi^\alpha(t) \rangle_\xi = 0 \\ \\ \langle \xi_i^\alpha(t) \xi_k^\beta(t') \rangle_\xi = \delta^{\alpha\beta}\delta_{ik}\delta(t-t') \end{cases} \tag{4.19}$$

4.3.1 Model potential

The interactions among the molecules are linear combinations of pairwise potentials regularized as follows:

$$U_{kl}(r_{i_k j_l}) = \begin{cases} U_{SC}(r_{i_k j_l}) & r_{i_k j_l} \leq 1.01\, R_{kl} \\ U_{ElStat}(r_{i_k j_l}) & r_{i_k j_l} > 1.01\, R_{kl} \end{cases} \tag{4.20}$$

where $R_{kl} = R_k + R_l$ is the sum of the two molecular radii, $U_{SC}(r_{i_k j_l})$ is a soft-core potential and $U_{ElStat}(r_{i_k j_l})$ is the Coulomb electrostatic potential. The choice of a soft-core potential is related to the fact that a small ficticious compenetration among the interacting molecules is allowed in numerical simulations for computational reasons (that is, to avoid the need of very short integration time steps). The soft-core potential has the form:

$$U_{SC}(r_{i_k j_l}) = A_{SC_{kl}} \exp\left[-\frac{r_{i_k j_l}}{R_{kl}} + 1\right] . \tag{4.21}$$

The parameter related with the potential strength $A_{SC_{kl}}$ has been chosen such that:

$$\Delta r_{SCi_k}(0.95\, R_{kl}) + \Delta r_{SCj_l}(0.95\, R_{kl}) = 0.05\, R_{kl} \ , \tag{4.22}$$

where Δr_{SCi_k} is the drift of the particle i_k due to the soft-core potential in a discrete time interval Δt:

$$\Delta r_{SCi_k}(r_{i_k j_l}) = \frac{\Delta t}{\gamma_k} \left| \frac{\mathrm{d}U_{SC}(r_{i_k j_l})}{\mathrm{d}r} \right| . \tag{4.23}$$

This yields the following expression for $A_{SC_{kl}}$:

$$A_{SC_{kl}} = 0.05 \ \exp\left[-0.05\right] \frac{R_{kl}^2}{\Delta t} \left(\frac{1}{\gamma_k} + \frac{1}{\gamma_l}\right)^{-1} . \tag{4.24}$$

The electrostatic Coulomb potential $U_{ElStat}(r_{i_k j_l})$, describing the experimental condition where no salt is dissolved in solution, is:

$$U_{\mathrm{Coul}}(r_{i_k j_l}) = \frac{Z_k\, Z_l\, e^2}{\varepsilon\, r_{i_k j_l}} \ , \tag{4.25}$$

where e is the elementary charge and ε is the electric permittivity of the medium, for which the static value at room temperature is $\varepsilon = \varepsilon_{water} \simeq 80$.

4.3.2 Numerical algorithm

We have numerically studied systems of two populations of molecules confined in a cubic volume of size L. The number of particles for each type is fixed: N_A is the number of A-type particles (Lysozyme molecules), and N_B is the number of B-type particles (AF488 molecules). To avoid spurious boundary effects, periodic boundary conditions (PBC) have been assumed, which is equivalent to the existence of an infinite number of images/replicas throughout the space. In order to study diffusion at different concentrations, the numbers of molecules N_A and N_B are kept fixed, and the average intermolecular distance $\langle d \rangle$ among the molecules of type A and B is then controlled according to the relation

$$L = \sqrt[3]{N_A + N_B}\, \langle d \rangle \ . \tag{4.26}$$

We remark that such a choice is not entirely equivalent to the experimental situation described in the previous paragraphs where the dye (AF488) concentration was fixed; in fact, in molecular dynamics simulations (MDS) both the concentration of Lysozyme and dye change with $\langle d \rangle$, the ratio of concentrations being constant. This choice is justified by the fact that in real experiments N_A/N_B varies in a range $[1-5\times10^5]$; fixing $N_B = 50$, the experimental situation would correspond to taking N_A in a range $[1-2.5\times 10^6]$, which is very highly demanding for computation. In MDS the ratio N_A/N_B has been chosen as large as possible ($N_A/N_B = 10$ in our case) to avoid that dye molecules (AF488) dynamics could significantly affect the biomolecules (Lysozyme) dynamics. In the presence of long-range interactions and PBC, each molecule contained in the previously mentioned box interacts with all the molecules contained in the above mentioned images/replicas, that is, the pairwise potential

$$U_{kl}(r_{i_k j_l}) = U(|\boldsymbol{r}_{i_k} - \boldsymbol{r}_{j_l}|) \tag{4.27}$$

in Eq. (4.19) has to be replaced by an effective potential $U_{kl}^{\text{eff}}(r_{i_k j_l})$ of the form:

$$U_{kl}^{\text{eff}}(r_{i_k j_l}) = \sum_{\boldsymbol{n}\in\mathbb{Z}^3} U(|\boldsymbol{r}_{i_k} - \boldsymbol{r}_{j_l} + \boldsymbol{n}L|) \ , \tag{4.28}$$

where $\mathbb{Z}^3$ is the space of 3-dimensional integer vectors. It is clear that short and long-range interactions (in the sense specified in the Introduction) have to be managed in two different ways. For short range interactions it is always possible to define a cutoff length scale λ_{cut} such that the effects of the interactions beyond this distance are negligible. In the systems we have studied by means of numerical simulations, the Debye electrostatic potential is a short range potential with a cutoff scale of the order of some units of the Debye length λ_D. For long-range interactions as the Coulomb potential Eq.(4.25), it is not possible to define a cutoff length scale λ_{cut} so that, in principle, an infinite sum should be considered. A classical way to account for long-range interactions resorts to the so called Ewald summation [5]. In the following section we describe a more recent and practical method - replacing Ewald's one - known as Isotropic Periodic Sum (IPS). The equations of motion (4.19) were numerically solved using a second order Euler-Heun algorithm [22], that is, a predictor-corrector scheme. The initial position of each particle is randomly assigned at t_0 using a uniform probability distribution in a cubic box of edge L.

IPS correction to long-range potentials

Because of the long-range nature of the Coulomb potential described by Eq.(4.25), the force acting on each particle is given by the sum of the forces exerted by all the particles in the box and by the particles belonging to the images. For the computation of these forces, we used the IPS method [178, 179], a cutoff algorithm based on a statistical description of

the images isotropically and periodically distributed in space. Let us consider an infinite system obtained when assuming PBC for an elementary cubic cell with edges of length L. Under the hypothesis that the system is homogeneous on a length scale R_{cut}, an effective interaction potential for the molecules contained in the elementary cell is given by

$$U_{\mathrm{IPS}}(r) = \begin{cases} U(r) + \phi_{\mathrm{IPS}}(r) \ , & r \leq R_{cut} \\ 0 \ , & r > R_{cut} \end{cases} \tag{4.29}$$

where $\phi_{\mathrm{IPS}}(r)$ is a correction to the potential energy which takes in account the interactions of a single particle with the isotropically distributed images of the system. Such a potential can be written as the sum of two contributions. The first one takes into account the interaction of a test particle with the infinite number of images of the source particle along the axes joining the two particles of the pairwise potential

$$\phi_{\mathrm{IPS}axial}(r) = \xi \sum_{m=1}^{\infty} [U(2mR_{cut} - r) + U(2mR_{cut} + r)] \ . \tag{4.30}$$

The other contribution is given by the average of the potential over all the images isotropically distributed around the region delimited by the cutoff radius

$$\phi_{\mathrm{IPS}random}(r) = \sum_{m=1}^{\infty} [n(m) - 2\xi] \, \phi_{shell}(r, m) \ . \tag{4.31}$$

where $n(m) = 24m^2 + 2$ is the number of images in a shell around the source particle with radii $[(2m-1)R_{cut}; (2m+1)R_{cut}]$ in 3D-space, and

$$\begin{aligned} \phi_{\mathrm{IPS}shell}(r, m) =& \frac{1}{2} \int_0^{\pi} \big[U\big(r^2 + (2mR_{cut})^2 + \\ & - 4mR_{cut}\big) \cos\theta \big]^{1/2} \sin\theta \mathrm{d}\theta \end{aligned} \tag{4.32}$$

is an average of the contribution to the potential of the images which are not along the axes joining the test and source particles. It has to be noticed that for some potentials the series appearing in the equations above do not converge: for this reason a different reference level is chosen for the potential energy, i.e.

$$\begin{aligned} \phi_{\mathrm{IPS}}(r) =& [\phi_{\mathrm{IPS}axial}(r) - \phi_{\mathrm{IPS}axial}(0)] + \\ & + [\phi_{\mathrm{IPS}random}(r) - \phi_{\mathrm{IPS}random}(0)] \ . \end{aligned} \tag{4.33}$$

Finally, the parameter ξ is set to a value such that the force due to the effective potential vanishes on the cut off radius:

$$\frac{\partial}{\partial r}\left[U(r)+\phi_{\mathrm{IPS}}(r)\right]\Big|_{r=R_{cut}} = 0 \ . \tag{4.34}$$

The IPS potential allows to control the introduction of spurious effects due to the presence of infinite replicas of the system in a way that generalises Ewald's sums also to potentials other than the electrostatic one. Assuming that the system is homogeneous on a length scale R_c, we can define an effective pairwise IPS potential $U^{IPS} = U^{IPS}(|\boldsymbol{r}_{i,j}|, R_c)$ which takes into account the sum of pair interactions within the local region around a particle

$$U^{IPS}(|\boldsymbol{r}_{i,j}|, R_c) = \begin{cases} U(|\boldsymbol{r}_{i,j}|) + \phi(|\boldsymbol{r}_{i,j}|, R_c) \ , & |\boldsymbol{r}_{i,j}| \leq R_c \\ \\ 0 \ , & |\boldsymbol{r}_{i,j}| > R_c \end{cases} \tag{4.35}$$

where $\phi(|\boldsymbol{r}_{i,j}|, R_c)$ is a correction to the potential obtained by computing the total contribution of the interactions with the particle images beyond the cutoff radius R_c [178, 179]. For the Coulomb potential of Eq.(4.25), we obtained an analytical expression for the IPS correction $\phi_{\mathrm{Coul}}(\boldsymbol{r}_{i,j}, R_c)$. For computational reasons this has been approximated by a polynomial of degree seven in $x = |\boldsymbol{r}_{i,j}|/R_c$ with x in the interval $(0; 1]$:

$$\begin{aligned} \phi_{\mathrm{Coul}}(x) = &- 9.13636 \times 10^{-7} + 0.000100298x + \\ &+ 0.298588x^2 + 0.0151595x^3 + \\ &+ 0.00881283x^4 + 0.10849x^5 + \\ &- 0.0930264x^6 + 0.0482434x^7 \end{aligned} \tag{4.36}$$

We have chosen $R_c = L/2$ under the hypothesis that on this scale the system is homogeneous.

4.3.3 Long-time diffusion coefficient

We aim at assessing the experimental detectability of long-range interactions between biomolecules using quantities accessible by means of standard experimental techniques. A meaningful approach to this issue is the study of transport properties. For this reason, in our simulations we chose the long-time diffusion coefficient D as the main observable of the system described by Eqs.(4.19). This coefficient is defined, consistently with Einstein's relation [5], as:

$$D = \lim_{t\to+\infty} \frac{\langle|\Delta\boldsymbol{r}_i(t)|^2\rangle}{6t} \ , \tag{4.37}$$

$\Delta \mathbf{r}_i(t) = \boldsymbol{r}_i(t) - \boldsymbol{r}_i(0)$ being the total displacement of a particle in space and $\langle a_i \rangle = 1/N \sum_{i=1}^{N} a_i$ the average over the particle set. We remark that in our system the displacements $\Delta \boldsymbol{r}_i(t)$ are not mutually independent due to the interaction potential $U(|\boldsymbol{r}_i - \boldsymbol{r}_j|)$ in Eqs.(4.19), which establishes a coupling between different particles; in that case, the average over particles index concerns correlated stochastic variables. Nevertheless, as our system is non-linear with more than three degrees of freedom, it is expected to be chaotic [74] so that, in this case, the statistical independence of particle motions is recovered. Moreover, when a chaotic diffusion gives $\langle |\Delta \boldsymbol{r}_i(t)|^2 \rangle \propto t$ (which is the case of the models considered in the present work), the diffusion coefficient D is readily computed through a linear regression of $\langle |\Delta \boldsymbol{r}_i(t)|^2 \rangle$ expressed as a function of time. In what follows we refer to $\langle |\Delta \boldsymbol{r}_i(t)|^2 \rangle$ as Mean Square Displacement (MSD).

4.3.4 Simulation Parameters

Molecular Dynamics simulations were performed considering a solution with $N_A = 500$ and $N_B = 50$ representing respectively Lysozyme molecules and AF488 molecules. This choice seemed to be a good compromise between the need of a large N_B for a good statistics, a sufficiently large ratio N_A/N_B and the request of a not too high computation time. The A-type particles, which represent Lysozyme molecules, have a

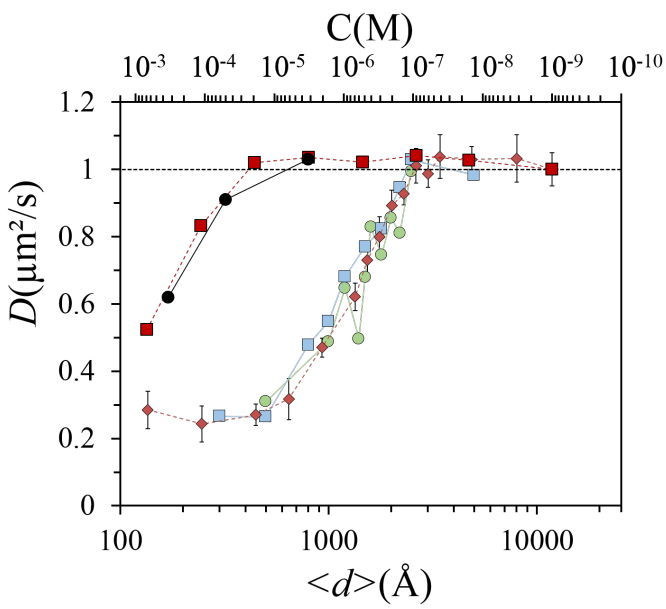

Figure 4.7: Comparison among experimental results and numerical simulations for non-screened Coulomb potential.. Semilog plot of the normalized diffusion coefficients D/D_0: experimental values (red diamonds), $N_A = 200$ and $N_B = 20$ (light green circles), $N_A = 500$ and $N_B = 50$ (light blue squares). Red squares and full black circles correspond to experimental and numerical results, respectively, in the case of a Debye-Hückel potential with a Debye length $\lambda_D = 27\mathring{A}$.

radius $R_A = 2 \times 10^{-3}\,\mu$m and a net electric charge expressed in elementary charge

units $Z_A = +10$. The B-type particles, which represent AF488 molecules, have a radius $R_B = 0.5 \times 10^{-3}\,\mu$m and a net electric charge expressed in elementary charge units $Z_B = -2$. The medium where diffusion takes place represents an aqueous solution, so that the viscosity $\eta = 8.90 \times 10^{-4}\mathrm{Pa}\cdot\mathrm{s}^{-1}$ is the water viscosity at $T \simeq 300K$. The relative dielectric permittivity has been taken to be $\varepsilon = 80$ as for pure water. The time step has been chosen to $\Delta t = 5 \times 10^{-4}\,\mu$s: this choice can allow important compenetration among particles in MDS and does not permit a correct description of excluded volume effects, i.e. the drift due to stochastic forces on dye molecules in a single time steps is comparable with R_B. Nevertheless the effects we are interested in concern the diffusive behaviour of dyes on larger length and time scales and we considered acceptable such compenetrations. The number of time steps was fixed such that the dynamics was simulated for $t_{max} = 5000\mu$s so that for the dye particles $\sqrt{6\,D_0 t_{max}} \simeq 4\,\mu\mathrm{m} \gg \langle d \rangle$, where D_0 is the brownian self-diffusion coefficient of the dye molecules, for any considered case. These 5 ms-long simulations are considered adequate because this time interval is much longer than the relevant dynamical processes (like trapping and free diffusion) which occur in the real system on much shorter time scales, as estimated in Section 4.2.1. In Figure 4.7 the outcomes of the above described numerical simulations are compared to the experimental results obtained for the same quantity: the diffusion coefficient D, normalized with respect to its Brownian value D_0, as a function of the average interparticle distance $\langle d \rangle$. The numerical outcomes for D quantify the diffusion of the small particles that model the dye molecules. We observe that the choice $N_A = 500$ and $N_B = 50$ yields a less noisy pattern with respect to the choice $N_A = 200$ and $N_B = 20$, what is of course sound. In Figure 4.7 we have also reported the outcomes of numerical simulations performed with $N_A = 500$ and $N_B = 50$ and replacing the Coulombic potential with a screened one, that is, the Debye-Hückel potential. We used a Debye length $\lambda_D = 27\mathring{A}$. In so doing a direct comparison can be made with the experimental outcomes obtained with 50 mM of NaCl in solution. Also in this case the agreement is very good. Even though the number of particles considered in our numerical simulations is very small with respect to the actual number of molecules in laboratory experiments the agreement among numerical and experimental results is excellent. This is not surprising because it is a common situation in standard Molecular Dynamics simulations. The birth and success of Molecular Dynamics was just due to the possibility of obtaining good values of macroscopic observables out of numerical simulations performed with a few hundreds of particles [2].

[2] In his seminal paper, A. Rahman, studied a system of 864 argon atoms, in liquid state, on a CDC 3600 computer, using a Lennard-Jones potential and finding a surprisingly good agreement of the pair-correlation function and of the constant of self-diffusion with experiment: A. Rahman, Correlations in the Motion of Atoms in Liquid Argon, Phys. Rev. **136**, A405 - A411 (1964). This was the dawning of Molecular Dynamics, and A. Rahman is considered its father.

4.4 Additional information

4.4.1 Quenching of the dye

The fluorescence intensity of AF488 is known to be influenced by a quenching effect that the protein exerts on the fluorophore via four aminoacids: Trytophan and Tyrosine (strong quenchers) and Histidine and Methionine (weaker quenchers) [29, 30]. These effects are attributed to photoinduced electron transfer (PET) occurring when the two molecules are in close contact, thus due to short-range interactions ($< 2\mathring{A}$) [93].This van der Waals contact takes place on time scales which are not resolved by our FCS apparatus. When AF488 binds to the Lysozyme the consequent conformational rearrangement influences the dye diffusion time and it also changes the dye fluorescence quantum yield [110]. The non specific binding of AF488 on the protein surface is supported by the observed fluorescence quenching factor of about 1.6 between free AF488 and AF488 bound to Lysozyme, as shown in the table reported in Figure 4.11. This value is compatible with steady state fluorescence measures reported in the literature [110] where the same quenching factor has been found equal to 1.9.

4.4.2 Checking possible crowding effects

Even though a-priori we do not expect any relevant role played by molecular crowding at our low working concentrations, we have also fitted our ACFs by means of the following analytic expression

$$G(\tau) = 1 + \frac{1}{N} \frac{1 + n_T \exp\left(-\frac{\tau}{\tau_T}\right)}{\left[1 + \left(\frac{\tau}{\tau_D}\right)^{\alpha}\right] \sqrt{1 + s^2 \left(\frac{\tau}{\tau_D}\right)^{\alpha}}} \,. \tag{4.38}$$

where the anomalous exponent α becomes a free parameter in the fitting. Using FCS, it has been shown that anomalous diffusion, which corresponds to a mean square displacement of the molecules proportional to t^{α} with α smaller than 1, is an indication of the degree of molecular crowding. Figure 4.8 clearly indicates that crowding effects are negligible because there is no evidence of anomalous diffusion which is commonly assumed when $\alpha < 0.6 - 0.7$ [45].

4.4.3 Comparison between FCS and FCCS outcomes

In Figure 4.9 some typical outcomes of the FCCS measurements are displayed. These are cross-correlation functions of the fluorescence intensity fluctuations $\delta F_1(t)$ and $\delta F_2(t)$ measured by two independent photo-detectors to eliminate afterpulsing artefacts. The

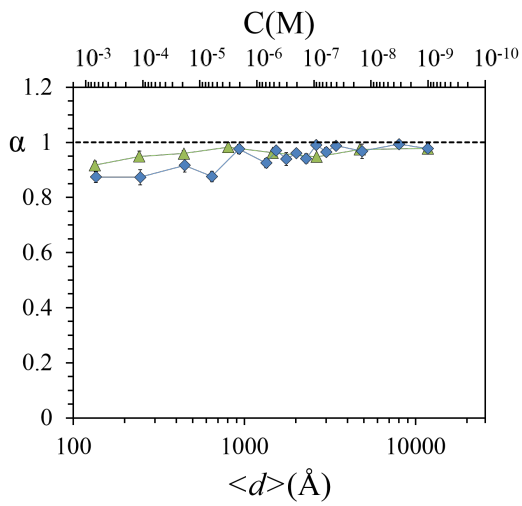

Figure 4.8: Check of Brownian versus anomalous diffusion. The α values reported here refer to 0 mM of NaCl in solution (blue diamonds), and 100mM (green triangles). $\alpha = 1$ corresponds to Brownian diffusion, $\alpha < 0.6 - 0.7$ can be attributed to anomalous diffusion.

cross-correlation functions are defined by

$$G(\tau) = \frac{\langle \delta F_1(t) \delta F_2(t+\tau) \rangle}{\langle F_1(t) \rangle \langle F_2(t) \rangle} \tag{4.39}$$

(for graphical reasons the normalized versions are displayed). The reported cross-correlation functions correspond to the same concentrations (average intermolecular distance) of the autocorrelation functions reported in Figure 4.2. Some difference in their shape is observed at very short times (where afterpulsing artefacts are expected), but this does not significantly affect the diffusion time, apart from the fact that the FCS measurements were performed at 30°C, whereas the FCCS measurements were performed at 20°C (because of a technical constraint of our FCCS equipment). A comparison between the non normalised values of the diffusion coefficient obtained with FCS and FCCS is provided in Figure 4.10. The experimental points lying on the horizontal lines correspond to Brownian diffusion of AF488 molecules; the discrepancy between these values is explained by the temperature difference, in fact, by inverting Equation (4.8) to get $D = k_B T/(6\pi R_H \eta)$, with $R_H(AF488) \simeq 5.2\AA$, $\eta(20^oC) = 10^{-3}$ Pa s, and $\eta(30^oC) = 0.797 \times 10^{-3}$ Pa s, we obtain $D_{20^o} = 410\mu\text{m}^2$ s^{-1} and $D_{30^o} = 532\mu\text{m}^2$ s^{-1}, respectively. Whence the ratio $D_{30^o}/D_{20^o} = 1.3$ to be compared with the value 1.31 of the fraction of the Brownian diffusion coefficients reported in Figure 4.10. In Figure 4.10 we also observe a discrepancy in the transition value of $\langle d \rangle$, which appears smaller in the FCCS case. Again, this is a temperature dependent effect the physics of which is qualitatively understood by inspecting Eqs. (4.19). In fact, by lowering the temperature of the solution the viscosity of water η increases, and the coefficient $1/\gamma = 1/(6\pi R_H \eta)$ results in a weakening of the Coulombic interactions; then also the strength of thermal noise is weakened but

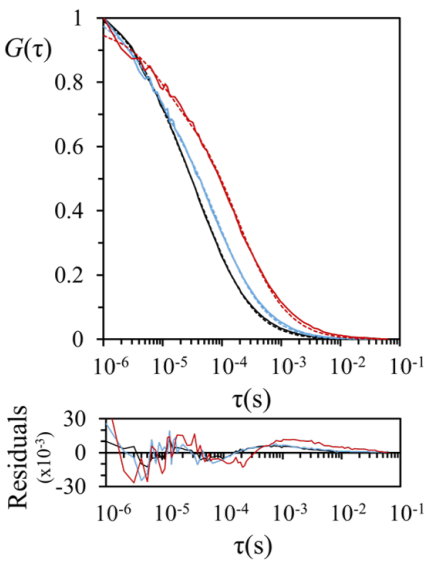

Figure 4.9: FCCS measurements. Semilog plot of the normalized autocorrelation function of fluorescence fluctuations, defined in Eq.(4.6), obtained at $\langle d \rangle = 240$Å (red line), at $\langle d \rangle = 920$Å (blue line), and at $\langle d \rangle = 4200$Å (black line). Working temperature 20^oC.

only through a $\sqrt{1/\gamma}$ factor so that the net effect is a reduction of the strength of the Coulombic interactions.

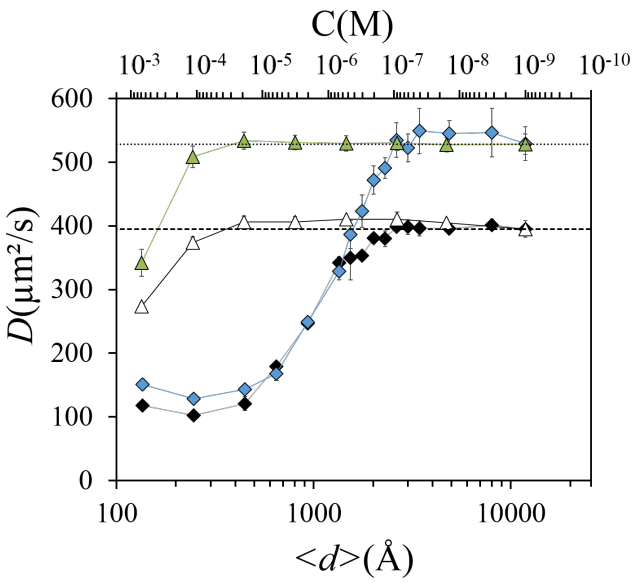

Figure 4.10: Comparison between the FCS and the FCCS measurements. Semilog plot of the diffusion coefficients D of AF488 as a function of the distance in Å - and of the concentration of the solution in Moles - between proteins and dyes.The FCS results have been obtained at 30°C, 0 mM (blue diamonds), and 100mM (green triangles), of NaCl in solution. The FCCS results have been obtained at 20°C, 0 mM (black diamonds), and 100mM (white triangles), of NaCl in solution.

d (Å)	136	246	448	646	931	1343	1537	1758	2012	2301	2631	3006	3432	4872	8014	11842
N	2.0	1.9	1.6	2.2	1.9	2.5	1.7	2.4	1.8	2.5	2.0	2.6	2.8	3.9	3.7	4.3
±	0.2	0.3	0.1	0.4	0.1	0.3	0.2	0.4	0.1	0.2	0.1	0.1	0.3	0.6	0.1	0.6
τ (μs)	273.3	319.9	287.3	245.4	165.1	125.1	106.5	97.4	87.2	83.7	77.0	78.7	75.1	75.5	75.5	77.8
±	16.0	17.4	9.1	15.2	4.7	5.1	6.4	6.0	4.4	2.8	4.2	3.3	5.3	3.0	5.7	4.1
N_t	0.36	0.28	0.21	0.22	0.24	0.28	0.27	0.28	0.27	0.27	0.26	0.27	0.26	0.27	0.26	0.27
±	0.04	0.02	0.01	0.01	0.00	0.01	0.00	0.00	0.00	0.00	0.00	0.00	0.01	0.01	0.00	0.00
T_t (μs)	3.4	4.4	4.6	4.3	3.3	4.2	3.7	3.9	3.6	3.8	3.3	3.4	3.3	3.4	3.1	3.3
±	0.1	0.5	0.3	0.7	0.2	0.2	0.2	0.1	0.2	0.2	0.1	0.1	0.2	0.1	0.1	0.2
R/M ($x10^3$)	77.8	77.5	103.5	78.9	111.7	81.3	123.1	106.2	130.9	104.9	143.7	117.0	135.1	119.6	142.0	126.1
±	5.5	9.4	4.5	18.4	7.7	11.7	8.4	18.0	7.8	10.1	8.1	6.3	12.9	25.5	7.1	21.5

Figure 4.11: Table reporting the fitted values of the parameters for solutions of variable concentrations of Lysozyme and 1nM of AF488. Solutions containing 0mM of NaCl (blue diamonds visible in Figure 4.3, Figure 4.4, Figure 4.5 and Figure 4.10). Each value is the result of the averaging of the data recorded during 20 measurements on four different samples and for three independent experiments. The fitted parameters are: the number of molecules (N), the diffusion time in microseconds (τ), the number of molecules in the triplet state (N_t), the time spent in the triplet state in microseconds (T_t) and the emission rate (number of photons emitted per second) per molecule (R/M). All these data are displayed according to the average intermolecular distance between the molecules given in Angstroms ($\langle d \rangle$).

4.5 Concluding remarks

The work reported in the present chapter concludes a feasibility survey aimed at assessing the adequacy of diffusion studies to detect long-range intermolecular forces, hence - among them - electrodynamic intermolecular interactions in a future adequate experimental setup. The two preceding works of Refs. [140, 117] dealt with this problem from the theoretical and numerical sides, respectively. The present work contains a leap forward in what it provides an experimental assessment of the adequacy of Fluorescence Correlation Spectroscopy to detect intermolecular long range interactions. Even though our ultimate goal is to detect long range *electrodynamic* intermolecular interactions, for the time being we have tested this technique against a system where long range interactions are built-in, that is, a solution of oppositely charged molecules interacting through non-screened electrostatic interactions. As a matter of fact, we have found that FCS is certainly appropriate to detect intermolecular interactions in dilute systems, that is, when the solvated molecules interact at large distances, in the present study up to 2500Å approximately. Furthermore, the excellent quantitative agreement between the experimental outcomes and the corresponding numerical simulations has a twofold relevance. From the one side it confirms that the observed phenomenology, namely, the sudden bending of the diffusion coefficient when the average intermolecular distance is lowered

below a critical value, as well as its pattern as a function of the intermolecular distance, are actually due to the electrostatic interaction among the solvated molecules. From the other side this validates the numerical algorithm and approximations adopted, suggesting that this numerical scheme can be safely applied to interpret the readouts of experiments where electrodynamic interactions will be possibly excited.

CHAPTER 5 FCS at high concentrations

The following chapter deals with the first experiments performed with out-of-equilibrium proteins in the the FCS setup. As seen in the first part, the use of a sub-population of labeled BSA did not give the expected results, thus solutions with all labeled proteins had to be used. This also significantly increases the fluorescence and blinds the detector. To overcome this issue we have studied the use of optic density filters, and concluded about their use, in the second part of this chapter.

5.1 BSA with subpopulation labeled

5.1.1 Pilot experiments previously performed

The first campaign of experiment has been performed some years ago by Ilaria Nardecchia during her PhD studies [115]. The reaction mixture used is visible on figure 5.1, and it contains:

- A fixed volume of labelled BSA with AF488, to obtain a final concentration of 1nM
- A fixed volume of NaCl, in order to have 150mM of NaCl is the final solution
- A fixed volume of water and not labeled BSA, but with different ratio according to the wanted BSA concentration

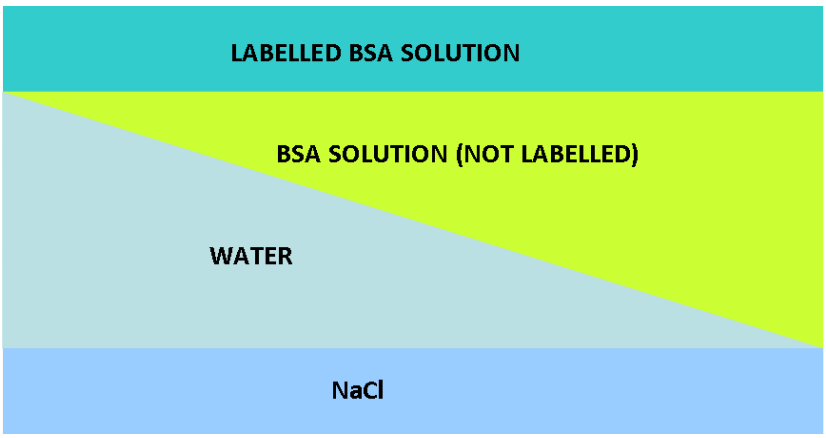

Figure 5.1: Reaction mixture, from [115]

The working hypothesis was that the labelled BSA molecules, when excited through the attached fluorochromes, would have induced by resonance the same oscillation in the

non-labelled proteins. Unfortunately the existence of an excitation threshold (as seen in chapter 3) rather high made the resonance excitation non effective.

5.1.2 Experiments involving wells coating

An experimental artifact to carefully avoid is the adsorption of the BSA molecules by the labtek walls. To prevent BSA adsorption, we have made anew the past experiments by treating the walls before their use. They have been coated with BSA solution of 10mg/mL diluted in PBS, letting the BSA molecules be adsorbed overnight. Then the wells were rinsed gently twice with PBS and dried before use.

An overview of the results is shown on figure 5.2. The normalized diffusion coefficients measured for the labeled BSA stay close to 1, indicating no changes in the protein behavior. One can notice higher values, reaching 1.2, which are probably explained by a release of the fluorescent dyes in solution, leading to shorter diffusion time measured and longer diffusion coefficients.

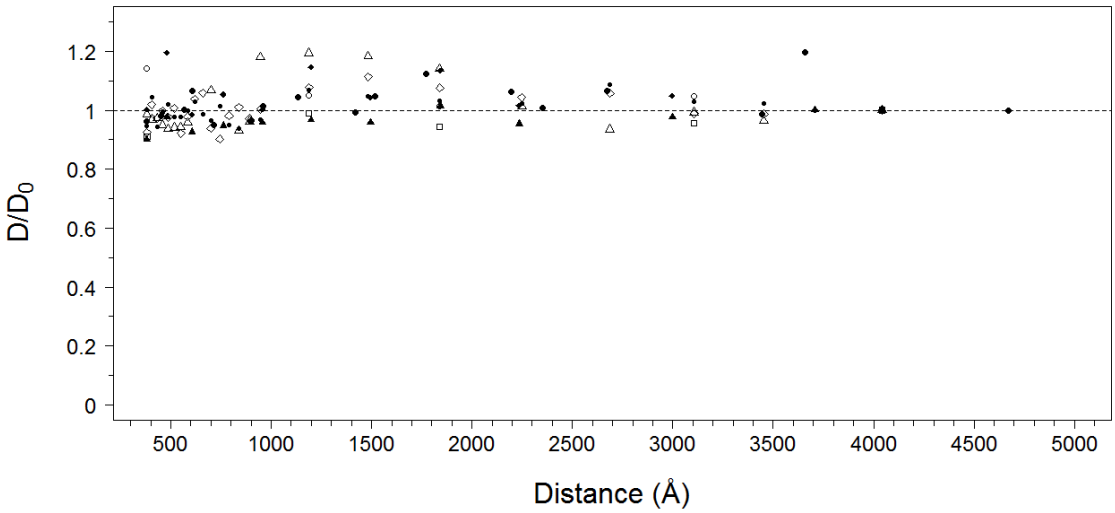

Figure 5.2: Diffusion coefficient of BSA tracer (5nM) versus the average distance between BSA molecules for several experiments. Each type of symbol represent an experiment.

5.2 Preliminary results with Optic Density filters

Fluorescence Correlation Spectroscopy (FCS) has been developed in the '70s [102] and rapidly became a useful technique in various fields from biology to chemistry. But FCS users get in troubles when dealing with highly concentrated solutions. First of all, the autocorrelation functions (ACFs) tend to be squeezed as the number of fluorescent molecules in solution is increased, this fact leads to the common belief that these curves

cannot be fitted any longer. Then, a second problem is introduced by the detector, because at increasing dye-concentration it can quickly attain saturation. Moreover, some authors have drawn attention to another problem: fluorescence fluctuations stemming from laser emission variations, become comparable to the fluorescence fluctuation level coming from the dyes. To fix these problems, some authors resorted to techniques conceived to reduce the observable volume with plasmonic nanoantennas [86] or plasmonic gold bowtie nanoantennas [87]. Laurence et al. [95] also show that the mentioned difficulties can be overcome by using several connected detectors, each one receiving part of the fluorescent beam - coming from the sample - after having separated it through beam-splitters. Thus, this setup needs many detectors and sometimes cannot be the optimal choice. An alternative, that we are putting forward here, is based on the use of absorptive filters to attenuate fluorescent light, and long time averaging in order to overcome the bad Signal to Noise Ratio (SNR).

5.2.1 FCS with density filters

Experiments have been performed using watery solutions of the Alexa Fluor 488 dye (AF488), at different concentrations of the dye, that is 1 nM, 10 nM and 500 nM respectively, and with different optical density filters of density 2.0 (OD2, 1% transmission), 1.3 (OD1.3, 5% transmission) and 1.0 (OD1, 10% transmission) on a spot-variation FCS setup (svFCS), built on a confocal microscope. The watery solutions of the AF488-dye were put in 8 wells Labtek supports. Our results, reported in Figure 5.3, show that for short lag times the combined effect of a bad SNR and of the afterpulsing [182] tend to deform the ACFs. On the other hand, the ACFs recorded with different filters are found to be overlapping for a lag time interval ranging from several microseconds to several seconds, as shown in Figure 5.3. These results were found to agree independently of the density of the filter used, whereas, for the same acquisition duration, the higher the OD value the noisier the ACF, as shown by Figure 5.3. We report just the most unfavorable SNR condition obtained with the OD2 filter.

5.2.2 Improvement of SNR through statistics

Following a standard practice, in order to improve the SNR for data records obtained with OD filters, we resort to an increase of statistics by performing longer data recording. Figure 5.4 shows two ACFs obtained with the OD2 filter but with different acquisition durations: the green curve being recorded for a time interval 80 times longer than that corresponding to the black curve (4000 seconds and 50 seconds, respectively). More precisely, the green curve corresponds to the average of 80 different ACFs, each one worked out for a 50 seconds of acquisition. As expected, the SNR has been increased, obtaining less noisy average ACFs, and better global fitting results for the multiple runs.

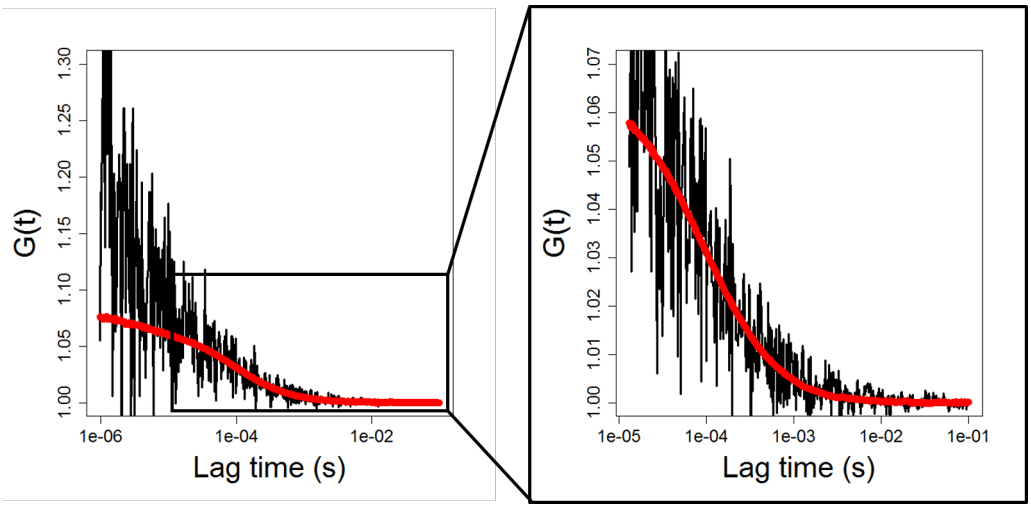

Figure 5.3: Comparison of ACFs recorded without filter in red, and with a OD2 in black. On the left panel, there are the ACFs from a 10nM AF488 solution. On the right panel, the x-axis has been truncated, starting from 10μs, to highlight the overlapping parts of the ACFs.

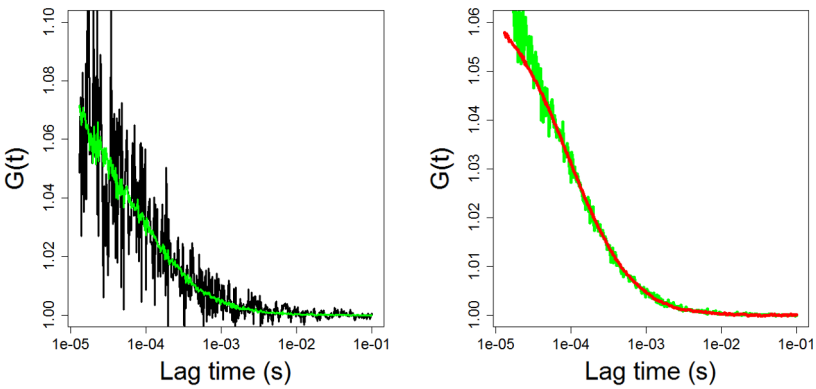

Figure 5.4: Comparison of ACFs recorded with OD2 and for different durations. In black, it is shown the ACF recorded for 50 seconds (1 acquisition of 50 seconds) for a 10nM AF488 solution. In green, the ACF has been recorded from the same solution but for 4000 seconds (80 acquisitions of 50 seconds).

5.2.3 FCS measurements at high concentration

What we learn from the results reported in Figure 5.4 is that the standard smooth pattern of the ACF, which is obtained without filter and displayed in Figure 5.3 (red line), is recovered also in presence of an OD2 filter provided that the acquisition duration is sufficiently long: the ACF reported in the right panel of Figure 5.4 has been worked out with an overall acquisition time of 4000 seconds. Thus we observe that a good statistics can convert a very noisy pattern into a definitely smoother one, not surprisingly indeed. The further and main step now consists in comparing the ACFs obtained with two samples at different concentrations of 1nM and 500nM without filter and with OD2 filter respectively. Both ACFs refer to 20 acquisitions of a duration of 50 seconds each. By fitting the ACFs on a time interval ranging from 20μs to 4 seconds, their characteristic

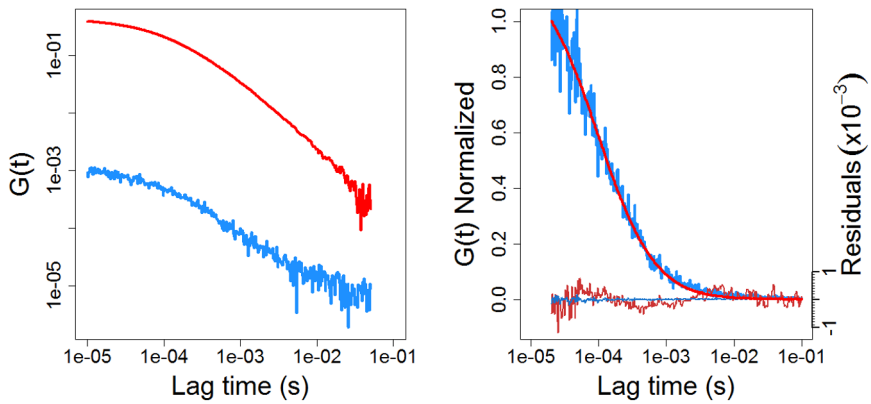

Figure 5.5: Comparison of the ACFs recorded without filter for 1 nM AF488 solution (in red), and for 500 nM AF488 solution with OD2 filter for an overall acquisition time of 1000 seconds (in blue).

parameters have been estimated by skipping the triplet state and the afterpulsing peak; this led to a diffusion time of 96.2±1.3μs and 2.0 molecules in the confocal volume for the 1nM solution, and a diffusion time of 94.4±1.3μs and 963.0 molecules in the confocal volume for the 500nM solution. And, in fact, after a suitable normalisation of the two ACFs, the right panel of Figure 5.5 clearly shows a very good superposition of the two curves.

5.3 Understanding the phenomenon at short lag times

As seen previously, working on a single solution of dye with different OD filters gives different patterns of the ACFs at short and long lag times. For longer lag times, the ACFs overlap leading to appropriate results considering a sufficiently high lag time threshold. But on the other hand, the ACFs are different for shorter lag times, and results obtained with OD filters seem to show a divergence of the ACF at short lag times. The following section focuses on this phenomenon, trying to understand and fix the issue.

5.3.1 Methods

5.3.1.1 Experimental setup

Experiments have been performed using watery solutions of the Alexa Fluor 488 (AF488) for the waist size calibration and Atto 488 dye (AT488), at different concentrations of the dye, that is 1 nM and 1μM respectively, and with different optical density filters of density 2.0 (OD2, 1% transmission), 1.3 (OD1.3, 5% transmission) and 1.0 (OD1, 10% transmission). The watery solutions of the AF488-dye were put in 8 wells Labtek supports to prevent evaporation with 400μL volume.

We have performed the experiment on the same equipment operating as FCS or FCCS devices respectively, than the ones described in section (4.1.1).

5.3.1.2 Simulation of diffusion and its detection

Simulations have been adapted from Wawrezinieck et al. [171] to work in 3 dimensions. A virtual cube is created with an edge size of d=10μm^2 and periodic boundary conditions. The box contains n independant objects moving randomly in order to mimic Brownian motion, with a temporal resolution of $\Delta t = 10^{-6}s$. Each jump ΔR with ΔX, ΔY, ΔZ performed by the moving objects is dependent of the diffusion coefficient, here $D = 408\mu m^2 s^{-1}$, and is determined by three independent random variables with a Gaussian distribution centered on 0 and a standard deviation $\sigma_x = \sigma_y = \sigma_z$. As $D = \sigma^2/(6\Delta t)$ and $\Delta R = \sqrt{\Delta X^2 + \Delta Y^2 + \Delta Z^2}$, $\sigma_x = \sigma/\sqrt{3}$. The objects are defined to move for a duration t, and three vectors of length $l = t/\Delta t$ are created with each value corresponding to a Gaussian random variable centered at 0 and with σ_x. The cumulative sum of each vector thus creates a Brownian path for the objects.

To mimic FCS experiments we have considered the detection volume as a 3D Gaussian ellipsoid such as:

$$W(x, y, z) = exp\left(\frac{2(x^2 + y^2)}{r_{xy}^2} - \frac{2z^2}{r_z^2}\right) , \tag{5.1}$$

with x, y and z the object position, r_{xy} the minor radius of the confocal volume, and r_z the major radius, with $r_z = k * r_{xy}$. To stick with experimental parameters, we has set k=5 and r_{xy}=466nm. The number of photons emitted n_{ph} by a particle at time t and position (x, y) in the confocal volume is defined by a Poisson distribution function. This parameter has been experimentally recorded as n_{ph} ≈0.14, we did not use it in our simulation. Indeed with such a low value the discretization tends to lower the number of emitted photons which drastically decreases the diffusion time recorded. On the other hand, if n_{ph} is too high, the OD filters effects are erased. Thus this parameter has been empirically fixed at n_{ph}=5, giving results comparable to the experimental data. The result is then an intensity trace coming from the particles passing through the 3D Gaussian ellipsoid and emitting photons with a Poisson distribution.

The trace signal is then rounded to obtain a discrete signal with real numbers,then it is filtered. To mimic the absorption filters, each photon of the signal created previously has a probability P to pass the filter and $1 - P$ to be absorbed. We have simulated OD filters with 10% transmission (OD1, visible in red on figure 5.8), 5% transmission (OD1.3, in green), 1% transmission (OD2, in blue) and 0.1% transmission (OD3, in light brown).

5.3.1.3 Data treatment

The experiments have been made with 60 measurements of 30 seconds each. Raw data have been exported as .csv files with an temporal resolution of 10^{-7} seconds. The correlation have been made using the Fast Fourier Transform (FFT) technique. By indicating the fluorescence fluctuations with $\delta F(t_k)$, where $t_k = k\Delta t$ with Δt the sampling time interval, by performing a Fast Fourier Transform we obtain the power spectrum $\left|\delta\widetilde{F}(\omega_n)\right|^2$, where

$$\delta\widetilde{F}(\omega_n) = \frac{1}{\sqrt{N}} \sum_{k=0}^{N} \delta F(t_k) e^{i\omega_n t_k} \tag{5.2}$$

Then the inverse FFT gives the final result

$$G(t_k) = \frac{\frac{1}{\sqrt{N}} \sum\limits_{n=0}^{N} \delta\widetilde{F}(t_k) e^{-i\omega_n t_k}}{\frac{1}{N} \sum\limits_{k=0}^{N} |\delta F(t_k)|^2 - 1} \tag{5.3}$$

And individual curves have been averaged, to get rid of the noise.

5.3.2 Results

5.3.2.1 Second campaign with FCS and OD filters

With a first experiment we considered a watery solution of 1 nM of the fluorescent dye Atto 488 (AT488) which has a strong absorption peaked at 500 nm and high fluorescence quantum yield peaked at 520 nm, and measured its diffusion coefficient by means of FCS. The measurements have been carried on both using OD filters and without them. The transmission coefficients of the OD filters that we adopted were: 10% (OD1), 5% (OD1.3) and 1% (OD2), respectively. We have also recorded the background noise obtained without the solution and with switched off laser. A measure of the laser light fluctuations have been also performed.

Figure 5.6 summarizes the outcomes of the above mentioned measurements. Figure 5.6a displays the autocorrelation curves of AT488 without filter (black curve), with the filters described above (red, green and blue for OD1, OD1.3 and OD2 respectively) and the background noise (light grey, also displayed in figure 5.6c). Higher transmission coefficient filters (OD1 and OD1.3) show an excellent agreement with the black curve. To the contrary, lower transmission coefficient filter (OD2) yields an autocorrelation curve which is more similar to the background noise curve. This discrepancy can be attributed to the strong attenuation of the fluorescence operated by the OD2 filter which makes the SNR very poor. To confirm this, we have increased the fluorescence level by performing experiments with higher concentrations of AT488 (figure 5.6b), that is 10nM (cyan curve),

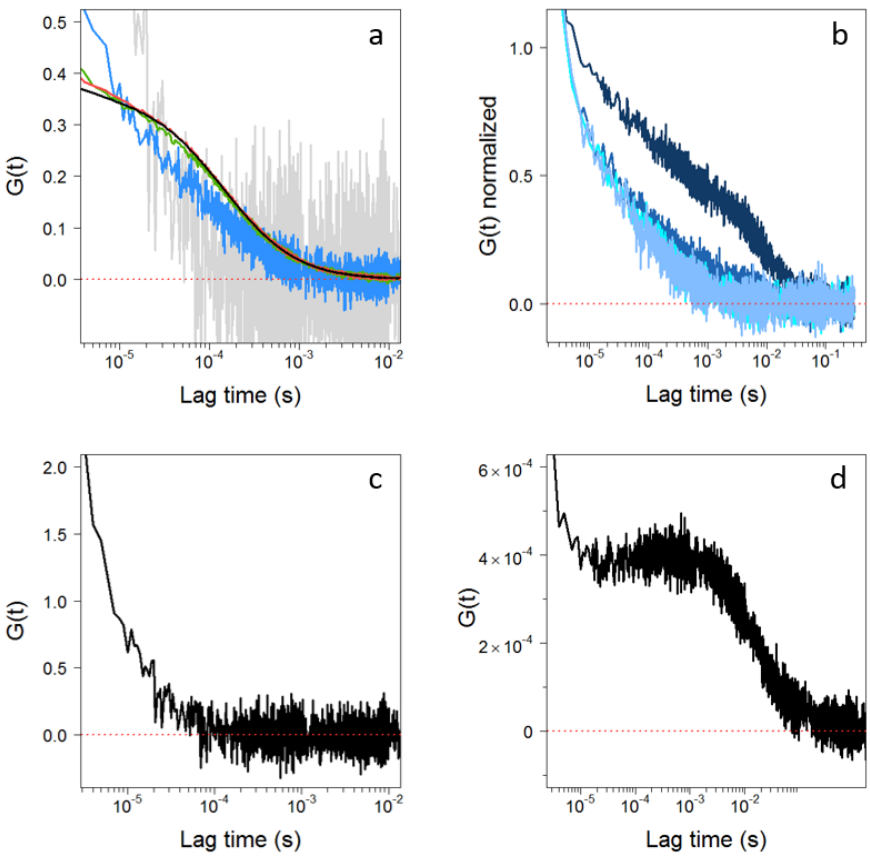

Figure 5.6: On image a, results of ACF recorded for a 1nM solution of AT488 recorded without filter (black curve), with OD1 filter (red curve), with OD1.3 filter (green curve) and with OD2 (blue curve). The ambient noise has also been recorded and its ACF has been drawn in light grey. On image b, the OD2 filter has been used to record ACF with solutions of 1nM (clear blue curve), 10nM (cyan curve), 100nM (blue curve) and 500nM (dark blue curve). Image c shows the ambient noise ACF. And image d shows the laser correlation (the optical path has been modified so the laser beam goes straight to the APD, then is filtered to avoid detector blinding).

100nM (blue) and 500nM (dark blue). The autocorrelation function obtained with the solution of 10nM AT488 perfectly overlaps with the previously found one shown in figure 5.6a. But when the fluorescence intensity increases with higher concentrated solutions, the autocorrelation functions are slightly distorted at 100nM and strongly distorted at 500nM. To understand the origin of these distortions we have measured detector's intrinsic background noise (figure 5.6c shows its autocorrelation) that strongly affects the autocorrelation curves when the fluorescence signal is highly attenuated. In addition, in the figure 5.6d, we report the autocorrelation function of a signal obtained with a fluorescent screen replacing the dye solution. Apparently, the upper curve in figure 5.6b, is the result of the combined effects of the detector noise and the laser fluctuations shown on figures 5.6c and 5.6d respectively. The detector noise is the so called and well known afterpulsing phenomenon [182], and the problems related with laser light fluctuations

have been addressed by Laurence et al.[95]. Let us remark that the values on the function $G(t)$ in figure 5.6d are very small and that in figure 5.6b, all the autocorrelation functions have been normalized. Therefore without this normalisation the upper curve would be squeezed at very low values comparable to those of figure 5.6d.

5.3.2.2 FCS simulations

To verify and understand our first results we have performed FCS simulations considering similar parameters. We have simulated the diffusion of fluorescent particles of a 1nM solution and recorded the signal as if it was recorded with OD filters. As it can be read in more details in the methods section, we have used the following parameters: a cube container with 10μm edges, with a solution of 1nM of fluorescent particles which corresponds to 602 molecules. Based on the experimental measurements we have set the diffusion coefficient of the particles to $408\mu m^2/s$ to fit with AT488 diffusion at 20 degrees Celsius, and the number of photons emitted per particle and per acquisition time has been fixed at n_{ph}=5. A simulation of a moving particle in these conditions has been done, and three screenshots are visible on figure 5.7.

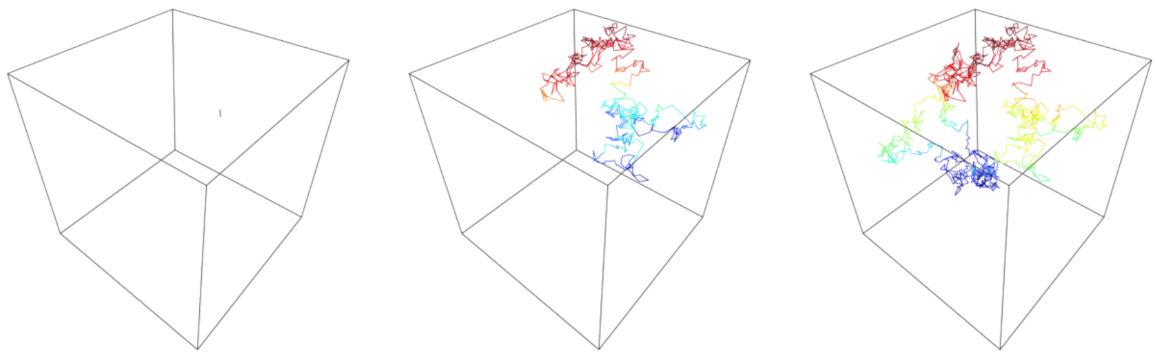

Figure 5.7: Three screenshots made on a video simulating the diffusion of a particle based on experimental parameters.

The OD filters used in the experiments have also been simulated. The results are reported on figure 5.8. Unlike experimental results shown in figure 5.6, all the curves overlap no matter the OD filter used. As expected, the higher the OD filter, the noisier the ACF. We can also note that the light-grey ACF visible on figure 5.6a is missing on figure 5.8: to simulate ambient noise, a random signal has been simulated and correlated, however the results have not been shown because there was no correlation and a high noise level on the ACF compared the others ACFs.
These results thus show that simple simulations of fluorescent diffusing particles detected in a confocal volume with OD filters give similar ACF shapes leading to equal diffusion times after fitting. These proves that the OD filters add noise to the ACF, but do not affect the ACF shape and subsequently the diffusion time of the particles. Moreover this

confirms that the phenomenon observed in figure 5.8c is an artefact. To further confirm that corresponds to afterpulsing of the detector we have run experiments on an FCCS device, in order to remove any afterpulsing effect.

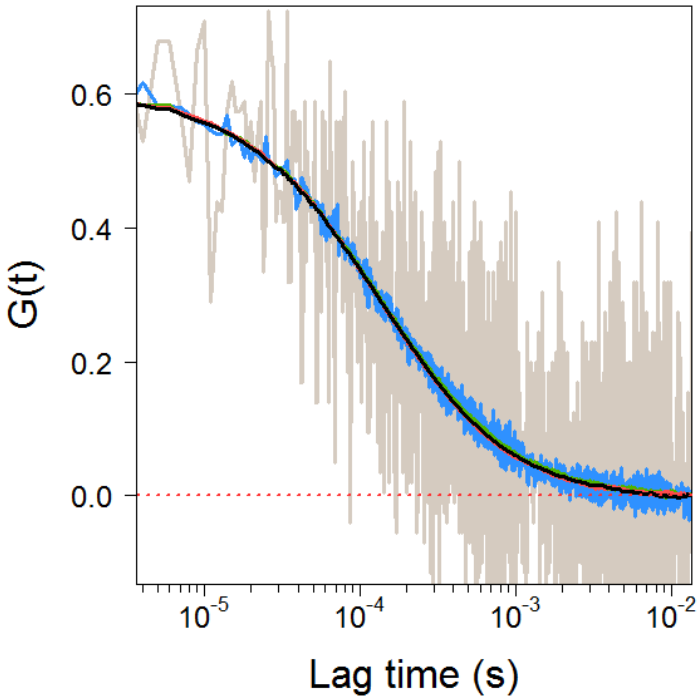

Figure 5.8: Numerical autocorrelation simulations results for freely diffusing particles. The parameters have been chosen so that we are simulating the FCS experiment described above. The simulations correspond to autocorrelated fluorescent signals of a 1nM solution of diffusing particles recorded without without filter (black curve), with OD1 (red curve), OD1.3 (green curve), OD2 (blue curve) and OD3 (light brown curve).

5.3.2.3 FCCS measurements with filters

Figure 5.9 shows the results of a cross-correlation analysis realized on a sample containing 1nM of AT488. On panel (a) the results obtained with the different filters and without OD filter are visible. One can notice that the CCFs have been rescaled, in order to have a better comparison of the curves. Overlapping CCFs are expected as seen on figure 5.8, however because the cross-correlation is obtained through two different detectors, and because the beams take different paths, the fluorescent signals recorded have a slightly different intensity, resulting in different amplitudes at G(0) [50]. This can be observed on panels (b) and (c). The results of the auto-correlation analysis of each detector independently is also visible on panels (b) and (c). The same phenomenon has been observed in figure 5.6a, confirming the hypothesis that the curve deformation

is due to the afterpulsing when performing auto-correlation of the fluorescence signals. The similarities between the results obtained with FCS simulations 5.8 and the results obtained on the FCCS device also confirm that the use of OD filters does not modify the CCF curve, but the curves tend to be noisier with higher OD values.

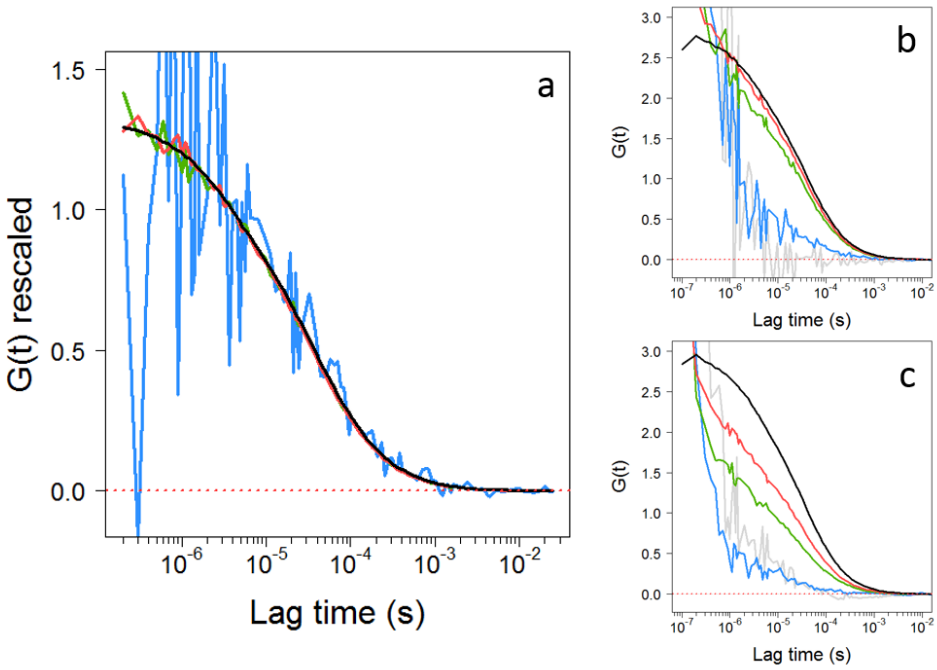

Figure 5.9: Panel *a* displays cross-correlation functions of FCCS experiments obtained without filter (black curbe) and with OD1 (red), OD1.3 (green) and OD2 (blue) on a solution of 1nM AT488. Panel *b* and *c* shows the auto-correlation functions with the same color conventions for detector 1 and 2 respectively. Afterpulsing have also been added on panels *b* and *c*, with light grey color.

We have therefore compared the results of averaged CCFs obtained from single CCF, as seen of figure 5.10. As expected, the more CCFs are averaged, the less noisy the resulting averaged CCF. And this is also visible on the residuals below the CCFs.

Going further in the analysis, we have compared the diffusion time obtained with the fitting, according the averaged CCFs (figure 5.11). The diffusion times estimated with OD filters oscillate around the diffusion time obtained without OD filter (red dashed line), and it gets closer to the value obtained without OD filters for the highest number of averaged CCFs.

Finally measurements obtained with different concentrations of AT488 have been compared, and are visible on figure 5.12. Diffusion times obtained for concentrations of 1nM, 1μM and 50μM show diffusion times estimated at 39.9μs, 37.3μs and 36.9μs respectively. As surprisingly as it could appear on a first overview, the diffusion time measured has an error of less than 10% compared to the solution of 1nM recorded without

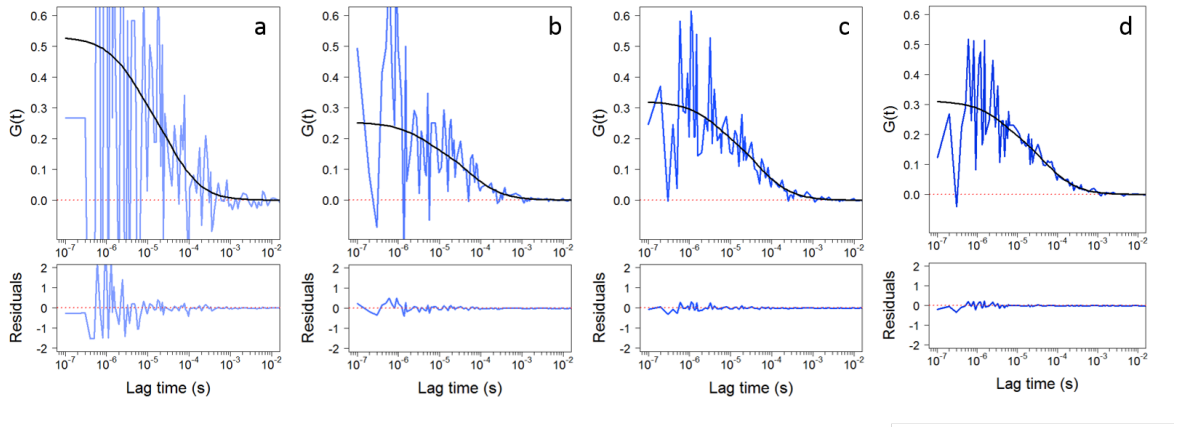

Figure 5.10: FCCS experiments outcomes. From left to right results of 1, 15, 30 and 60 averaged cross-correlated curves respectively.

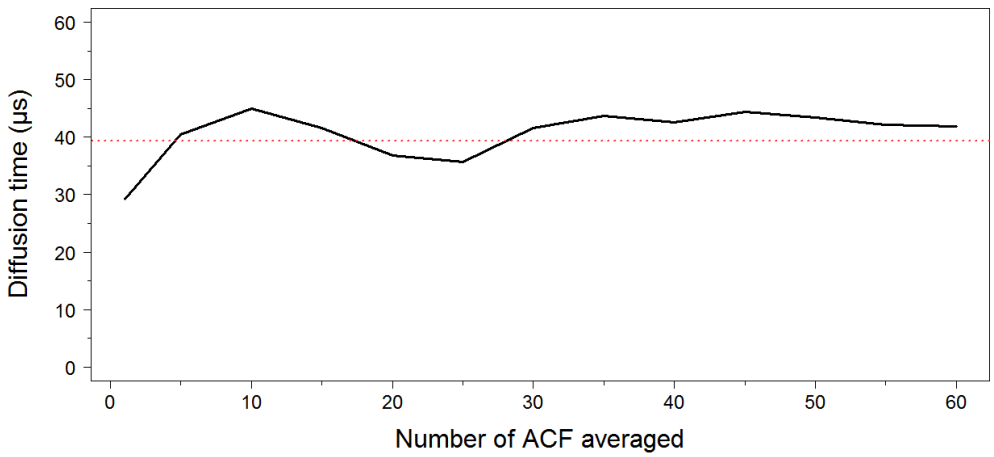

Figure 5.11: Diffusion time obtained after fitting (black curve), according to the number of CCF averaged with OD2 filter, and compared to the diffusion time without filter (dashed red line).

filters. One can also notice the oscillating pattern of the residual curve around zero. We do not claim the results are relevant, however we consider that more statistics and choosing other parameters for the auto-correlation process could lead to correct diffusion time for AT488 at 50μM recorded with some OD filters.

5.4 Discussion

As stated by Gregor et al.[67], the statistical accuracy of an FCS measurement roughly scales with the square of fluorescent rate. According to this assumption and considering a 1 minute measurement of a fluorescent dye at fixed concentration, the time needed to make similar measurements with OD1, OD1.3 and OD2 filters would be approximately

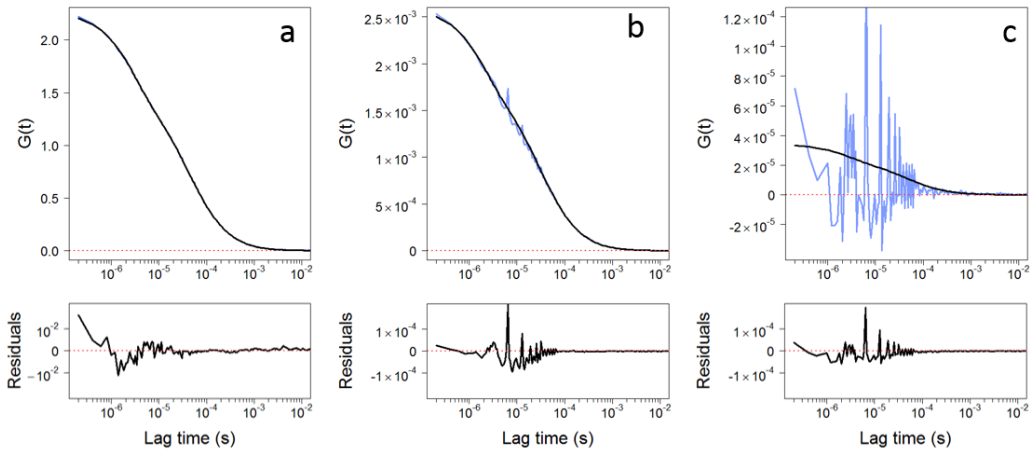

Figure 5.12: CCFs have been drawn in blue and their fitting in black. Residuals have also been added below the CCFs. Panel *a* shows the FCCS results recorded on a 1nM solution of AT488 without OD filter. Panel *b* shows results on a 1μM solution of AT488 with an OD1.3 filter (to confirm). And panel *c* shows results on a 50μM of AT488 sultion with two OD2 filters.

of 100 minutes, 2000 minutes and 10000 minutes respectively.

Based on the results obtained from our FCS simulations, and FCCS experiments, we can conclude that the use of OD filters does not change the CCFs shape, but increases their noise. Comparison of AT488 at different concentrations of 1nM, 1μM and 50μM shows diffusion times with error of less than 10%. This difference could probably be decreased, reaching equal diffusion times, by increasing the number of acquisitions performed with the increase of OD filter values, but also considering different parameters for the correlation function, in order to decrease the noise level.

Article	Technique	Concentration
Khatua et al.[86]	Single gold nanorod	1μM
Kinkhabwala et al. [87]	Gold bowtie nanoantennas	1μM
Laurence et al.[95]	APD banks	38μM
This work	OD filters	1μM, (50μM)

Table 5.1: Comparison between FCS techniques to measure highly concentrated solutions

CHAPTER 6 Experimental evidence of activation of long-range electrodynamic interactions

To this point, the previous work has lead to the following observations:

- First, labeled BSA molecules have shown absorption peaks that appeared in the terahertz range around 314GHz, only when they were illuminated. This observation is a proof of concept confirming the possibility of exciting collective vibrations of proteins brought out-of-thermal-equilibrium.

- Second, FCS techniques have been used to detect long range interactions by addressing a feasibility study with non screened electrostatic forces (impure water), and it came out that long range interactions markedly affect the diffusion behavior of soluted particles, thus this is a suitable technique to detect also electrodynamic interactions.

- Third, we have investigated how well could a FCS device record the diffusion time of particles moving in an extremely bright and concentrated solution, and concluded that solutions of more than 1μM concentration of fluorescent molecules can be recorded with OD filters without troubles.

A major question then arises from the previous work: are the forces produced by the collective vibrations of the BSA, recorded in the THz spectrum, strong enough to drive proteins displacements in the solution resulting in large deviation from the Brownian motion? And can we observe this behavior?
This chapter thus deals with the study of the protein dynamics. Experiments have been made in order to analyze the protein behavior when activated, i.e. when the proteins are out of equilibrium. Two different types of results were expected based on the our previous FCS experiments [116]:

- Either a change in the value of the diffusion coefficient when the protein concentration is varied, decreasing with respect to the Brownian one in both cases of repulsive and attractive interactions [117].

- Or the formation of clusters when the average intermolecular distance is shorter than some threshold value, thus leading to heavier species in solutions and thus decreasing the measured diffusion coefficient.

The experiments reported in this chapter show relevant evidences about the activation of sufficiently strong long range electrodynamic interactions to make them detectable, and recorded with the help of FCS and FCCS devices. As detailed in the sections below, the ACFs and CCFs so obtained have been fitted and the diffusion times have been used to estimate the diffusion coefficients at different concentrations. Then, the results at each concentration have been compared.
Through this chapter many results have been compared according to the average distance separating the proteins in solution, each distance corresponding to a given concentration. For the sake of clarity, the following table 6.1 helps converting the average distances into the corresponding concentrations:

Distance (Å)	650	700	750	800	850	900	950
Concentration (nM)	6047	4841	3936	3243	2704	2278	1937
Distance (Å)	1000	1050	1200	1350	1500	1650	2000
Concentration (nM)	1661	1434	961	675	492	370	208

Table 6.1: Conversion table between the averaged distances between molecules used to compare the following results and the corresponding concentrations

6.1 All BSA molecules labeled

Considering the negative results recorded with the BSA and only a sub population labeled with AF488 as developed in chapter 5, and considering the encouraging results obtained with the THz spectroscopy described in 3, we have decided to pursue the FCS experiments with similar conditions that are: experiments performed with fully labeled solution of BSA, and additional light sources (with respect to the FCS laser) with a 490nm LED with a typical power LED output of 250mW and 255nm LED. Moreover, the BSA proteins have been labeled with an average number of AF488 molecules between 4 and 5 per molecule of BSA. The mixture solution can thus be represented as in figure 6.1.

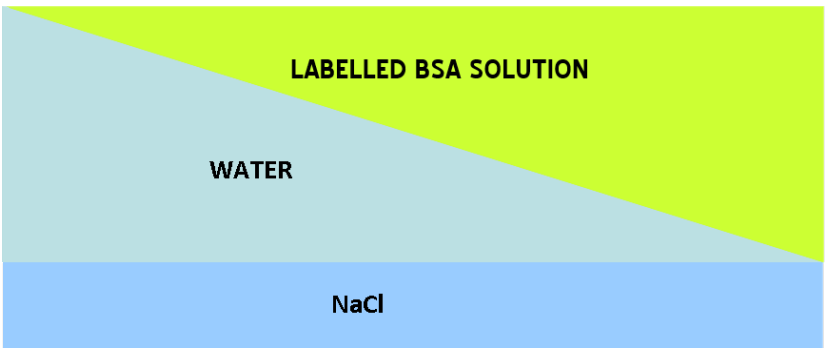

Figure 6.1: Reaction mixture for experiment involving solutions of all BSA molecules labeled.

However these experiments with solutions of all BSA molecules labeled and at high concentrations give fluorescent signals which are too bright to be recorded by detectors used in FCS. The techniques developed in chapter 5 thus allowed us to perform such experiments with high concentrations and extremely bright solutions with the use of OD filters and FCCS device.
We have first focused on the fluorescence traces recorded which are reported in figure 6.2. In order to compare the traces from different concentration involving different intensities, they have been normalized dividing them by the highest values. The results corresponding to traces of all concentrations and performed at fixed laser power (33μW or 320μW) are visually similar, and also do not show differences between the two laser powers used.

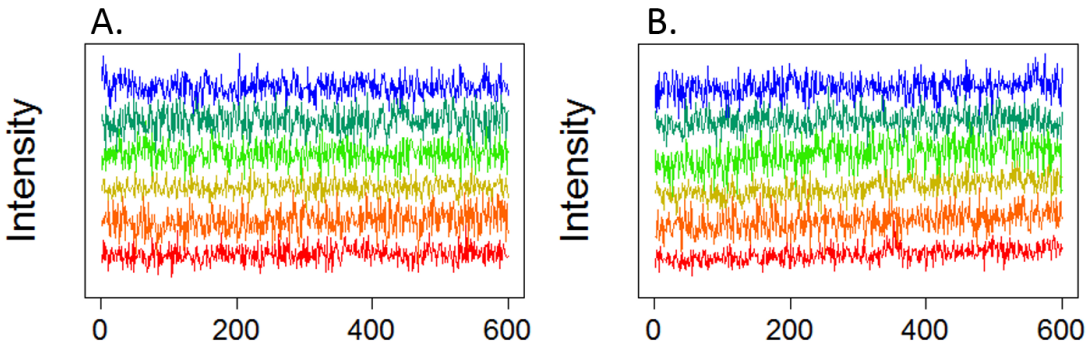

Figure 6.2: Normalized traces recorded on solution of fully labeled BSA. The colors correspond from blue to red to the following average distances among the proteins: 4000Å, 2000Å, 1000Å, 750Å, 650Å and 441Å. Panel A corresponds to traces recorded with the 488nm laser at 33μW as the only input of light. Panel B corresponds to traces obtained with the laser light set at 320μW and the addition of a 488nm LED and a 255nm LED.

On figure 6.3, one can see the comparison between the CCFs obtained from the traces visible on figure 6.2. Both scales have been set logarithmic for a better comparison of samples with different concentrations of fluorescent molecules. Indeed, G(0) is inversely proportional to the number of molecules, meaning that the higher the number of molecules in the solution, the more squeezed the CCF. Filters have been used to record the fluorescent signals, by adapting the OD filter according to the brightness of the sample in such a way that at the same time the signal is strong enough, the noise on the CCFs is minimum, and the signal does not blind the APD. This is visible on figure 6.3: at higher concentrations (from red to green) the CCFs are noisier than in the case recorded without filters (CCFs in blue and dark green). Similarly, on panel B each sample has been recorded with the help of OD filters. The presence of OD filter is revealed by the noise level of the CCFs. A priori G(0) should be the same in panels A and B at fixed concentrations. Since apparently this is not the case, this could be explained by the

fact that LEDs have been used to illuminate the samples (whose CCFs are represented in panel B), and these probably led to aberrations changing the confocal volume and increasing the fluorescence intensity eventually leading to a lowering of G(0).

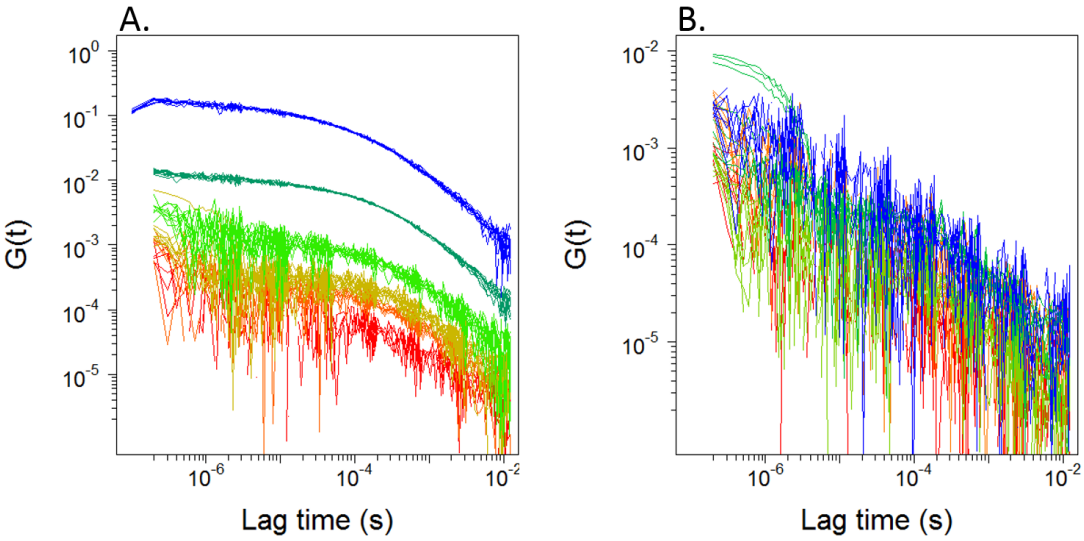

Figure 6.3: CCFs obtained from traces recorded on solutions of fully labeled BSA, visible on 6.2. To allow a better comparison, they have been kept in logarithmic scales due the larges differences of concentrations. The colors correspond from blue to red to the following average distances among the proteins: 4000Å, 2000Å, 1000Å, 750Å, 650Å and 441Å. Panel A corresponds to CCFs obtained with the 488nm laser at 33μW as the only input of light. Panel B corresponds to CCFs obtained with the laser light set at 320μW and the addition of a 488nm LED and a 255nm LED.

In order to compare the CCFs on semi-logarithmic plots, as is usually done for FCS analysis, they have been normalized by dividing by the CCFs with the estimated number of molecules obtained after having fitted them (figure 6.4). Most of the CCFs overlap, meaning that no relevant changes are observed concerning the diffusion properties of the proteins in solution, independently of the laser power used (laser at 33μW or laser at 320μW with the LEDs). Even though one can notice that the CCF obtained for the lowest concentration (with molecules separated with an average distance of 4000Å, in blue) is shifted to the left, in both panel A and B. This shift can be seen as due to a solution containing fluorescent molecules diffusing faster than those of other samples. This fact can mainly be explained by of some coating issues in the solution: while the labtek coating has been performed to ensure that labeled proteins keep on diffusing in solution, if the coating is damaged or insufficient, then labeled BSA molecules can be adsorbed to the glass and plastic of the labtek, thus increasing the ratio of free AF488 to BSA-AF488. As AF488 has a diffusion coefficient higher than that of the BSA, an

increase of the latter ratio tends to decrease the diffusion time measured, which is the phenomenon such as the phenomenon displayed by the blue curves of 6.4.

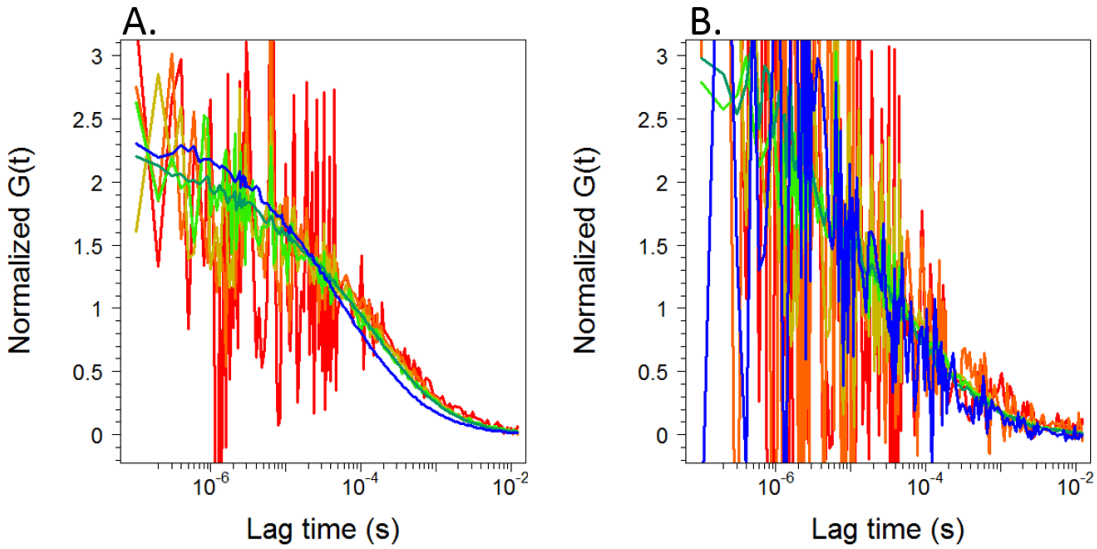

Figure 6.4: Normalized CCFs from the CCFs shown on figure 6.3. The normalization have been done by dividing the CCFs with the estimated number of molecules in the confocal volumes obtained with a fitting.

Finally, we have also plotted the normalized diffusion coefficient D/D_0, as seen in figure 6.5. As previously explained, the fitting is not fully pertinent if we consider the high noise and the small number of measurements made for each sample. Even though these are still preliminary results, and require to be confirmed and refined, the solution of BSA exposed to 320μW laser with the LEDs shows a drop of the D/D_0 (in blue), while the D/D_0 of BSA exposed to 33μW laser remains more stable. We consider this a rough indication in the good direction.

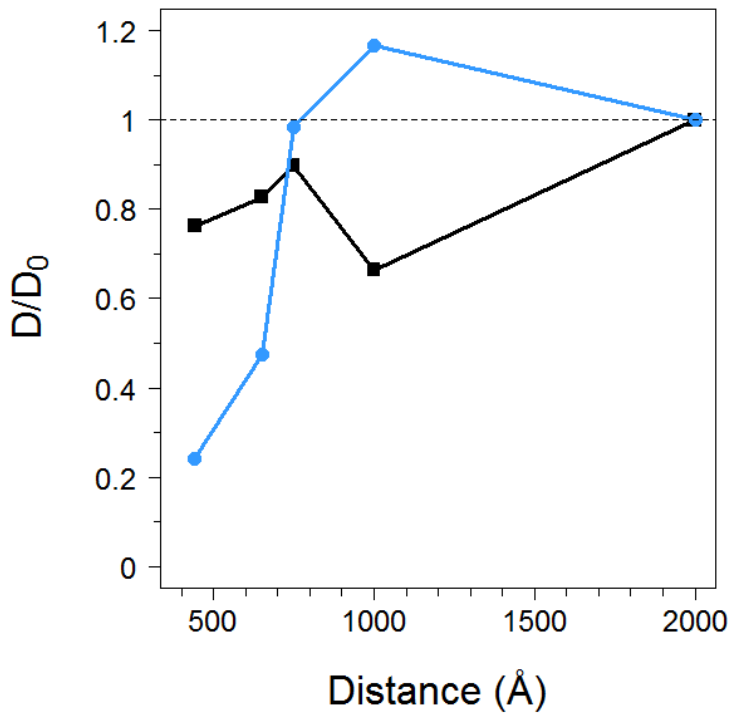

Figure 6.5: Plot of the normalized diffusion coefficients D/D_0 of fully labeled BSA solution as a function of the distance in Å between proteins. The black curve with the squares represents the D/D_0 obtained with the 488nm laser input at 33μW, while the blue curve with the round symbols has been obtained for the laser at 320μW, with the addition of the 488nm LED and the 255nm LED.

Thus the experiments involving all BSA molecules labeled with AF488 have been performed in presence of many difficulties:

- First of all, the BSA labeling is not completely efficient, and a fraction of AF488 molecules always remain free in solution thus decreasing the diffusion time estimated after the CCFs fittings.
- Then, even if the wells coating has been made to prevent BSA adsorption, this is not well controlled, and in case of non effective or non homogeneous coating, the BSA adsorption can increase the ratio of free AF488 compared to labeled BSA, leading to a decrease of the diffusion time again.
- Finally, due to the increasing brightness of the solution with the concentration, we have used OD filters leading to noisier CCFs with somewhat insufficient statistics.

For the time being, these results are not as relevant as expected, but taking in consideration the issues encountered, we expect to be able to perform new experiments in better conditions and confirm and improve the preliminary results shown in figure 6.5

6.2 RPE

According to the difficulties encountered with the labeled BSA, we have decided to perform experiments with a naturally fluorescent protein with similar optical properties than AF488 considering the absorption and fluorescence ranges. The choice of a naturally fluorescent protein has been preferred to avoid protein modification before use, and for example it does not require a covalent labeling of the fluorochrome. About the absorption and fluorescent properties, the choice mainly comes from experimental and technical constraints due to the laser used on the FCS device which excites at 488nm.
Considering these constraints we have selected a protein called R-Phycoerythrin (RPE), represented in figure 6.6, which is a light harvesting hexameric phycobiliprotein, found in bacteria, algae and plants. It belongs to a family of proteins called the phycobiliproteins (PBPs), making the phycobilisome (PBS), a macromolecular complex harvesting and conducting light with an efficiency of approximately 95% in the energy transfer process. It is build in such a way so that the allophycocyanin (APC), which has a maximum absorbance at 650 nm, makes the central core of the complex and is attached to the stromal surfaces of the thylakoids, then there are peripheral rods containing phycocyanins (PC) on the proximal parts with an absorbance maximum near 620 nm, and a distal part made of phycoerythrins absorbing light at a maximum near 565 nm and with an additional peak at 498 nm. What mainly differentiates the different PBPs are the quality and the quantity of their chromophoric groups [108].

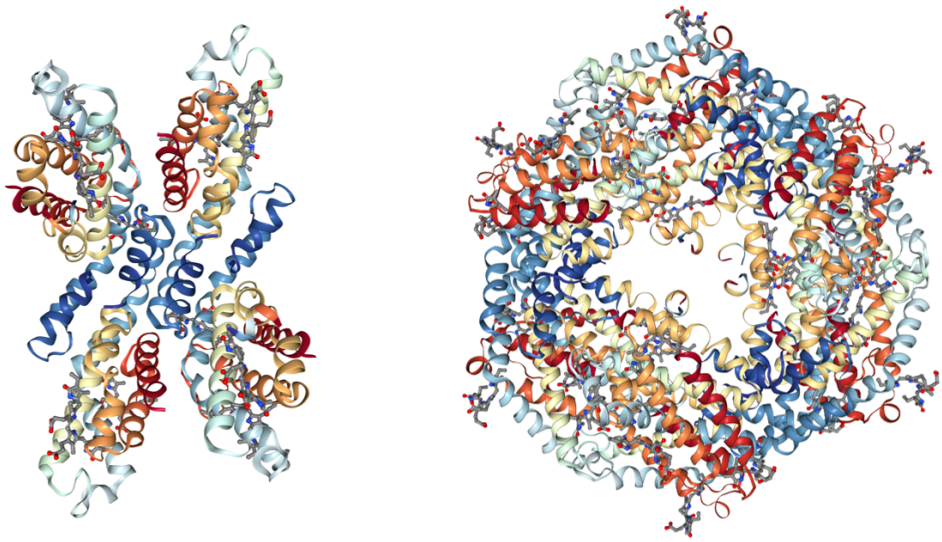

Figure 6.6: Images from Protein Data Bank. On the left, the assembly $\alpha_2\beta_2$ which forms a subunit of the RPE. On the right, an unit of RPE $(\alpha_2\beta_2)_3$

These groups are open-chain tetrapyrroles, and are bound to cysteines residues with thioether bonds [27]. They are also classified by their spectral differences as phycoerythrobilin (PEB), phycocyanobilin (PCB), phycobiliviolin (PXB) and phycourobilin (PUB). The chromophores found in the RPE are PEB and PUB.
The RPE has been purchased at Sigma-Aldrich (52412), centrifuged at 10,000g for 10 minutes. The supernatant has been removed and replaced with a solution of 150mM of NaCl.

6.2.1 Light intensity peaks as clusters evidences

The first results were obtained with an FCCS device observing the CCFs of the solvated RPE considered at different concentrations, always illuminated with an argon laser working at 100μW. The most concentrated solutions gave at first sight disappointing results, each CCF being different from the others at similar concentrations, sometimes deformed and leading to problems with the fitting. Moreover, the recorded fluorescence traces used work out the CCF, were showing sharp intensity peaks compared to the signal fluctuations recorded at lower concentrations. These results were similar to the ones reported in figure 6.7B. We thus hypothesized that if several R-PE molecules stick together, this would create clusters yielding an increased fluorescence emission coming from each individual molecule,whence the observed intensity peaks and long diffusion time given by the fitted CCF. Two main questions naturally arise:

- Are these intensity peaks really coming from cluster formation?
- If yes, are these clusters coming from protein crowding due to highly concentrated solutions or are the clusters made with the aid of long range electrodynamic forces?

Based on the theory previously developed, the energy input has to exceed an unknown threshold to excite the protein dipole, leading to its collective oscillation. Therefore we have performed experiments at different concentrations of RPE, also changing the laser power input. Different fluorescence traces are shown in figure 6.7, with three different laser powers: 33μW (A.), 76μW (B.) and 320μW (C.) for 14 average distances among the proteins that are 2000Å, 1650Å, 1500Å, 1350Å, 1200Å, 1050Å, 1000Å, 950Å, 900Å, 850Å, 800Å, 750Å, 700Å and 650Å (colors from blue to red respectively).
The results clearly show some changes when using a different laser power. When the laser power is 33μW (figure 6.7A.) no intensity peak appears on the traces. When the power is 76μW (figure 6.7B.) sharp intensity peaks are visible for average distances from 650Å to 750Å. Finally, when the laser power is 320μW (figure 6.7C.) the traces show wide intensity peaks for average distances starting from 1050Å up to 650Å. The frequency and the width of the intensity peaks seem to increase with the concentration.

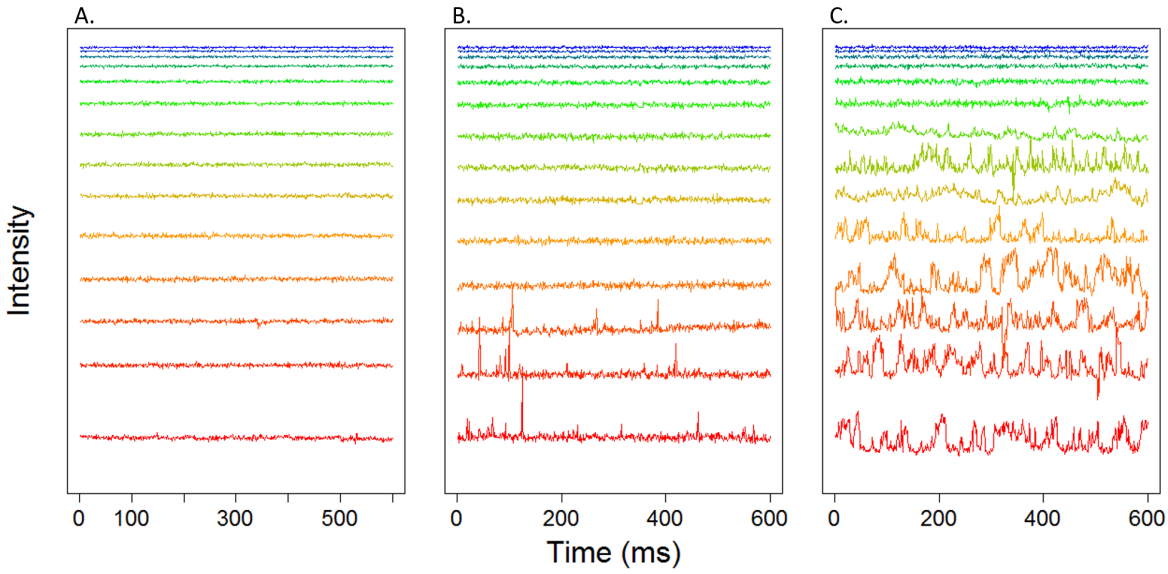

Figure 6.7: Traces recorded by channel 1 of the FCCS device during 60 seconds, for solutions of RPE. The average distances among the proteins are, from blue to red respectively: 2000Å, 1650Å, 1500Å, 1350Å, 1200Å, 1050Å, 1000Å, 950Å, 900Å, 850Å, 800Å, 750Å, 700Å and 650Å. Panel A shows the results with the laser output set at 33μW, panel B with the laser set at 76μW and panel C with the laser set at 320μW.

To obtain a better comparison among the traces, we have normalized them by means of their highest values, obtaining what is shown in figure 6.8. This figure confirms that when the laser power is 33μW the fluctuation patterns appear independent of the concentration. However, for the experiments performed with the laser powers of 76μW and 320μW, the traces at higher concentrations clearly show different fluctuation patterns starting at an average distance of 750Å (and below) for figure 6.8B. and at 1050Å (and below) for figure 6.8C, respectively.

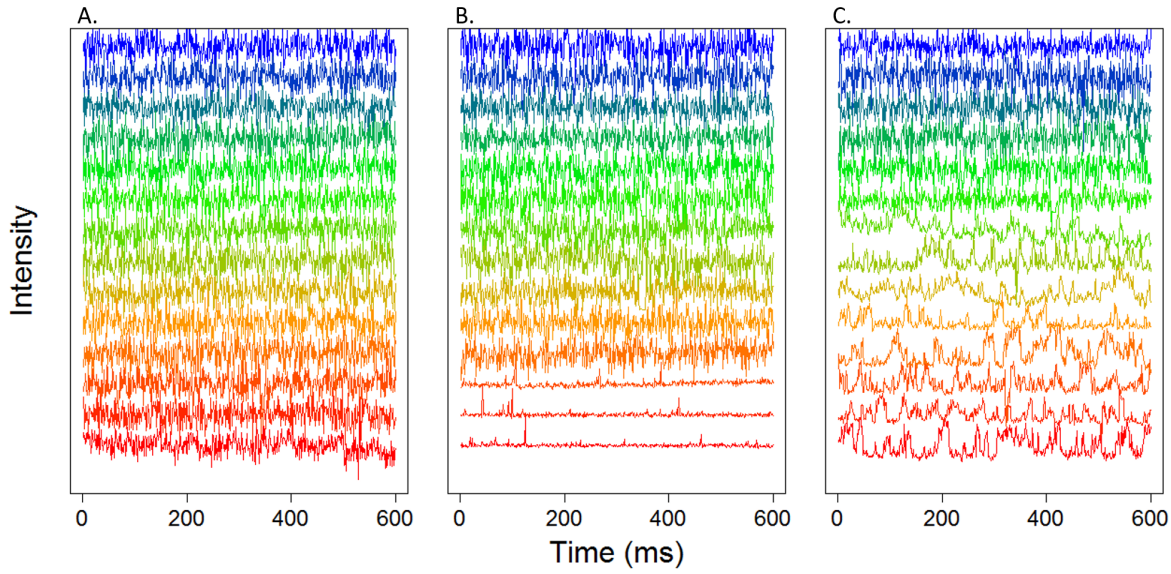

Figure 6.8: These traces are the same that the ones showed in 6.7, normalized by the highest value of each trace for a better comparison. The average distances among the proteins are, from blue to red respectively: 2000Å, 1650Å, 1500Å, 1350Å, 1200Å, 1050Å, 1000Å, 950Å, 900Å, 850Å, 800Å, 750Å, 700Å and 650Å. Panel A shows the results with the laser output set at 33μW, panel B with the laser set at 76μW and panel C with the laser set at 320μW.

These first results based on the traces comparison at different concentrations and different laser powers indicate that large intensity peaks appear only when the laser power is above a threshold value and above a definite concentration. Similar patterns to the ones reported here for the fluctuation traces have been found in experiments involving formation of oligomeres [150], and the large peak intensities have also been used by Perevoshchikova et al. [130] to develop a technique called Peak Intensity Analysis (PIA) to estimate the degree of binding of particles.

Going even further, videos have been recorded with a confocal microscope to observe the behavior of RPE molecules. The scanning has been made on a 256x256 matrix on X and Y, the pixel dwell time has been set to 0.01 ms and the frames repeated each 1 second. Finally the laser power has been set to 33μW and 320μW. Though the laser is scanning the sample leading to a lower energy input due to the non continuous excitation of the solution, the video recorded with the laser at 320μW shows multiple bright spots moving. This can be seen on figure 6.9, where snapshots from the video are shown at times t=0s, 60s, 120s and 180s.
The video directly confirms the formation of clusters as seen through the size of the bright spots. Indeed, some involve many pixels, making us think that some wide aggregates, bigger than the waist are diffusing in the solution. Moreover, the spots seem to follow a continuous path due to the small distances separating one bright spot followed through

two subsequent images. Another interesting information is also given by the average number of counts received in the scanned area: the longer the area has been exposed to the laser light, the brighter it is, and a blue halo is formed at the center of each picture in figure 6.9.

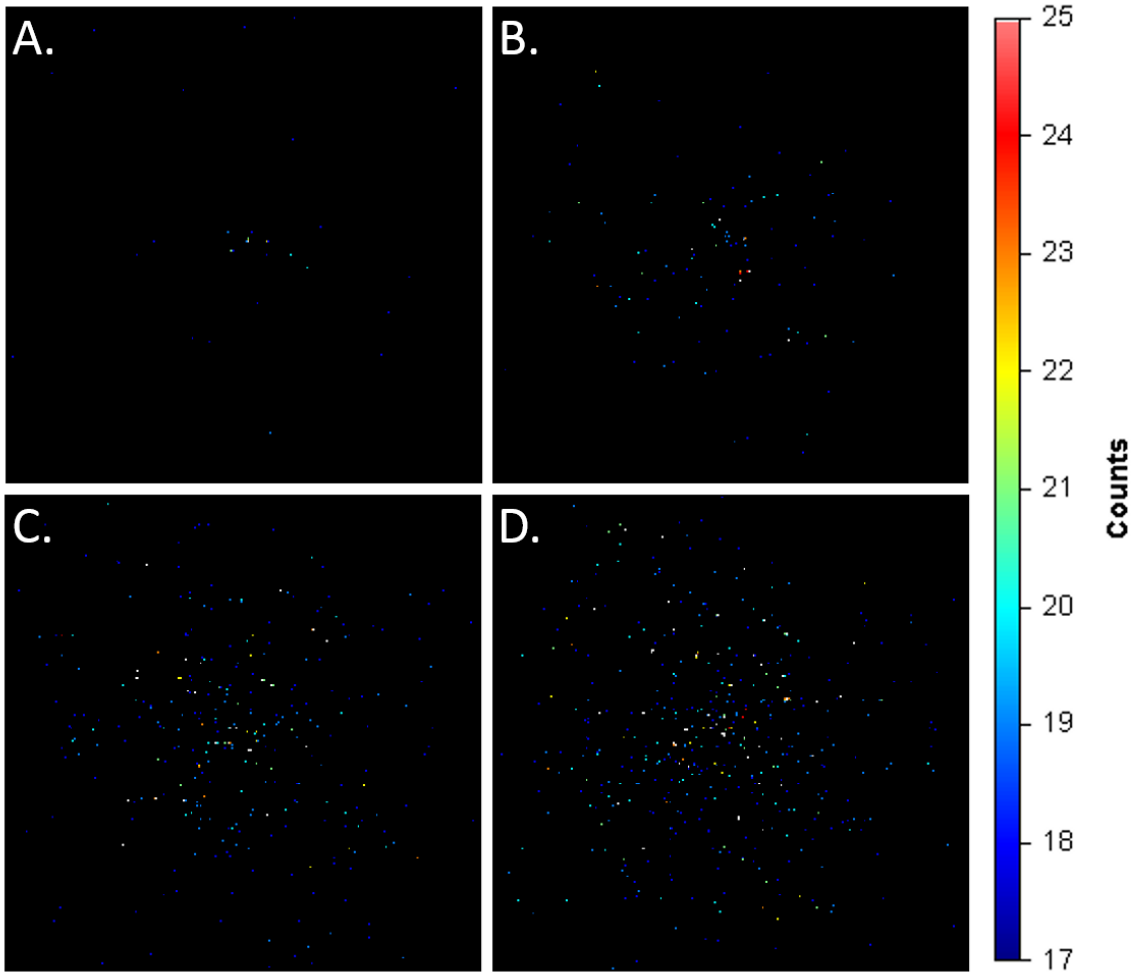

Figure 6.9: Screenshots of a video recorded for a solution RPE with an average molecule distance of 650Å with the laser output set at 320μW. The images have been saved at times t=0s, t=60s, t=120s and t=180s, from left to right and up to down respectively. The scan has been made over an area of 15μm^2 with 256 pixels per edges.

In figure 6.10, five consecutive snapshots taken from the video are visible. The images have been zoomed on a place where a cluster is being recorded, either being formed or passing through the z axis.

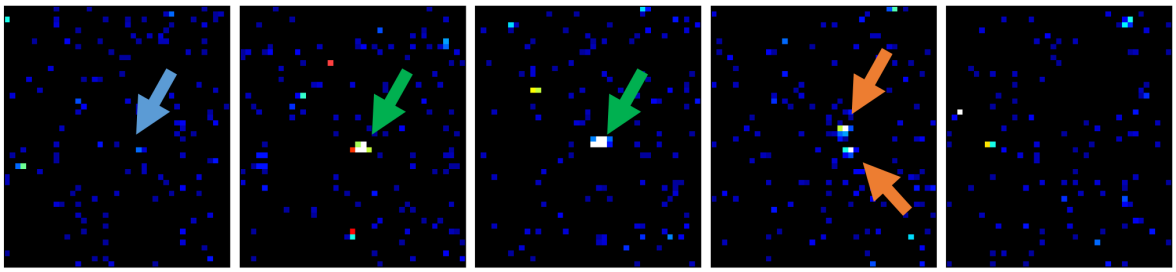

Figure 6.10: This figure shows 5 consecutive zoomed images saved from the video previously mentioned 6.9. On the first image the blue arrow shows the place where a cluster is going to be formed. On the second and third images the green arrows are pointing to a cluster that seem to be the same considering its position. On the fourth image the red arrows show two smaller clusters, that seem to come from the previous cluster. Then on the fifth image, it disappears.

We have claimed on the basis of what is reported in figures 6.9 and 6.10 to have observed the formation of clusters in the solution of RPE, when the laser power is high enough, in this case 320μW. To go even further in the confirmation of clusters formation we have recorded another video of the same solution of RPE with the laser power set at 320μW, but using a CMOS camera. The video is again showing the formation of bright spots after few minutes of illumination.

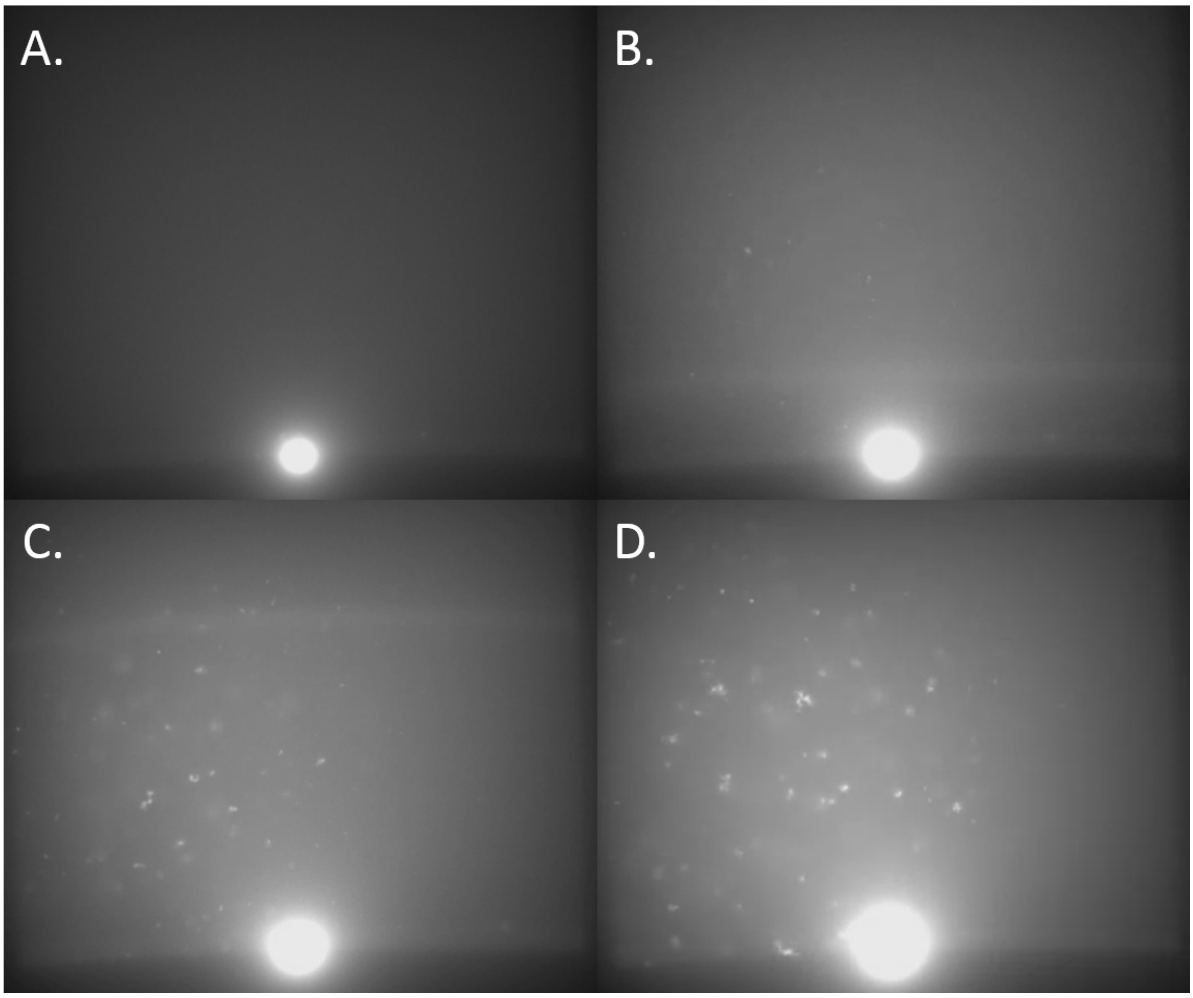

Figure 6.11: Screenshots saved on a video of a solution of RPE with an average molecular distance of 650Å. The video has been recorded with a CMOS camera. The bright spot shows the starting position of the laser during the scanning.

We have also made a similar video with the laser power set at 33μW and some images are visible in the figure 6.12. Confirming again the results shown in figures 6.7A. and 6.8A., no bright spots are observed, and neither the halo, as can be seen in figure 6.9. However a fluorescent noise is visible on the 4 images, which can be attributed to the fluorescence emitted by the individual RPE proteins moving in solution.

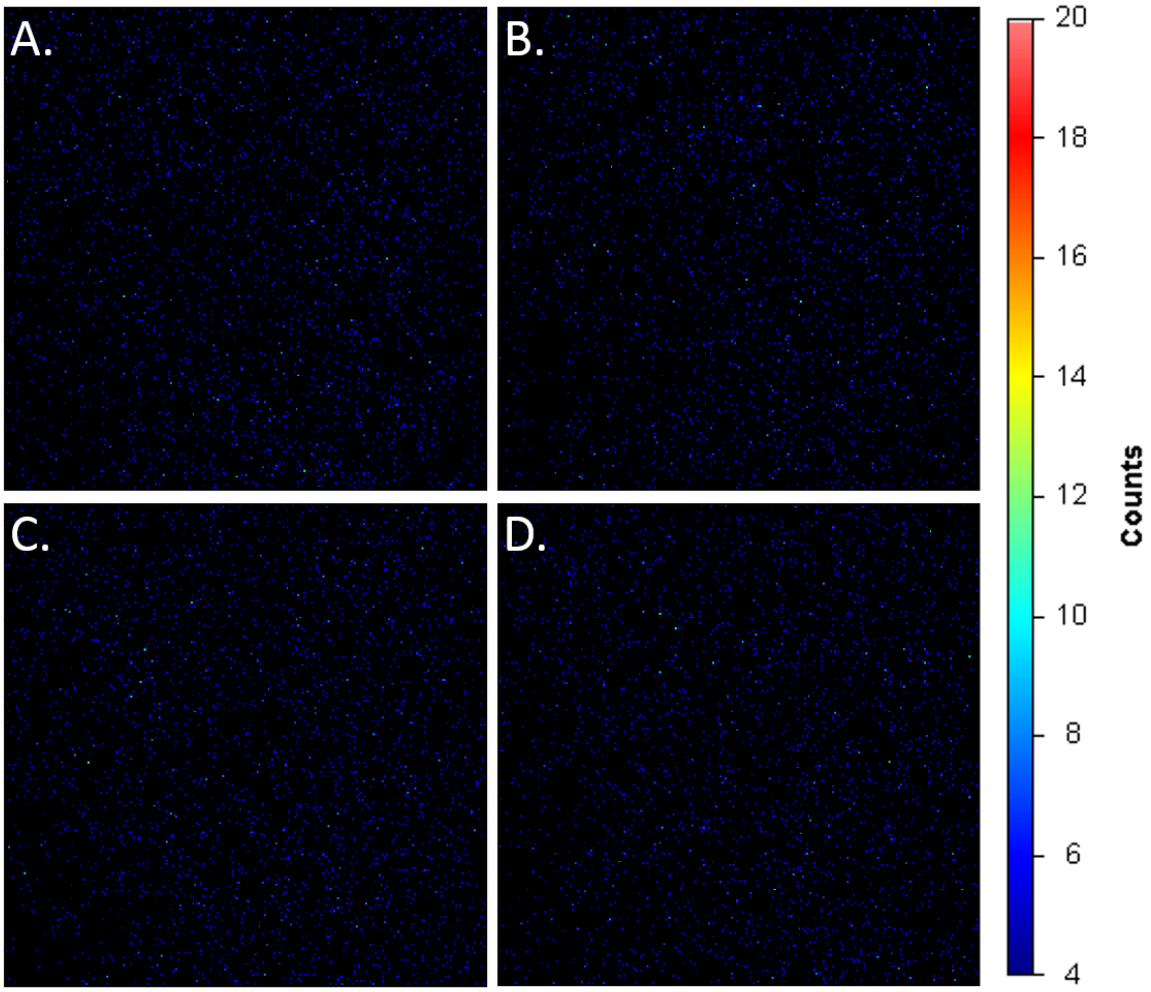

Figure 6.12: Screenshots of a video recorded for a solution RPE with an average molecule distance of 650Å with the laser output set at 33μW. The images have been saved at times t=0s, t=60s, t=120s and t=180s, from left to right and up to down respectively. The scan has been made over an area of 15μm^2 with 256 pixels per edges.

6.2.2 Information out of correlated data

To complete the analysis, we have correlated the traces recorded and we have plotted the results in figure 6.13. In this figure the CCF of each concentration has been added using the similar color code as previously adopted, the blue being the most diluted, and the red the most concentrated solution. The use of logarithmic scales on X and Y aims at better comparing the results corresponding to different concentrations. As explained before, G(0) is inversely proportional to the number of estimated molecules in the observed volume, leading to CCFs starting at different values.

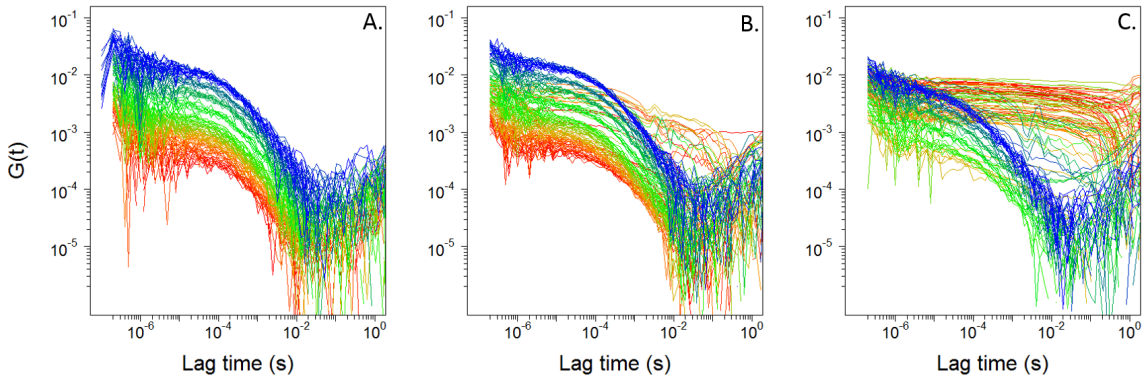

Figure 6.13: CCFs from solution of RPE with average distance between the proteins (from blue to red respectively) of: 2000Å, 1650Å, 1500Å, 1350Å, 1200Å, 1050Å, 1000Å, 950Å, 900Å, 850Å, 800Å, 750Å, 700Å and 650Å. Panels A, B and C show respectively the results for the laser output of 33μW, 76μW and 320μW.

We have also calculated and plotted the average CCFs based on the previous samples shown in figure 6.13, as seen in figure 6.14, to appreciate the global behavior of the CCFs.

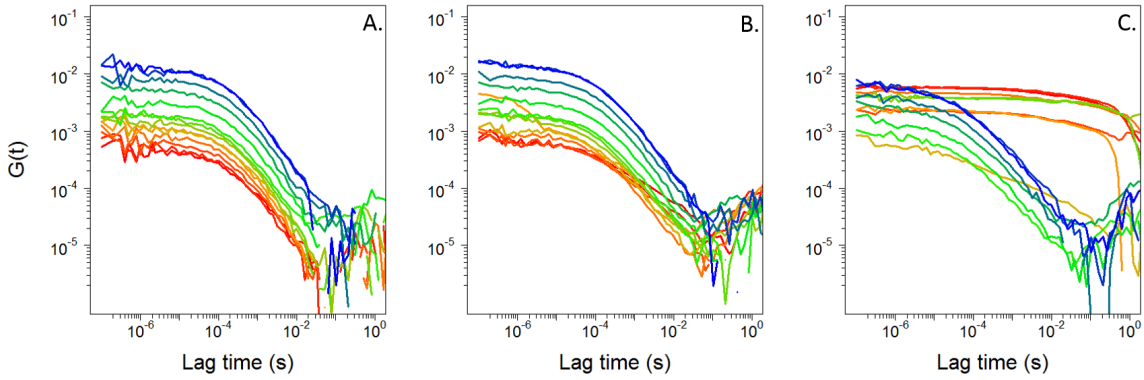

Figure 6.14: Average CCFs from solution of RPE with average distance between the proteins (from blue to red respectively) of: 2000Å, 1650Å, 1500Å, 1350Å, 1200Å, 1050Å, 1000Å, 950Å, 900Å, 850Å, 800Å, 750Å, 700Å and 650Å. Panels A, B and C show respectively the results for the laser output of 33μW, 76μW and 320μW.

Finally, the same results are shown in figure 6.15 with a linear Y scale as is usually done in FCS analysis. According to the differences between G(0) among the different solutions, due to their concentrations, we have normalized the CCFs to make them appear on the same scale by dividing by the estimated number of molecules in the waist after fitting.

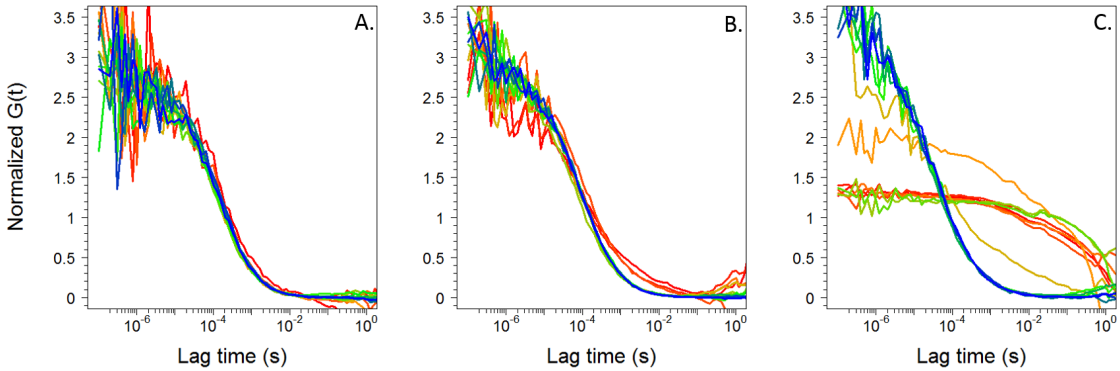

Figure 6.15: Normalized CCFs from solution of RPE with average distance between the proteins (from blue to red respectively) of: 2000Å, 1650Å, 1500Å, 1350Å, 1200Å, 1050Å, 1000Å, 950Å, 900Å, 850Å, 800Å, 750Å, 700Å and 650Å. Panels A, B and C show respectively the results for the laser output of 33μW, 76μW and 320μW.

By inspecting figure 6.15, one can better compare the RPE molecules behavior. Overlapping CCFs as seen on panel A, imply that the diffusion times of the RPE molecules in solutions of different concentrations are practically coincident. Panel B shows that increasing the laser power to 76μW leads to two behaviors of RPE molecules: on one side overlapping CCFs are found for lower concentrations, corresponding to average distances from 4000Å to 800Å; on the other side, right shifted CCFs for the most concentrated solutions. Finally, on Panel C, one can see that the bimodality seen on panel B has been amplified, with remaining overlapping CCFs for the lowest concentrations (with average distances from 4000Å to 1200Å), and far right shifted CCFs for the highest concentrated RPE solutions.

6.2.3 Input energy and threshold

We have also tested the relaxation time of the clusters, that is the time needed to disaggregate them, and the outcome is displayed in figure 6.16. To do so, we have used a highly concentrated solution of RPE (with an average distance among the molecules of 650Å) to be sure that cluster formation would happen, then we have used a laser excitation power of 320μW to let the clusters form. After making sure that high intensity peaks were visible on the traces, we have switched the laser excitation power down to 33μW. As shown by panel A., the 25 first seconds are recorded with the laser power at 320μW,then from second 25 to second 60 the laser power has been dropped and kept at 33μW.
Panel B. is focused on the transition from 25 seconds to 35 seconds. One can first notice that the laser power drop from 320μW to 33μW is not perfectly sharp. However there are also intensity peaks that appear in many different samples. Panel C. then shows the standard deviation of the intensity fluctuations worked out through different samples,

giving a statistical information about the dynamics of cluster disintegration following the decrease of the power of the excitation source. One can see on this panel that up to 2 or 3 seconds large intensity peaks are still present, then between 3 and 7 seconds, few small intensity peaks remain, and eventually the solution gets to a fluorescence steady state after 7 seconds. Considering the fact that the intensity peaks completely disappear shortly after reducing the laser power to 33μW, we have here found further evidence of the light induced clustering formation through their disaggregation.

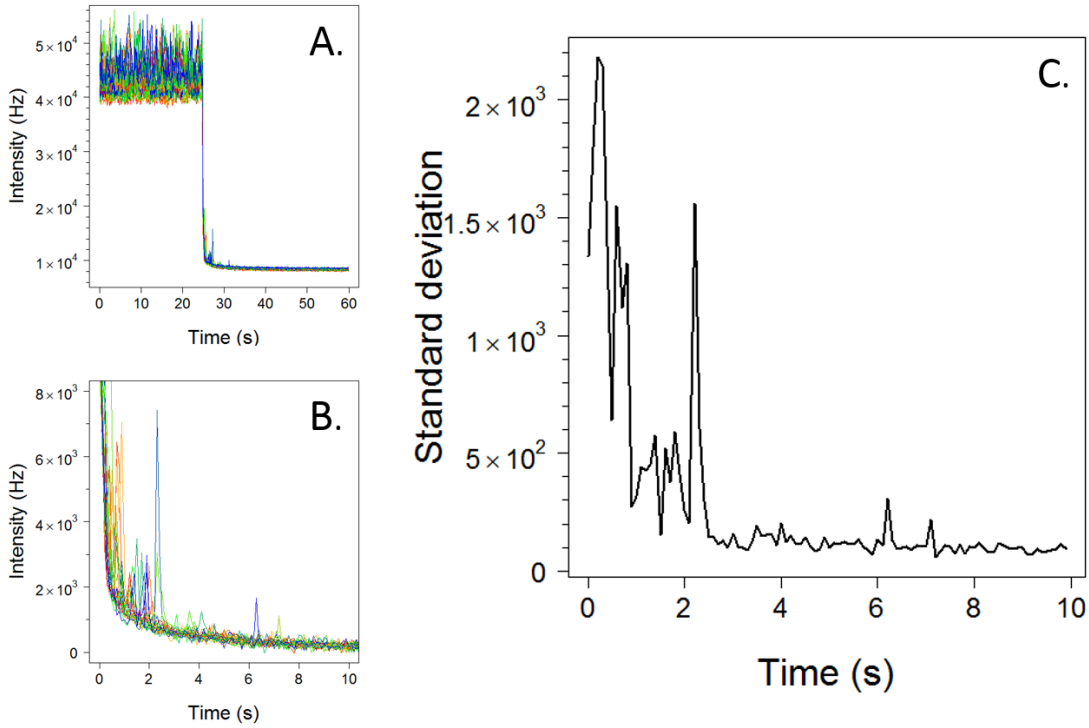

Figure 6.16: Study of the relaxation of the cluster formation, made on ten samples with average distance of 650Å. On panel A, the laser input have been change from 320μW to 33μW at t=25s. Panel B is a zoom of panel A, starting at t=25s. Panel C is the standard deviation of the intensity of the different samples recorded and visible on panels A and B.

Further analyses have also been done to investigate about the threshold behavior of the cluster formation according to the distance among the molecules. To do so, the variance of the traces has been calculated for each sample with the average distance used in the previous sections, and with the laser power set at 33μW, 76μW and 320μW (red squares, green disks and blue triangles respectively in figure 6.17). Panel A. shows the variance of the intensity. Due to the change of excitation power of the laser, the curves are shifted upward when the power increases, leading to a more difficult comparison. On panel B., we have subtracted to each curve the intensity variance measured at 2000Å. It is interesting to note that the three curves overlap for the longer distances separating the

molecules, from 2000Å to 1050Å. The red and green curves also overlap up to 800Å. These two values, 1050Å and 800Å have already been noticed in figure 6.7 and 6.8. Finally, we have hypothesized that the variance behavior or the red curve was the one expected for an homogeneous solution of RPE diffusion with Brownian motion and we have subtracted the values of the red curve to the corresponding values of the green and blue curves for similar average distances among the molecules, as seen on panel C. On this panel, the intensity variance increase is more visible at the distances previously mentioned, that is, 800Å and 2000Å, and in agreements with the analysis of the fluorescence traces made above.

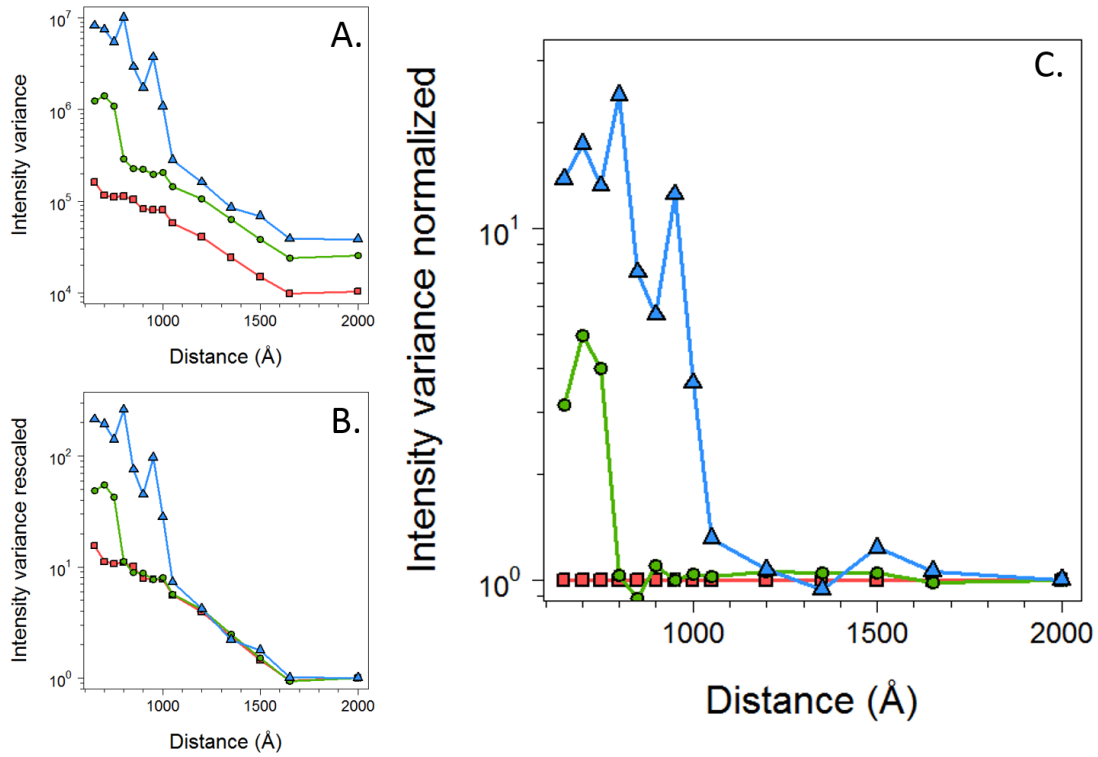

Figure 6.17: Study of the intensity variance of the traces visibles on figures 6.7 and 6.8 according to the average distance between the RPE proteins in Å, with the laser set at 33μW (in red), 76μW (in green) and 320μW (in blue). Panel A shows the intensity variance; panel B shows the intensity variance re-scaled according to the variance at d=2000Å; panel C shows the intensity variance normalized with the intensity variance of respective measurements taken for the laser set at 33μW in red.

Finally, we have tried to compare the diffusion times estimated by means of the fittings of the CCFs (visible in figure 6.15). Unfortunately, the diffusion times obtained by the fitting suffer of two main issues, mainly the noise at short lag time and the unexpected shapes taken by the CCFs when traces are affected by the presence of the clusters. The correlation algorithm, used to cross correlate the traces, explains the noise at short lag

times. The duration of the trace record is also an important factor in the noise creation. But both these issues could not be fixed due to technical properties of the FCCS device. The panel A on figure 6.18 is borrowed a previous article [117] and shows the position of 100 particles interacting with a Coulomb potential and a dipolar potential, after having run a simulation of 5000 μs (displayed in the left panel), and the mean square displacement displayed in the right panel. The first line considers an average interparticle distance of 0.18μm and the second line 0.04μm. From these simulations we can observe the sudden formation of clusters below a given interparticle threshold distance, which is in excellent (qualitative) agreement with the results previously described concerning our experimental findings obtained with the RPE protein.

Panel B also comes from [117] and displays the normalized diffusion coefficient estimated according to average distance between the particles. One can see out of this figure that the particles interacting through Coulomb potential and attractive dipole-dipole potential make a sharp drop of the D/D_0 below a threshold distance. This is however not observed when the particles interact only through Coulomb potential.

Finally, panel C shows the D/D_0 measured on RPE samples. This panel can be directly compared to panel B. The results are strikingly similar to the simulation with sharp drops at 800Å and 1050Å when RPE measurements have been made with the laser output at 33μW and 320μW respectively.

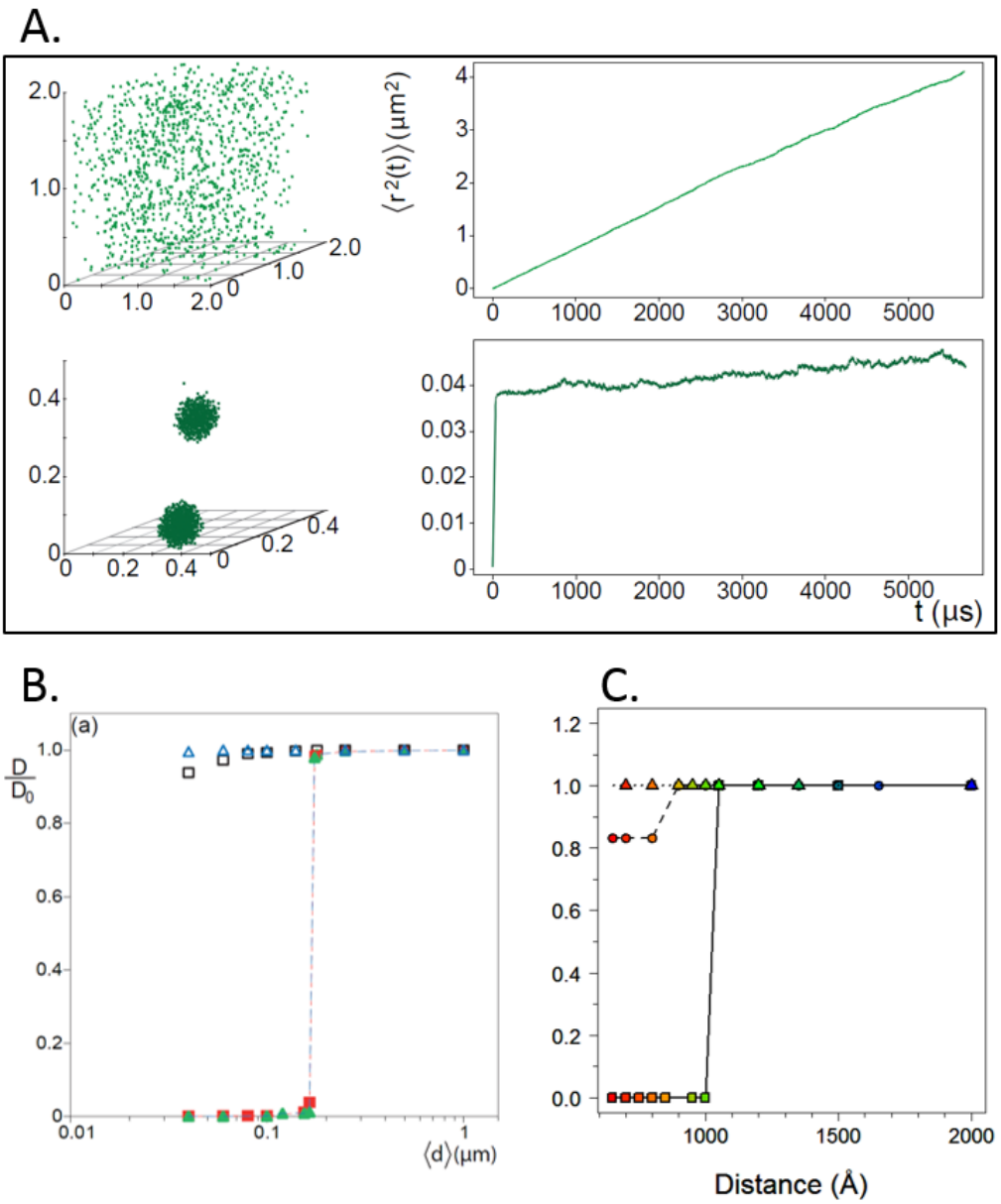

Figure 6.18: Panel A from [117], shows particles position snapshots at the final simulation time and mean square displacement versus time at two average interparticle distance $\langle d \rangle = 0.18\mu$m (first line) and $\langle d \rangle = 0.04\mu$m (second line) for particles of $Z = 100$ interacting with a Coulomb potential [Eq.(4.25) with $\lambda_D = 0.001\mu$m] and with a dipolar potential [Eq.(**??**)]. In the snapshots the axis units of r are μm, as well as the units of the snapshots axis to the right. In the right-hand panels, the units are μm^2 for the MSD and μs for the time. Panel B from [117], is a semi-log plot of the normalized self-diffusion coefficient D/D_0 versus the average distance of the particles interacting only through Coulomb potential [Eq.(4.25)] and through Coulomb potential and the attractive dipole-dipole potential [Eq.(**??**)] for different combinations of λ_D values at $Z = 10$. The symbol shapes indicate the Debye length values, $\lambda_D = 0.001\mu$m correspond to triangles and $\lambda_D = 0.01\mu$m to squares, while open symbols represent Coulomb potential and full ones the combined action of Coulomb and dipole-dipole potentials. Panel C comes from the data shown on 6.15, and corresponds to the time measured at half maximum of the CCFs according to the distance separating the RPE proteins. Triangles show the results obtained for a solution of RPE illuminated by the laser at 33μW, the disks with the laser at 76μW and the squares with the laser at 320μW.

6.3 Toward biologically relevant excitation sources

While the results previously obtained with RPE are quite promising, laser light sources are obviously not available in nature to allow the out-of-equilibrium excitation as seen before. RPE are light-harvesting proteins, so that we could think that diffused sunlight in the atmosphere might be sufficient to activate such long range electrodynamic interactions. However, most of the proteins are not light harvesting and supposedly not interacting with light. Thus we have started to think of alternative excitation mechanisms for long range electrodynamic interactions.

Adenosine Triphosphate (ATP) hydrolysis could be a suitable candidate to provide the required energy. It is an interesting approach because ATP is found in all forms of life and is often referred to as the "molecular energy currency unit" for the intracellular energy transfer. The Gibbs free energy is negative in the ATP hydrolysis reaction, so that energy is released, according to:

$$ATP + H_2O = ADP + Pi \qquad (\Delta G = -30.5 kJ/mol) \tag{6.1}$$

Where ADP stands for Adenosine Diphosphate, Pi stands for inorganic phosphate. When coupled with positive Gibbs free energy reactions, if the ΔG is negative, the reaction becomes energetically favorable. Therefore we need to clarify the following questions:

- Can the release of the free Pi in solution be powerful enough to hit the proteins and create mechanical and dipolar oscillations of collective kind?
- In other words, can the free Pi in solution excite collective vibrations through non thermal collisions?

In order to use ATP hydrolysis as energy source, we had to find a way to trigger it and understand its kinetics in order to control the release rate of the Pi. To follow the kinetic, we have used a technique, described in [92], to quantify the Pi. We have then performed the calibration by testing the method on solutions, observing the absorbance as a function to the Pi concentrations, as seen in figure 6.19. Following Ref [92] we have used 2 mL of the solution containing the desired concentration of phosphate, 1.5 mL of Triton X-100, 1.5 mL of ammonium molybdate reagent. After shaking and after waiting for 10 minutes, the absorbance has been measured at 375 nm.

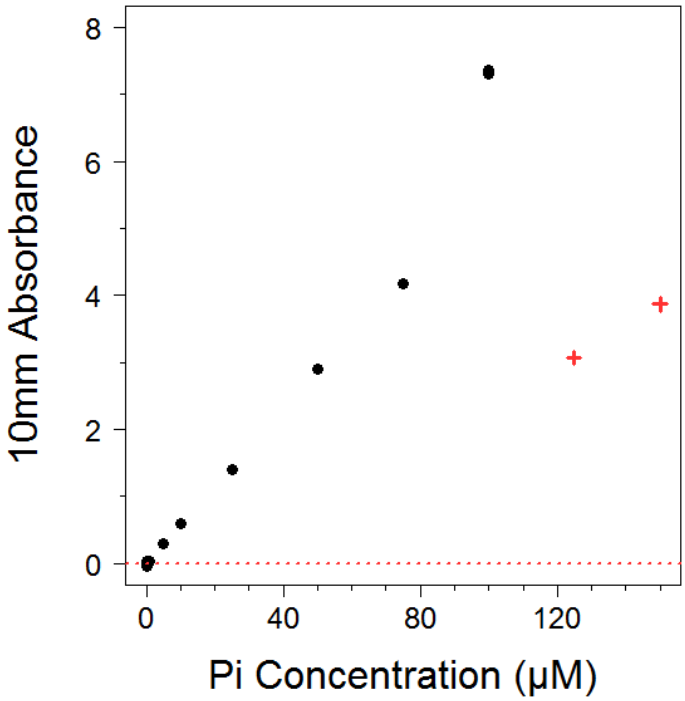

Figure 6.19: Inorganic Phosphate absoprtion according to its concentration. Blacks dots show homogeneous solutions, and red crosses show Pi precipitation.

As seen in figures 6.19 and 6.20, the absorbance increases linearly with the Pi concentration up to 100 μM, then the Pi begins to precipitate entailing lower measured absorbance.

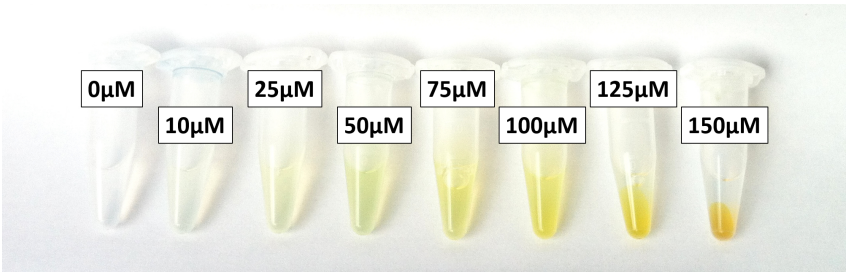

Figure 6.20: Solutions of Pi at different concentrations. Tubes at 125μW and 150μW show an orange precipitate.

The experiments have not yet been finished, however we have decided a protocol that will be followed. Different methods have been compared to hydrolyze the ATP [76, 180], and we finally choose to use a copper complex as described in the article in Ref [151]. We will then perform experiments using solutions containing ATP and copper complexes, and use the method previously described [92] to quantify the Pi concentration that has

been released by the ATP hydrolysis. After having worked out a preliminary analysis about the ATP hydrolysis rate driven by copper complexes, we will use ATP hydrolysis to repeat the experiments performed with the BSA protein, needing only a small fraction of fluorescently labeled proteins. In fact, the excitation of collective vibrations should be driven by ATP hydrolysis. All these is at present only conjectural and will be practically implemented in the near future.

6.4 Discussion

Here, proteins diffusion in solution has been studied to investigate if long range electrodynamic interactions among these proteins can be strong enough to be detectable. In a set of experiments performed before this thesis work, FCS has been used to study the diffusion of solvated BSA proteins of which only a sub-population was fluorescently labeled as discussed in chapter 5, but the diffusion times did not change with the distance among the proteins, at variance with a-priori expectations.

The results reported in chapter 3, concerning the observed out-of-equilibrium collective vibrations of the BSA protein, tell us that the BSA molecules behave as microscopic antennas that absorb the electromagnetic radiation tuned at their "breathing (collective) oscillation frequency. But, antennas at the same time absorb and re-emit electromagnetic radiation, thus, according to the theoretical predictions mentioned throughout this thesis, these antennas (biomolecules) can attractively interact at a large distance through their oscillating near-fields. Moreover, since these collective vibrations display a threshold effect for the energy input rate, we realized that directly exciting all the molecules is necessary. This means that all the BSA molecules have to be fluorescently labeled, possibly with more than one fluorochrome per molecule.

Thus we have made some experiments using the same solution of the THz experiments, i.e. with all the BSA molecules labeled, so that OD filters became necessary to prevent detector blinding as explained in chapter 5, and using an FCCS device to prevent afterpulsing. As we have seen in this chapter, we have not yet been able to fix some problems (the presence of non controlled fraction of free AF488 molecules and the BSA adsorption to the walls of the labtek) so that our preliminary results with the BSA are still rough and need additional work to provide a reliable result.

Finally, taking advantage of its properties, we have chosen a naturally fluorescent protein, the RPE. The results obtained show that when the laser power used with the FCCS device is low enough (experiments performed at 33μW), the diffusion is Brownian from the lowest concentration (26nM corresponding to an average inter-molecular distance of 4000Å) up to the highest concentration tested (6.05μM corresponding to an average dis-

tance between the proteins of 650 Å).
However, when the laser power is increased (76μW and 320μW), some high intensity peaks show up on the fluorescence traces recorded for the highest concentrations (800Å and 1050Å respectively). This phenomenon is also accompanied with bright spots observed on videos. The correlation analysis of the traces thus shows diffusion times much longer than the ones expected for Brownian motion. These results are in agreement with the previously developed theoretical computations reported in figure 6.18, and the only explanation that we can give of the presence of these intensity peaks and of the spots visible on the videos are clusters formed through the action of long range electrodynamic interactions. Finally, the relaxation time of the intensity peaks, corresponding to the cluster disaggregation due to a sudden lowering of the laser power, is another evidence of the origin of clusters transition. The evidence of aggregate formation is also supported by the observation of similar intensity peaks in experiments involving fluorescent probes binding nanoparticles, where large peaks of fluorescence are visible when multiple dyes bind to large particles [130]. And the peak intensity analysis (PIA) has also been used to measure the protein binding to lipid vesicles and erythrocytes [7].
A constructive criticism about the formation of clusters and against the explanation based on long-range electrodynamic interactions would be to relate the formation of aggregates to the RPE denaturation. However, in a first side, its oligomerization state makes its structural stability extremely high [108]. The loss of optical properties of the RPE gives information about the departure from its native conformation, either induced by heat or by chemical denaturation [167]. The pH is an important factor that can lead to protein denaturation, and RPE has been reported to be denaturated at low pH (pH=3) and hence to create irreversible aggregates, as studied by Ogawa et al. [121]. In this article, they also compare the RPE sedimentation according to the pH, as seen in figure 6.21.

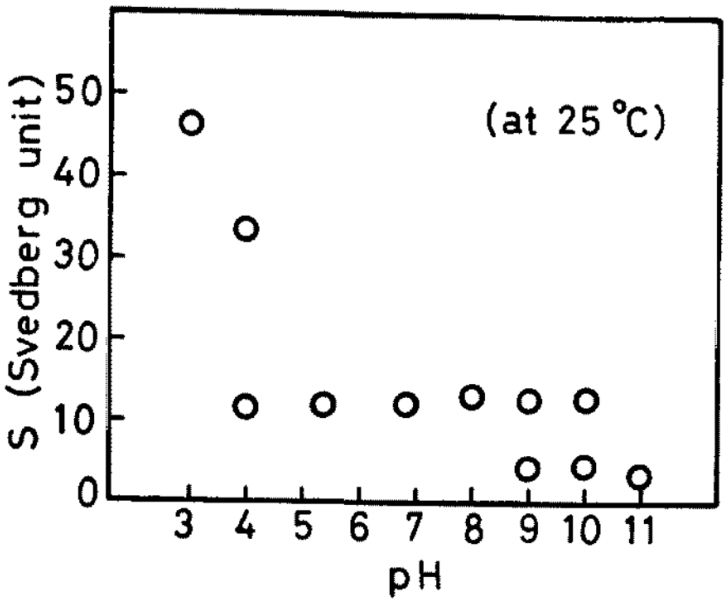

Figure 6.21: The pH dependance on sedimentation constant of phycoerythrin at 25°C and ionic strength 0.1, from [121].

In their article, Liu and al. [98] say that the RPE presents stronger functional stability in the pH range of 3.5-10 compared to the structural stability. In our experiments involving RPE, pH measurements gave pH=5 for a solution with inter-molecular distance between the RPE proteins of 2000Å, and the aggregation observed is reversible, reproducible, has a short relaxation, and the clustering phenomenon occurs suddenly by crossing the threshold value of 1050Å.
The temperature is another parameter that can lead to protein denaturation. In their article, Vaidya et al. [167] have shown that the RPE is experiencing a decrease of its fluorescent for temperatures higher than 62.8°C. Considering the intensity analysis reported in figure 6.17, the intensity does not experience any decrease when reaching the highest concentration of RPE.

Many articles in the literature also deal with some properties of the PBS proteins that could be closely related to the behavior previously observed. This is the case, for example, of the Orange Carotenoid Protein (OCP) that quenches the fluorescence of the PBS to reduce the excess of absorbed energy [155]. The superradiance of excitons in RPE crystal have also been described [170], and defined as *a phenomenon of spontaneous collective emission of light arising from an ensemble of optically excited systems.* This has been observed around 600 nm with a bandwidth of 19.6nm and has been supposed to be used for energy transfer between the PBS proteins such as the RPE and the PC. This phenomenon is closely related to the theory we developed, and it is possible that another exciton could be activated at shorter wavelengths and could originate electrodynamic

long range force.

CHAPTER 7 Conclusion

In conclusion, our goal was to find experimental evidence of long-range electrodynamic interactions taking place between biomolecules. This is a first step providing a proof of concept of prospective relevance to biology. This work has been motivated by the poor understanding of the dynamics of intermolecular encounters in cellular signaling pathways, taking place with great precision and effectiveness both in time and space. Brownian motion, usually invoked to explain this encounters, fails to characterize such an organization due to its randomness leading to low efficiency. Whereas deterministic and selective forces acting at a long distance could accelerate the encounter between cognate partners of biochemical reactions. The first natural candidates of this kind are electrostatic forces but these are screened due to the high ionic strength of the intracellular medium and the high dielectric constant of water, thus leading to short distance interactions (up to 10Å). Some theories developed in the 60's proposed that electrodynamic forces could be used by macromolecules to interact selectively at long distances, in fact the theoretical prediction is that the interaction potential is proportional to $1/r^6$ if the electric dipoles of the molecules vibrate out of resonance, but is proportional to $1/r^3$ at resonance. These long-range interactions could therefore be switched on and off according to the presence of some external energy input. If these forces are sufficiently strong, one can expect the encountering process of cognate partners to be possibly driven by such forces. And the following crucial question arises: *Is it possible to experimentally observe such interactions?*

In order to get the mentioned proof of concept, two preliminary steps were needed: to get an experimental evidence of the possibility of activating out-of-equilibrium collective vibrations of biomolecules, which would bring about giant dipole oscillations; then to validate an experimental method to detect the presence of intermolecular electrodynamic interactions. For what concerns the first preliminary step, experiments have been performed fulfilling two necessary conditions. First, the experiments have been performed with watery solutions of proteins. Then, since according to a theoretical prediction the activation of intermolecular electrodynamic interactions requires that the excitation of collective vibrations occurs *out-of-thermal-equilibrium*, the experiments have been performed by bringing the proteins out-of-equilibrium. This has been achieved through the use of covalently bonded fluorochromes which allow light excitation of these proteins, eventually leading to their collective vibration.

The first experiments focused on the signature of collective vibrations of proteins

through terahertz spectroscopy. Based on rough theoretical predictions of the expected frequency of fundamental vibrational modes for globular proteins, we have performed absorption spectroscopy in a sub-terahertz range for Bovine Serum Albumin covalently labeled with Alexa Fluor 488. An absorption peak has been observed through two independent experiments (that we performed in Roma and Montpellier) when the protein solution was illuminated by means of an argon laser (bringing the proteins out-of-equilibrium), thus confirming the possibility to excite out-of-equilibrium collective vibrations of biomolecules.

The second campaign of experiments has been performed in order to test the validity of the Fluorescence Correlation Spectroscopy technique to detect long-range forces between molecules in solution. We resorted to built-in long-range interactions, that is electrostatic ones. Thus we have observed the diffusion of a negatively charged dye (Alexa Fluor 488) in solution in presence of different concentrations of a positively charged protein (lysozyme). For low concentrations of lysozyme, the dye diffusion is Brownian, and if the concentration of protein is increased, then the electrostatic molecular attraction becomes sufficiently strong to overcome thermal noise en thus to entail a decrease of the diffusion coefficient of the dye. This technique successfully allows to determine the critical concentration of protein needed to make the transition between Brownian diffusion of the dye and an electrostatic driven diffusion. Consequently, the critical distance between the molecules is identified.

The third part of the work has been focused on the use of Fluorescence Correlation Spectroscopy for high concentrations of fluorescent particles. Because the proteins used are covalently labeled with Alexa Fluor 488, the measurements made with proteins concentrations ranging from hundreds of nanomolar to tens of micromolar tend to blind the detector of the device. The issue has been overcome by adding optical density filters to the fluorescence optical path of the device. In a first time, numerical simulations have been run, and afterwards compared with experiments performed by using the filters. This methodology proved to be an effective one. However, the experiments suffered from another technical issue called afterpulsing, which has been fixed by replacing the autocorrelation analysis of the signal with a cross-correlation analysis, going together with the use of Fluorescence Cross-Correlation Spectroscopy.

The fourth campaign of experiments concerns the observation of the diffusion properties of proteins in solution (excited out-of-equilibrium) when their concentration is varied. The use of Bovine Serum Albumin labeled with Alexa Fluor 488 has not yet given conclusive results due to technical issues concerning protein adsorption to the cuvette walls and to the dye release by the proteins. Whereas successful results have been found by using a fluorescent protein from a light harvesting complex, the R-phycoerythrin, which similarly to the Bovine Serum Albumin is mainly made of α-helices, but has naturally attached several covalently bonded fluorochromes. The results showed a remarkable clus-

tering transition of the proteins under two conditions: when the laser power exceeds a threshold value, and when the concentration of the protein is also above some threshold value. A sharp transition between the Brownian diffusion and the clustering of the protein molecules has been recorded depending on the average distance between the proteins. This is in excellent agreement with our preceding theoretical predictions and numerical simulations.

To conclude, in this thesis work we provide the first experimental evidence of the possibility of activating long-range electrodynamic intermolecular interactions between biomolecules. We anticipate that this might open many new research lines to extend what we have here reported to other identical molecules, to interacting molecules of different kinds (ligand-receptor, DNA-protein), and to different excitation mechanisms (e.g. ATP hydrolysis), both in vitro and, hopefully, in vivo.

Appendix

3D printed parts

Some experiments have been done with the help of a 3D printer, and especially the experiment performed with the FCCS device explained on chapter 5. As visible on panel A from 1, filter supports have been specially designed for the experiment. Panel B also show the two fluorescent path of the FCCS device, the green arrow showing a mounted filter on its support, the red arrow pointing at the lens were the second support is usually placed. These supports have been made in order to rapidly change them, and add any type of filter with similar dimension.

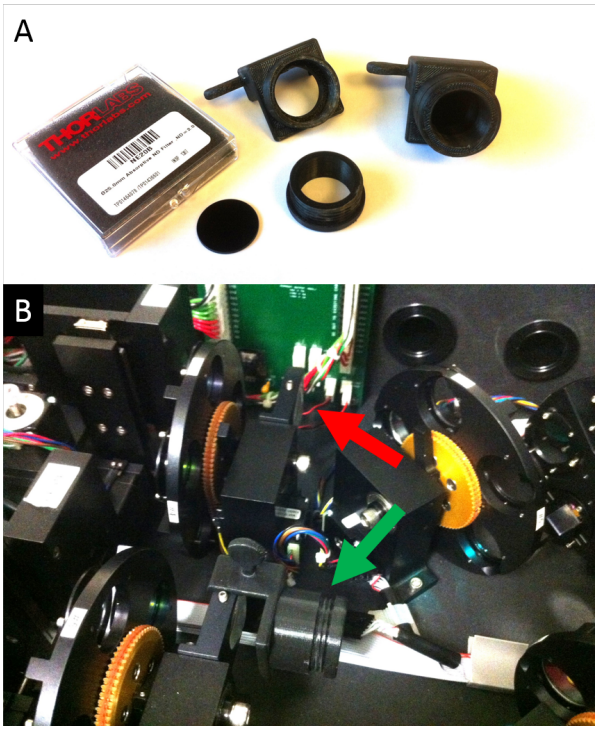

Figure 1: On panel A, filters and supports. On panel B, FCCS paths; the green arrow shows a support with a filter, the red arrow the place of the second support.

Other 3D printed pieces have been designed for example in the experiments involving THz spectroscopy in chapter 3, as cuvettes for the proteins solution. They have been designed in order to place the protein solution at the exact same place for the experiment on the THz beam. Unfortunately they have not been used long because of the porous properties of the poly-lactic acid (PLA) material used to print the pieces.

As seen in the next section, lids have been designed to fit on Lab-Tek wells, in order to add speakers, as visible on figure 3 (read explanation bellow).

Finally a lab centrifuge fidget spinner have been designed and 3D printed to help in quick spin the proteins used in the experiments, as seen on figure 2.

Figure 2: Lab centrifuge fidget spinner

Sound vibrations and Arduino board

As briefly explained in chapter 2, some research groups are working on sound vibrations effects on gene transcription. Considering their work, we have tried a quick experiment on FCS device involving labeled BSA proteins exposed to sound vibrations with a frequency sweep from 200Hz to 20kHz. On this purpose, an Arduino board has been used to control the frequency sweep. The board is connected to a small speaker, which has been placed on the labtek lid (specially designed and 3D printed), above the protein solution as seen on figure 3. This part of our researches concerning sound vibrations effect on proteins has been placed in the appendix because the experiments have been performed only during few days, and with empiric parameters. Though this aspect of protein excitation could be further studied with the help of FCS techniques in the near future.

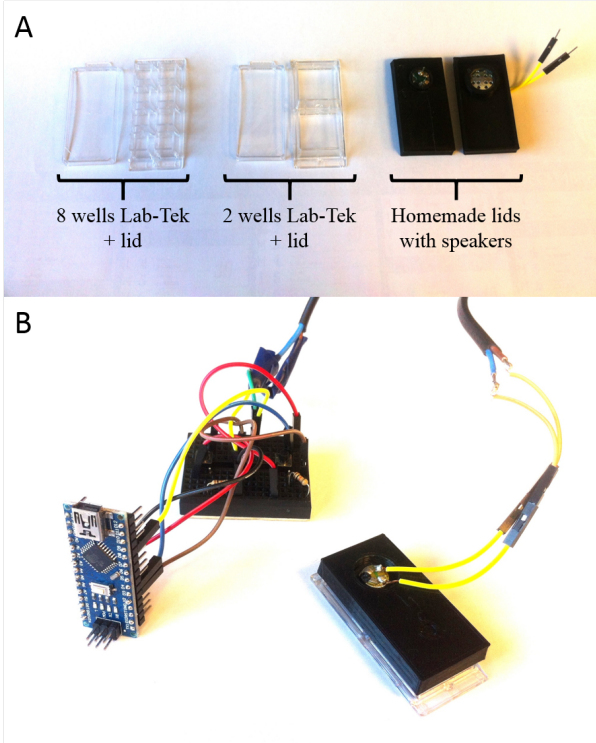

Figure 3: On panel A, different Lab-Tek wells lids. Two other lids containing a speaker have been designed to fit on the wells wells. On Panel B, an arduino board connected to a breadboard, and to the lid with the speaker.

Bibliography

[1] G. Acbas, K. A. Niessen, E. H. Snell, and A. G. Markelz. Optical measurements of long-range protein vibrations. Nature Communications, 5:3076 –, 2014.

[2] R. H. A. Aihua Xie, Alexander F. G. van der Meer. Excited-state lifetimes of far-infrared collective modes in proteins. Physical Review Letters, 88(1):018102–1 – 018102–4, 2002.

[3] T. Al-Shemmeri. Engineering Fluid Mechanics. Ventus Publishing ApS, 2012.

[4] B. Alberts, A. Johnson, J. Lewis, M. Raff, K. Roberts, and P. Walter. Molecular Biology of the Cell, 4th edition. Garland Science, 2002.

[5] M. P. Allen and D. J. Tildesley. Computer Simulation of Liquids. Oxford University Press, USA, 1989.

[6] A. Ansari, J. Berendzen, S. Bowne, H. Frauenfelder, I. Iben, T. Sauke, E. Shyamsunder, and R. Young. Protein states and proteinquakes. Proc Natl Acad Sci U S A., 82:5000–5004, 1985.

[7] Y. N. Antonenko, A. S. Lapashina, E. A. Kotova, A. A. Ramonova, M. M. Moisenovich, and I. I. Agapov. Application of peak intensity analysis to measurements of protein binding to lipid vesicles and erythrocytes using fluorescence correlation spectroscopy: Dependence on particle size. The Journal of Membrane Biology, 250(1):77–87, nov 2016.

[8] H. M. Appel and R. B. Cocroft. Plants respond to leaf vibrations caused by insect herbivore chewing. Oecologia, 175(4):1257–1266, 2014.

[9] D. Arnlund, L. C. Johansson, C. Wickstrand, A. Barty, G. J. Williams, E. Malmerberg, J. Davidsson, D. Milathianaki, D. P. DePonte, R. L. Shoeman, D. J. Wang, D. James, G. Katona, S. Westenhoff, T. A. White, A. Aquila, S. Bari, P. Berntsen, M. Bogan, T. B. van Driel, R. B. Doak, K. S. Kjaer, M. Frank, R. Fromme, I. Grotjohann, R. Henning, M. S. Hunter, R. A. Kirian, I. Kosheleva, C. Kupitz, M. N. Liang, A. V. Martin, M. M. Nielsen, M. Messerschmidt, M. M. Seibert, J. Sjohamn, F. Stellato, U. Weierstall, N. A. Zatsepin, J. C. H. Spence, P. Fromme, I. Schlichting, S. Boutet, G. Groenhof, H. N. Chapman, and R. Neutze. Visualizing a protein quake with time-resolved x-ray scattering at a free-electron laser. Nature Methods, 11(9):923–926, 2014.

[10] K. Bacia and P. Schwille. A dynamic view of cellular processes by in vivo fluorescence auto- and cross-correlation spectroscopy. Methods, 29(1):74–85, 2003.

[11] A. Bancaud, S. Huet, N. Daigle, J. Mozziconacci, J. Beaudouin, and J. Ellenberg. Molecular crowding affects diffusion and binding of nuclear proteins in heterochromatin and reveals the fractal organization of chromatin. The EMBO Journal, 28(24):3785–3798, 2009.

[12] D. S. Banks and C. Fradin. Anomalous diffusion of proteins due to molecular crowding. Biophysical Journal, 89(5):2960–2971, 2005.

[13] L. R. Barbosa, M. G. Ortore, F. Spinozzi, P. Mariani, S. Bernstorff, and R. Itri. The importance of protein-protein interactions on the ph-induced conformational changes of bovine serum albumin: A small-angle x-ray scattering study. Biophysical Journal, 98(1):147 – 157, 2010.

[14] S. I. Bastrukov. Low-frequency elastic response of a spherical particle. Physical Review E, 49:3166–3170, 1994.

[15] M. Bauer and R. Metzler. Generalized facilitated diffusion model for DNA-binding proteins with search and recognition states. Biophysical Journal, 102(10):2321–2330, may 2012.

[16] O. G. Berg and P. H. von Hippel. Diffusion-controlled macromolecular interactions. Annu Rev Biophys Biophys Chem, 14:131–60, 1985.

[17] C. Billaudeau, S. Mailfert, T. Trombik, N. Bertaux, V. Rouger, Y. Hamon, H.-T. He, and D. Marguet. Probing the plasma membrane organization in living cells by spot variation fluorescence correlation spectroscopy. In Methods in Enzymology, pages 277–302. Elsevier, 2013.

[18] K. Blinowska, W. Lech, and A. Wittlin. Cell membrane as a possible site of fröhlich's coherent oscillations. Physics Letters A, 109(3):124–126, may 1985.

[19] S. Boubanga-Tombet, F. Teppe, J. Torres, A. El Moutaouakil, D. Coquillat, N. Dyakonova, C. Consejo, P. Arcade, P. Nouvel, H. Marinchio, T. Laurent, C. Palermo, A. Penarier, T. Otsuji, L. Varani, and W. Knap. Room temperature coherent and voltage tunable terahertz emission from nanometer-sized field effect transistors. Applied Physics Letters, 97:262108, 2010.

[20] L. U. L. Brinkmann and J. S. Hub. Ultrafast anisotropic protein quake propagation after co photodissociation in myoglobin. Proceedings of the National Academy of Sciences of the United States of America, 113(38):10565–10570, 2016.

[21] K. G. Brown, S. C. Erfurth, E. W. Small, and W. L. Peticolas. Conformationally dependent low-frequency motions of proteins by laser raman spectroscopy. Proc Natl Acad Sci U S A, 69(6):1467–9, 1972.

[22] K. Burrage, I. Lenane, and G. Lythe. Numerical methods for second-order stochastic differential equations. SIAM J. Scientific Computing, 29(1):245–264, 2007.

[23] J. W. Bye, S. Meliga, D. Ferachou, G. Cinque, J. A. Zeitler, and R. J. Falconer. Analysis of the hydration water around bovine serum albumin using terahertz coherent synchrotron radiation. Journal of Physical Chemistry A, 118(1):83–88, 2014.

[24] R. E. Canfield. The amino acid sequence of egg white lysozyme. J Biol Chem, 238:2698–707, 1963.

[25] H. Casimir and D. Polder. The influence of retardation on the london-van der waals forces. Physical Review, 73(4):360, 1948.

[26] I. Casuso, P. Sens, F. Rico, and S. Scheuring. Experimental evidence for membrane-mediated protein-protein interaction. Biophys J, 99(7):L47–9, 2010.

[27] W. R. Chang, T. Jiang, Z. L. Wan, J. P. Zhang, Z. X. Yang, and D. C. Liang. Crystal structure of r-phycoerythrin from polysiphonia urceolata at 2.8 a resolution. J Mol Biol, 262(5):721–31, 1996.

[28] A. Chaudhuri, B. Bhattacharya, K. Gowrishankar, S. Mayor, and M. Rao. Spatiotemporal regulation of chemical reactions by active cytoskeletal remodeling. Proceedings of the National Academy of Sciences, 108(36):14825–14830, 2011.

[29] H. Chen, S. S. Ahsan, M. B. Santiago-Berrios, H. D. Abruna, and W. W. Webb. Mechanisms of quenching of alexa fluorophores by natural amino acids. Journal of the American Chemical Society, 132(21):7244–7245, jun 2010.

[30] H. Chen, E. Rhoades, J. S. Butler, S. N. Loh, and W. W. Webb. Dynamics of equilibrium structural fluctuations of apomyoglobin measured by fluorescence correlation spectroscopy. Proceedings of the National Academy of Sciences, 104(25):10459–10464, jun 2007.

[31] A. G. Cherstvy, A. B. Kolomeisky, and A. A. Kornyshev. Protein-dna interactions: Reaching and recognizing the targets. Journal of Physical Chemistry B, 112(15):4741–4750, 2008.

[32] K. Chou. Low-frequency motions in protein molecules. beta-sheet and beta-barrel. Biophysical Journal, 48(2):289–297, August 1985.

[33] K. C. Chou. Low-frequency vibrations of dna molecules. Biochem J, 221(1):27–31, 1984.

[34] G. Cilento and W. Adam. From free radicals to electronically excited species. Free Radic Biol Med, 19(1):103–14, 1995.

[35] R. M. Clegg. Chapter 1 forster resonance energy transfer (fret) what is it, why do it, and how it's done. In Fret and Flim Techniques, pages 1–57. Elsevier, 2009.

[36] J. R. de Xammar Oro, G. Ruderman, and J. R. Grigera. [electrodynamics of interactions in electrolyte solutions and their biological significance]. Biofizika, 53(3):397–401, 2008.

[37] P. Debye. Reaction rates in ionic solutions. 82:265–272, 1942.

[38] P. J. W. Debye. Molekularkräfte und ihre elektrische deutung. Hirzel, 1921.

[39] A. Di Gaspare, R. Casini, V. Foglietti, V. Giliberti, E. Giovine, and M. Ortolani. Terahertz current oscillations in a gated two-dimensional electron gas with antenna integrated at the channel ends. Applied Physics Letters, 100:203504, 2012.

[40] M. Dyakonov and M. Shur. Shallow water analogy for a ballistic field effect transistor: New mechanism of plasma wave generation by dc current. Physical Review Letters, 71(15):2465–2468, Oct 1993.

[41] S. Ebbinghaus, S. J. Kim, M. Heyden, X. Yu, M. Gruebele, D. M. Leitner, and M. Havenith. An extended dynamical hydration shell around proteins. Proc. Natl. Acad. Sci. USA, 104:20749–20752, 2007.

[42] S. Ebbinghaus, S. J. Kim, M. Heyden, X. Yu, M. Gruebele, D. M. Leitner, and M. Havenith. Protein sequence- and ph-dependent hydration probed by terahertz spectroscopy. Journal of the American Chemical Society, 130:2374–2375, 2008.

[43] A. Einstein. Über die von der molekularkinetischen Theorie der Wärme gefordert Bewegung von in ruhenden Flüßigkeiten suspendierten Teilchen. (German) [On the molecular-kinetic theory of the movement by heat of particles suspended in liquids at rest]. 322(8):549–560, 1905.

[44] R. Eisenschitz and F. London. Über das verhältnis der van der waalsschen kräfte zu den homöopolaren bindungskräften. Zeitschrift für Physik, 60(7-8):491–527, 1930.

[45] R. Ellis. Macromolecular crowding: obvious but underappreciated. Trends in Biochemical Sciences, 26(10):597–604, oct 2001.

[46] W. J. Ellison. Permittivity of pure water, at standard atmospheric pressure, over the frequency range 0-25 thz and the temperature range 0-100 degrees c. Journal of Physical and Chemical Reference Data, 36(1):1–18, 2007.

[47] E. L. Elson. Fluorescence correlation spectroscopy: past, present, future. Biophys J, 101(12):2855–70, 2011.

[48] R. Falconer and A. Markelz. Terahertz spectroscopic analysis of peptides and proteins. J Infrared Milli Terahz Waves, 33:973–988, 2012.

[49] B. M. Fischer, M. Walther, and P. Uhd Jepsen. Far-infrared vibrational modes of dna components studied by terahertz time-domain spectroscopy. Phys. Med. Biol., 47(21):3807–3814, Nov 2002.

[50] Y. H. Foo, N. Naredi-Rainer, D. C. Lamb, S. Ahmed, and T. Wohland. Factors affecting the quantification of biomolecular interactions by fluorescence cross-correlation spectroscopy. Biophys J, 102(5):1174–83, 2012.

[51] R. FOORD, E. JAKEMAN, C. J. OLIVER, E. R. PIKE, R. J. BLAGROVE, E. WOOD, and A. R. PEACOCKE. Determination of diffusion coefficients of haemocyanin at low concentration by intensity fluctuation spectroscopy of scattered laser light. Nature, 227(5255):242–245, jul 1970.

[52] H. Fröhlich. Long-range coherence and energy storage in biological systems. International Journal of Quantum Chemistry, 2(5):641–649, 1968.

[53] H. Fröhlich. Long range coherence and the action of enzymes. Nature, 228:1093–1093, 1970.

[54] H. Fröhlich. Selective long range dispersion forces between large systems. Physics Letters A, 39(2):153–154, apr 1972.

[55] H. Fröhlich. The extraordinary dielectric properties of biological materials and the action of enzymes. Proc. Nat. Acad. Sci. USA, 72(11):4211–4215, 1975.

[56] H. Fröhlich. Long-range coherence in biological systems. Rivista Nuovo Cimento, 7:399–418, 1977.

[57] H. Fröhlich. The biological effects of microwaves and related questions. Advances in electronics and electron physics, 53:85–152, 1980.

[58] H. Fröhlich. Further evidence for coherent excitations in biological systems. Physics Letters A, 110(9):480–481, aug 1985.

[59] M. Gagliano, M. Grimonprez, M. Depczynski, and M. Renton. Tuned in: plant roots use sound to locate water. Oecologia, 184(1):151–160, 2017.

[60] C. Gardiner. Stochastic Methods: A Handbook for the Natural and Social Sciences. Springer, 2009.

[61] W. M. Gelbart, R. F. Bruinsma, P. A. Pincus, and V. A. Parsegian. DNA-inspired electrostatics. Physics Today, 53(9):38–44, sep 2000.

[62] L. Genzel, F. Keilmann, T. P. Martin, G. Winterling, Y. Yacoby, H. Fröhlich, and M. W. Makinen. Low-frequency raman spectra of lysozyme. Biopolymers, 15(1):219–225, Jan 1976.

[63] R. Ghosh, M. A. Gururani, L. N. Ponpandian, R. C. Mishra, S. C. Park, M. J. Jeong, and H. Bae. Expression analysis of sound vibration-regulated genes by touch treatment in arabidopsis. Frontiers in Plant Science, 8, 2017.

[64] R. Ghosh, R. C. Mishra, B. Choi, Y. S. Kwon, D. W. Bae, S. C. Park, M. J. Jeong, and H. Bae. Exposure to sound vibrations lead to transcriptomic, proteomic and hormonal changes in arabidopsis (vol 6, 33370, 2016). Scientific Reports, 6, 2016.

[65] V. Giliberti, A. Di Gaspare, E. Giovine, M. Ortolani, L. Sorba, G. Biasiol, V. Popov, D. Fateev, and F. Evangelisti. Downconversion of terahertz radiation due to intrinsic hydrodynamic nonlinearity of a two-dimensional electron plasma. Physical Review B, 91:165313 – 165319, 2015.

[66] T. Globus, D. Woolard, T. W. Crowe, T. Khromova, B. Gelmont, and J. Hesler. Terahertz fourier transform characterization of biological materials in a liquid phase. Journal of Physics D: Applied Physics, 39(15):3405, 2006.

[67] I. Gregor, D. Patra, and J. Enderlein. Optical saturation in fluorescence correlation spectroscopy under continuous-wave and pulsed excitation. Chemphyschem, 6(1):164–70, 2005.

[68] W. Grundler and F. Keilmann. Sharp resonances in yeast growth prove nonthermal sensitivity to microwaves. Physical Review Letters, 51(13):1214–1216, sep 1983.

[69] W. Grundler, F. Keilmann, and H. Fröhlich. Resonant growth rate response of yeast cells irradiated by weak microwaves. Physics Letters A, 62(6):463–466, sep 1977.

[70] H. Hamaker. The londonvan der waals attraction between spherical particles. physica, 4(10):1058–1072, 1937.

[71] E. Haustein and P. Schwille. Fluorescence correlation spectroscopy: novel variations of an established technique. Annu Rev Biophys Biomol Struct, 36:151–69, 2007.

[72] S. T. Hess, S. Huang, A. A. Heikal, and W. W. Webb. Biological and chemical applications of fluorescence correlation spectroscopy: a review. Biochemistry, 41(3):697–705, 2002.

[73] M. Heyden, D. J. Tobias, and D. V. Matyushov. Terahertz absorption of dilute aqueous solutions. J Chem Phys, 137(23):235103, 2012.

[74] M. Hirsch, S. Smale, and R. Devaney. Differential Equations, Dynamical Systems, and an Introduction to Chaos. Number v. 60. Academic Press, 2004.

[75] E. F. Y. Hom and A. S. Verkman. Analysis of coupled bimolecular reaction kinetics and diffusion bytwo-color fluorescence correlation spectroscopy: Enhanced resolution of kinetics by resonance energy transfer. Biophysical Journal, 83(1):533–546.

[76] M. W. Hosseini, J. M. Lehn, K. C. Jones, K. E. Plute, K. B. Mertes, and M. P. Mertes. Supramolecular catalysis - polyammonium macrocycles as enzyme mimics for phosphoryl transfer in atp hydrolysis. Journal of the American Chemical Society, 111(16):6330–6335, 1989.

[77] G. J. Hyland. Herbert frohlich, frs (1905-1991) - a physicist ahead of his time. Electromagnetic Biology and Medicine, 24(3):161–182, 2005.

[78] K. Itoh and T. Shimanouchi. Vibrational frequencies and modes of α-helix. Biopolymers, 9(4):383–399, 1970.

[79] H. Jehle. INTERMOLECULAR FORCES AND BIOLOGICAL SPECIFICITY. Proceedings of the National Academy of Sciences, 50(3):516–524, sep 1963.

[80] J. Q. Jia, H. L. Ma, W. R. Zhao, Z. B. Wang, W. M. Tian, L. Luo, and R. H. He. The use of ultrasound for enzymatic preparation of ace-inhibitory peptides from wheat germ protein. Food Chemistry, 119(1):336–342, 2010.

[81] P. Jolls. Lysozymes: A chapter of molecular biology. Angewandte Chemie International Edition in English, 8(4):227–239, 1969.

[82] S. Jones and J. M. Thornton. Principles of protein-protein interactions. Proc Natl Acad Sci U S A, 93(1):13–20, 1996. Jones, S Thornton, J M eng Research Support, Non-U.S. Gov't Review 1996/01/09 Proc Natl Acad Sci U S A. 1996 Jan 9;93(1):13-20.

[83] P. Jordan. Phys. Z., 39(711), 1938.

[84] P. Jordan. Phys. Z., 113(431), 1939.

[85] F. Keilmann. Fir microscopy. Infrared Phys. Techno., 36:217–224, 1995.

[86] S. Khatua and et al. Enhanced-fluorescence correlation spectroscopy at micro-molar dye concentration around a single gold nanorod. Physical Chemistry Chemical Physics, 17(33):21127–21132, 2015.

[87] A. A. Kinkhabwala and et al. Fluorescence correlation spectroscopy at high concentrations using gold bowtie nanoantennas. Chemical Physics, 406:3, 2012.

[88] J. Knab, J.-Y. Chen, Y. He, and A. Markelz. Terahertz measurements of protein relaxational dynamics. Proceedings of the IEEE, 95(8):1605 – 1610, 2007.

[89] W. Knap, V. Kachorovskii, Y. Deng, S. Rumyantsev, J.-Q. Lü, R. Gaska, M. S. Shur, G. Simin, X. Hu, M. A. Khan, C. A. Saylor, and L. C. Brunel. Nonresonant detection of terahertz radiation in field effect transistors. Journal of Applied Physics, 91(11):9346–9353, 2002.

[90] G. R. Kneller. Quasielastic neutron scattering and relaxation processes in proteins: analytical and simulation-based models. Phys . Chem. Chem. Phys., 7:2641 – 2655, 2005.

[91] F. Koch, R. Fenouil, M. Gut, P. Cauchy, T. K. Albert, J. Zacarias-Cabeza, S. Spicuglia, A. L. de la Chapelle, M. Heidemann, C. Hintermair, D. Eick, I. Gut, P. Ferrier, and J.-C. Andrau. Transcription initiation platforms and gtf recruitment at tissue-specific enhancers and promoters. Nat Struct Mol Biol, 18(8):956–963, 2011.

[92] A. Kyaw, U. K. Maung, and T. Toe. Determination of inorganic phosphate with molybdate and triton x-100 without reduction. Anal Biochem, 145(2):230–4, 1985.

[93] J. R. Lakowicz. *Principles* of Fluorescence Spectroscopy. Springer-Verlag, 2006.

[94] K. A. Lamia, U. M. Sachdeva, L. DiTacchio, E. C. Williams, J. G. Alvarez, D. F. Egan, D. S. Vasquez, H. Juguilon, S. Panda, R. J. Shaw, C. B. Thompson, and R. M. Evans. Ampk regulates the circadian clock by cryptochrome phosphorylation and degradation. Science, 326(5951):437–40, 2009.

[95] T. A. Laurence and et al. Fluorescence correlation spectroscopy at micromolar concentrations without optical nanoconfinement. Journal of Physical Chemistry B, 118(32):9662–9667, 2014.

[96] M. Levantino, G. Schiro, H. Lemke, G. Cottone, J. Glownia, D. Zhu, M. Chollet, H. Ihee, A. Cupane, and M. Cammarata. Ultrafast myoglobin structural dynamics observed with an x-ray free-electron laser. Nature Communications, 6:6772 EP –, 2015.

[97] V. R. Lili Wang, Adolfas K. Gaigalas. Optical properties of alexa^{TM} 488 and cy^{TM}5 immobilized on a glass surface. Microarray Technologies, 38(1):127, 2005.

[98] L.-N. Liu, H.-N. Su, S.-G. Yan, S.-M. Shao, B.-B. Xie, X.-L. Chen, X.-Y. Zhang, B.-C. Zhou, and Y.-Z. Zhang. Probing the pH sensitivity of r-phycoerythrin: Investigations of active conformational and functional variation. Biochimica et Biophysica Acta (BBA) - Bioenergetics, 1787(7):939–946, jul 2009.

[99] F. London. The general theory of molecular forces. Trans. Faraday Soc., 33:8b–26, 1937.

[100] I. Lundholm, H. Rodilla, W. Wahlgren, A. Duelli, G. Bourenkov, J. Vukusic, R. Friedman, J. Stake, T. Schneider, and G. Katona. Terahertz radiation induces non-thermal structural changes associated with fröhlich condensation in a protein crystal. Structural Dynamics, 2:054702(12), 2015.

[101] D. Magde, E. L. Elson, and W. W. Webb. Fluorescence correlation spectroscopy. ii. an experimental realization. Biopolymers, 13(1):29–61, 1974.

[102] D. Magde and et al. Thermodynamic fluctuations in a reacting system - measurement by fluorescence correlation spectroscopy. Physical Review Letters, 29(11):705–708, 1972.

[103] S. Maiti, U. Haupts, and W. W. Webb. Fluorescence correlation spectroscopy: Diagnostics for sparsemolecules. Proceedings of the National Academy of Sciences, 94(22):11753–11757, 1997.

[104] G. S. Manning. Counterion condensation theory constructed from different models. Physica A: Statistical Mechanics and its Applications, 231(1-3):236–253, sep 1996.

[105] A. Markelz, A. Roitberg, and E. Heilweil. Pulsed terahertz spectroscopy of DNA, bovine serum albumin and collagen between 0.1 and 2.0 THz. Chemical Physics Letters, 320(1-2):42–48, mar 2000.

[106] A. Markelz, S. Whitmire, J. Hillebrecht, and R. Birge. Thz time domain spectroscopy of biomolecular conformational modes. phys. Med. Biol, pages 3797–3805, 2002.

[107] P. E. Marszalek and Y. F. Dufrene. Stretching single polysaccharides and proteins using atomic force microscopy. Chemical Society Reviews, 41(9):3523–3534, 2012.

[108] J. MARTÍNEZ-OYANEDEL, C. CONTRERAS-MARTEL, C. BRUNA, and M. BUNSTER. Structural-functional analysis of the oligomeric protein r-phycoerythrin. Biological Research, 37(4), 2004.

[109] A. D. McLACHLAN and M. A. BALL. Time-dependent hartreefock theory for molecules. Reviews of Modern Physics, 36(3):844855, Jul 1964.

[110] A. M. Melo, M. Prieto, and A. Coutinho. Quantifying lipid-protein interaction by fluorescence correlation spectroscopy (FCS). In Methods in Molecular Biology, pages 575–595. Humana Press, aug 2013.

[111] R. Milo. What is the total number of protein molecules per cell volume? a call to rethink some published values. Bioessays, 35(12):1050–1055, 2013.

[112] B. Mugnier, B. Nal, C. Verthuy, C. Boyer, D. Lam, L. Chasson, V. Nieoullon, G. Chazal, X. J. Guo, H. T. He, D. Rueff-Juy, A. Alcover, and P. Ferrier. Coronin-1a links cytoskeleton dynamics to tcr alpha beta-induced cell signaling. PLoS One, 3(10):e3467, 2008.

[113] C. B. Muller, A. Loman, V. Pacheco, F. Koberling, D. Willbold, W. Richtering, and J. Enderlein. Precise measurement of diffusion by multi-color dual-focus fluorescence correlation spectroscopy. Epl, 83(4), 2008. 345VP Times Cited:77 Cited References Count:23.

[114] E. Mylonas and D. I. Svergun. Accuracy of molecular mass determination of proteins in solution by small-angle X-ray scattering. Journal of Applied Crystallography, 40(s1):s245–s249, 2007.

[115] I. Nardecchia. Détection expérimentale de recrutements longues portées entre biomolécules dues á une force sélective et résonante : tude de faisabilité. 2012.

[116] I. Nardecchia, M. Lechelon, M. Gori, I. Donato, J. Preto, E. Floriani, S. Jaeger, S. Mailfert, D. Marguet, P. Ferrier, and M. Pettini. Detection of long-range electrostatic interactions between charged molecules by means of fluorescence correlation spectroscopy. Physical Review E, 96(2), 2017.

[117] I. Nardecchia, L. Spinelli, J. Preto, M. Gori, E. Floriani, S. Jaeger, P. Ferrier, and M. Pettini. Experimental detection of long-distance interactions between biomolecules through their diffusion behavior: Numerical study. Physical Review E, 90:022703 – 022717, 2014.

[118] I. Nardecchia, J. Torres, M. Lechelon, V. Giliberti, M. Ortolani, P. Nouvel, M. Gori, I. Donato, J. Preto, L. Varani, J. Sturgis, and M. Pettini. Out-of-equilibrium collective oscillation as phonon condensation in a model protein, 2017.

[119] P. Nouvel, H. Marinchio, J. Torres, C. Palermo, D. Gasquet, L. Chusseau, L. Varani, P. Shiktorov, E. Starikov, and V. Gružinskis. Terahertz spectroscopy of plasma waves in high electron mobility transistors. Journal of Applied Physics, 106(1):013717, 2009.

[120] R. Noyes. 1:129, 1961.

[121] H. Ogawa, H. Mizuno, T. Saito, Y. Yamada, T. Oohusa, and N. Iso. Effects of pH on the conformation of phycoerythrin from nori porphyra sp. NIPPON SUISAN GAKKAISHI, 57(5):899–903, 1991.

[122] J. R. D. Oro, G. Ruderman, J. R. Grigera, and F. Vericat. Threshold frequency for the ionic screening of electric-fields in electrolyte-solutions. Journal of the Chemical Society-Faraday Transactions, 88(5):699–703, 1992.

[123] J. R. D. Oro, G. Ruderman, J. R. Grigera, and F. Vericat. Threshold frequency for the ionic screening of electric-fields in electrolyte-solutions. Journal of the Chemical Society-Faraday Transactions, 88(5):699–703, 1992.

[124] P. Painter, L. Mosher, and C. Rhoads. Low-frequency modes in the raman spectrum of dna. Biopolymers, 20:243–247, 1981.

[125] P. Painter, L. Mosher, and C. Rhoads. Low-frequency modes in the raman spectra of proteins. Biopolymers, 21(7):1469–1472, July 1982.

[126] P. Painter, L. Mosher, and C. Rhoads. Low-frequency modes in the raman spectra of proteins. Biopolymers, 21:1469–1472, 1982.

[127] R. Paul, R. Chatterjee, J. Tuszyski, and O. Fritz. Theory of long-range coherence in biological systems. i. the anomalous behaviour of human erythrocytes. Journal of Theoretical Biology, 104(2):169 – 185, 1983.

[128] L. Pauling. Molecular basis of biological specificity. Nature, 248(5451):769–771, apr 1974.

[129] L. PAULING and M. DELBRUCK. THE NATURE OF THE INTER-MOLECULAR FORCES OPERATIVE IN BIOLOGICAL PROCESSES. Science, 92(2378):77–79, jul 1940.

[130] I. Perevoshchikova, D. Zorov, and Y. Antonenko. Peak intensity analysis as a method for estimation of fluorescent probe binding to artificial and natural nanoparticles: Tetramethylrhodamine uptake by isolated mitochondria. Biochimica et Biophysica Acta (BBA) - Biomembranes, 1778(10):2182–2190, oct 2008.

[131] J. Perrin. L'agitation moléculaire et le mouvement brownien. pages 967 – 970, 1908.

[132] J. Perrin and F. Soddy. Brownian movement and molecular reality. Dover Books on Physics. Dover, Mineola, NY, 2005.

[133] S. Perticaroli, J. D. Nickels, G. Ehlers, H. O'Neill, Q. Zhang, and A. P. Sokolov. Secondary structure and rigidity in model proteins. Soft Matter, 9:9548–9556, 2013.

[134] Z. Petrasek and P. Schwille. Precise measurement of diffusion coefficients using scanning fluorescence correlation spectroscopy. Biophys J, 94(4):1437–48, 2008. Petrasek, Zdenek Schwille, Petra eng Research Support, Non-U.S. Gov't 2007/10/16 09:00 Biophys J. 2008 Feb 15;94(4):1437-48. Epub 2007 Oct 12.

[135] E. P. Petrov and P. Schwille. State of the art and novel trends in fluorescence correlation spectroscopy. In Springer Series on Fluorescence, pages 145–197. Springer Berlin Heidelberg.

[136] V. Pingoud, W. Wende, P. Friedhoff, M. Reuter, J. Alves, A. Jeltsch, L. Mones, M. Fuxreiter, and A. Pingoud. On the divalent metal ion dependence of dna cleavage by restriction endonucleases of the ecori family. Journal of Molecular Biology, 393(1):140160, Oct 2009.

[137] J. Pokorny and T. Wu. Biophysical aspects of coherence and biological order. 2013.

[138] F. A. Popp. Properties of biophotons and their theoretical implications. Indian J Exp Biol, 41(5):391–402, 2003.

[139] J. W. Powell, G. S. Edwards, L. Genzel, F. Kremer, A. Wittlin, W. Kubasek, and W. Peticolas. Investigation of far-infrared vibrational modes in polynucleotides. Physical Review A, 35(9):39293939, May 1987.

[140] J. Preto, E. Floriani, I. Nardecchia, P. Ferrier, and M. Pettini. Experimental assessment of the contribution of electrodynamic interactions to long-distance recruitment of biomolecular partners: Theoretical basis. Physical Review E, 85(4), 2012.

[141] J. Preto and M. Pettini. Resonant long-range interactions between polar macromolecules. Phys.Lett. A, 377(8):587 – 591, 2013.

[142] J. Preto, M. Pettini, and J. Tuszynski. On the role of electrodynamic interactions in long-distance biomolecular recognition @ONLINE, Mar. 2014.

[143] J. Preto, M. Pettini, and J. A. Tuszynski. Possible role of electrodynamic interactions in long-distance biomolecular recognition. Physical Review E, 91:052710 – 052728, 2015.

[144] J. R. Reimers, L. K. McKemmish, R. H. McKenzie, A. E. Mark, and N. S. Hush. Weak, strong, and coherent regimes of frohlich condensation and their applications to terahertz medicine and quantum consciousness. Proc Natl Acad Sci U S A, 106(11):4219–24, 2009.

[145] M. Rief, F. Oesterhelt, B. Heymann, and H. E. Gaub. Single molecule force spectroscopy on polysaccharides by atomic force microscopy. Science, 275(5304):1295–7, 1997.

[146] R. Rigler and E. S. Elson. Fluorescence Correlation Spectroscopy. Springer Berlin Heidelberg, 2001.

[147] S. Rowlands. Coherent excitations in blood. In Proceedings in Life Sciences, pages 145–161. Springer Berlin Heidelberg, 1983.

[148] S. Rowlands, L. Sewchand, R. Lovlin, J. Beck, and E. Enns. A fröhlich interaction of human erythrocytes. Physics Letters A, 82:436–438, 1981.

[149] S. Rowlands, L. S. Sewchand, and E. G. Enns. A quantum mechanical interaction of human erythrocytes. Canadian Journal of Physiology and Pharmacology, 60(1):5259, Jan 1982.

[150] B. Sahoo, K. W. Drombosky, and R. Wetzel. Fluorescence correlation spectroscopy: A tool to study protein oligomerization and aggregation in vitro and in vivo. In Methods in Molecular Biology, pages 67–87. Springer New York, 2016.

[151] K. Selmeczi, M. Giorgi, G. Speier, E. Farkas, and M. Reglier. Mono-versus binuclear copper(ii) complexes in phosphodiester hydrolysis. European Journal of Inorganic Chemistry, (5):1022–1031, 2006.

[152] V. Seshadri and K. Lindenberg. Extrema statistics of wiener-einstein processes in one, two, and three dimensions. 22:69, 1980.

[153] A. Smekal. Zur quantentheorie der dispersion. Die Naturwissenschaften, 11(43):873–875, oct 1923.

[154] J.-H. Son, editor. Terahertz Biomedical Science and Technology. CRC Press, jun 2014.

[155] I. N. Stadnichuk, M. F. Yanyushin, E. G. Maksimov, E. P. Lukashev, S. K. Zharmukhamedov, I. V. Elanskaya, and V. Z. Paschenko. Site of non-photochemical quenching of the phycobilisome by orange carotenoid protein in the cyanobacterium synechocystis sp. PCC 6803. Biochimica et Biophysica Acta (BBA) - Bioenergetics, 1817(8):1436–1445, aug 2012.

[156] M. J. Stephen. Firstorder dispersion forces. The Journal of Chemical Physics, 40(3):669673, Feb 1964.

[157] M. Stroppolo, M. Falconi, A. Caccuri, and A. Desideri. Superefficient enzymes. Cellular and Molecular Life Sciences CMLS, 58(10):1451–1460, 2001.

[158] K. Suhre and Y. Sanejouand. Elnemo: a normal mode web-server for protein movement analysis and the generation of templates for molecular replacement. Nucleic Acids Research, 32:W610–W614, 2004.

[159] J. Sun, G. Niehues, H. Forbert, D. Decka, G. Schwaab, D. Marx, and M. Havenith. Understanding thz spectra of aqueous solutions: glycine in light and heavy water. J Am Chem Soc, 136(13):5031–8, 2014.

[160] O. Sushko, R. Dubrovka, and R. Donnana. Sub-terahertz spectroscopy reveals that proteins influence the properties of water at greater distances than previously detected. The Journal of Chemical Physics, 142:055101(9), 2015.

[161] J. SzöllÖsi and D. R. Alexander. The application of fluorescence resonance energy transfer to the investigation of phosphatases. In Methods in Enzymology, pages 203–224. Elsevier, 2003.

[162] D. Tischer and O. D. Weiner. Illuminating cell signalling with optogenetic tools. Nat Rev Mol Cell Biol, 15(8):551–8, 2014.

[163] D. Turton, H. Senn, T. Harwood, A. Lapthorn, E. Ellis, and K. Wynne. Terahertz underdamped vibrational motion governs protein-ligand binding in solution. Nature Communications, 5:3999, 2014.

[164] H. Urabe, H. Hayashi, Y. Tominaga, Y. Nishimura, K. Kubota, and M. Tsuboi. Collective vibrational modes in molecular assembly of DNA and its application to biological systems. low frequency raman spectroscopy. The Journal of Chemical Physics, 82(1):531–535, jan 1985.

[165] H. Urabe and Y. Tominaga. Low-lying collective modes of DNA double helix by raman spectroscopy. Biopolymers, 21(12):2477–2481, dec 1982.

[166] V. Ushakov, E. Alipov, V. Shcheglov, and I. Belyaev. Nonthermal effects of extremely high-frequency microwaves on chromatin conformation in cells in vivo-dependence on physical, physiological, and genetic factors. IEEE Transactions on Microwave Theory and Techniques, 48(11):2172–2179, 2000.

[167] S. Vaidya, A. Orta-Ramirez, D. M. Smith, and R. Y. Ofoli. Effect of heat on phycoerythrin fluorescence: Influence of thermal exposure on the fluorescence emission of r-phycoerythrin. Biotechnology and Bioengineering, 83(4):465–473, jun 2003.

[168] M. von Smoluchowski. Zur kinetischen theorie der brownschen molekularbewegung und der suspensionen. Annalen der Physik, 326(14):756–780, 1906.

[169] T. A. Waigh. Microrheology of complex fluids. Reports on Progress in Physics, 68:685 – 742, 2005.

[170] H. Wang, X. Zheng, F. Zhao, Z. Gao, Z. Yu, J. Zhu, L. Jiang, J. Zhang, and D. Liang. Time-resolved excitation density dependent fluorescence of r-phycoerythrin single crystal. Chemical Physics Letters, 222(3):204–208, may 1994.

[171] L. Wawrezinieck, H. Rigneault, D. Marguet, and P. F. Lenne. Fluorescence correlation spectroscopy diffusion laws to probe the submicron cell membrane organization. Biophys J, 89(6):4029–42, 2005.

[172] S. Webb, M. Stoneham, and H. Fröhlich. Evidence for non-thermal excitation of energy levels in active biological systems. Physics Letters A, 63(3):407–408, nov 1977.

[173] H. Weingärtner. An introduction to aqueous electrolyte solutions . by margaret robson wright. ChemPhysChem, 9(10):1482–1482, jul 2008.

[174] L. R. Wetter and H. F. Deutsch. Immunological studies on egg white proteins. iv. immunochemical and physical studies of lysozyme. J Biol Chem, 192(1):237–42, 1951.

[175] J. Widengren, U. Mets, and R. Rigler. Fluorescence correlation spectroscopy of triplet states in solution: a theoretical and experimental study. The Journal of Physical Chemistry, 99(36):13368–13379, sep 1995.

[176] D. K. Wilkins, S. B. Grimshaw, V. Receveur, C. M. Dobson, J. A. Jones, and L. J. Smith. Hydrodynamic radii of native and denatured proteins measured by pulse field gradient NMR techniques†. Biochemistry, 38(50):16424–16431, dec 1999.

[177] T. Wu and S. Austin. Bose condensation in biosystems. Physics Letters A, 64(1):151 – 152, 1977.

[178] X. Wu and B. R. Brooks. Isotropic periodic sum: A method for the calculation of long-range interactions. The Journal of Chemical Physics, 122(4):044107, jan 2005.

[179] X. Wu and B. R. Brooks. Isotropic periodic sum of electrostatic interactions for polar systems. The Journal of Chemical Physics, 131(2):024107, jul 2009.

[180] Y. H. Wu, H. B. Chen, G. D. Lin, X. S. Yu, H. T. Zhang, H. L. Wan, and K. R. Tsai. Cluster-complex mediated electron-transfer and atp hydrolysis. Pure and Applied Chemistry, 60(8):1291–1298, 1988.

[181] J. Xu, K. W. Plaxco, and S. J. Allen. Probing the collective vibrational dynamics of a protein in liquid water by terahertz absorption spectroscopy. Protein Science, 15:1175–1181, 2006.

[182] M. Zhao, L. Jin, B. Chen, Y. Ding, H. Ma, and D. Chen. Afterpulsing and its correction in fluorescence correlation spectroscopy experiments. Appl Opt, 42(19):4031–6, 2003.

Résumé

Le fonctionnement dynamique des organismes à l'échelle moléculaire est encore à ce jour incompris. De très grandes avancées scientifiques ont permis de décrire en détail les voies de signalisation cellulaire et les interactions à courte distance entre les biomolécules impliquées dans ces voies de signalisation, cependant le phénomène permettant une telle précision et rapidité d'interaction à la fois spatiale et temporelle entre ces biomolécules reste en bonne partie à déceler. Nos recherches se basent sur une succession de propositions concernant des interactions électrodynamiques à longue distance (notamment proposées par Herbert Fröhlich dans les années 1970). D'après de récents résultats basés sur les premiers principes de l'électromagnétisme, il est possible de déduire l'existence d'interactions électrodynamiques entre des biomolécules - dues aux vibrations de leur dipôle électrique agissant avec un potentiel proportionnel à $1/r^3$ en résonance, et $1/r^6$ hors résonance. Pour que ces dipôles entrent en résonance, un apport d'énergie est nécessaire afin que le système soit hors équilibre. Nous avons donc dans un premier temps utilisé une protéine globulaire connue (l'Albumine de Serum Bovin ou BSA) marquée de manière covalente avec un fluorochrome (Alexa Fluor 488) pour permettre un transfert d'énergie à partir de la lumière absorbée. L'utilisation de dispositifs de spectroscopie terahertz basés sur des détecteurs à champs proche a permis de confirmer l'apparition de pics d'absorption vers des fréquences proches de 314 GHz, une fois les protéines de l'échantillon mises hors équilibre thermique. Ces premiers résultats sont en accord avec la théorie et semblent donc confirmer la possibilité d'activer des vibrations collectives de protéines hors équilibre. Des expérimentations ont aussi été réalisées pour étudier la dynamique des protéines dans des conditions similaires. Premièrement, une étude expérimentale a été réalisée dans le but de déterminer si l'utilisation d'un appareil de Spectroscopie à Corrélation de Fluorescence (ou FCS) serait adapté pour mesurer la diffusion de particules soumises à des forces longue distance, ici électrostatiques. Après validation de la technique, et compte tenu des concentrations trop importantes de protéines fluorescentes dans les échantillons, nous avons testé et rapporté l'utilisation de filtres de densité optique (filtres OD) pour des appareils de FCS et FCCS (Spectroscopie à Cross-Corrélation de Fluorescence). Les mesures ont pu être réalisées avec succès en FCCS, mais des problèmes techniques mettant en cause l'adsorption de la protéine aux puits, et la présence de fluorochromes libres en solution ne nous ont pas permis de conclure de manière satisfaisante quant à la diffusion de la BSA. Pour pallier à ces problèmes nous avons utilisé pour ces mêmes expérimentations en FCCS avec filtres OD, une protéine ayant un rôle important dans la photosynthèse en tant que pigment assimilateur absorbant la lumière verte et bleue, la R-phycoerythrine. Les résultats ont alors montré l'apparition d'agrégats de protéines qui se forment à partir d'une certaine concentration de protéines, seulement lorsqu'un seuil d'excitation laser est dépassé, la diffusion Brownienne des protéines libres étant maintenue sous ce seuil. La formation de ces agrégats se comporte comme estimé par des simulations obtenues quelques années plus tôt, semblant confirmer la présence des interactions longue distance via des vibrations collectives des protéines. En conclusion, la possibilité d'exciter des interactions électrodynamiques longue distance entre biomolécules est pour la première fois démontrée dans cette thèse.

Abstract

The dynamics of organisms at the molecular level is still poorly understood to this day. Great scientific advances have made it possible to describe in detail the cellular signaling pathways and short distance interactions between biomolecules involved in these signaling pathways, but the phenomenon allowing such precise and rapid interactions between these biomolecules, both in space and time, remains largely to be identified. Our research is based on a series of proposals concerning long-distance electrodynamic interactions (notably proposed by Herbert Fröhlich in the 1970s). According to recent results based on the first principles of electromagnetism, it is possible to deduce the existence of electrodynamic interactions between biomolecules - due to the vibrations of their electric dipoles - acting with potential proportional to $1/r^3$ at resonance and $1/r^6$ out of resonance (r is the intermolecular distance). In order for these dipoles to resonate, an energy supply is necessary so that the system is out-of-equilibrium. We have therefore initially used a broadly studied globular protein (Bovine Serum Albumin or BSA) covalently labeled with a fluorochrome (Alexa Fluor 488) to allow an internal energy conversion into collective vibrations of an external energy supply through laser light. A relevant experimental outcome has been obtained by using terahertz spectroscopy devices based on near-field detectors. This concerned the appearance of absorption peaks near 314 GHz, once the sample proteins were brought out of thermal equilibrium. These initial results are consistent with the theory and therefore confirm the possibility of stimulating out-of-equilibrium collective vibrations of proteins. Experiments were also carried out to study protein dynamics under similar conditions. Firstly, an experimental feasibility study has been performed to determine whether the use of a Fluorescence Correlation Spectroscopy (or FCS) device would be suitable for detecting long-range forces through the diffusion properties of particles. Built-in electrostatic interactions have been used for this purpose. After validation of the technique, since the needed high concentrations of fluorescent molecules constitutes a technical problem (causing detector blinding), we have tested and reported the use of optical density filters (OD filters) for FCS and FCCS (Fluorescence Cross-Correlation Spectroscopy) devices. The measurements were successfully carried out in FCCS, but technical problems involving the adsorption of protein by the wells of cuvettes and the releasing of free fluorochromes by the proteins, hitherto did not allow us to satisfactorily conclude on the diffusion of the BSA. To overcome these problems, we have performed the same experiments using another protein called R-phycoerythrin, which has an important role in photosynthesis as part of light-harvesting complexes, absorbing green and blue light. The results showed a clustering transition of the solvated proteins when the average intermolecular distance is below 1050Å, and provided that a threshold value of the laser excitation is exceeded. Brownian diffusion of free proteins being maintained below the mentioned laser power threshold and/or above an average intermolecular distance of 1050Å. The formation of these aggregates in similar conditions have been predicted by numerical simulations recently obtained. The tight similarity between the experimental results and theoretical predictions lends strong support to the interpretation of the experimental observations as due to the presence of long-distance electrodynamic interactions. In conclusion, this thesis documents for the first time the possibility of activating these long-distance interactions among biomolecules. We anticipate that these findings will lead to a broad domain of investigations both in vitro and in vivo.